Abstract

Al-QASIR, IYAD IBRAHIM. Thermal Neutron Scattering in Graphite. (Under the direction of Prof. Ayman I. Hawari).

Generation IV Very High Temperature Reactor (VHTR) concepts, are graphite moderated and gas cooled thermal spectrum reactors. The characteristics of the low energy (E < 1 eV) neutron spectrum in these reactors will be dictated by the process of neutron slowing-down and thermalization in the graphite moderator. The ability to accurately predict this process in these reactors can have significant neutronic and safety implications. In reactor design calculations, thermal neutron scattering cross section libraries are needed for the prediction of the thermal neutron environment in the core. Currently used libraries (ENDF/B-VII) are a product of the 1960s and remain based on many physical approximations. In addition, these libraries show noticeable discrepancies with experimental data.

In this work, investigation of thermal neutron scattering in graphite as a function of temperature was performed. The fundamental input for the calculation of thermal neutron scattering cross sections, i.e., the phonon frequency distribution and/or the dispersion relations, was generated using a modern approach that is based on quantum mechanical electronic structure (*ab initio*) simulations combined with a lattice dynamics direct method supercell approach. The calculations were performed using the VASP and PHONON codes. The VASP calculations used the local density approximation, and the projector augmented-wave pseudopotential. A supercell of 144 atoms was used; and the integration over the Brillouin zone was confined to a 3×3×4 k-mesh generated by the Monkhorst-Pack scheme. A plane-wave basis set with an energy cutoff of 500 eV was applied. The corresponding dispersion relations, heat capacity, and phonon frequency distribution show excellent agreement with experimental data.

Despite the use of the above techniques to produce more accurate input data, the

examination of the results indicated persistence of the inconsistencies between calculations and measurements at neutron energies below the Bragg cutoff (~ 1.8 meV). Consequently, this motivated the examination of the principal assumption in thermal scattering cross section calculations for graphite, i.e., the incoherent approximation. For a strongly coherent scatterer like graphite, the coherent one-phonon scattering law and corresponding cross section were calculated exactly and without approximations. The required input to perform such calculation, e.g., the dispersion relations and polarization vectors were taken from the results of the graphite lattice dynamics calculations mentioned above. As a result, significant improvements were achieved especially in the scattering law characteristic behavior at small momentum and energy transfers, and excellent agreement was found between the calculated inelastic scattering cross sections and the experimental data of pyrolytic graphite.

Furthermore, a consistent approach for defining the parabolic region in the phonon frequency distribution of graphite for use in calculations using the incoherent approximation was developed. This approach is based on the graphite mean square displacement and the agreement of the one-phonon cross sections as generated using both the incoherent approximation and the self part of the coherent one-phonon cross section. In this case, the parabolic energy cutoff was found to be 5.60 meV (equivalent to 65 K).

Finally, the effect of temperature (anharmonicity) on the phonon frequency distribution was addressed and investigated by estimating the effects of energy shift and broadening of the distribution as a function of temperature. It was found that in graphite at low energies an energy shift is expected towards higher values. This is due to negative Gruniesen parameters. The phonon frequency distribution was broadened using a Lorentzian distribution, where the broadening effect has linear temperature dependence at high temperatures. Therefore, the broadening and shift operations are two competing processes at low energies, resulting in relative differences in the calculated cross sections of less than 10 % at all temperatures.

THERMAL NEUTRON SCATTERING IN GRAPHITE

by

IYAD IBRAHIM AL-QASIR

A dissertation submitted to the Graduate Faculty of
North Carolina State University
in partial fulfillment of the
requirements for the Degree of
Doctor of Philosophy

Nuclear Engineering

Raleigh, North Carolina

2007

APPROVED BY:

Ayman I. Hawari (Chair of Advisory Committee)	K. L. Murty
Bernard W. Wehring	Marco B. Nardelli

Biography

Iyad Al-Qasir was born in Salt, Jordan on March, 7th 1976. He grew up there and graduated from Salt High School in 1994. He received a Bachelor of Science degree in Physics from the University of Jordan in 1998 where he graduated first in his class. After that he continued his graduate studies there and obtained a Master of Science degree in Physics in 2002. He attended the PhD program at the Department of Nuclear Engineering at North Carolina State University also during 2002 under the supervision of Dr. Ayman I. Hawari. In 2006 he married Huda Al-Hyari.

Acknowledgments

I would like to express my sincere gratitude and deepest appreciation to Dr. Ayman I. Hawari who encouraged me in working in this field. I would like to thank him for the constant source of guidance, and for the patience and encouragement throughout my studies. I will always remember his great motivation and enthusiasm in my career life.

Also, I would like to thank Dr. Bernard W. Wehring for his advice, help, and support of this work. I am also grateful to Dr. Marco B. Nardelli for the useful and interesting discussions throughout this work. Also, I am thankful to Dr. K. L. Murty for serving in my dissertation committee.

Special thanks to Dr. Victor Gillette and Dr. Tong Zhou for their collaboration and friendship.

I am deeply indebted to my family for their endless love, encouragement, and constant supplication to God to protect me. I would like to dedicate this work to my parents, brothers Ahmad, his wife and his little kids (Mudar, and Mera), Anmar, and Osama, and to my dearest wife Huda, without their support, and patience, this work would not have become a true.

Table of Contents

List of Figures

List of Tables

Chapter 1 Introduction

1.1 Generation IV Very High Temperature Reactors (VHTR)

Today, Nuclear power reactors generate electricity for nearly 1 billion people; they account for approximately 17 percent of worldwide electricity generation and provide half or more of the electricity in a number of industrialized countries. In the approaching decades, industrialized countries, and the entire world will need energy and an upgraded energy infrastructure to meet the growing demands for electric power and transportation fuels [1].

Nuclear power reactors have an excellent operating record and generate electricity in a reliable, environmentally safe, and affordable manner without emitting noxious gases into the atmosphere. Concerns over energy resource availability, climate change, air quality, and energy security suggest an important role for nuclear power in future energy supplies. While the current Generation II and III nuclear power plant designs provide a secure and low-cost electricity supply in many markets, further advances in nuclear energy system design can broaden the opportunities for the use of nuclear energy.

To explore these opportunities, the Generation IV International Forum (GIF) identified nuclear energy system concepts for producing electricity that excel at meeting the goals of superior economics, safety, sustainability, proliferation resistance, and physical security. The Generation IV International Forum (GIF) was established in January 2000 to investigate innovative nuclear energy system concepts for meeting future energy challenges. GIF

members include Argentina, Brazil, Canada, Euratom, France, Japan, South Africa, South Korea, Switzerland, United Kingdom, and United States, with the OECD-Nuclear Energy Agency and the International Atomic Energy Agency as permanent observers. In July 2006, the GIF voted unanimously to extend an offer of membership to China and Russia, with formal entry expected in November of 2006. The forum serves to coordinate international research and development on promising new nuclear energy systems-known as Generation IV-for meeting future energy challenges. Generation IV nuclear energy systems are future, next-generation technologies that will compete in all markets with the most cost-effective technologies expected to be available over the next three decades. Comparative advantages include reduced capital cost, enhanced nuclear safety, minimal generation of nuclear waste, and further reduction of the risk of weapons materials proliferation. Generation IV systems are intended to be responsive to the needs of a broad range of nations and users. The purpose of Gen IV is to develop nuclear energy systems that would be available for worldwide deployment by 2030 or earlier. The Generation IV Systems selected in 2002 are: Gas-Cooled Fast Reactor (GFR), Supercritical-Water-Cooled Reactor (SCWR), Sodium-Cooled Fast Reactor (SFR), Lead-Cooled Fast Reactor (LFR), Molten Salt Reactor (MSR), and Very-High-Temperature Reactor (VHTR) [2, and 3].

GIF members have selected six concepts to develop in order to meet the technology goals for new nuclear systems. One of these systems—the Very-High-Temperature (VHTR), shown in figure1-1 is uniquely suited for producing hydrogen. The Very-High-Temperature Reactor (VHTR) system is a graphite-moderated, helium-cooled reactor with thermal neutron

spectrum and a once-through uranium cycle. It is primarily aimed at relatively faster deploy of a system for high temperature process heat applications, such as coal gasification and thermochemical hydrogen production, with superior efficiency. The reference reactor concept has a 600-MWth helium cooled core based on either the prismatic block fuel of the Gas Turbine–Modular Helium Reactor (GT-MHR) or the pebble fuel of the Pebble Bed Modular Reactor (PBMR). The VHTR system has coolant outlet temperatures above 1000 °C. It is intended to be a high-efficiency system that can supply process heat to a broad spectrum of high temperature and energy-intensive, non-electric processes. The system has the flexibility to adopt U/Pu fuel cycles and offer enhanced waste minimization. The VHTR system is highly ranked in economics because of its high hydrogen production efficiency, and in safety and reliability because of the inherent safety features of the fuel and reactor. It is rated good in proliferation resistance and physical protection, and neutral in sustainability because of its open fuel cycle. It is primarily envisioned for missions in hydrogen production and other process-heat applications, although it could produce electricity as well.

The VHTR can produce hydrogen from only heat and water by using the thermochemical iodine-sulfur (I-S) process or from heat, water, and natural gas by applying the steam reformer technology to core outlet temperatures greater than about 1000 °C. A 600 MWth VHTR dedicated to hydrogen production can yield over 2 million cubic meters per day. The VHTR can also generate electricity with high efficiency, over 50% at 1000 °C, compared with 32% at 315 °C and 2500 psi in the pressurized water reactor (PWR) [1, 4].

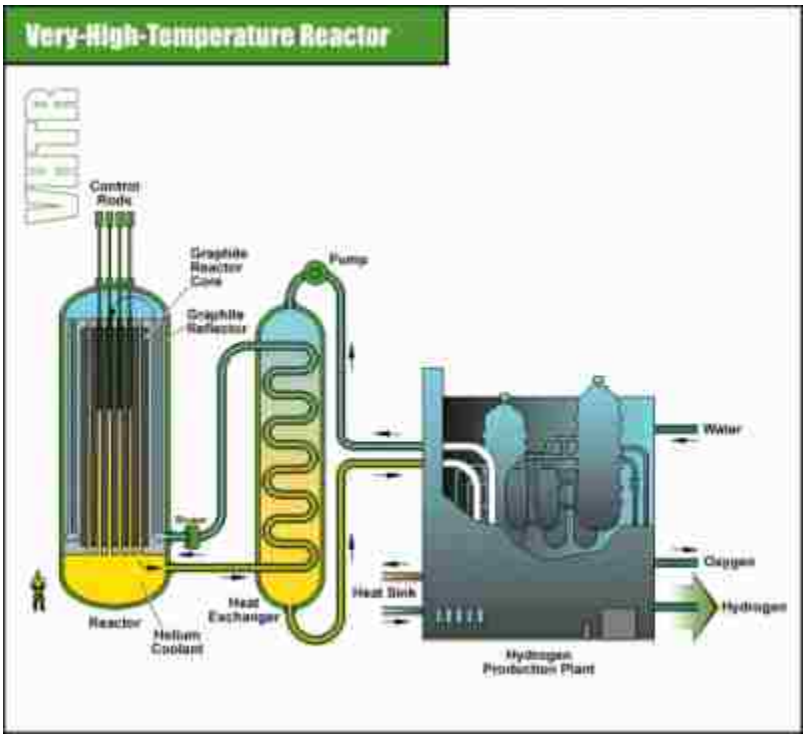

Figure 1-1 The Very-High-Temperature Reactor (VHTR) [1].

1.2 Graphite as a Neutron Moderator

Graphite was employed as a moderator in the first reactor CP1, by Enrico Fermi at the University of Chicago, in 1942. The function of a moderator is to slow down fast neutrons effectively with minimum absorption of neutrons. Neutrons emitted at fission are fast, with average energy of 2 MeV. These neutrons are not readily captured by fuel nuclei. Thermal neutrons are much more efficient in producing fission in (^{233}U, ^{235}U and ^{239}Pu). That is the fission cross section becomes quite high at thermal energies. Nuclear graphite is employed with considerable success in nuclear reactors as a moderator because of its low atomic weight, low neutron absorption cross section, and high neutron scattering cross section. In addition, the high strength of graphite at elevated temperatures, its exceedingly high sublimation point, and its excellent resistance to rupture by thermally induced stress make it of great value in

high temperature reactors [5].

The effectiveness of a substance in slowing down neutrons can be characterized by the average lethargy gain ξ, and consequently the average number of collisions $\langle \# \rangle$ necessary to thermalize a fission neutron. Also, moderators have large scattering cross section Σ_s. Thus a more appropriate measure of the effectiveness of a substance in slowing down neutrons is the moderating power $\xi\Sigma_s$. However, the scattering process competes with the absorption process; therefore moderators must have small absorption cross section Σ_a. It is convenient to define as a figure of merit the moderating ratio $\frac{\xi\Sigma_s}{\Sigma_a}$. Table 1-1 shows ξ, $\langle \# \rangle$, moderating ratio, and moderating power for several moderators. The cross section values are evaluated at 2200 m/s [6].

Table 1- 1 A, ξ, $\langle \# \rangle$, moderating power , and moderating ratio for several moderators

Moderator	A	ξ	$\langle \# \rangle$	$\xi\Sigma_s$	$\xi\Sigma_s/\Sigma_a$
H_2O	18.015	0.920	16	1.35	71
D_2O	20.028	0.509	29	0.176	5670
Be	9.012	0.209	69	0.158	143
Graphite	12.011	0.158	91	0.060	192

In terms of the above data, D_2O is the superior moderator. However, light water and heavy water are both liquids or gases at the operating temperatures, thus neither can serve a

structural function, necessitating the incorporation of a structure. The hydrogen in water has a large neutron absorption cross section ($\Sigma_a = 0.022\,\text{cm}^{-1}$) which makes it impossible to achieve a critical reactor of natural uranium moderated with water, even though hydrogen is the best slowing down atom possible. Heavy water has a very small absorption cross section ($\Sigma_a = 3.323\times10^{-5}\,\text{cm}^{-1}$) so its large moderating ratio makes it as a superior moderator that can be used to construct a reactor fueled with natural uranium. However, D_2O is very expensive to be used in commercial reactors.

1.3 Graphite Neutron Cross Section

Fast neutrons emitted by fission slow down by elastic and inelastic scattering. A scattering is said to be inelastic if any of the internal quantum states of the scatterer are changed as a result of collision with a neutron, and to be elastic if there is no such change. That is, in case of the inelastic scattering the nucleus is left in an excited state after the collision, and in the case of the elastic scattering the nucleus remains in its ground state. At lower energies (intermediates energies), elastic scattering is the dominant process, resonance absorption becomes important, no inelastic scattering occurs, since for inelastic scattering process to occur, the incident neutron energy must be above the threshold energy corresponding to the lowest excited state of the target nucleus (4.4 MeV in ^{12}C). At low energies neutrons tend to be in thermal equilibrium with the scattering medium, and chemical binding plays a role in both elastically (Bragg scattering) and inelstically (phonon emission and absorption) scattered neutrons. Figure1-2 shows the total scattering cross section of graphite (^{12}C) from ENDF/B-VII [7]. One can define five different regions in the cross

section behavior, labeled from one to five [6]. In the first three regions the reactions are nuclear while for regions 4 and 5 the reactions depend on the atomic arrangement and dynamics.

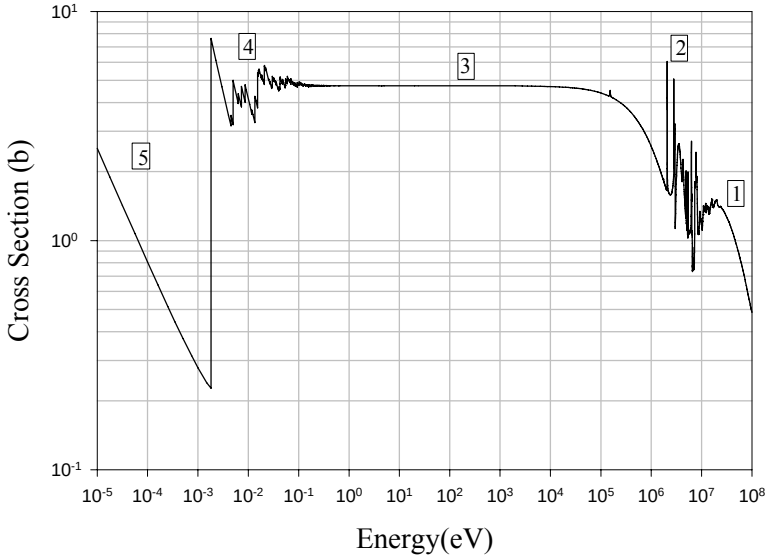

Figure 1-2 The graphite total scattering cross section.

Region one corresponds to very high energy neutrons (>10 MeV). At such energies, neutron wavelengths are very small, thus the probability of neutron interaction with the nucleus will decrease, and nucleon interactions become possible. Region two, which is represented by a jagged behavior, corresponds to resonance reaction mechanism, where the neutron incident energy is comparable to that of the lowest energy levels of the compound nucleus ^{13}C. Region three has a constant cross section, and is dominated by potential scattering, that is, the neutrons are elastically scattered by nuclei like billiard ball collisions. In regions four and five, neutrons have wave lengths that are comparable to the spacing between atoms, and they no longer interact with the free carbon atom, but instead they interact with an aggregate of atoms. For crystalline materials like graphite, the planes of

atoms work as a diffracting grating, and neutrons will elastically scatter showing the jagged behavior known as Bragg scattering, represented by region four. No Bragg scattering occurs in region five, since below a certain energy (the Bragg energy cutoff), the neutron's wavelength becomes larger than the interatomic spacing. However, inelastic scattering can occur in regions four and five where in these regions the dynamics of the graphite lattice plays an important role, that is, neutrons are inelastically scattered by the creation (dominant in region four) or annihilation (dominant in region five) of a vibrations known as phonons.

1.4 The Status of Graphite Thermal Neutron Scattering Cross Section

In nuclear reactor design, the effects of atomic and/or molecular binding become important as the neutrons slow down and enter the thermal region. The interactions of thermal neutrons (i.e., absorption and scattering) within the reactor core define the thermal neutron energy spectrum, which affects several properties such as criticality, safety, and feedback response. Therefore, the ability to accurately predict the slowing down and thermalization of neutrons in moderating materials can have significant neutronic and safety implications on nuclear power generation.

Moderator thermal neutron scattering libraries were generated in the 1960's based on many approximations. The libraries were also recalculated and released in 1994 by Los Alamos National Lab [8]. These libraries introduced some improvements on the coherent and incoherent elastic scattering, including the multiphonon expansion, extending the momentum and energy transfer grids beyond that of previous libraries, and the capability of

producing mixed scattering law of materials like BeO and Benzene [8]. However, the same approximations were used and no significant changes have been made to introduce new theories and data. In the case of graphite the incoherent approximation was used, and the same dynamical lattice model was used (Young-Koppel model) [9], even though scattering law measurements and inelastic scattering cross section measurements show a significant discrepancy between calculations and measurements. The inelastic scattering cross section of graphite at 300 K using the same standard library ENDF/B-VI compared to measured data [10, 11, 12, and 13] is shown in figure1-3. As seen, large discrepancy (~100%) between the calculated and measured data [11, 12, and 13) is observed. Also, two experimental sets for graphite with different values are shown, this issue was not addressed to date and will be interpreted later in this work.

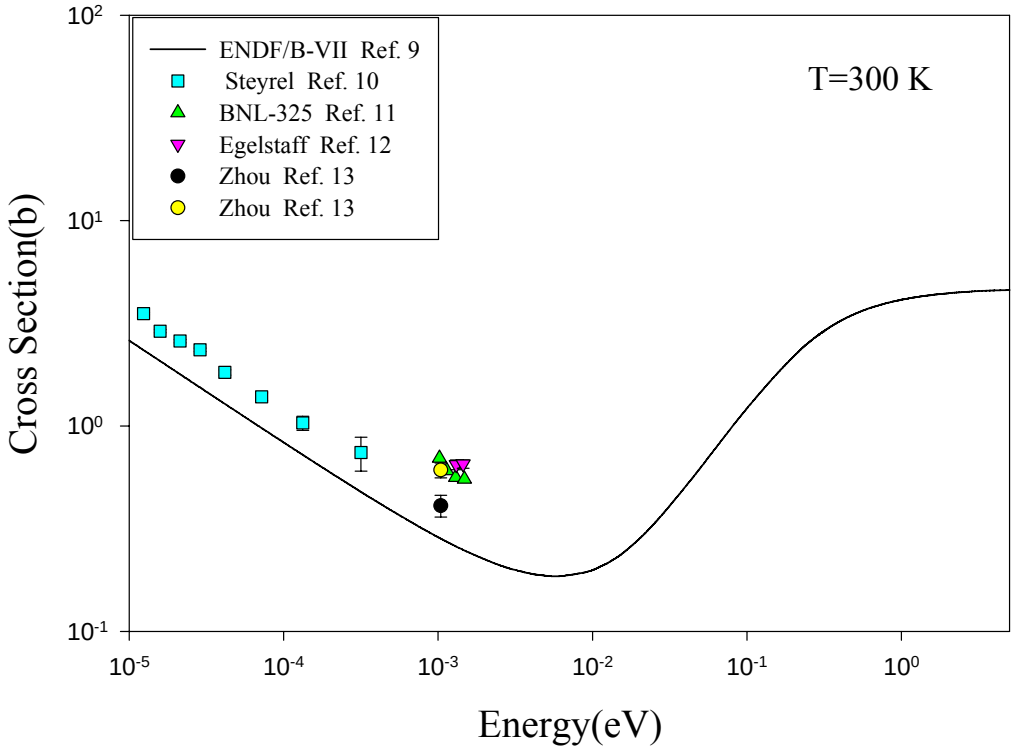

Figure 1-3 The inelastic scattering cross section in the incoherent approximation at T=300 K compared to experimental data.

This study will concentrate on investigating temperature dependence of thermal neutron scattering in graphite. Specifically, the objectives of this study are:

a) To critically review the currently used thermal neutron scattering laws of graphite as a function of temperature
b) To update models and model parameters introducing the new developments in solid-state physics, and the coherent part of the inelastic scattering
c) To generate new sets of temperature dependent neutron scattering laws
d) To include the effect of temperature on the graphite dynamical models, specifically the Anharmonicity effect

1.5 Graphite: The Perfect Single Crystal Lattice

Carbon, as one of the elements in the fourth column in the periodic table, it can unite easily with itself, with hydrogen, and with other elements to give rise to an extraordinary number of compounds. Carbon can crystallize in different forms (allotropes); graphite, diamond, carbines, and fullerene [14]. The properties of such allotropes can vary widely, for example, diamond is the hardest known material and is transparent to visible light. Graphite can be considered as one of the softest and is opaque.

Carbon atoms can bond together in various ways to form molecules and solids. This kind of bonding is covalent and takes the forms: *sp* (as in acetylene C_2H_2), sp^2 (as in graphite and ethylene C_2H_4), and sp^3 (as in diamond and methane CH_4). The graphite structure can be understood via a look at its bonding sp^2. Bonding in graphite exhibits one of the largest

anisotropies of any solid. The nearest-neighbor bond in graphite is considered stronger than the nearest neighbor bond in diamond [15]. This strong bond is a covalent sp^2 (σ-bond), and has a short length 1.42 Å. In contrast, the bonding between planes is very weak and exhibits a Van der Waals interaction. The spacing between layers is relatively large (3.35 Å), that is, more than twice the spacing between atoms within the basal plane. This is due to the pairing between the hybridized fourth valence electron with another delocalized electron of the adjacent plane (π-bond). The electron configuration of the six electrons of the carbon atom in the ground state is $1s^2 2s^2 3p^2$, that is, two electrons are in the K shell, and four in the L shell. To form an sp^2 hybridization, the arrangement of the electrons of the L shell is modified such that one of the *2s* electrons is promoted and combined with two of the *2p* orbitals (hence the designation sp^2) to form three sp^2 orbitals and unhybridized free (or delocalized) *p* orbital electron as shown in figure 1-4. The three identical sp^2 orbitals are in the same plane and their orientation is 120° from each other, as shown in figure 1-5. The fourth orbital (delocalized non-hybridized p electron) is directed perpendicularly to the plane of the three sp^2 orbitals and becomes available to form $(\pi - bond)$ with other atoms [14, 16]. The sp^2 bond is covalent and is a strong bond, because of the three sp^2 valence electrons and the small size of the atom. The sp^2 is directional and is called a σ-orbital, and the bond is a σ-bond. Each sp^2 hybridized carbon atom combines with three other sp^2 hybridized atoms to form a series of planar hexagons, as shown in figure 1-6. Unlike the σ-orbital, the delocalized electron is non symmetric, and called by convention a π-orbital, and the bond is π-bond. This electron can move from one side of the plane layer to the other but can not easily move from one layer to another. As a result graphite is anisotropic.

Carbon Atom Ground State

K-Shell Electrons	L-Shell Electrons			
1s	2s	$2p_x$	$2p_y$	$2p_z$
↑↓	↑↓	↑	↑	

⇓

sp^2 Hybridization

K-Shell Electrons	L-Shell Electrons			
1s	$2sp^2$	$2sp^2$	$2sp^2$	$2p$
↑↓	↑	↑	↑	Delocalized electron

Figure 1-4 The sp^2 hybridization of carbon orbitals.

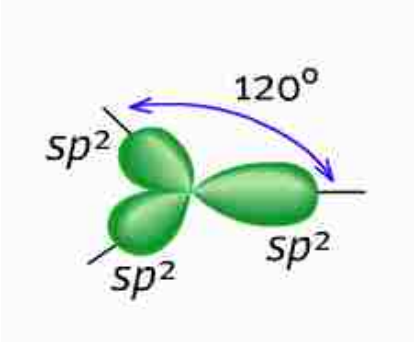

Figure 1-5 The sp^2 hybrid orbitals of the carbon atom.

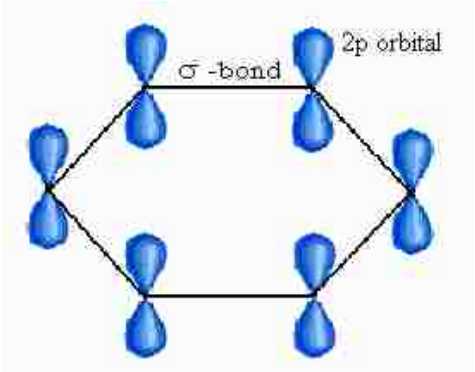

Figure 1-6 A schematic of the sp^2 hybridized structure of graphite.

Graphite has two crystalline forms, a hexagonal crystal structure, and a rhombohedral form as a minor subsistuent (few percent of the well crystalline graphite). Rhombohedral graphite is thermodynamically unstable, and can be considered as an extended stacking fault of hexagonal graphite. It is never found in pure form, but always in combination with hexagonal graphite. Mechanical processes such as grinding and chemical treatments can increase the relative portion of rhombohedral graphite up to ~20%, which indicates that such changes are due to the movements of carbon layers with respect to one another.

The fact that the properties of rhombohedral packing are reduced by high temperature –heat treatment (2000-3000 °C), and it is almost absent in synthetic graphite indicates that the hexagonal form is more stable [17]. Figure 1-7 shows the hexagonal ABAB- and the rhombohedral ABCABC-stacking. However, hexagonal graphite is the most common stacking sequence of graphite. Carbon atoms are joined together in sheets (graphene planes) and each atom has three nearest neighbors forming a series of continuous hexagons. These sheets are loosely bound to one another.

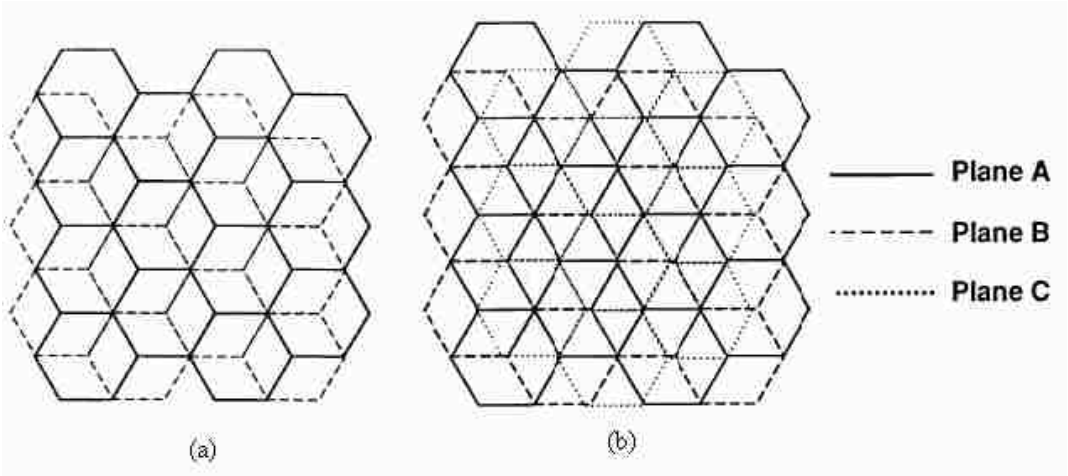

Figure 1-7 A schematic of (a) Hexagonal graphite (AB-stacking), and (b) rhombohedral graphite (ABC –stacking).

A single sheet of such atoms provides an example of two dimensional crystals, as shown in figure 1-8. The arrangement of atoms can be described by choosing a small unit such as $OXYZ$, then by repeating the unit until the space is filled with identical units. The chosen unit represents a 2-dimensional unit (unit parallelogram). In such a unit, the lengths OX and OY are denoted by the vectors $\vec{a}$, and $\vec{b}$, respectively, where the angle between them is γ. In the case of graphite, the nearest neighbor atomic spacing in the net plane is 1.42 Å. As a result $\vec{a}=\vec{b}$ =2.46 Å, and $\gamma = 120^{\circ}$. As we see there are four atoms, one at each corner (O, X, Y, and Z), and one atom P inside the parallelogram. To describe their positions, we take the sides of the parallelogram $\vec{a}$ and $\vec{b}$ as one unit of length. Thus, their coordinates are $O(0,0)$, $X(1,0)$, $Y(0,1)$, $Z(1,1)$, and $P(1/3,\ 2/3)$. Note that, the atoms at the corners (O, X, Y, and Z) are identical, and each atom contributes to the unit parallelogram by $1/4$, so the total number of atoms is two located at $(0,0)$ and $(1/3,\ 2/3)$.

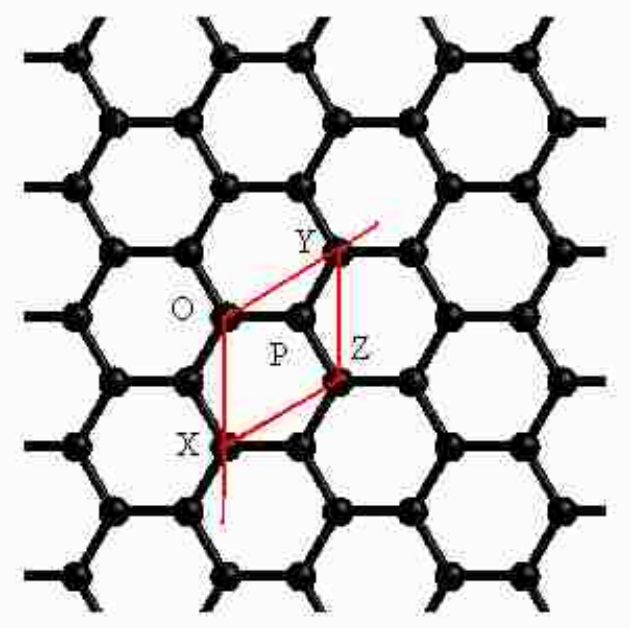

Figure 1-8 A single sheet of graphite which shows the unit parallelogram.

The three dimensional unit cell of graphite is shown in figure 1-9, it belongs to space group number 194 $(P6_3/mmc)$ and has four atoms, located at $(0,0,1/4)$, $(1/3,2/3,1/4)$, $(0,0,3/4)$, and $(2/3,1/3,3/4)$. Extending the unit cell will create layers, where no basal plane lies directly over another one.

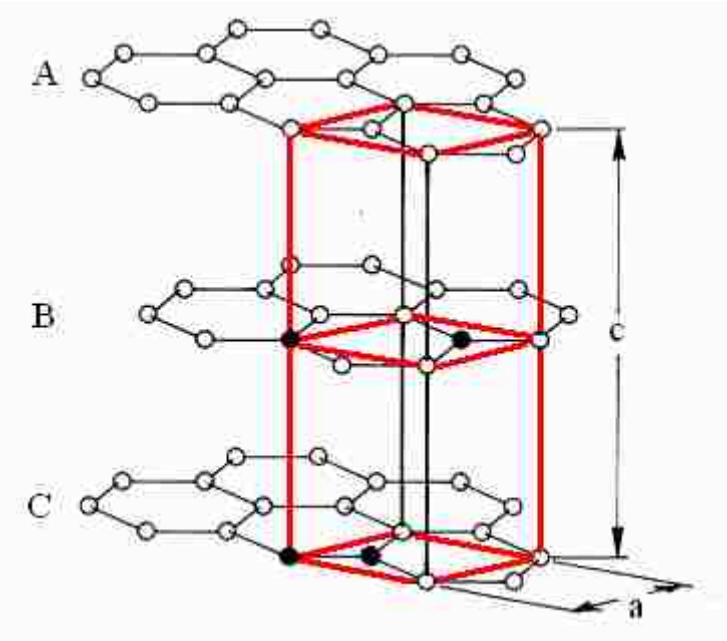

Figure 1-9 The three Dimensional crystal structure of the graphite hexagonal lattice. The graphite unit cell is shown in red, and its atoms are shown in black solid circles.

Chapter 2 Thermal Neutron Scattering Cross Section

2.1 Neutron Thermalization

The subject of neutron thermalization is interested in two kinds of problems; the study of the thermal neutron scattering cross section in various materials, and the study of the energy spectrum of thermal neutrons that develops using these cross sections.

Thermal neutrons have wavelengths comparable to the separation distances of atoms in solids or liquids; therefore, interference effects take place, that is, neutrons will interact with an aggregate of atoms rather than with a single atom. As a consequence thermal neutrons are a useful tool in studying the structure of different scattering systems. Moreover, the energy of thermal neutrons is of the same order of magnitude as that of excitations in a scattering medium (e.g., phonons in a solid). Therefore, thermal neutrons are a useful tool in providing information about the excitation spectra and hence the dynamics of the scattering medium.

In considering thermal neutron interactions with matter, the thermal motion of atoms can no longer be ignored (as we see will later, this thermal motion is the basic key in connecting quantum mechanics, solid state physics, and statistical mechanics to derive an expression for the thermal scattering cross section), and since these neutrons have energies comparable to the binding energies of the scattering medium, these atoms can not be assumed to be free, that is, there is an interaction between the scattering nucleus and its surrounding nuclei.

Furthermore, thermal neutrons can gain energy due to up scattering or lose energy due to down scattering. As a result, the thermal neutron scattering cross section is a complicated function of energy, angle, physical state (solid, liquid, or gas) chemical form, and temperature [18, 19, and 20].

2.2 Scattering Cross Section Concepts

The interaction probability of neutrons with matter is described by a quantity called the cross section. Figure 2.1 below shows the geometry of a scattering experiment where a thin target of area A and thickness x containing N_v atoms per unit volume is placed in a mono-directional and mono-energetic beam of neutrons. A neutron detector is placed at some distance from the target to measure the neutrons scattered in a given direction. The distance between the detector and the target is large compared to the dimensions of the detector, so a small solid angle $d\Omega$ subtended by the detector and the target is well defined. Experimentally, the number of neutrons dn scattered into the detector per unit time is proportional to the beam intensity I (per unit area per unit time), atomic density N_v, target area A, target thickness x, and the solid angle $d\Omega$. That is,

$$dn = \frac{d\sigma}{d\Omega} I N_v A x d\Omega . \tag{2.1}$$

The above equation defines the proportionality factor $\frac{d\sigma}{d\Omega}$ which is called the differential scattering cross section. It is defined as the number of neutrons scattered per second per solid angle $d\Omega$ divided by the incident flux Φ. This definition can be related to a quantum mechanical expression as follow: a neutron with state $\left|\vec{k}\right\rangle$ interacts with a

scattering medium (target) in state $|\lambda\rangle$ via the interacting potential V, after the interaction, the neutron has a new state $|\vec{k}'\rangle$ and the scattering medium has a state $|\lambda'\rangle$.

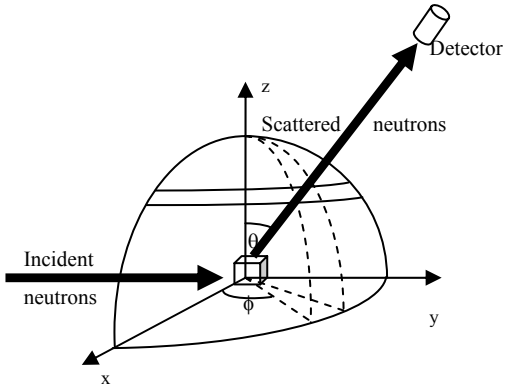

Figure 2-1 The geometry of scattering experiment.

If $W\left(|\vec{k}\lambda\rangle \to |\vec{k}'\lambda'\rangle\right)$ is the transition rate from the initial state $|\vec{k}\lambda\rangle$ to the final state $|\vec{k}'\lambda'\rangle$, then the differential scattering cross section is written as

$$\left(\frac{d\sigma}{d\Omega}\right)_{|\vec{k}\lambda\rangle\to|\vec{k}'\lambda'\rangle} = \frac{W\left(|\vec{k}\lambda\rangle \to |\vec{k}'\lambda'\rangle\right)}{\Phi\ d\Omega}. \tag{2.2}$$

The transition rate based on time-dependent first order perturbation theory can be evaluated either by using (the first) Born approximation, or Fermi's golden rule. This leads to

$$\left(\frac{d\sigma}{d\Omega}\right)_{|\vec{k}\lambda\rangle\to|\vec{k}'\lambda'\rangle} = \frac{k'}{k}\left(\frac{m}{2\pi\,\hbar^2}\right)^2 \left|\langle k'\lambda'|V|k\lambda\rangle\right|^2 \tag{2.3}$$

where m is the neutron mass and $\hbar$ is the reduced Planck's constant.

2.2.1 Transition Matrix and Born Approximation

The Schrödinger equation describes the interaction of two particles through a potential $V\left(\vec{R}-\vec{r},t\right)$. In scattering type experiments the incident beam of particles is switched on for times very long compared with the time a particle would take to cross the interaction region,

so the interaction potential can be considered as a time-independent potential $V(\vec{R}-\vec{r})$. Consider the time-dependent Schrödinger equation:

$$\left[i\hbar \frac{\partial}{\partial t} + \frac{\hbar^2}{2m}\nabla_r^2 + \frac{\hbar^2}{2M}\nabla_R^2 \right] \Psi_{\lambda k}\left(\vec{R},\vec{r},t\right) = V(\vec{R}-\vec{r})\,\Psi_{\lambda k}\left(\vec{R},\vec{r},t\right). \tag{2.4}$$

where $i\hbar\frac{\partial}{\partial t}$ is the energy operator, $-\frac{\hbar^2}{2m}\nabla_r^2$ is the neutron kinetic energy operator, and $-\frac{\hbar^2}{2M}\nabla_R^2$ is the nucleus kinetic energy operator. $\Psi_{\lambda k}\left(\vec{R},\vec{r},t\right)$ is the exact wave function of the time-dependent Schrödinger equation which can be written as

$$\Psi_{\lambda k}\left(\vec{R},\vec{r},t\right) = \chi_\lambda\left(\vec{R}\right)\Psi_k\left(\vec{r},t\right), \tag{2.5}$$

$\chi_\lambda\left(\vec{R}\right)$ is the scattering medium wave function, and $\Psi_k(\vec{r},t)$ is the neutron wave function. Since the interacting potential effect is small, the scattering medium atoms remain fixed before and after the collision (Born approximation), as a result the scattered neutrons will be represented by plane waves with momentum $\hbar\vec{k}'$. Thus, equation (2.4) can be simplified to take into account the neutron Hamiltonian only.

$$\left[i\hbar \frac{\partial}{\partial t} + \frac{\hbar^2}{2m}\nabla_{\mathrm{r}}{}^2 \right] \Psi_{\lambda k}\left(\vec{R},\vec{r},t\right) = V(\vec{R}-\vec{r})\,\Psi_{\lambda k}\left(\vec{R},\vec{r},t\right). \tag{2.6}$$

There exists a stationary solution corresponding to neutron incident energy $E = \frac{\hbar^2 k^2}{2m}$

$$\Psi_{\lambda k}\left(\vec{R},\vec{r},t\right) = \frac{1}{\sqrt{(2\pi)^3}}\Psi_{\lambda k}\left(\vec{R},\vec{r}\right)exp\left(-iEt/\hbar\right), \tag{2.7}$$

where $\Psi_{\lambda k}(\vec{R},\vec{r}) = \chi_\lambda\Psi_k$ is the solution of the time-independent Schrödinger equation:

$$\left[-\frac{\hbar^2}{2m}\nabla_{\mathrm{r}}{}^2 + V(\vec{R}-\vec{r}) \right] \Psi_{\lambda k}\left(\vec{R},\vec{r}\right) = E\Psi_{\lambda k}\left(\vec{R},\vec{r}\right), \tag{2.8}$$

which can be written in terms of the reduced potential $U(\vec{r}-\vec{R}) = \frac{2m}{\hbar^2}V(\vec{r}-\vec{R})$ as

$$\left[\nabla^2 - U(\vec{r}-\vec{R}) + k^2\right]\Psi_{\lambda k}\left(\vec{R},\vec{r}\right) = 0 \cdot \tag{2.9}$$

Of interest are wave functions at large *r*, because the detector is so far from the region of interaction. As $r \to \infty, U(\vec{r}-\vec{R}) \to 0$, and equation (2.9) reduces to

$$\left[\nabla^2 + k^2\right]\Psi^{un}{}_k\left(\vec{r}\right) = 0 \cdot \tag{2.10}$$

This equation represents a free particle Schrödinger equation. $\Psi^{un}{}_k\left(\vec{r}\right)$ is the unperturbed wave function that corresponds to $U(\vec{r}-\vec{R}) \to 0$ represented by a plane wave with momentum $\hbar\vec{k}$

$$\Psi^{un}{}_k\left(\vec{r}\right) = e^{i\vec{k}\cdot\vec{r}} . \tag{2.11}$$

Let

$$\varphi_k(\vec{r},t) = \frac{1}{\sqrt{(2\pi)^3}}\Psi^{un}{}_k\left(\vec{r}\right) exp\left(-iEt/\hbar\right) = \frac{1}{\sqrt{(2\pi)^3}} exp[i\{\vec{k}\cdot\vec{r} - Et/\hbar\}], \tag{2.12}$$

be the solution of the time-dependent unperturbed Schrödinger equation

$$\left[i\hbar\frac{\partial}{\partial t} + \frac{\hbar^2}{2m}\nabla_r{}^2\right]\varphi_k\left(\vec{r},t\right) = 0 \cdot \tag{2.13}$$

So that $\varphi_k(\vec{r},t)$ has the standard normalization

$$\int \varphi^*_{k'}\varphi_k d\vec{r} = \delta(\vec{k}-\vec{k}') . \tag{2.14}$$

The functions $\varphi_k(\vec{r},t)$ form a complete set, so the exact solution $\Psi_{\lambda k}\left(\vec{R},\vec{r},t\right)$ can be expanded as

$$\Psi_{\lambda k}\left(\vec{R},\vec{r},t\right) = \int c(t)\,\chi_\lambda\left(\vec{R}\right)\varphi_k(\vec{r},t)\, d\vec{k} . \tag{2.15}$$

By substituting equation (2.15) into the left hand side of equation (2.6) and making use of equation (2.12 and 2.13), the following form is obtained

$$\int i\hbar\,\dot{c}(t)\,\chi_\lambda(\vec{R})\,\varphi_k(\vec{r},t)d\vec{k} = V(\vec{R}-\vec{r})\Psi_{\lambda k}\left(\vec{R},\vec{r},t\right). \tag{2.16}$$

Multiplying both sides of equation (2.16) from the left by $\chi^*_{\lambda'}\,\varphi^*_{k'}$ and integrating over

$d\vec{R}\,d\vec{r}$ to obtain

$$i\hbar\,\dot{c}(t) = \iint \chi^{*}_{\lambda'}(\vec{R})\,\varphi^{*}_{k'}(\vec{r},t)\,V(\vec{r}-\vec{R})\,\Psi_{\lambda k}(\vec{R},\vec{r},t)\,d\vec{R}\,d\vec{r}\,. \tag{2.17}$$

Substituting equations (2.7) and (2.16) into equation (2.17)

$$i\hbar\,\dot{c}(t) = \frac{1}{(2\pi)^3}\,e^{i\omega t}\iint \chi^{*}_{\lambda'}\,e^{i\vec{k}'\cdot\vec{r}}\;V(\vec{r}-\vec{R})\,\chi_{\lambda}\;\Psi_{\mathrm{k}}(\vec{\mathrm{r}})\,d\vec{R}\,d\vec{r}\,, \tag{2.18}$$

where

$$\omega = \frac{E(k') - E(k)}{\hbar}\,. \tag{2.19}$$

The integrand in equation (2.18) is called a transition matrix element $T(|\lambda k\rangle \to |\lambda' k'\rangle)$, namely,

$$T(|\lambda k\rangle \to |\lambda' k'\rangle) = \langle \lambda' k'|V|\lambda k\rangle = \iint \chi^{*}_{\lambda'}\,e^{i\vec{k}'\cdot\vec{r}}\;V(\vec{r}-\vec{R})\;\chi_{\lambda}\;\Psi_{k}(\vec{r})\,d\vec{R}\,d\vec{r}\,. \tag{2.20}$$

It holds during the period $0 \le t \le t_{\circ}$, where $t_{\circ}$ is the duration of the experiment, which is long compared with the time any scattered particle spends in an interaction with the target. Integrating equation (2.18) with respect to time between 0 and $t_{\circ}$, and setting $c(0) = 0$

$$c(t) = \frac{1}{(2\pi)^3}\,\frac{1-e^{i\omega t}}{\hbar\omega}\iint \chi^{*}_{\lambda'}\,e^{i\vec{k}'\cdot\vec{r}}\;V(\vec{r}-\vec{R})\,\chi_{\lambda}\;\Psi_{\mathrm{k}}(\vec{\mathrm{r}})\,d\vec{R}\,d\vec{r}\,. \tag{2.21}$$

The transition rate $\mathrm{W}(|\mathbf{k}\lambda\rangle \to |\mathbf{k}'\lambda'\rangle)\,d\vec{k}'$ for scattering into a final state in which the wave vector $\vec{k}'$ lies in the interval $\vec{k}'$ and $\vec{k}' + d\vec{k}'$ is

$$\begin{aligned} W(|\mathbf{k}\lambda\rangle \to |\mathbf{k}'\lambda'\rangle)\,d\vec{k}' &= \frac{1}{t_{\circ}}|c(t)|^2\,d\vec{k}' \\ &= \frac{1}{(2\pi)^6\hbar^2}\left|T(|\lambda k\rangle \to |\lambda' k'\rangle)\right|^2\,\frac{2(1-\cos\omega t_{\circ})}{\omega^2 t_{\circ}}\,d\vec{k}'. \end{aligned} \tag{2.22}$$

The above equation represents the probability that a particle, which started out in the state $|\lambda\vec{\mathrm{k}}\rangle$ will be found at time $t_{\circ}$ in state $|\lambda'\vec{\mathrm{k}}'\rangle$. The direction of $\vec{k}'$ is the direction of

propagation of the scattered particle, that is

$$d\vec{k}' = k'^2 dk' sin\theta \, d\theta \, d\varphi = k'^2 dk' d\Omega \,, \tag{2.23}$$

which can be written in terms of $d\omega$ as follow

$$d\vec{k}' = \frac{k' m}{\hbar} d\omega \, d\Omega \,. \tag{2.24}$$

For large $t_\circ$ (the detector is far from the scattering medium)

$$\lim_{t_\circ \to \infty} \frac{2(1-\cos \omega t_\circ)}{\omega^2 t_\circ} \to 2\pi\delta(\omega) \tag{2.25}$$

Substituting equations (2.24) and (2.25) into equation (2.22)

$$W(|\mathbf{k}\lambda\rangle \to |\mathbf{k}'\lambda'\rangle)\, d\vec{k}' = \frac{m}{(2\pi)^5 \hbar^3} \left|T(|\lambda k\rangle \to |\lambda' k'\rangle)\right|^2 k' \delta(\omega)\, d\omega \, d\Omega \,. \tag{2.26}$$

The transition rate for scattering into the element of solid angle $d\Omega$ can be obtained by integrating equation (2.26) over ω, that is $\mathrm{W}(|\mathbf{k}\lambda\rangle \to |\mathbf{k}'\lambda'\rangle)\, d\Omega$

$$W(|\mathbf{k}\lambda\rangle \to |\mathbf{k}'\lambda'\rangle)\, d\Omega = \frac{m}{(2\pi)^5 \hbar^3} k' \left|T(|\lambda k\rangle \to |\lambda' k'\rangle)\right|^2 d\Omega \,. \tag{2.27}$$

If the number of neutrons scattered per second form the state $|\mathbf{k}\lambda\rangle$ to the state $|\mathbf{k}'\lambda'\rangle$ into a solid angel $d\Omega$ is written in term of $\mathrm{W}(|\mathbf{k}\lambda\rangle \to |\mathbf{k}'\lambda'\rangle)$ as a transition rate $\mathrm{W}(|\mathbf{k}\lambda\rangle \to |\mathbf{k}'\lambda'\rangle)\, d\Omega$, then one can write $d\sigma$ as

$$d\sigma = \frac{\mathrm{W}(|\mathbf{k}\lambda\rangle \to |\mathbf{k}'\lambda'\rangle)}{\text{Incident flux}} d\Omega \cdot \tag{2.28}$$

The flux is defined as

$$\text{Flux= speed} \times \varphi^*{}_k(\vec{r},t)\, \varphi_k(\vec{r},t) \cdot \tag{2.29}$$

But the speed of the incident neutrons is $\frac{\hbar k}{m}$, and the $\varphi^*{}_k(\vec{r},t)\, \varphi_k(\vec{r},t) = \frac{1}{(2\pi)^3}$, so

$$\text{Incident flux}=\frac{1}{(2\pi)^3}\frac{\hbar k}{m}. \tag{2.30}$$

Thus, by substituting equations (2.30), and (2.27) into equation (2.28), the differential scattering cross section can be written as

$$\frac{d\sigma}{d\Omega}=\frac{k'}{k}\left(\frac{m}{2\pi\hbar^2}\right)^2\left|T(|\lambda k\rangle\rightarrow|\lambda' k')\rangle\right|^2. \tag{2.31}$$

2.2.2 The Double Differential Scattering Cross Section

The double differential scattering cross section is defined as the number of neutrons scattered per second per solid angle $d\Omega$ per unit final energy dE' divided by the incident flux. The double differential scattering cross section is related to the differential scattering cross section through the relation

$$\left(\frac{d^2\sigma}{d\Omega\, dE'}\right)_{|\vec{k}\lambda\rangle\rightarrow|\vec{k}'\lambda'\rangle}=\frac{k'}{k}\left(\frac{m}{2\pi\hbar^2}\right)^2\left|\langle k'\lambda'|V|k\lambda\rangle\right|^2\delta\left(\hbar\omega+E_\lambda-E_{\lambda'}\right), \tag{2.32}$$

where E_λ and $E_{\lambda'}$ are the initial and final energies of the scattering medium, and $\hbar\omega$ - the energy of excitation- is the difference between the incident and scattered neutron energies.

Even though the interaction potential is short, it is very strong, thus perturbation theory is not strictly applicable. However, it gives the exact form of isotropic *s*-wave scattering when combined with an artificial potential known as the Fermi-pseudopotential, where for the j^{th} nucleus at position $\vec{R}_j$ with scattering length b_j and a neutron at position $\vec{r}$, it is given by

$$V_j=\frac{2\pi\hbar^2}{m}b_j\delta\left(\vec{r}-\vec{R}_j\right). \tag{2.33}$$

Experimentally, the total double differential scattering cross section for all possible states $\frac{d^2\sigma}{d\Omega\, dE'}$ is measured, not only $\left(\frac{d^2\sigma}{d\Omega\, dE'}\right)_{|\vec{k}\lambda\rangle\to|\vec{k}'\lambda'\rangle}$. To obtain $\frac{d^2\sigma}{d\Omega\, dE'}$, the sum over all the final sates $|\lambda'\rangle$ and the average over all the initial states $|\lambda\rangle$ that occur with probability p_λ are taken. In addition, the Fermi- pseudopotential is used, and the delta-function in equation (2.33) is rewritten in an integral form. As a consequence, the total double differential neutron scattering cross section per atom of a scattering medium contains $\mathcal{N}$ atoms can be written as:

$$\frac{d^2\sigma}{d\Omega\, dE'} = \frac{k'}{k}\frac{1}{2\pi\hbar}\frac{1}{\mathcal{N}}\sum_{jj'} b_j b_{j'} \int_{-\infty}^{\infty} \left\langle \exp\left\{-i\vec{\kappa}\cdot\vec{R}_{j'}(0)\right\}\exp\left\{i\vec{\kappa}\cdot\vec{R}_j(t)\right\}\right\rangle \exp(-i\omega t)dt\,, \tag{2.34}$$

$\mathcal{N} = nN$, where N is the number of unit cells in the crystal, and n is the number of atoms per unit cell. The integrand brackets are thermal average of $\exp\left\{-i\vec{\kappa}\cdot\vec{R}_{j'}(0)\right\}\exp\left\{i\vec{\kappa}\cdot\vec{R}_j(t)\right\}$ over all states $|\lambda\rangle$ with probability p_λ, where $p_\lambda = \exp(-E_\lambda / k_B T)/\sum_\lambda \exp(-E_\lambda / k_B T)$.

2.3 Coherent and Incoherent Scattering

An element with various isotopes will scatter neutrons differently. Also if the nucleus has a spin, the scattering will depend upon whether the neutron spin $(1/2)$ and the nucleus spin (I) combine to scatter in a state of spin $I+1/2$ or $I-1/2$. Let b^+ be the amplitude of the scattering in the $I+1/2$ spin state of neutron-nucleus system, and b^- is the amplitude of the scattering in the $I-1/2$ state. There are $2(I+1/2)+1 = 2I+2$ states for spin $I+1/2$ and $2(I-1/2)+1 = 2I$ stats for $I-1/2$. So the probability of interaction in $I+1/2$ state is $\frac{2I+2}{(2I+2)+2I} = \frac{I+1}{2I+1}$ while the probability of interaction in the $I-1/2$

state is $\frac{2I}{(2I+2)+2I} = \frac{I}{2I+1}$. So the scattering length is written as

$$\bar{b} = \frac{I+1}{2I+1} b^{+} + \frac{I}{2I+1} b^{-}, \tag{2.35}$$

and

$$\overline{b^2} = \frac{I+1}{2I+1} \left(b^{+}\right)^2 + \frac{I}{2I+1} \left(b^{-}\right)^2. \tag{2.36}$$

If there are several isotopes in the scattering system, where the i^{th} isotope has a relative abundance c_i, then equations (2.35) and (2.36) can be generalized to

$$\bar{b} = \sum_i c_i \left\{ \frac{I_i+1}{2I_i+1} b_i^{+} + \frac{I_i}{2I_i+1} b_i^{-} \right\}, \tag{2.37}$$

and

$$\overline{b^2} = \sum_i c_i \left\{ \frac{I_i+1}{2I_i+1} \left(b^{+}\right)^2 + \frac{I_i}{2I_i+1} \left(b^{-}\right)^2 \right\}. \tag{2.38}$$

The bound atom coherent and incoherent scattering cross sections σ_{coh}, σ_{incoh} are given by

$$\sigma_{coh} = 4\pi(\bar{b})^2 \qquad \text{and} \qquad \sigma_{incoh} = 4\pi \{\overline{b^2} - (\bar{b})^2\}, \tag{2.39}$$

where the bound scattering cross section is defined as

$$\sigma_b = 4\pi\overline{b^2} = \sigma_{coh} + \sigma_{incoh}. \tag{2.40}$$

The scattering cross section of moderating materials such as Be and graphite is almost entirely coherent. Carbon-12, the dominant isotope of graphite (%98.89), does not have a nuclear spin, while carbon-13 has a nuclear spin due to the presence of unpaired spins. Carbon has $\sigma_{coh} = 5.50 \pm 0.04$ barn and $\sigma_b = 5.53 \pm 0.03$ barn [11].

Assuming the scattering length is real, and written in terms of its average value that is measured experimentally, where the average is taken over the random spin orientation, and

the random isotopes distribution, then $\overline{b_j b_{j'}}$ can be substituted for $b_j b_{j'}$, so that equation (2.34) becomes

$$\frac{d^2\sigma}{d\Omega\, dE'} = \frac{k'}{k}\frac{1}{2\pi\hbar}\frac{1}{\mathcal{N}}\sum_{jj'}\overline{b_j b_{j'}}\int_{-\infty}^{\infty}\left\langle \exp\left\{-i\vec{\kappa}\cdot\vec{R}_{j'}(0)\right\}\exp\left\{i\vec{\kappa}\cdot\vec{R}_j(t)\right\}\right\rangle \exp(-i\omega t)dt\,. \qquad (2.41)$$

Assuming no correlations between the values of b_j and $b_{j'}$, if j and j' refer to different sites, then

$$\overline{b_j b_{j'}} = \bar{b}^2 + (\overline{b^2} - \bar{b}^2)\,\delta_{jj'}\,. \qquad (2.42)$$

By substituting equation (2.42) into equation (2.41), the double differential scattering cross section can be written as a sum of coherent and incoherent double differential scattering contributions [21]

$$\frac{d^2\sigma}{d\Omega\, dE'} = \left(\frac{d^2\sigma}{d\Omega\, dE'}\right)_{coh} + \left(\frac{d^2\sigma}{d\Omega\, dE'}\right)_{incoh}\,, \qquad (2.43)$$

where

$$\left(\frac{d^2\sigma}{d\Omega\, dE'}\right)_{coh} = \frac{\sigma_{coh}}{4\pi}\frac{k'}{k}\frac{1}{2\pi\hbar}\frac{1}{\mathcal{N}}\sum_{jj'}\int_{-\infty}^{\infty}\left\langle \exp\left\{-i\vec{\kappa}\cdot\vec{R}_{j'}(0)\right\}\exp\left\{i\vec{\kappa}\cdot\vec{R}_j(t)\right\}\right\rangle \exp(-i\omega t)dt\,, \qquad (2.44)$$

and

$$\left(\frac{d^2\sigma}{d\Omega\, dE'}\right)_{incoh} = \frac{\sigma_{incoh}}{4\pi}\frac{k'}{k}\frac{1}{2\pi\hbar}\frac{1}{\mathcal{N}}\sum_{j}\int_{-\infty}^{\infty}\left\langle \exp\left\{-i\vec{\kappa}\cdot\vec{R}_{j}(0)\right\}\exp\left\{i\vec{\kappa}\cdot\vec{R}_j(t)\right\}\right\rangle \exp(-i\omega t)dt\,. \qquad (2.45)$$

It is common to write equations (2.44) and (2.45) in terms of the intermediate function $I(\vec{\kappa},t)$ and the scattering law $S(\vec{\kappa},\omega)$, such that

$$S(\vec{\kappa},\omega) = \frac{1}{2\pi\hbar}\int_{-\infty}^{\infty} I\,(\vec{\kappa},t)e^{-i\omega t}dt\,, \qquad (2.46)$$

and

$$S_s(\vec{\kappa},\omega) = \frac{1}{2\pi\hbar}\int_{-\infty}^{\infty} I_{incoh}(\vec{\kappa},t)e^{-i\omega t}dt\,, \qquad (2.47)$$

where the intermediate functions are defined as

$$I(\vec{\kappa},t)=\frac{1}{\mathcal{N}}\sum_{jj'}\left\langle \exp\left\{-i\vec{\kappa}\cdot\vec{R}_{j'}(0)\right\}\exp\left\{i\vec{\kappa}\cdot\vec{R}_{j}(t)\right\}\right\rangle, \tag{2.48}$$

and

$$I_{incoh}(\vec{\kappa},t)=\frac{1}{\mathcal{N}}\sum_{j}\left\langle \exp\left\{-i\vec{\kappa}\cdot\vec{R}_{j}(0)\right\}\exp\left\{i\vec{\kappa}\cdot\vec{R}_{j}(t)\right\}\right\rangle. \tag{2.49}$$

$S(\vec{\kappa},\omega)$ is known as the scattering law per atom, it may be written as a sum of two parts:

$$S(\vec{\kappa},\omega)=S_s(\vec{\kappa},\omega)+S_d(\vec{\kappa},\omega), \tag{2.50}$$

where $S_s(\vec{\kappa},\omega)$ is known as the self scattering law per atom, which accounts for non-interference (incoherent) effects, while $S_d(\vec{\kappa},\omega)$ is the distinct scattering law and accounts for interference (coherent) effects. In coherent scattering there is a strong interference between the waves scattered from each nucleus. In incoherent scattering there is no interference and the cross section is completely isotropic. As a consequence equations (2.44) and (2.45), becomes

$$\left(\frac{d^2\sigma}{d\Omega\, dE'}\right)_{coh}=\frac{\sigma_{coh}}{4\pi}\frac{k'}{k}S(\vec{\kappa},\omega), \tag{2.51}$$

and

$$\left(\frac{d^2\sigma}{d\Omega\, dE'}\right)_{incoh}=\frac{\sigma_{incoh}}{4\pi}\frac{k'}{k}S_s(\vec{\kappa},\omega). \tag{2.52}$$

The total double differential scattering cross section now can be written as

$$\frac{d^2\sigma}{d\Omega\, dE'}=\frac{1}{4\pi}\frac{k'}{k}\left\{\sigma_{coh}\,S_d(\vec{\kappa},\omega)+(\sigma_{coh}+\sigma_{incoh})S_s(\vec{\kappa},\omega)\right\}. \tag{2.53}$$

Equation (2.34) is the fundamental expression for calculating the cross section. The detailed calculations start by calculating the thermal average integrand. This average depends only on the scattering medium structure and its dynamics. So the problem of neutron scattering is reduced to a statistical mechanics and quantum mechanics problem. In other words, equation (2.34) is a combination of two parts, one is nuclear represented by the nuclear scattering length, and the other is atomic represented by thermal average integrand.

Furthermore, if the atoms in the scattering medium are assumed to be bound to each other by harmonic forces, an expansion can be performed to allow the decomposition of the coherent and incoherent double differential scattering cross sections into elastic and inelastic components. For crystalline materials, this expansion is known as the phonon expansion. That is, the self and distinct components of the scattering law can be written as

$$S_s = {}^0S_s + {}^1S_s + {}^2S_s + \cdots$$

$$S_d = {}^0S_d + {}^1S_d + {}^2S_d + \cdots \tag{2.54}$$

Substituting equation (2.54) into equation (2.53), the following expression is obtained

$$\frac{d^2\sigma}{d\Omega\, dE'} = \frac{1}{4\pi}\frac{k'}{k}\left\{\sigma_{coh}\sum_{P=0}{}^{P}S_d(\vec{\kappa},\omega) + (\sigma_{coh}+\sigma_{incoh})\sum_{P=0}{}^{P}S_s(\vec{\kappa},\omega)\right\}. \tag{2.55}$$

The terms that have superscript $P=0$ represent 0 phonon creation (or annihilation), and they represent coherent elastic scattering events, while the terms that have higher superscripts $P=1,2,3,\cdots$ represent the creation (or annihilation) of 1, 2, 3,…, phonons respectively, and they represent inelastic coherent scattering. A scattering event is said to be inelastic if any of the internal quantum states of the scatterer are changed as a result of the

collision with a neutron, and is said to be elastic if there is no change. In inelastic scattering of thermal neutrons from a crystal, the vibrational excitation of the crystal will be changed as a result of the collision. A quantum of vibrational energy in a crystal is called phonon, and inelastic scattering is accompanied by the emission or absorption of phonons. In elastic scattering from a crystal, the crystal as whole recoils so as to conserve momentum with the neutron, but the resulting change in the neutron energy is negligible.

It is convenient to write the scattering law $S(\vec{\kappa},\omega)$ in terms of the dimensionless variables α, and β representing the energy and momentum transfer respectively, that is

$$S(\alpha,\beta) = k_B T e^{\beta/2} S(\vec{\kappa},\omega)\,, \tag{2.56}$$

where,

$$\alpha = \frac{E' + E - 2\mu\sqrt{EE'}}{Ak_B T} = \frac{\hbar^2\kappa^2}{2Ak_B T}\,, \tag{2.57}$$

and

$$\beta = \frac{E' - E}{k_B T} = -\frac{\hbar\omega}{k_B T}\,. \tag{2.58}$$

E, and E' are the incident and scattered neutron energies respectively, μ is the cosine of the scattering angle, A is the ratio of nuclear to neutron masses, k_B is Boltzmann constant, and T is the temperature of the scattering medium. Note that $S(\vec{\kappa},\omega)$ has unit of $[energy]^{-1}$, while $S(\alpha,\beta)$ is dimensionless. As a consequence, equation (2.55) can be written as

$$\frac{d^2\sigma}{d\Omega\, dE'} = \frac{1}{4\pi k_B T}\sqrt{\frac{E'}{E}}e^{-\beta/2}\left\{\sigma_{coh}\sum_{P=0}{}^{P}S_d(\alpha,\beta) + (\sigma_{coh}+\sigma_{incoh})\sum_{P=0}{}^{P}S_s(\alpha\kappa,\beta)\right\}. \tag{2.59}$$

2.4 Thermal Neutron Scattering Cross Section Approximations

a) The incoherent approximation

To calculate the thermal neutron scattering cross section it is necessary to find an expression for the intermediate function characterized by the dynamics of the system. For solid moderators many assumptions and approximations are employed in order to simplify such calculations [18], one of these –and the most important- approximation is *the incoherent approximation*: in which the interference effects are neglected by setting $S_d(\alpha,\beta)$ equal to zero, that is, the inelastic $(P \geq 1)$ double differential scattering cross section per atom is given by

$$\frac{d^2\sigma}{dE'\,d\Omega} = \frac{\sigma_{coh}+\sigma_{incoh}}{4\pi k_B T}\sqrt{\frac{E'}{E}}e^{-\beta/2}\sum_{P=1}{}^{P}S_s(\alpha,\beta)\,. \qquad (2.60)$$

Since graphite is a strong coherent scatterer, interference effects will be significant, and the incoherent approximation is expected to be inaccurate. The major point of this work is removing the incoherent approximation by including the coherent one phonon component of the scattering law.

b) Other Approximations

The other approximations and assumptions that were used to simplify the calculations of the scattering law are that $S_s(\alpha,\beta)$ is assumed to have a Gaussian-like function (Gaussian approximation), the solid interatomic forces are harmonic, only one kind of atom is present in the solid, the solid has one atom per unit cell, the unit cell has a cubic symmetry, and the vibrational modes of the crystal are described by a continuous spectrum, called the phonon

frequency distribution $\rho(\beta)$ [18]. Based on the above approximation and assumptions, $S_s(\alpha,\beta)$ may be written as [see Appendix A.1]

$$S_s(\alpha,\beta)=\frac{1}{2\pi}\int_{-\infty}^{\infty}e^{i\beta\tau}e^{-\gamma^2(\tau)}d\tau\,, \tag{2.61}$$

where τ is time in units of $\hbar/k_BT$ seconds, and $\gamma^2(\tau)$ is given by

$$\gamma^2(\tau)=\alpha\int_{-\infty}^{\infty}\frac{\rho(\beta)[1-e^{i\beta\tau}]e^{\frac{-\beta}{2}}}{2\beta\,sinh(\beta/2)}d\beta\,. \tag{2.62}$$

The above formulation represents the basis of the computer programs such as GASKET [22] and LEAPR/NJOY [8, 23], which are used to calculate thermal neutron scattering cross sections.

2.5 Coherent One Phonon Scattering Cross Section

In order to include the coherent one phonon law the calculation of the thermal neutron scattering cross section equation (2.44) will be considered to develop an expression for the coherent one phonon scattering law [19].

The instantaneous position $\vec{R}_{ld}(t)$ of the d^{th} atom in the l^{th} unit cell that is displaced from the equilibrium position by a displacement $\vec{u}_{ld}(t)$ is

$$\vec{R}_{ld}(t)=\vec{l}+\vec{d}+\vec{u}_{ld}(t)\,. \tag{2.63}$$

By substituting the above equation into equation (2.44) and replacing the subscript *j* by *l, d*

$$\left(\frac{d^2\sigma}{d\Omega\,dE'}\right)_{coh}=\frac{\sigma_{coh}}{4\pi}\frac{k'}{k}\frac{1}{2\,\pi\,\hbar}\frac{1}{\mathcal{N}}\sum_{l\,d}\sum_{l'\,d'}\exp\left\{i\vec{\kappa}\cdot\left(\vec{l}+\vec{d}-\vec{l}\,'-\vec{d}\,'\right)\right\}$$
$$\int_{-\infty}^{\infty}\left\langle\exp\left\{-i\vec{\kappa}\cdot\vec{u}_{l'd'}(0)\right\}\exp\left\{i\vec{\kappa}\cdot\vec{u}_{ld}(t)\right\}\right\rangle\exp(-i\omega t)dt, \tag{2.64}$$

but

$$\vec{u}_{l\,d}(t)=\left(\frac{\hbar}{2MN}\right)^{1/2}\sum_{s}\frac{1}{\omega_s}\left\{\vec{e}_{ds}\,a_s\exp\left[i\left(\vec{q}\cdot\vec{l}-\omega_s t\right)\right]+\vec{e}^{\,*}_{ds}\,a_s^{+}\exp\left[-i\left(\vec{q}\cdot\vec{l}-\omega_s t\right)\right]\right\},\qquad(2.65)$$

and

$$\vec{u}_{l'd'}(0)=\left(\frac{\hbar}{2MN}\right)^{1/2}\sum_{s}\frac{1}{\omega_s}\left\{\vec{e}_{ds}\,a_s\exp\left[i\left(\vec{q}\cdot\vec{l}\,'\right)\right]+\vec{e}^{\,*}_{ds}\,a_s^{+}\exp\left[-i\left(\vec{q}\cdot\vec{l}\,'\right)\right]\right\}.\qquad(2.66)$$

For simplicity, the following definitions are introduced

$$\begin{aligned}\hat{A}&=-i\vec{\kappa}\cdot\vec{u}_{l'd'}(0)=-i\sum_{s}g_s a_s+g_s^{*}a_s^{+}\\ \hat{B}&=i\vec{\kappa}\cdot\vec{u}_{l\,d}(t)=i\sum_{s}h_s a_s+h_s^{*}a_s^{+}\end{aligned}\qquad(2.67)$$

where

$$\begin{aligned}g_s&=\left(\frac{\hbar}{2MN}\right)^{1/2}\frac{\vec{\kappa}\cdot\vec{e}_{d's}}{\sqrt{\omega_s}}e^{i\vec{q}\cdot\vec{l}\,'}\\ h_s&=\left(\frac{\hbar}{2MN}\right)^{1/2}\frac{\vec{\kappa}\cdot\vec{e}_{ds}}{\sqrt{\omega_s}}e^{i\left(\vec{q}\cdot\vec{l}-\omega_s t\right)}\end{aligned}\qquad(2.68)$$

Since the operators $\hat{A}$ and $\hat{B}$ do not commute, the thermal average expectation value can be written as

$$\left\langle\exp\left\{-i\vec{\kappa}\cdot\vec{u}_{l'd'}(0)\right\}\exp\left\{i\vec{\kappa}\cdot\vec{u}_{l\,d}(t)\right\}\right\rangle=\left\langle\exp\hat{A}\exp\hat{B}\right\rangle=\left\langle\exp\left(\hat{A}+\hat{B}\right)\right\rangle\exp\left\{\frac{1}{2}\left[\hat{A},\hat{B}\right]\right\}.\qquad(2.69)$$

Note that $\hat{A}+\hat{B}$ is a linear combination of harmonic displacements, each displacement has a Gaussian probability function. The probability function for a linear combination of Gaussian functions is a Gaussian function also.

$$\left\langle\exp\left(\hat{A}+\hat{B}\right)\right\rangle=\exp\left\{\frac{1}{2}\left\langle(A+B)^2\right\rangle\right\}.\qquad(2.70)$$

Thus, equation (2.20) becomes

$$\left\langle \exp\left\{-i\vec{\kappa}\cdot\vec{u}_{l'd'}(0)\right\}\exp\left\{i\vec{\kappa}\cdot\vec{u}_{ld}(t)\right\}\right\rangle = \left\langle \exp\hat{A}\exp\hat{B}\right\rangle = \exp\left\langle\frac{1}{2}\left(\hat{A}^2+\hat{B}^2\right)\right\rangle\exp\left\langle\hat{A}\hat{B}\right\rangle. \qquad (2.71)$$

The following quantites can also be defined

$$\begin{aligned}\frac{1}{2}\left\langle\hat{A}^2\right\rangle &= \frac{1}{2}\left\langle\left(\vec{\kappa}\cdot\vec{u}_{l'd'}(0)\right)^2\right\rangle = -W_{d'}\\ \frac{1}{2}\left\langle\hat{B}^2\right\rangle &= \frac{1}{2}\left\langle\left(\vec{\kappa}\cdot\vec{u}_{ld}(t)\right)^2\right\rangle = -W_{d}\end{aligned} \qquad (2.72)$$

where the exponential term e^{-2W} is known as the Debye-Waller factor. In this case, $2W$ is the mean square displacement of a nucleus multiplied by κ^2, and the presence of e^{-2W} means the intensity decreases with increasing $|\vec{\kappa}|$. Substituting equations (2.71) and (2.72) into equation (2.64)

$$\left(\frac{d^2\sigma}{d\Omega\, dE'}\right)_{coh} = \frac{\sigma_{coh}}{4\pi}\frac{k'}{k}\frac{1}{2\,\pi\,\hbar}\frac{1}{\mathcal{N}}\sum_{ld}\sum_{l'd'}\exp\left\{i\vec{\kappa}\cdot\left(\vec{l}+\vec{d}-\vec{l}\,'-\vec{d}\,'\right)\right\} e^{-W_{d'}}\, e^{-W_d}\int_{-\infty}^{\infty}\exp\left\langle\hat{A}\hat{B}\right\rangle\exp(-i\omega t)dt. \qquad (2.73)$$

2.5.1 Phonon Expansion

Expanding the exponential term $\exp\left\langle\hat{A}\hat{B}\right\rangle$ that appears in equation (2.73) in a Taylor series gives

$$\exp\left\langle\hat{A}\hat{B}\right\rangle = \hat{1}+\left\langle\hat{A}\hat{B}\right\rangle+\cdots+\frac{1}{p_!}\left\langle\hat{A}\hat{B}\right\rangle^p+\cdots=\sum_{p=0}^{\infty}\frac{\left\langle\hat{A}\hat{B}\right\rangle^p}{p!}. \qquad (2.74)$$

and the double differential scattering cross section can be written as

$$\begin{aligned}\left(\frac{d^2\sigma}{dE'\,d\Omega}\right)_{coh} &= \left(\frac{d^2\sigma}{dE'\,d\Omega}\right)_{coh}^{0}+\sum_{P=1}^{\infty}\left(\frac{d^2\sigma}{dE'\,d\Omega}\right)_{coh}^{P}\\ &= \left(\frac{d^2\sigma}{dE'\,d\Omega}\right)_{coh}^{el}+\left(\frac{d^2\sigma}{dE'\,d\Omega}\right)_{coh}^{inel}\end{aligned}. \qquad (2.75)$$

The second term in equation (2.74) corresponds to P=1 gives the one-phonon scattering cross section, in which all the quantum numbers of the oscillating system (crystal) remain unchanged except for one oscillator, where its corresponding quantum number changes by unity. The one-phonon coherent scattering cross section is therefore

$$\left(\frac{d^2\sigma}{d\Omega\, dE'}\right)_{coh}^{1ph} = \frac{\sigma_{coh}}{4\pi}\frac{k'}{k}\frac{1}{2\,\pi\,\hbar}\frac{1}{\mathcal{N}}\sum_{l\,d}\sum_{l'\,d'}\exp\left\{i\vec{\kappa}\cdot\left(\vec{l}+\vec{d}-\vec{l}\,'-\vec{d}\,'\right)\right\} \\ e^{-W_{d'}}\; e^{-W_d}\int_{-\infty}^{\infty}\left\langle \hat{A}\hat{B}\right\rangle \exp(-i\omega t)dt. \tag{2.76}$$

Utilizing equation (2.67) to evaluate $\left\langle \hat{A}\hat{B}\right\rangle$, and keeping in mind that

$$\left\langle a_s a_s^+\right\rangle = n_s + 1 \quad \text{and} \quad \left\langle a_s^+ a_s\right\rangle = n_s, \tag{2.77}$$

results in

$$\left\langle \hat{A}\hat{B}\right\rangle = \sum_s\sum_{s'}\left\langle \left(g_s a_s + g_s^* a_s^+\right)\left(h_{s'}a_{s'} + h_s^* a_s^+\right)\right\rangle \\ = \sum_s g_s h_s^*\left\langle n_s + 1\right\rangle + g_s^* h_s\left\langle n_s\right\rangle \tag{2.78}$$

Substituting equation (2.68) into equation (2.78) gives

$$\left\langle \hat{A}\hat{B}\right\rangle = \left(\frac{\hbar}{2MN}\right)\sum_s \frac{\left(\vec{\kappa}\cdot\vec{e}_{ds}\right)^2}{\omega_s}\left\{e^{i\vec{q}\cdot\left(\vec{l}\,'-\vec{l}\right)}e^{i\omega_s t}\left\langle n_s+1\right\rangle + e^{-i\vec{q}\cdot\left(\vec{l}\,'-\vec{l}\right)}e^{-i\omega_s t}\left\langle n_s\right\rangle\right\}. \tag{2.79}$$

thus the coherent one phonon double differential scattering cross section is

$$\left(\frac{d^2\sigma}{d\Omega\, dE'}\right)_{coh}^{1ph} = \frac{\sigma_{coh}}{4\pi}\frac{k'}{k}\frac{1}{2\,\pi}\frac{1}{\mathcal{N}}\left(\frac{1}{2MN}\right)\sum_{d\,d'}e^{i\vec{\kappa}\cdot\left(\vec{d}-\vec{d}\,'\right)}\,e^{-W_{d'}}\; e^{-W_d} \\ \sum_s\sum_{ll'}\frac{\left(\vec{\kappa}\cdot\vec{e}_{ds}\right)^2}{\omega_s}\int_{-\infty}^{\infty}\exp(-i\omega t)\left\{e^{i(\vec{\kappa}-\vec{q})\cdot\left(\vec{l}-\vec{l}\,'\right)}e^{i\omega_s t}\left\langle n_s+1\right\rangle + e^{i(\vec{\kappa}+\vec{q})\cdot\left(\vec{l}-\vec{l}\,'\right)}e^{-i\omega_s t}\left\langle n_s\right\rangle\right\}dt \tag{2.80}$$

which is equivalent to

$$\left(\frac{d^2\sigma}{d\Omega\, dE'}\right)^{1ph}_{coh} = \frac{\sigma_{coh}}{4\pi}\frac{k'}{k}\frac{1}{2\,\pi}\frac{1}{\mathcal{N}}\left(\frac{1}{2MN}\right)\sum_s \frac{1}{\omega_s}\left|\sum_d e^{i\vec{\kappa}\cdot(\vec{d})}\, e^{-W_d}\left(\vec{\kappa}\cdot\vec{e}_{ds}\right)^2\right|^2$$
$$\sum_l \int_{-\infty}^{\infty} \exp(-i\omega t)\left\{\left|e^{i(\vec{\kappa}-\vec{q})\cdot\vec{l}}\right|^2 e^{i\omega_s t}\left\langle n_s+1\right\rangle + \left|e^{i(\vec{\kappa}+\vec{q})\cdot\vec{l}}\right|^2 e^{-i\omega_s t}\left\langle n_s\right\rangle\right\} dt \tag{2.81}$$

but

$$\int_{-\infty}^{\infty} e^{i(\omega\pm\omega)t}\, dt = 2\pi\delta\left(\omega\pm\omega_s\right)$$

and (2.82)

$$\frac{1}{N}\left|\sum_l e^{i(\vec{\kappa}\pm\vec{q})\cdot\vec{l}}\right|^2 = \frac{(2\pi)^3}{v}\sum_{\vec{\tau}}\delta\left(\vec{\kappa}\pm\vec{q}-\vec{\tau}\right)$$

Substituting equation (2.79) into equation (2.78) we get

$$\left(\frac{d^2\sigma}{d\Omega\, dE'}\right)^{1ph}_{coh} = \frac{\sigma_{coh}}{4\pi}\frac{k'}{k}\frac{(2\pi)^3}{2\,v}\frac{1}{M\mathcal{N}}\sum_s\sum_{\vec{\tau}}\frac{1}{\omega_s}\left|\sum_d e^{i\vec{\kappa}\cdot(\vec{d})}\, e^{-W_d}\left(\vec{\kappa}\cdot\vec{e}_{ds}\right)^2\right|^2 \times$$
$$\left\{\left\langle n_s+1\right\rangle\delta\left(\omega-\omega_s\right)\delta\left(\vec{\kappa}-\vec{q}-\vec{\tau}\right)+\left\langle n_s\right\rangle\delta\left(\omega+\omega_s\right)\delta\left(\vec{\kappa}+\vec{q}-\vec{\tau}\right)\right\}. \tag{2.83}$$

Equation (2.83) is a sum of two terms, the first term which contains $\left\langle n_s+1\right\rangle$, represents a process in which a phonon is created, while the second term contains $\left\langle n_s\right\rangle$ represents phonon annihilation. The delta functions $\delta\left(\omega\pm\omega_s\right)$ and $\delta\left(\vec{\kappa}\pm\vec{q}-\vec{\tau}\right)$ represent the conservation of energy and momentum respectively. In the limit $T\to 0$ only the first process occurs, since there are no phonons to be created at absolute zero Kelvin. The above equation can be written in a similar fashion to equation (2.51), that is

$$\left(\frac{d^2\sigma}{d\Omega\, dE'}\right)^{1ph}_{coh} = \frac{\sigma_{coh}}{4\pi}\frac{k'}{k}\,{}^1S\left(\vec{\kappa},\omega\right), \tag{2.84}$$

where

$${}^1S\left(\vec{\kappa},\omega\right) = \frac{(2\pi)^3}{2\,v}\frac{1}{M\mathcal{N}}\sum_s\sum_{\vec{\tau}}\frac{1}{\omega_s}\left|\sum_d e^{i\vec{\kappa}\cdot(\vec{d})}\, e^{-W_d}\left(\vec{\kappa}\cdot\vec{e}_{ds}\right)^2\right|^2 \times$$
$$\left\{\left\langle n_s+1\right\rangle\delta\left(\omega-\omega_s\right)\delta\left(\vec{\kappa}-\vec{q}-\vec{\tau}\right)+\left\langle n_s\right\rangle\delta\left(\omega+\omega_s\right)\delta\left(\vec{\kappa}+\vec{q}-\vec{\tau}\right)\right\}. \tag{2.85}$$

Recall that for graphite $\sigma_{incoh} \sim 0$, that is, $\sigma_b \sim \sigma_{coh}$. As a consequence the inelastic double differential scattering cross section for graphite as a result of the incoherent approximation ($S_d(\vec{\kappa},\omega) = 0$) can be written as

$$\frac{d^2\sigma}{d\Omega\, dE'} \cong \frac{\sigma_{coh}}{4\pi}\frac{k'}{k}\sum_{P=1}{}^{P}S_s(\vec{\kappa},\omega). \tag{2.86}$$

By adding the exact coherent one phonon double differential scattering cross section given by equation (2.84) and subtracting the one phonon double differential scattering cross section in the incoherent approximation $\frac{1}{4\pi}\frac{k'}{k}\sigma_{coh}\left({}^{1}S_s(\vec{\kappa},\omega)\right)_{Incoh\ Approx.}$, equation (2.86) becomes

$$\frac{d^2\sigma}{d\Omega\, dE'} \cong \frac{\sigma_{coh}}{4\pi}\frac{k'}{k}\left\{\left(\sum_{P=2}{}^{P}S_s(\vec{\kappa},\omega)\right)_{Incoh\ Approx.} + \left({}^{1}S_s(\vec{\kappa},\omega)+{}^{1}S_d(\vec{\kappa},\omega)\right)_{exact}\right\}, \tag{2.87}$$

where ${}^{1}S={}^{1}S_s+{}^{1}S_d$. Note that the summation for the incoherent approximation in the above equation starts from *P*=2.

Appendix A.2 shows the one phonon double differential scattering cross section formula in the incoherent approximation, while Appendix A.3 shows a step by step derivation of the one phonon double differential scattering cross section in the incoherent approximation starting from the coherent one phonon equation (2.83).

2.6 Fundamental Input to scattering Formulation

In order to generate the graphite thermal neutron scattering cross section, there are basic inputs that are required to perform the calculations such as the temperature of interest *T*, the

mass of the scattering atom relative to that of the neutron A (in case of graphite, A= 11.898 [8]), the bound atom cross section, in fact LEAPR uses the free atom cross section σ_{free} instead, where the bound and free atom cross sections are related together by the relation [18]

$$\sigma_b = \left(\frac{A+1}{A} \right)^2 \sigma_{free} . \tag{2.88}$$

where for graphite $\sigma_{free} = 4.7392\,\text{b}$ [8]. The basic input to the formula implemented in LEAPR is represented by equations (2.61 and 2.62) is the phonon frequency distribution. LEAPR requires the phonon frequency distribution to be represented in a uniform grid. On the other hand, the basic inputs to the coherent one phonon scattering law represented by equation (3.84) are dispersion relations, polarization vectors, atomic positions, and Debye-Waller factor. In the formulation of LEAPR the exponent of the Debye-Waller factor $2W$ is considered isotropic. In this work, in order to calculate the coherent one phonon scattering cross section $2W$ is treated both isotropically and non-isotropically, see section (4.3). The dispersion relations and polarization vectors are obtained using the *ab initio* simulations of graphite, as will be discussed later.

Chapter 3 Lattice Dynamics; The Input for Thermal Neutron Scattering Calculations

The calculation of thermal neutron scattering cross sections requires knowledge of the dynamics of an atomic system. This includes the atomic structure and the allowed modes of vibrations as represented by dispersion relations and polarization vectors. The information can also be used in the form of vibrational (i.e., phonon) frequency spectra. However, the relation between thermal neutron scattering and lattice dynamics is a mutual relation, that is, while lattice dynamics is fundamental in studying inelastic neutron scattering, coherent inelastic neutron scattering is used to measure the dispersion relations (frequencies of vibrational modes) of crystals and even the atomic displacement pattern in a given normal mode, and inelastic incoherent neutron scattering is used to measure the phonon frequency distribution.

3.1 Lattice Dynamics

Assuming a perfect crystal, in which, the atoms are arranged in a pattern that shows long- range order, and any arbitrary region in the crystal is representative of the bulk properties of the solid - no surface boundary effects. In this case, the mean feature of the solid is periodicity, in which one can describe the mean (equilibrium) atomic positions by a set of mathematical points called the crystal lattice. At any temperature (including 0 K) the atoms are oscillating around their equilibrium positions (lattice points). Assuming the oscillations are small (relative to interatomic spacing), developing the phonon frequency starts by displacing the atoms from their equilibrium positions harmonically. For a

3-dimensional crystal, the position of the d^{th} atom in the l^{th} unit cell is defined as $\vec{R}(l,d) = \vec{R}(l) + \vec{R}(d)$. Due to thermal fluctuations, each atom (l,d) is displaced from its equilibrium position by $\vec{u}(l,d)$, the η component of this displacement is $u_\eta(l,d)$ where η is x, y, or z in Cartesian coordinates.

The total kinetic energy T of the crystal is the sum of the kinetic energies of each atom in the crystal, written as

$$T = \frac{1}{2} M \sum_{ld\eta} \dot{u}_\eta^2 \quad , \tag{3.1}$$

the total potential energy of the crystal Φ is assumed to be a result of two-body interactions, and is a function of the instantaneous positions of all atoms. If Φ is written as a Taylor series in terms of the atomic displacements around the equilibrium position up to the quadratic term (harmonic approximation), then the following term is obtained

$$\Phi = \Phi_\circ + \sum_{ld\eta} \left(\frac{\partial \Phi}{\partial u_\eta(l,d)} \right)_0 u_\eta(l,d) + \sum_{\substack{ld\eta \\ l'd'\theta}} \left(\frac{\partial^2 \Phi}{\partial u_\eta(l,d) \partial u_\theta(l',d')} \right)_0 u_\eta(l,d) u_\theta(l',d'), \tag{3.2}$$

the first term $\Phi_\circ$ is just a constant (step function) that represents the equilibrium potential energy of the crystal. The partial derivative $\left(\frac{\partial \Phi}{\partial u_\eta(l,d)} \right)_{u_\eta = 0}$ represents the negative of the η component of the force on the atom at the position (l,d) in its equilibrium position when all $u_\eta(l,d) = 0$. This term is zero, since the force on each particle must be zero when all displacements are zero. That is, each term in the sum vanishes when the crystal is in equilibrium. The second partial derivative $\Phi_{\eta\theta}(l,d;l',d') = \left(\frac{\partial^2 \Phi}{\partial u_\eta(l,d) \partial u_\theta(l',d')} \right)_0$ is known

as the atomic force constant.

The equations of motion of the lattice can be established by setting its Lagrangian L, where

$$\begin{aligned} L &= Kinetic\ Energy - Potential\ Energy \\ &= \frac{1}{2}\sum_{ld\eta} M_d \dot{u}_\eta^2(l,d) - \Phi_\circ - \frac{1}{2}\sum_{\substack{ld\eta \\ l'd'\theta}} \Phi_{\eta\theta}(ld;l'd')u_\eta(l,d)u_\theta(l',d'), \end{aligned} \tag{3.3}$$

and

$$\frac{d}{dt}\left(\frac{dL}{d\dot{u}_\eta(l,d)}\right) - \frac{\partial L}{\partial u_\eta(l,d)} = 0\,. \tag{3.4}$$

Thus the equations of motion are

$$M_d \ddot{u}_\eta(l,d) = -\sum_{l'd'\theta} \Phi_{\eta\theta}(l,d;l',d')u_\theta(l',d')\,. \tag{3.5}$$

The solution to the above equation has the form of a plane wave traveling through the lattice, which is given by

$$u_\eta(l,d) = \frac{1}{\sqrt{M_\eta}} u_\eta(d)\exp\left[-i\left(\omega t - \vec{q}\cdot\vec{R}(l)\right)\right], \tag{3.6}$$

where $u_\eta(d)$ is an amplitude independent of l, and it is the unknown that will be solved for. The vector $\vec{q}$ is called the wave vector, its magnitude is equal to $\frac{2\pi}{\lambda}$, where λ the wavelength of the elastic wave which propagates through the medium, and its direction is the direction of the wave propagation. Substituting equation (3.5) into equation (3.6) gives,

$$\omega^2 u_\eta(d) = \frac{1}{\sqrt{M_d M_{d'}}} \sum_{l'd'\theta} \Phi_{\eta\theta}(l,d;l',d')\, e^{-i\vec{q}\cdot\left(\vec{R}(l)-\vec{R}(l')\right)} u_\theta(d')\,. \tag{3.7}$$

Due to periodicity, the infinite set of coupled linear differential equations represented by equation (3.5) is reduced to a problem of 3*r* linear homogenous equations (eigenvalue

problem) in 3*r* unknowns, $u_\eta(d)$. Conventionally, equation (3.7) is written as

$$\omega^2 u_\eta(d) = \sum_{d'\theta} D_{\eta\theta}(\vec{q};d,d')u_\theta(d'), \tag{3.8}$$

where

$$D_{\eta\theta}(\vec{q};d,d') = \frac{1}{\sqrt{M_d M_{d'}}} \sum_{l'} \Phi_{\eta\theta}(l,d;l',d') e^{-i\vec{q}\cdot\left(\vec{R}(l)-\vec{R}(l')\right)}, \tag{3.9}$$

are the elements of the dynamical matrix $\overline{\overline{D}}(\vec{q})$. For a crystal with *r* atoms per unit cell, the dynamical matrix is a $3r \times 3r$ matrix obtained by combining (η,d) and (θ,d'). The set of equations (3.8) has a non-trivial solution only if

$$\left| D_{\eta\theta}(q;d,d') - \omega^2 \delta_{dd'}\delta_{\eta\theta} \right| = 0. \tag{3.10}$$

Where for each $\vec{q}$ there are $3r$ solutions (branches) denoted by $\omega_j^2(\vec{q})$, where $j = 1,2,\cdots,3r$ is called the polarization index. The dynamical matrix is a Hermitian matrix, that is,

$$D_{\eta\theta}(\vec{q};d,d') = D^*_{\theta\eta}(\vec{q};d',d). \tag{3.11}$$

As a consequence, the eigenvalues $\omega_j^2(\vec{q})$ are real, so $\omega_j(\vec{q})$ (*called the dispersion relations*) are either real or imaginary. For a 3 dimensional crystal with *r* atoms per unit cell, there are $3r$ modes for each value of $\vec{q}$. Three of these modes go to zero as $\vec{q}$ goes to zero; such modes are called acoustic, where all the atoms of the unit cell move in parallel and with equal amplitudes, that is, acoustic modes involve a displacement of the center of mass of the unit cell. The remaining $3(r-1)$ modes that do not vanish as $\vec{q}$ goes to zero are called optical modes [24, 25].

The energy of a mode of vibration of the crystal is called a *phonon*- a Greek word that means voice [26]. This energy is distributed throughout the crystal in real space but is

localized in the space defined by $\vec{q}$ and j. Acoustic phonons are analogous photons in optics. Phonons are bosons with zero spin. However, $E_{phonon} < E_{photon}$ for equal wavelengths.

For each eigenvalue $\omega_j^2(\vec{q})$ there exists eigenvectors $\vec{e}^{\,j}(\vec{q};d)$ called the polarization vector whose components are a solution to the set of equations (3.8), which can now be written as

$$\omega_j^2(\vec{q})e_\eta^j(\vec{q};d) = \sum_{d'\theta} D_{\eta\theta}(\vec{q};d,d')\,e_{\theta'}^j(\vec{q};d'). \tag{3.12}$$

The polarization vectors describe the orientation of the atomic vibration corresponding to a particular mode defined by $\vec{q}$ and j. Polarization vectors are complex and satisfy the orthonoramlity conditions

$$\begin{aligned} \sum_{d\eta} e_\eta^{*j}(\vec{q};d)e_\eta^{j'}(\vec{q};d) &= \delta_{jj'} \\ \sum_{j} e_\theta^{*j}(\vec{q};d')e_\eta^{j}(\vec{q};d) &= \delta_{\eta\theta}\delta_{dd'}. \end{aligned} \tag{3.13}$$

Traditionally phonons have been calculated by proposing an analytic model for the interaction between atoms, evaluating the force constants between atoms, and constructing the dynamical matrix and diagonlizing it. The force constants used in the dynamical matrix calculation can be estimated in various ways. In some cases they are derived from thermodynamic properties such as specific heat or compressibility data. Alternatively they could be deduced from experimental measurements of phonon dispersion relations using inelastic neutron scattering techniques. Basically both approaches represent the fitting of theoretical models to experimental data. This approach suffers from two major deficiencies. The first is that it is not predictive, producing atomic force constants and dispersion relations

that are inferred from experimental data. The second is that the results are not unique and can possibly be reproduced by alternative dynamical models [27].

An alternative way to calculate the atomic force constant is by utilizing the *ab initio* (first principle) approach, in which the analytic model is replaced by a full quantum mechanic electronic structure calculation, with no need for fitting to experimental data. The calculations of phonons within *ab initio* approach fall into to two classes [28, and 29]:

- The linear response method: where the dynamical matrix is expressed in terms of the inverse dielectric matrix describing the response of the valence electron density to a periodic lattice perturbation.
- The direct method, which has two categories
    a) The frozen-phonon method: the phonon energy is calculated as a function of the displacement amplitude in terms of the difference in the energies of the distorted and ideal lattices. However, it is restricted to phonons whose wavelengths are compatible with the periodic boundary conditions applied to the supercell.
    b) The *ab initio* force constant method, where the forces are calculated utilizing Hellmann-Feynman theorem by using the supercell method. It derives from them the values of the force constant matrices assuming a finite range of interactions, and utilizing the crystal symmetry and periodicity.

In the linear response method the response to a perturbation is calculated either by

inverting the dielectric matrix (computationally cumbersome and restrictive) or by iterating or solving an integral equation for the change in the electron density (can handle perturbations of arbitrary wave vectors, and only linear effects can be considered). On the other hand, the direct approach is computationally straightforward; it allows studying both linear and nonlinear effects. However, a disadvantage is that the supercell size increases rapidly as the symmetry of the structure decreases [30].

In this work the computer code called PHONON [31], which works within the framework of the *ab initio* force constant direct method was used. The *ab initio* force direct method is based on a supercell with periodic boundary conditions. The supercell is a finite crystallite that has the form of a parallelepiped, and is a multiplication of the primitive unit cell.

As a consequence of using a supercell with periodic boundary conditions in the *ab initio* force direct method, PHONON deals with the supercell force constant $\Phi_{\eta\theta}^{SC}(l,d;l',d')$ rather than the atomic force constant $\Phi_{\eta\theta}(l,d;l',d')$. That is, due to periodic boundary conditions, displacing the atom (l,d) causes the same displacement of the corresponding atoms $(l+L,d)$ in all images of the supercell, where $L=(L_a,L_b,L_c)$ are the indices of the lattice constants of the supercell. Therefore, a convenient way to calculate the dynamical matrix is to locate the center of the supercell at the considered atom (l,d). In this case, one can define an extended supercell which has the same size as the original one, but which includes atoms on all of its edges and corners. The extended supercell contains more atoms than the

conventional one. Special care has to be taken when the displaced atom (l,d) in the original supercell and those of the images $(l+L,d)$ are located on surfaces of the extended supercell and the same distance from the original atom (l,d). Those atoms will influence the central atom (l,d) with similar strength. To take this effect into account, the supercell force constant $\Phi_{\eta\theta}^{SC}(l,d;l',d')$ is defined as

$$\Phi_{\eta\theta}^{SC}(l,d;l',d') = w\sum_{L}\Phi_{\eta\theta}(l,d;l'+L,d') \tag{3.14}$$

$w=\frac{1}{n'}$, where n' is the number of equivalent atoms on the surfaces of the extended supercell. PHONON uses the Hellmann-Feynman force $\vec{F}(l,d)$ and solves the following equation

$$F_{\eta}(l,d) = -\sum_{(l,d)\in SC}\Phi_{\eta\theta}^{SC}(l,d;l',d')u_{\theta}(l',d'), \tag{3.15}$$

with respect to the supercell force constants. Hellmann-Feynman forces [32] are calculated via the *ab initio* approach. Once the supercell force constants are known, the supercell dynamical matrix can be defined:

$$D_{\eta\theta}^{SC}(\vec{q};d,d') = \frac{1}{\sqrt{M_d M_{d'}}}\sum_{l'\in SC}\Phi_{\eta\theta}^{SC}(0,d;l',d')e^{-i\vec{q}\cdot\left(\vec{R}(0,d)-\vec{R}(l',d')\right)}. \tag{3.16}$$

Note that atom $(0,d)$is always placed at the center of the extended supercell. The supercell dynamical matrix, equation (3.17), and the conventional dynamical matrix, equation (3.9) are equal in the following cases:

- The interaction range is confined to the interior of the extended supercell. That is, the force constants at and beyond the extended supercell can be neglected.
- The interaction range spreads out beyond the extended supercell. Then the two

dynamical matrices are equal at special wave vectors $\vec{q}_s$ fulfilling the condition $\exp\left(-i\vec{q}_s \cdot \vec{L}\right)=1$. Usually, the $\vec{q}_s$ wave vectors correspond to high-symmetry points of the Brillouin zone. Increasing the size of the supercell will increase the density of the wave vector grid $\vec{q}_s$ and more accurate phonon frequencies can be achieved. That is, the direct method does not impose any limit to the range of interaction.

The phonon modes are calculated by diagonalizing the dynamical matrix. Usually the dispersion relations are calculated along straight lines (high symmetry points) of the reciprocal space (Brillouin zone) of the crystal. Dispersion relations give detailed information about modes behavior in such a space. However, it is more common to deal with the phonon frequency distribution function, or phonon density of states rather than the individual frequencies. The phonon frequency distribution $\rho(\omega)$ is defined such that $\rho(\omega)d\omega$ is the fraction of frequencies in the interval $(\omega, \omega + d\omega)$. In the harmonic approximation, thermodynamic quantities are additive functions of the normal modes $\omega_j(\vec{q})$. Therefore, all of these functions can be expressed as averages over the phonon frequency distribution. The phonon frequency distribution is build as a histogram from the relation

$$\rho(\omega) = \frac{1}{3nr\Delta\omega} \sum_{\vec{q}j} \delta\left(\omega - \omega_j(\vec{q})\right). \tag{3.17}$$

where

$$\rho(\omega) = \int_0^{\omega_{\max}} \rho(\omega) d\omega = 1 \tag{3.18}$$

n is the number of sampling wave vectors $\vec{q}$, r is the number of atoms in the primitive

unit cell, and $\Delta\omega$ is the frequency interval of the histogram. Thus, there are $3r$ phonon branches (equal to the dimension of the dynamical matrix). The summations run over the wave vectors $\vec{q}$ of the first Brillouin zone and all phonon branches j. The wave vectors are selected randomly with a homogenous distribution over the first Brillouin zone using Monte Carlo sampling. The first Brillouin zone is defined as the Wigner-Seitz primitive cell[1] of the reciprocal lattice, or it could be equivalently defined as the set of points in $\vec{q}$ space that can be reached from the origin without crossing any Bragg plane.

The phonon frequency distribution is important in calculating many thermodynamical quantities such as entropy, internal energy, Helmholtz free energy, and heat capacity. Since these quantities are additive functions of the normal modes of vibration in the harmonic approximation, they can be written as averages over the phonon frequency distribution. As an example, the heat capacity C_v and the Helmholtz free energy F are written as [24]

$$C_v = 3rNk_B \int_0^\infty \rho(\omega) \left(\frac{\hbar\omega}{k_B T}\right)^2 \frac{\exp\left(\frac{\hbar\omega}{k_B T}\right)}{\left[\exp\left(\frac{\hbar\omega}{k_B T}\right)-1\right]^2} d\omega, \tag{3.19}$$

and

$$F = 3rNk_B \int_0^\infty \rho(\omega) \ln\left[2\sinh\left(\frac{\hbar\omega}{2k_B T}\right)\right] d\omega, \tag{3.20}$$

where r is the number of degrees of freedom in the unit cell (r =12 in the case of graphite),

[1] Wigner--Seitz primitive cell is defined as the smallest volume enclosed by perpendicular planes made at midpoint of the lines between reciprocal lattice points

and N is the number of the primitive unit cells.

3.1.1 Graphite Lattice Dynamics

As mentioned in chapter one (section 1.5), there is a great difference between the interplaner and intraplaner of graphite, such that graphite is considered a Lameller or quasi-two-dimensional structure. The bonding in graphite exhibits one of the largest anisotropies of any solid. Evidence of the impact of graphite's structure on its properties can be seen when examining quantities such as heat capacity, which has been studied theoretically and experimentally [33-36]. The overall picture drawn by these studies is that graphite's heat capacity exhibits T^3 behavior below 2 K (i.e., a pure Debye spectrum $\sim E^2$), a transition region between 2 to 20 K, and a T^2 region above 20 K (i.e., a linear form of the phonon spectrum which corresponds to a two dimensional structure). Compared to other materials, graphite has a smaller elastic continuum region; therefore, it has a smaller temperature range of T^3 Debye behavior, and a smaller parabolic energy range of the phonon frequency distribution.

The above behavior can be understood by examining the quantum theory of solids, which successfully explains the specific heat of harmonic crystals either at low or high temperatures. According to this theory, for an n-dimensional harmonic crystal, the low-energy part of phonon density of states varies as E^{n-1}, whereas the specific heat at low temperatures varies as T^n [37]. One of the earliest and most important theories of specific heat is Debye's theory. Its importance is due to its simplicity and success for most

materials. The Debye spectrum of a solid is obtained by assuming isotropic continuum behavior throughout the frequency range [i.e., if the traveling wave has a wave length which is long compared with the spacing between the atoms, the crystal will look like an elastic continuum to the wave]. The Debye approximation for the density of states, $\rho(E)$, of a solid is

$$\begin{matrix} \rho(E) = 3E^2 / E_D^3 , & 0 \le E \le E_D \\ 0 & E > E_D \end{matrix} , \tag{3.21}$$

where E_D is the cutoff frequency, which leads to the correct normalization of $\rho(E)$ and bears no simple relation to the true maximum frequency of the crystal. In the limit of low temperatures, Debye's T^3 law for the specific heat is given by

$$C_v \approx \frac{12\pi^4 r N k_B}{5}\left(\frac{T}{\Theta_D}\right)^3 \tag{3.22}$$

where $\Theta_d = E_D / k_B$ is the Debye characteristic temperature [38].

On the other hand, lattice dynamical properties of graphite have been studied extensively during the last five decades, either through proposed theoretical models or experimentally. Experimentally, the phonon dispersion relations of bulk phonons have been studied using various techniques, such as inelastic neutron scattering [39], infrared [40], far-infrared [41] and Raman spectroscopy [42, and 43]. Surface phonons have been measured by inelastic He- atom scattering [44], inelastic electron tunneling spectroscopy (IETS) [45], High-Resolution Electron Energy-Loss Spectroscopy (HREELS) [46-48], and inelastic X-ray scattering [49]. Theoretical models of lattice vibrations of graphite have been developed using at several levels;

1. By proposing *simple* lattice vibrational models based on the theory of heat capacity [34, and 37]. Such models assign two vibrational frequencies, one in-plane and the other is out-of-plane, where the former contributes twice as much as the latter.
2. By using the *semi-continuum* model, which utilizes the elastic description of the crystal to solve the vibrational equation of motions [35, 50, and 51]. Such models give a good description of the low temperature thermal properties of graphite. However, the high energy part of the phonon frequency distribution is relatively smooth, because of the continuum nature of the model.
3. By employing *atomic interaction models* [9, 39, and 52-55], which produce more detailed phonon frequency distributions. The parameters of these models are fitted to experimental data such as heat capacity and dispersion relations.
4. By *extrapolating* phonon frequency distributions from neutron scattering data [56-59].
5. By calculating phonon dispersion relations [49, 59-64] and generating the phonon frequency distribution [63-65] via the first principle approach.
6. By measuring the phonon frequency distribution using inelastic neutron scattering technique [66].

Two phonon frequency distributions will be considered in more details. These are:

-Young and Koppel (YK) phonon frequency distribution [9].

-Nicklow, Wakabayashi, and Smith (NWS) phonon frequency distribution [39].

3.1.1.1 The Young and Koppel (YK) Phonon Frequency Distribution (1965)

This phonon frequency distribution is used in all the ENDF/B evaluations. It was based on the lattice viabrational theory of graphite proposed by Yoshimori and Kitano in 1956 [52]. In this model Yoshimori and Kitano assumed that an atom in the graphite lattice is subject to four restoring forces due to: (a) changes in the bond angles proportional to a force constant μ, (b) changes in the bond length between nearest neighbors in the same plane, proportional to a force constant κ, (c) a central force due to changes in the bond length between nearest neighbors in two adjacent planes, proportional to a force constant κ', and (d) a force due to the bending of the planes and proportional to the displacement in the c-direction of any relative to its nearest neighbors in the same plane and proportional to a force constant μ'. Yoshimori and Kitano determined the force constant κ' form compressibility, μ' from specific heat (15-60 K), and κ and μ from the benzene molecule. They used Houston's method to obtain the phonon frequency distribution, where this method is known to be quantitavely incorrect and results in to spurious singularities in the frequency spectrum.

Young and Koppel in turn, instead of using the same values of κ and μ obtained by Yoshimori and Kitano from the benzene molecule, they fit these constants to the specific heat of reactor grade graphite in the range (300-1000 K). Also they used the root sampling method to sample the phonon frequency distribution in the first irreducible Brillouin zone using 47788 equally spaced points. Figure 3-1 shows the phonon frequency distribution of Young and Koppel [9].

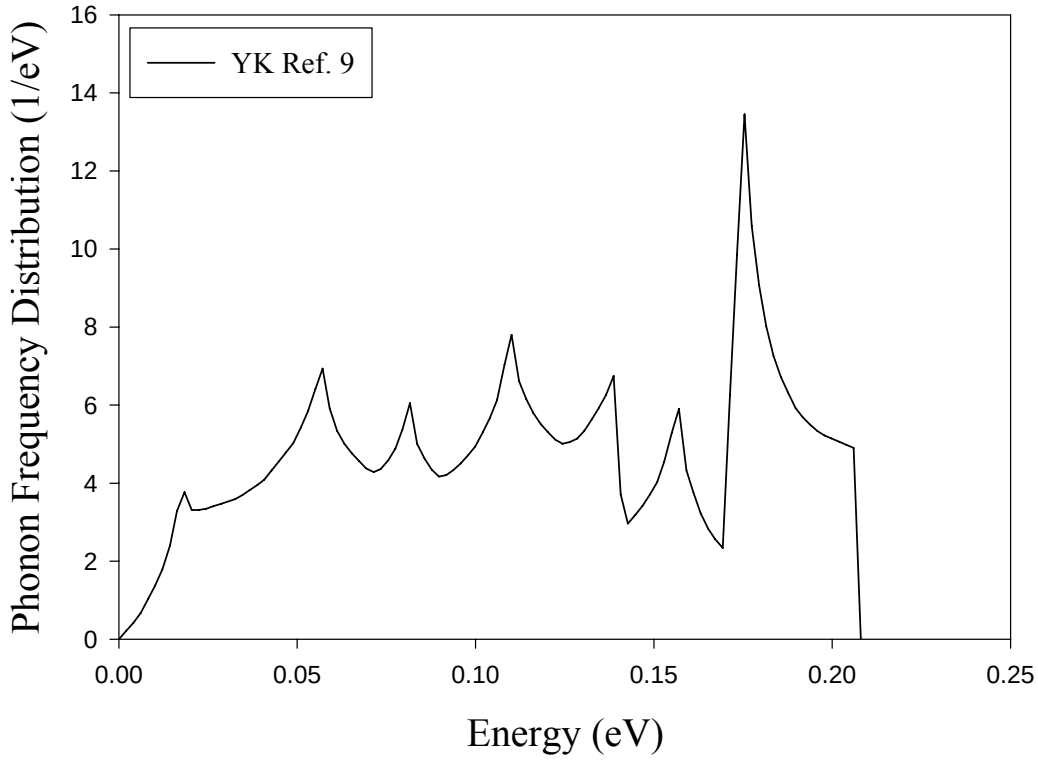

Figure 3-1 The phonon frequency distribution of Young-Koppel [9].

3.1.1.2 The Nicklow, Wakabayashi, and Smith Phonon Frequency Distribution

R. Nicklow, N. Wakabayashi, and H. Smith (NWS) [39] measured the phonon dispersion relations of high-quality pyrolytic graphite by using coherent inelastic neutron scattering techniques and the triple axis spectrometer located at the Oak Ridge high flux isotope reactor. The data was analyzed using an axially symmetric (AS) model assuming a two body interaction potential. A general tensor force constant model was used with 12 distinct parameters. The interaction between atoms is limited to the fourth nearest neighbors. The AS model was used to calculate the phonon frequency distribution shown in figure 3-2.

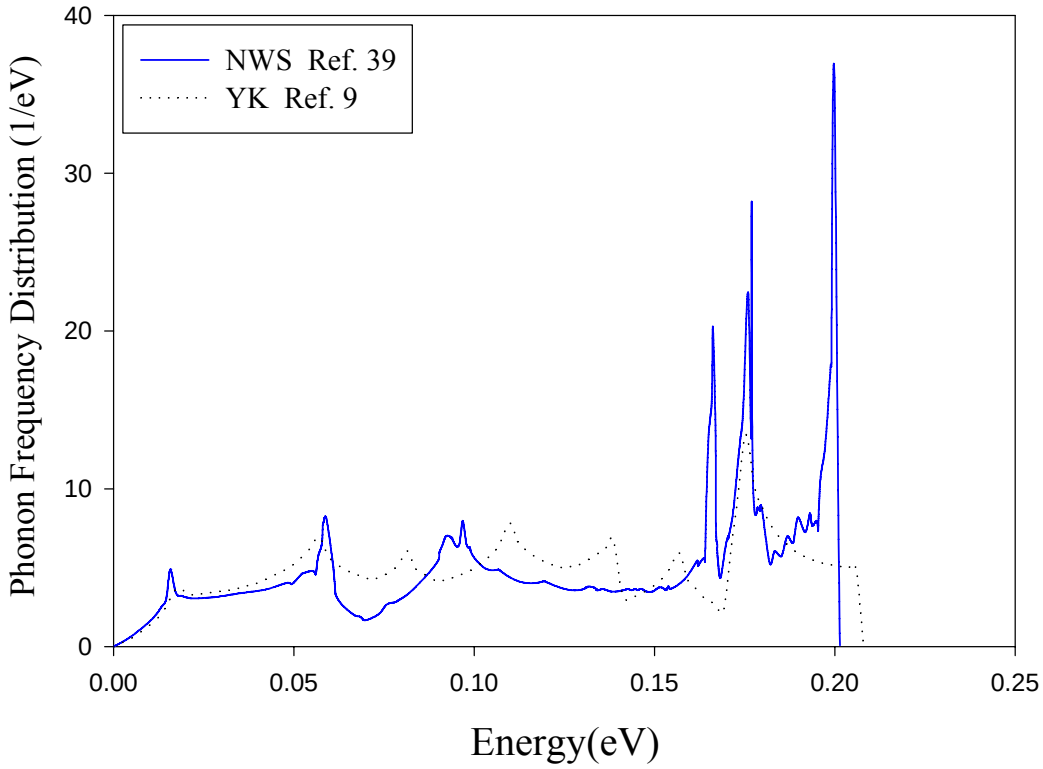

Figure 3-2 The Nicklow e*t al*, phonon frequency distribution (solid line) [39]. Also is shown the YK spectrum from figure 3-1 as a dotted line [9].

3.2 The *Ab initio* Approach

Due to advances in computational power, the possibility now exists to perform detailed quantum mechanical *ab initio* simulations of atomic systems. Using this approach, it is possible to predict the various properties of the material of interest. In lattice dynamic studies, the *ab initio* approach can be utilized to calculate the forces (Hellmann-Feynman forces) on the atoms of the system of interest. These forces will be used to calculate the force constants in order to construct the dynamical matrix and calculate the phonon frequency distribution [65, and 67].

3.2.1 Kohn-Sham Equations

Due to advances in computational power, the ability now exists to perform detailed quantum mechanical *ab initio* simulations for atomic systems. These simulations are currently used in fields such as physics, chemistry, and materials science. *Ab initio* [26] is a Latin term that means from the beginning. In sciences (especially physics and chemistry) it means from first principles, it relies on basic and established laws of nature without additional assumptions or special models. In the *ab initio* approach the physical properties of the material of interest are predicted using quantum mechanics and utilizing the fact that if the total energy of a system is known, then all its physical properties (that can be related to the total energy or the differences in total energy) can be calculated.

It is out of question to solve Schrödinger equation for a crystal of N atoms, such a crystal has N nuclei and ZN electrons (i.e., N+ZN electromagnetically interacting particles). The exact Hamiltonian of such many-body problem is

$$\begin{aligned}
&\hat{H} = \hat{T}_{ions} + \hat{T}_{ele} + \hat{V}_{ion-ele} + \hat{V}_{ele-ele} + \hat{V}_{ion-ion} \\
&\hat{H} = -\frac{\hbar^2}{2M}\sum_i \nabla_{R_i}^2 - \frac{\hbar^2}{2m_e}\sum_j \nabla_{r_j}^2 \\
&\quad -\frac{1}{4\pi\varepsilon_\circ}\sum_{i,j}\frac{Ze^2}{\left|\vec{R}_i - \vec{r}_j\right|} + \frac{1}{8\pi\varepsilon_\circ}\sum_{i\neq j}\frac{e^2}{\left|\vec{r}_i - \vec{r}_j\right|} + \frac{1}{8\pi\varepsilon_\circ}\sum_{i,j}\frac{Z^2e^2}{\left|\vec{R}_i - \vec{R}_j\right|} \quad ,
\end{aligned} \tag{3.23}$$

where M is the mass of the i^{th} nucleus at position $\vec{R}_i$. m_e is the electron mass, and $\vec{r}_i$ are the electronic position vectors. The first two terms represent the kinetic energy operators of the ions and electrons respectively. The last three terms represent the ion-electron $\hat{V}_{i-e}$, the electron-electron $\hat{V}_{e-e}$, and ion-ion $\hat{V}_{i-i}$ potential energy operators.

Due to the large difference in mass between electrons and nuclei, electrons respond instantaneously to the motion of the nuclei. That is, one can think of the nuclei as frozen particles at fixed positions. This is called the adiabatic approximation or the Born – Oppenheimer approximation. As a consequence of this approximation, the first term in equation (3.23) becomes zero (nuclei do not move), the last term reduces to a constant (step function). That is, the Hamiltonian is left with the kinetic energy operator of the electron gas, the electron-electron potential energy operator, and the ion-electron potential energy operator, which can be viewed as external potential to the electrons. The adiabatic approximation leads to the separation of nuclear and electronic coordinates, that is, ZN interacting electrons are left moving in external potential of nuclei $\hat{V}_{i-e} \equiv \hat{V}_{ext}$. So equation (2.23) becomes in short notation

$$\hat{H} = \hat{T}_e + \hat{V}_{e-e} + \hat{V}_{ext}. \tag{3.24}$$

The many-body problem is reduced to a many-electron problem. However, even with this simplification, the many-electron problem is still formidable to solve. Further simplification is reached using density functional[2] theory (DFT) [68, 69], which is introduced to model the electron-electron interaction, using the electronic density $\rho(\vec{r})$ instead of using the complicated many-electron wave function. Hohenberg and Kohn [68] proved that the total energy of an electron gas is a unique functional of the electron density, and the minimum value of the total energy functional $E[\rho]$ is the ground state energy of the system. The density which yields this minimum is the exact single particle ground state

[2] Functional means a function (operator) that takes functions as its argument, and gives a number as its output, or a function whose domain is aset of functiuons.

density. The Coulomb energy of a system of electrons can be reduced by keeping the electrons spatially separated. The spatial separation can occur to electrons having the same spin due to the anti-symmetric property of their wave function (electrons are fermions). The reduction in the energy of the electron system due to the anti-symmetric property of the wave function is called the exchange energy. Electrons can also be separated spatially if they have opposite spins. In this case, the Coulomb energy of the electronic system is reduced at the cost of increasing the kinetic energy of the electrons. The difference between the many-body energy of electronic system and the energy of the system calculated in the Hartree-Fock approximation is called the correlation energy [70, and 71].

Equation (3.24) can be rewritten in terms of its corresponding energy functional, and introduce the exchange and correlation contributions. The corresponding energy functional to equation (3.24) is

$$E[\rho] = T_e[\rho] + E_{e-e}[\rho] + E_{ext}[\rho]. \tag{3.25}$$

By adding and subtracting the kinetic energy functional of non-interacting electron gas $T_\circ[\rho]$ and the Hartree functional $E_H[\rho]$, equation (3.25) can be rearranged as

$$E[\rho] = T_\circ[\rho] + E_H[\rho] + E_{ext}[\rho] + (T_e[\rho] - T_\circ[\rho]) + (E_{e-e}[\rho] - E_H[\rho]). \tag{3.26}$$

But $E_{e-e}[\rho] - E_H[\rho]$ is defined as the correlation functional $E_c[\rho]$, and $T[\rho] - T_\circ[\rho]$ is defined as the exchange functional $E_x[\rho]$. Where $E_c[\rho] + E_x[\rho]$ is written as the exchange –correlation functional $E_{xc}[\rho]$. Therefore equation (3.26) becomes

$$E[\rho] = T_\circ[\rho] + E_H[\rho] + E_{ext}[\rho] + E_{xc}[\rho]. \tag{3.27}$$

The above expression is called Kohn-Sham energy functional; its corresponding Hamiltonian

is called the Kohn-Sham Hamiltonian and is given by

$$\hat{H}_{KS} = \hat{T}_{\circ} + \hat{V}_H(\vec{r};\rho) + \hat{V}_{ext}(\vec{r}) + \hat{V}_{xc}(\vec{r};\rho), \tag{3.28}$$

where $\hat{T}_{\circ} = -\frac{\hbar^2}{2m_e}\nabla^2$ is the kinetic energy operator of a single electron , the Hartree potential operator, $\hat{V}_H(\vec{r};\rho)$ is given by

$$\hat{V}_H(r;\rho) = \frac{e^2}{4\pi\varepsilon_{\circ}}\int \frac{\rho(\vec{r}')}{|\vec{r}-\vec{r}'|}d\vec{r}\,, \tag{3.29}$$

and the exchange-correlation potential operator, $\hat{V}_{xc}(\vec{r};\rho)$ is given formally by the functional derivative

$$\hat{V}_{xc}(\vec{r};\rho) = \frac{\delta E_{xc}[\rho]}{\delta\rho(\vec{r})}. \tag{3.30}$$

Only the minimum value of the Kohn-Sham energy functional has a physical meaning. At the minimum the Kohn-Sham energy functional is equal to the ground state energy of the system [70]. To find the ground state density of a non-interacting single particle, a Schrödinger- like equation, called Kohn Sham equation is used [69]

$$\hat{H}_{KS}\psi_i = \varepsilon_i\psi_i\,. \tag{3.31}$$

Where ψ_i is the wave function of he electronic state i and ε_i is the Kohn-Sham eigenvalue. The ground state density $\rho(\vec{r})$ for a system of ZN electrons is given-in terms of ψ_i - as

$$\rho(\vec{r}) = \sum_{i=1}^{ZN}|\psi_i|^2\,. \tag{3.32}$$

Both $\hat{V}_H(\vec{r};\rho)$ and $\hat{V}_{xc}(\vec{r};\rho)$ depend on the electronic density $\rho(\vec{r})$ which in turn depends on ψ_i. Thus, the Kohn-Sham equations are self consistent equations. The Kohn-Sham equation (3.31) is an exact equation, where the Hamiltonian of the

many-electron system has been reformulated into a Hamiltonian describing a system of non-interacting electrons moving in an effective potential $\hat{V}_{eff} = \hat{V}_H(\vec{r};\rho) + \hat{V}_{ext}(\vec{r}) + \hat{V}_{xc}(\vec{r};\rho)$. It is worth mentioning that the eigenvalues ε_i are not the energies of the single particle electron states. Also the single particle wave functions ψ_i are not the true eigenfunctions of the electrons, but the density of these particles is equal to the true electron density.

3.2.2 The Local Density Approximation (LDA)

The exchange-correlation functional $E_{xc}[\rho]$ contains what is missing from $T_{\circ}[\rho]$ and $E_H[\rho]$ to get $T_e[\rho] + E_{e-e}[\rho]$. Unfortunately, the form of $E_{xc}[\rho]$ is not known. However, actual calculations need an expression (even approximated) for $E_{xc}[\rho]$. A widely used approximation is the Local Density Approximation (LDA) [68]; which assumes the exchange-correlation energy per electron at a point $\vec{r}$ in the electron gas $\varepsilon_{xc}(\rho(\vec{r}))$ is equal to the exchange-correlation energy per electron in a homogenous electron gas $\varepsilon_{xc}^{\text{hom}}(\rho(\vec{r}))$ that has the same density as the electron gas at point $\vec{r}$, with this assumption, $E_{xc}[\rho]$ reads

$$E_{xc}^{LDA}[\rho] = \int \varepsilon_{xc}^{\text{hom}}(\rho(\vec{r}))\rho(\vec{r})d\vec{r}\,, \tag{3.33}$$

and the exchange-correlation potential is

$$\hat{V}_{xc}(\vec{r};\rho) = \frac{\delta E_{xc}[\rho(\vec{r})]}{\delta\rho(\vec{r})} = \varepsilon_{xc}^{\text{hom}}(\rho(\vec{r})) + \rho(\vec{r})\frac{\partial\varepsilon_{xc}^{\text{hom}}(\rho(\vec{r}))}{\partial\rho(\vec{r})}\,. \tag{3.34}$$

The LDA assumes the exchange –correlation energy functional is purely local, that is, the contribution at each point $\vec{r}$ is independent of other points. This assumption simplifies the calculations since there are several known expressions for the exchange- correlation energy of a homogenous electron gas [69, and 72]. It is expected that LDA will work very well in the limit of high density or in a slowly vary charge-density distribution. However, this

approximation works remarkably very well for other cases despite its simplicity. Equation (3.33) has been generalized to consider spin-polarized electron gas with spin up and down

$$E_{xc}^{LDSA}\left[\rho^{\uparrow},\rho^{\downarrow}\right]=\int \varepsilon_{xc}^{\text{hom}}\left(\rho^{\uparrow}(\vec{r}),\rho^{\downarrow}(\vec{r})\right)\rho(\vec{r})d\vec{r}\,, \tag{3.35}$$

where $\varepsilon_{xc}^{\text{hom}}\left(\rho^{\uparrow}(\vec{r}),\rho^{\downarrow}(\vec{r})\right)$ is the exchange-correlation energy per electron of a homogenous spin-polarized electron gas with spin up and spin down densities $\rho^{\uparrow}$, $\rho^{\downarrow}$ respectively.

3.2.3 The Generalized Gradient Approximation (GGA)

The next step to improve LDA is to make the exchange-correlation contribution depends both on the magnitude of the electronic density $\rho(\vec{r})$ and on its gradient $\vec{\nabla}\rho(\vec{r})$. That is, the exchange-correlation contribution to an infinitesimal volume of electron gas depends on the surrounding densities (gradient of densities will play a role). This approximation therefore, called the Generalized Gradient Approximation (GGA) [73, 74]. Under this approximation, equation (3.33) becomes

$$E_{xc}^{GGA}\left[\rho\right]=\int \varepsilon_{xc}^{\text{hom}}\left(\rho(\vec{r}),\vec{\nabla}\rho(\vec{r})\right)\rho(\vec{r})d\vec{r}\,. \tag{3.36}$$

3.2.4 Periodic Boundary Conditions

So far the many-electron problem is reduced to a single electron problem moving in an effective potential, in addition, the exchange-correlation term was approximated as discussed in the above sections.

For an infinite number of atoms we have an infinite number of electrons, where each electron is represented by a wave function. In order to reduce the number of wave functions,

the calculations are performed on periodic system. That is a large supercell is constructed and repeated periodically throughout the space. For crystalline solid the potential is periodic that is, $V(\vec{r}+\vec{R})=V(\vec{r})$, also, the kinetic part is periodic, therefore the total Hamiltonian is periodic. Since the Hamiltonian is periodic, Bloch's theorem can be applied, where the electronic wave function can be written as a sum of plane waves basis set $e^{i(\vec{k}+\vec{G})\cdot\vec{r}}$

$$\psi_i(\vec{r}) \rightarrow \psi_i^{\vec{k}}(\vec{r}) = \sum_{\vec{G}} C_i^{\vec{G}}\left(\vec{k}\right) e^{i\left(\vec{k}+\vec{G}\right)\vec{r}} = \sum_{\vec{G}} C_i^{\vec{G}}\left(\vec{k}\right)\left|\vec{k}+\vec{G}\right\rangle. \qquad (3.37)$$

Only a finite number of states are occupied at each $\vec{k}$ point, wave functions $\psi_i^{\vec{k}}(\vec{r})$ that have the same $\vec{k}$ point but different i will be expanded in the basis set with this particular $\vec{k}$ point. Whereas, wave functions with another $\vec{k}$ point, will be expended with a new set using the new $\vec{k}$ point. Bloch's Theorem changes the problem of calculating an infinite number of electronic wave functions to one of calculating a finite number of electronic wave functions at an infinite number of $\vec{k}$ point. Computationally, one can not work with an infinite basis set. Therefore, few concepts were introduced to reduce and simplify the computational efforts, these are $\vec{k}$ point sampling, cutoff energy E_{cut}, and Pseudopotential Approximation.

3.2.5 $\vec{k}$ Point Sampling

Calculation of many properties, such as density, total energy, number of electrons in a band, …etc. requires the integration over the Brillouin zone. Instead of calculating the finite electronic wave functions at an infinite number of $\vec{k}$ points, it is possible to represent these wave functions over a region of $\vec{k}$ space, at a single point. This is due to the fact that, electronic wave functions at $\vec{k}$ points that are very close to each other will be almost

identical. In this case the integration over the Brillouin zone will be replaced by a sum over a finite discrete set of states corresponds to different $\vec{k}$ points.

Different schemes have been proposed to produce sets of $\vec{k}$ points to perform an efficient integration (summation) over the Brillouin zone of smooth periodic functions [75, 76]. A general method that is the most widely used was proposed by Monkhorst and Pack [76] where a uniform set of $\vec{k}$ points is formed as a linear combination of the reciprocal lattice vectors $\vec{b}_1$, $\vec{b}_2$, and $\vec{b}_3$

$$\vec{k} = n_1\vec{b}_1 + n_2\vec{b}_2 + n_3\vec{b}_3, \tag{3.38}$$

n_1, n_2, and n_3 are chosen accordingly to the formula

$$n_i = \frac{2n_i - N_i - 1}{2N_i}, \tag{3.39}$$

where $i = 1, 2, 3$, $n_1 = 1, 2, \cdots . N_i$, and N_i is an integer that determine the number of the special points in the set (mesh size).

It is worth mentioning that, the special $\vec{k}$ points set has to be dense enough in regions where integral varies rapidly. Also, symmetry can be used to reduce the calculations (reduce number of $\vec{k}$ points) by involving only the $\vec{k}$ points in the reduced Brillouin zone.

3.2.6 Energy cutoff E_{cut}

The plane wave basis set can be truncated to include only plane waves that have kinetic energies E less than a particular cutoff energy E_{cut},

$$E \le E_{cut}, \tag{3.40}$$

where

$$E_{cut} = \frac{\hbar^2}{2m}\left|G_{cut}\right|^2, \tag{3.41}$$

and

$$E = \frac{\hbar^2}{2m}\left|\vec{G} + \vec{k}\right|^2. \tag{3.42}$$

This corresponds to a sphere with radius $\vec{G}_{cut}$ centered at the origin of reciprocal space. All vectors that are inside the sphere are taken into the basis set. Therefore, introducing an energy cutoff to the discrete plane wave basis set produces a finite basis set.

3.2.7 Pseudopotential Approximation

The core region of the nuclei is composed of tightly bound core electrons which respond very little to the presence of the neighboring atoms. The remaining volume of the atom contains the valence electron density; which is involved in binding atoms together. Therefore, most physical properties of solids depend on the valence electrons more than on the core electrons. The pseudopotential approximation, thus, replaces the strong electron-ion potential with a much weaker potential called a *pseudopotential*. The pseudopotential represents the nucleus and the core electrons so that out side the core region, the total potential and the pseudopotential have the same behavior [77]. The pseudopotential approximation was adopted from orthogonal plane wave method (OPW). The early work of pseudopotentials (up to 70s) was determined empirically by fitting the potential parameters to experimental measurements. Nowadays, norm-conserving *ab initio*

pseudopotential are most commonly used (no fitting to experimental data) [78], such kind of pseudopotentials are more *accurate, transferable*, and easier to use. By transferability we mean; the pseudopotential constructed in one environment (the atom) is capable of describing the physical properties in different environments (atoms, molecules, solids...). For instance, the pseudopotential of carbon can be used to study graphite, diamond, fullerene, Nanotube, either their bulk or surface properties.

Norm-conserving *ab initio* pseudopotentials are constructed such that [78] the pseudowave function has the same value as the true wave function outside the cutoff radius $\vec{r}_c$ which indicates the radius of the core region. The integrated value of the absolute square of the wave function has the same norm as the true wave function inside $\vec{r}_c$. The pseudowave function is made smooth as possible inside the sphere of radius $\vec{r}_c$ and is connected continuously to the true wave function, that is, it has the same value and the same derivative as those of the true wave function, at the cutoff radius. Figure 3-3 shows a schematic illustration of a pseudopotential model and its corresponding pseudowave function [71], as we see the rapid oscillations of the valence wave function in the core has been removed. The replacement of the true potential by a weak pseudopotential allows the wave functions to be expanded using smaller number of plane wave basis states, than it would be needed in full ionic potential. In construction of the norm-conserving pseudopotential there are some arbitrarily parameters such as $\vec{r}_c$. However, there is no one best pseudopotential for any given element, there maybe many choices.

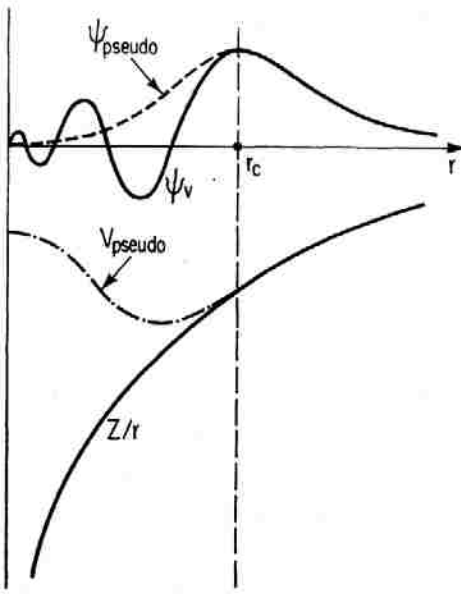

Figure 3-3 A schematic representation of the pseudopotential method [71].

As mentioned earlier good pseudopotentials are accurate and transferable, accuracy and transferability are competing with *smoothness* of the pseudopotential. Since accuracy and transferability require the choice of a small cutoff radius $\vec{r}_c$ (hard potential) in order to describe accurately the wave function near the ion, this in turn leads to expand the wave function with large number of plane wave basis states. On the contrary, smoothness requires a large $\vec{r}_c$ (soft potential), and fewer number of plane wave basis states are used. Norm-conserving pseudopotential achieves the goal of accuracy at some sacrifice of smoothness. Different approaches were proposed to produce highly accurate pseudopotentials that are smooth such as *Ultrasoft* pseudopotential [79] and P*rojected Augmented Waves* (PAW) [80]. Both approaches are formally related to the OPW equations, and the pseudowave functions are made as smooth as possible in the core region. The norm conservation is taken into account after solving the generalized eigenvalue equation.

3.2.8 Solving Kohn-Sham Equations

So far, the DFT approximations (LDA and GGA) were introduced to simplify and approximate the exchange correlation term. In addition, Bloch's theorem was utilized to expand the wave functions, whereas the energy cutoff concept, the $\vec{k}$ point sampling, and pseudopotential approximation were introduced to reduce the number of electrons in the system of interest, and to reduce the number of basis states used in expanding the wave function. At this level Kohn-Sham equation can be solved.

By substituting equation (3.37) into equation (3.31) and multiplying by $\left\langle \vec{k}+\vec{G}' \right|$ from left, the following form is obtained

$$\sum_{\vec{G}'} \left\langle \vec{k}+\vec{G}' \middle| \hat{H}_{KS} \middle| \vec{k}+\vec{G} \right\rangle C_i^{\vec{G}'}\left(\vec{k}\right) = \varepsilon_i C_i^{\vec{G}}\left(\vec{k}\right), \tag{3.43}$$

where

$$\left\langle \vec{k}+\vec{G}' \middle| \vec{k}+\vec{G} \right\rangle = \delta_{\vec{G}',\vec{G}}, \tag{3.44}$$

is utilized in writing the right hand side of equation (3.43), and finding the kinetic energy contribution

$$\left\langle \vec{k}+\vec{G}' \middle| -\frac{\hbar^2}{2m}\nabla^2 \middle| \vec{k}+\vec{G} \right\rangle = \frac{\hbar^2}{2m}\left|\vec{k}+\vec{G}\right|\delta_{\vec{G}',\vec{G}}. \tag{3.45}$$

For a crystal, the potential $\hat{V}_{eff}\left(\vec{r}\right)$ is periodic. Therefore, it can be expanded as

$$\hat{V}_{eff}\left(\vec{r}\right) = \sum_{\vec{G}} \hat{V}_{eff}\left(\vec{G}\right) e^{i\vec{G}\cdot\vec{r}} \tag{3.46}$$

Thus equation (3.44) becomes

$$\sum_{\vec{G}'}\left[\frac{\hbar^2}{2m}\left|\vec{k}+\vec{G}\right|^2 \delta_{\vec{G}',\vec{G}} + V_H\left(\vec{G}-\vec{G}'\right) + V_{ext}\left(\vec{G}-\vec{G}'\right) + V_{xc}\left(\vec{G}-\vec{G}'\right)\right] C_i^{\vec{G}'}\left(\vec{k}\right) = \varepsilon_i C_i^{\vec{G}}\left(\vec{k}\right). \tag{3.47}$$

The solutions to the above eigenvalue problem are obtained by diagonalizing the Hamiltonian matrix. After building the system (supercell) with defined atomic types, positions, and symmetry, choosing the type of the DFT to describe the exchange-correlation contribution, selecting the pseudopotential approximation, energy cut off, and the $\vec{k}$ point sampling mesh, an initial guess for the electron charge density is made. Then the Hartree and exchange-correlation potentials are calculated, and the Hamiltonian is constructed. Kohn-Sham equation is solved by diagonalzing the Hamiltonian. From this solution we obtain Kohn-Sham wave functions. From these wave functions a new density will be calculated, using this new density, a new Hamiltonian is constructed after calculating the Hartree and exchange-correlation potentials; again Kohn-Sham equation is solved. This process is repeated until the solution is self consistent. That is the procedure will converge to a density ρ_f which generates a Kohn-Sham Hamiltonian which yields as a solution again ρ_f. Kohn-Sham equations have to be solved self consistently. Only the minimum value of the Kohn-Sham energy functional has a physical meaning, that is, at the minimum, Kohn-Sham energy functional is equal to the ground state energy of the system [69]. Figure 3-4 shows a flow chart of solving Kohn-Sham equations.

3.2.9 Hellmann-Feynman Theorem

Hellmann-Feynman theorem simplifies the calculations of the physical forces on the ions [32]. It states that for any perturbation λ, the first derivative of the ground state energy of the Hamiltonian $\hat{H}$, can be calculated by using the variational property of the wave function ψ_λ, that is

$$\frac{\partial E}{\partial \lambda} = \int \psi_\lambda^* \frac{\partial \hat{H}}{\partial \lambda} \psi_\lambda d^3 r \,. \tag{3.48}$$

The above equation represents the general form of Hellmann-Feynman theorem. If λ_d represents the displacement of d^{th} ion, then equation (3.48) represents the negative of the force acting on the d^{th} nucleus. Note that, only the variation in the Hamiltonian is required to calculate the forces, while the variation in the wave function due to the variation in λ is not required.

The variational principle can be used in the frame work of the DFT to derive an explicit expression of the forces on ions by calculating the change in the energy functional $\delta E[\rho]$. The change in the energy functional given by equation (3.25) is written as

$$\delta E[\rho] = \delta T_e[\rho] + \delta E_{e-e}[\rho] + \delta E_{ext}[\rho] + \delta E_{II}\,, \tag{3.49}$$

where E_{II} is the nucleus-nucleus interaction is included, which is essential in the total energy calculation but is only a classical additive in the theory of electronic structure. The change can be due to a slight nucleus displacement, where a change $\delta\rho$ in the electronic density ρ is necessary to keep the electrons in the ground state of the corresponding new configuration of the nuclei. The change in $\delta E_{ext}[\rho]$ is

$$\delta E_{ext}[\rho] = \int \delta\rho V_{ext} d\vec{r} + \int \rho \delta V_{ext} d\vec{r}\,. \tag{3.50}$$

Thus equation (3.49) can be written as

$$\delta E[\rho] = \int \frac{\delta(T[\rho] + E_{e-e}[\rho])}{\delta\rho} \delta\rho\, d(\vec{r}) + \int \delta\rho V_{ext} d\vec{r} + \int \rho \delta V_{ext} d\vec{r} + \delta E_{II}\,. \tag{3.51}$$

The terms in $\delta\rho$ sum to zero since in the ground state the energy functional satisfies

$$\frac{\delta E[\rho]}{\delta\rho} = \frac{\delta T[\rho]}{\delta\rho} + \frac{\delta E_{e-e}[\rho]}{\delta\rho} + V_{ext} = \xi\,, \tag{3.52}$$

where ξ is a Lagrangian multiplier that has to be a constant independent of $\vec{r}$ when the system is in the ground state. So equation (3.51) becomes

$$\delta E[\rho] = \int \rho \delta V_{ext} d\vec{r} + \delta E_{II} \ . \tag{3.53}$$

The resulting force due to the displacement $\delta\vec{R}_I$ of nucleus *I* is given by

$$-\frac{\delta E[\rho]}{\delta R_I} = -\int \rho \frac{\delta V_{ext}}{\delta R_I} d\vec{r} - \frac{\delta E_{II}}{\delta R_I} \ . \tag{3.54}$$

As seen the above expression does not involve any change in ρ but it depends explicitly on the nuclear position.

In the frame of DFT the electronic wave functions must be eigenstates of the Kohn-Sham Hamiltonian so that Hellmann-Feynman theorem is applicable. Only the minimum value of Kohn-Sham energy functional has a physical meaning that is equal to the ground state energy of electrons.

The ab-initio force-constant direct approach is based on the solution of the Kohn-Sham equation, where the phonon frequencies are calculated from Hellmann-Feynman forces generated by a small atomic displacement, once at a time. The force constants are fitted to the provided Hellmann-Feynman forces by utilizing the crystal symmetry space group and assuming a finite range of interaction. Hellmann-Feynman forces are calculated using the soft ware VASP (Vienna A*b initio* Simulation Package) [81].

3.2.10 Graphite A*b Initio* Calculations

The first *ab initio* calculation was in 1984 to study structures of graphitic phases of

carbon and silicon [82]. While the first *ab initio* study of the dispersion relations was on a graphite sheet containing 24 atoms in1995 and was compared with other graphitic sheet structures of BN and BC_2N [59]. Both of these studies were performed within the frame work of LDA. The major breakthrough in the determination of graphite dispersion relations by first principles calculations were done by Kresse *et al*, in 1996 using the *ab initio* force constant direct method [60], and by Pavone *at a*l, using the linear response theory in 1996 [61]. Both of these calculations employed the LDA and introduced considerable changes in the behavior of the dispersion relations of graphite.

The discovery of carbon nanotubes paid much attention to investigate their vibrational properties [62, 64, 66, and 83]. The work on the vibrational properties of carbon nanotubes renewed the interest in the vibrational properties of graphite by using the first principle calculations. As a consequence of these studies the dispersion relations of graphite have been improved quantitatively both computationally and experimentally. As mentioned earlier graphite has unusual structure, because of the nature of bonding between its atoms. That is, the very strong local covalent bond between atoms in plane and weak non-local Van der Waals interactions between planes. However, the DFT does not account for the Van der Waals interaction properly [84]. The origin of Van der Waals interaction is non-local correlation between electrons. In addition, the Van der Waals energy is small compared with the total energy of a typical system. This makes it difficult to be treated accurately. As mentioned earlier, DFT is an exact theory which treats approximately the exchange-correlation energy via LDA or GGA. These approximations fail for describing the

large range Van der Waals interaction. In fact, this is not a failure of DFT itself, but an effect of the local nature of LDA and GGA. That is, the exchange-correlation potential at point $\vec{r}$ is determined by the density and its low-order gradients at the same point $\vec{r}$. The description of long-range forces such s the Van der Waals requires fully non-local functional. Therefore, it is not possible to correctly calculate some structure properties that related to Van der Waals interaction, such as interpalner spacing, or shear elastic constant. Calculations of cohesive properties of graphitic structure are sensitive to the choice of pseudopotential, exchange-correlation functional, and basis set. Also most of *ab initio* calculations of Van der Waals energies do not give correct results that agree with experimental measurements, but some have been successful due to some cancellation of errors, and specific details of the calculations [84].

Figure 3-5 shows a flow chart that connecting the *ab initio*, lattice dynamics, and thermal neutron scattering cross section theories in terms of computer codes that were used in this work. Appendix B1 shows an introduction to VASP interface and the input parameters. Similarly, appendix B2 shows PHONON interface and the input parameters used in the calculations.

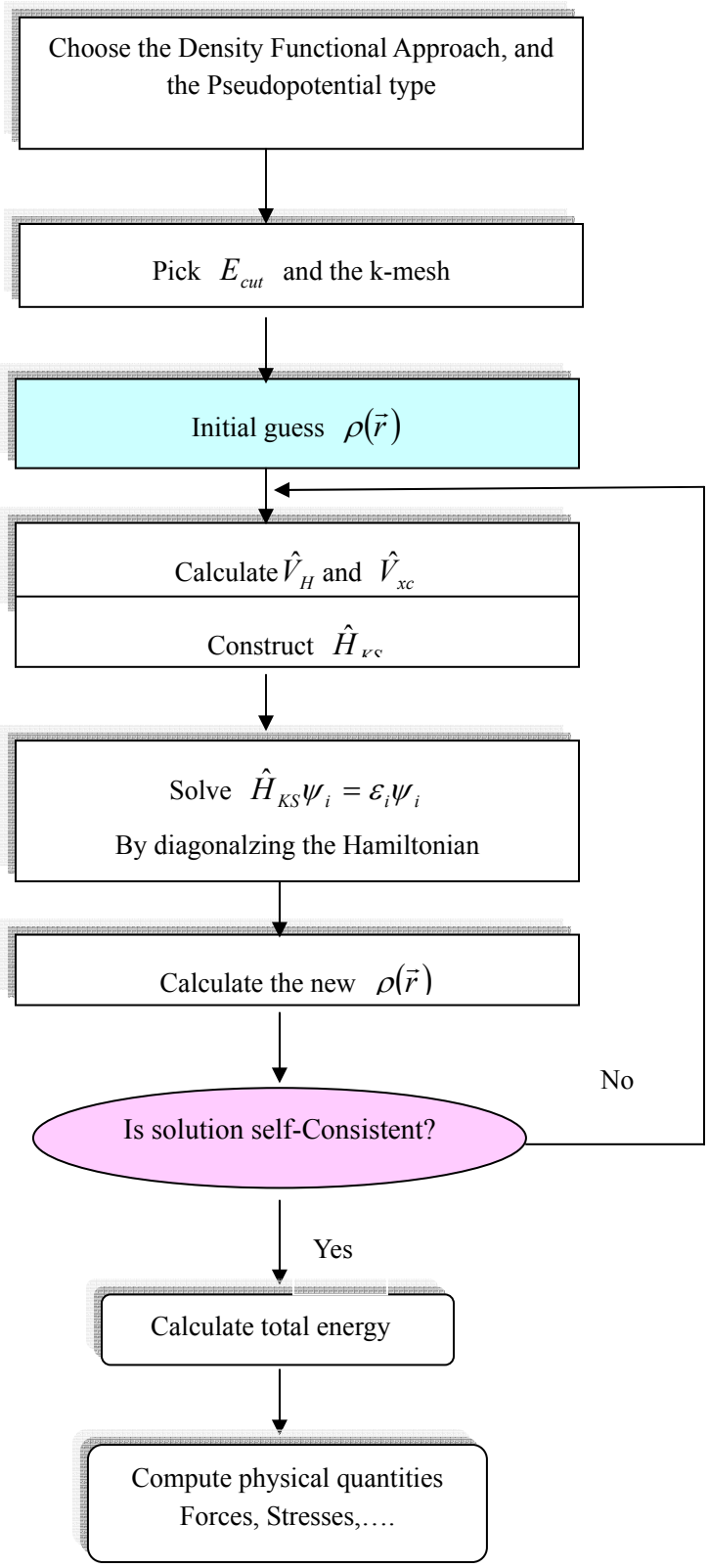

Figure 3-4 A flow chart for the self-consistent procedure to solve Kohn-Sham equation.

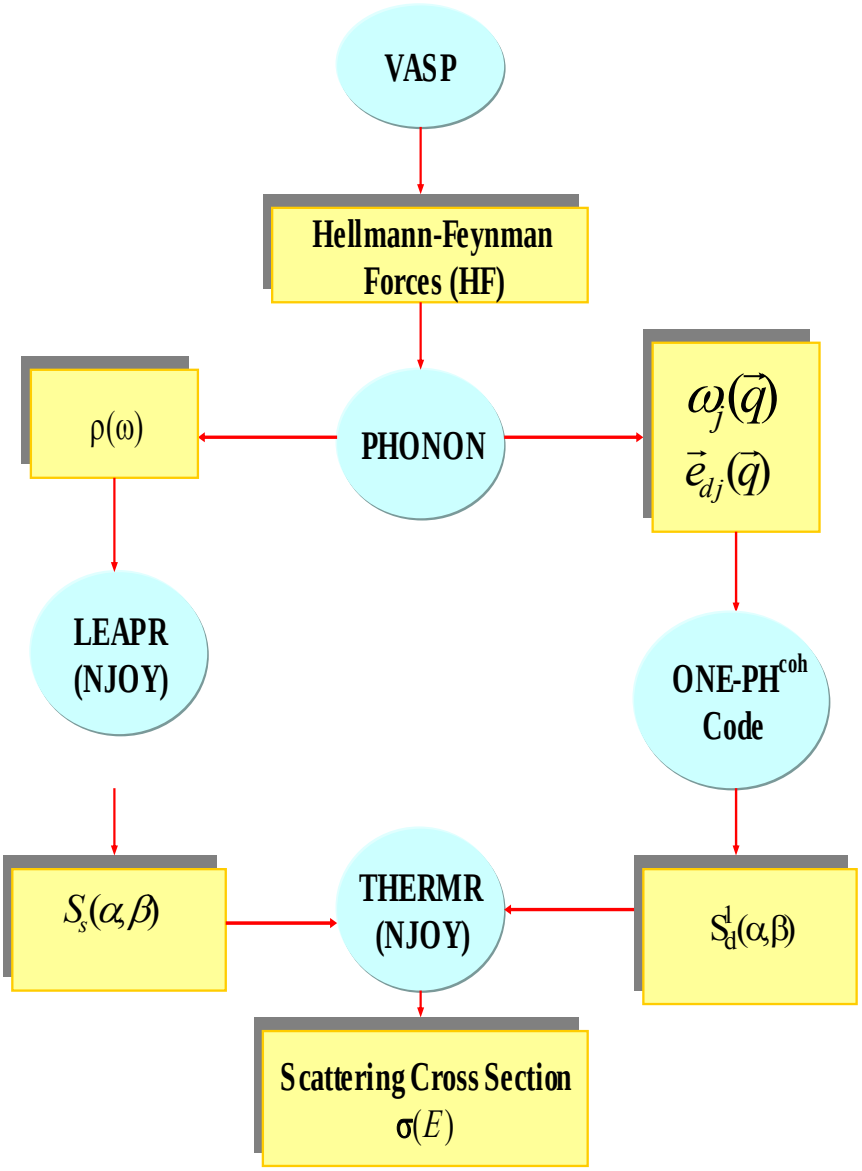

Figure 3-5 A flow chart that connects the software packages that are used to generate cross sections.

Chapter 4 Results and Discussion

4.1 *Ab Initio* Calculations

4.1.1 Structure Optimization

In this work *the ab initio* calculations are performed at 0 K. The first step in performing *ab initio* calculations is to optimize the lattice parameters of the unit cell, so that, the system is relaxed and in its ground state. In order to get the equilibrium lattice constants corresponding to 0 K, a *structure optimization* can be performed by relaxing the atomic positions, and changing the volume and shape of the unit cell, simultaneously, or an *energy versus volume minimization* can be used in which the lattice parameters of the system of interest can be changed for non-cubic systems like graphite in two ways: First, the lattice constants are varied separately, that is, the first lattice constant is varied while the other one is kept constant in order to minimize the energy of the system, then its corresponding value that minimizes the system energy is fixed and used while varying the second lattice constant for further minimization of the energy system. Second, both lattice constants can be varied together while keeping a constant ratio between them, this method requires fewer calculations. In order to optimize the structure, the total energy of the system must converge with respect to two critical parameters: the energy cutoff and the number of k-point (see sections 3.2.5 and 3.2.6).

Energy Cutoff

The energy cutoff convergence was conducted using the LDA and PAW pseudopotential. A $1\times1\times1$ supercell of graphite with lattice parameters, $a = 2.46$ Å and $c = 6.70$ Å [9, and

54] was built. The energy cutoff was increased in step of 50 eV. The k-mesh-generated by Monkhorst-pack scheme [76] was set to the default by setting a 0.5 Å space between k-points, this corresponds to a $6\times6\times2$ k-mesh. The self consistent field (SCF) convergence of Kohn-Sham equation was set to 10^{-6} eV. The precision of the calculations was set to high; (precision is a term used in VASP that influences the accuracy of the wave functions, the resolution of the Fourier meshes for the representation of the density and the potential, total energies, forces, and stress of a given structure). Figure 4-1 shows the total energy per unit cell versus the energy cutoff E_{cuoff} in (eV). As seen the total energy of the unit cell starts to converge at energy cutoff equal to 800 eV.

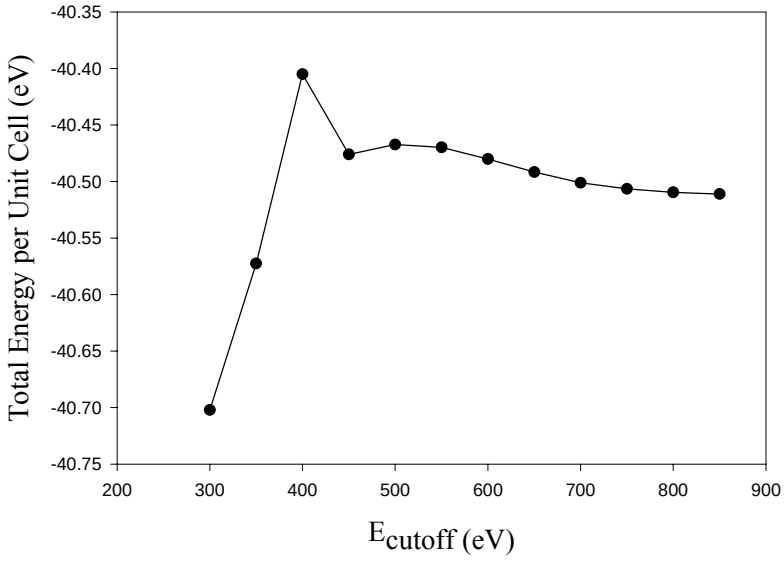

Figure 4-1 Total energy of the unit cell as a function of the energy cutoff, using a $6\times6\times2$ k-mesh and high precision.

K-mesh

After choosing the energy cutoff, the convergence of the total energy with respect to the k-mesh was studied, using the same parameters used in studying the energy cutoff. Table 4-1 shows the k-point grids, the number of irreducible k-points, the total number of

plane-waves used in the expansion, and the computational time in seconds.

Table 4-1 k-points grid, number of corresponding irreducible point, and plane-waves

K-point grid	Number of Irreducible points	Number of Plane- waves
2×2×2	2	3607
4×4×4	12	21665
6×6×6	36	64980
8×8×8	80	144371
10×10×10	150	270665

That is, on average 1800 plane waves are used to expand each node. The convergence of the total energy was reached with a grid of 8x8x8 corresponds to 80 irreducible points as seen in figure 4-2.

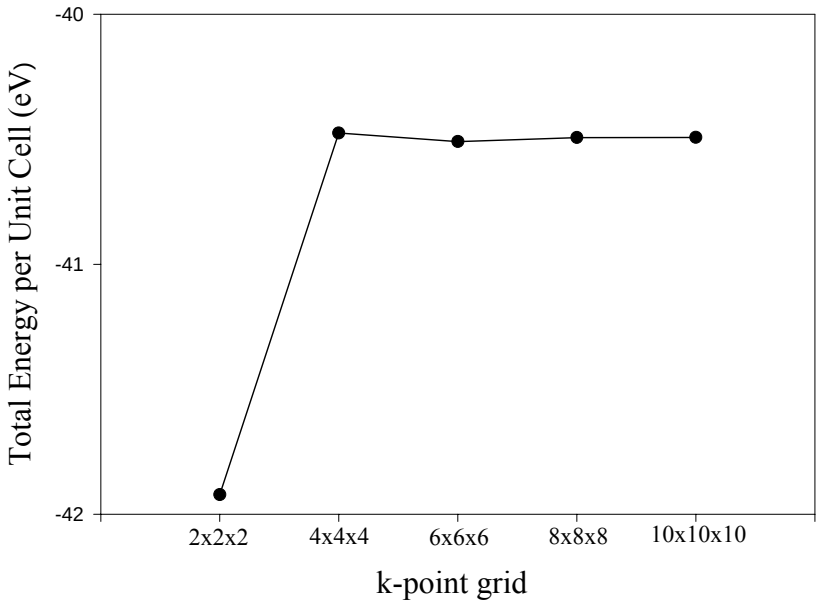

Figure 4-2 The total energy of the unit cell as a function of the k-point grids, using high precision with 800 eV energy cutoff.

Utilizing the energy cutoff, and k-mesh obtained by total energy convergence tests, and keeping other parameters (precision, and SCF) the same, the graphite structure was minimized by choosing a c/a ratio, and performing energy versus volume minimization. That is, the lattice constants were varied simultaneously while keeping a constant ratio between them. Based on the a = 2.46 Å and c = 6.674 Å ($V_{\exp}$ = 34.977 Å^3) [85,and 86] corresponds to 0 K, the ratio of the lattice constants c/a was fixed, and the c-value was increased in step of 0.02 Å. The total energy of the unit cell was calculated using $E_{cutoff} = 800\,\text{eV}$ and $8\times8\times8$ k-mesh. Figure 4-3 shows the total energy per unit cell versus the volume of the unit cell. The minimum energy corresponds to V = 34.420 Å^3 (%98 of the experimental volume), and the corresponding lattice constants are a = 2.447 Å and c = 6.639 Å. That is both values are decreased by ~ %0.5. As seen in the figure below, the energy versus volume curve is very smooth and not jagged, which is a good sign, due to the use of large energy cutoff and dense k-mesh. Therefore, these lattice constants will be used in the rest of the calculations. As mentioned, an issue of DFT is to predict lattice parameter c accurately when Van der Waals interaction is involved. By contrast, DFT can predict the lattice parameter a very well, indicating that, the strong covalent bond between graphite atoms in the graphitic plane is fairly well described by DFT. Several *ab initio* studies on graphitic structure tried to predict the lattice constants at 0 K are summarized in table 4-2.

4.1.2 Dispersion Relations

As mentioned in section 3.1.1, graphite dispersion relations have been studied either

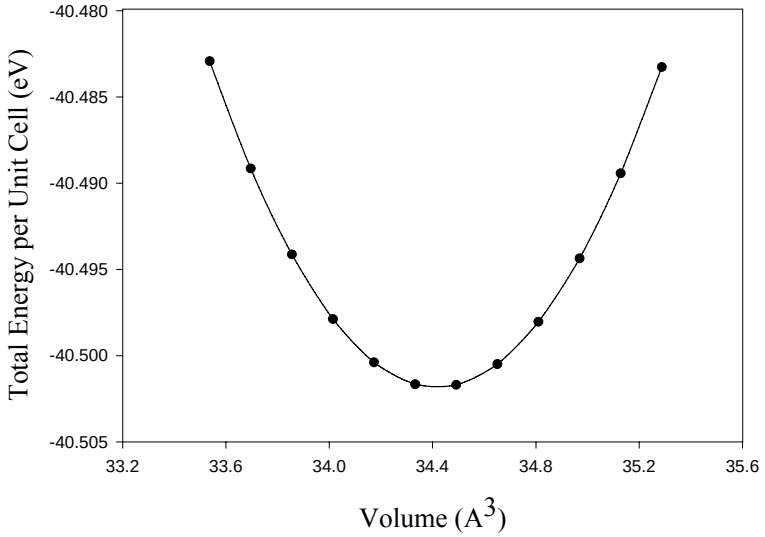

Figure 4-3 The total energy of the unit cell as a function of its volume, using a high precision with energy cutoff 800 eV , $8\times8\times8$ k-mesh, and c/a = 2.713. The lattice constants correspond to the minimum energy are a = 2.447 Å, and c = 6.639 Å.

Table 4-2 Comparison of DFT-Calculations in various approximations for the lattice parameters of graphite with experimental values

Reference	Method	a	c
Ref. 82	LDA	2.47	6.73
Ref. 60	LDA	2.443	6.679
Ref. 63	LDA	2.449	6.6
	GGA	2.457	7.8
Ref. 86	LDA	2.441	6.64
	GGA	2.461	~9.0
Ref. 87	LDA	2.459	6.828
Ref. 88	LDA	2.44	6.62
Ref. 85	Exp (0 K)	2.46	6.674
Ref. 89	Exp (0 K)	2.462	6.656
Ref. 90	Exp (300 K)	2.4612	6.7078
This work	LDA	2.447	6.639

either theoretically or experimentally. Using neutron or He-atom scattering techniques, low vibrational energies (below 50 meV) can be measured. While using the optical (infrared and Raman) techniques higher energy phonon modes can be detected but it's restricted to those at the Brillouin zone center (Γ-point). The lack of large enough graphite single crystal prevents the measurement of the full dispersion relations of graphite.

The dispersion relations are calculated or measured along the highest symmetry points of the first Brilluoin zone of the crystal of interest. Graphite has a hexagonal Brilluoin zone shown in figure 4-4 [91]. The highest symmetry directions in the reduced Brillouin zone for studying the dispersion relations are: $\overline{A\Gamma}$, $\overline{\Gamma M}$, $\overline{MK}$, and $\overline{K\Gamma}$. The coordinates (l_1, l_2, l_3) of the k-point in reciprocal space (shown in table 4-3) is

$$\vec{k} = l_1\vec{b}_1 + l_2\vec{b}_2 + l_3\vec{b}_3 . \qquad (4.1)$$

In order to calculate the graphite phonon dispersion relations and the phonon frequency distribution, we have investigated the supercell size, k-mesh, and energy cutoff. The calculations were performed using the density functional theory (DFT) in the local density approximation (LDA). The electron-ion interaction was described by the projector augmented-wave (PAW) pseudopotential, the 2s and $2p$ orbitals were treated as valence orbitals. The Hellmann-Feynman forces were computed from 6 independent displacements along x, y and z, corresponding to displacement amplitude of 0.03 Å.

The first model was a $1\times1\times1$ supercell (4 atoms). The integration over the first Brillouin zone was confined to a $6\times6\times2$ k-mesh (12 irreducible k-points) generated by the

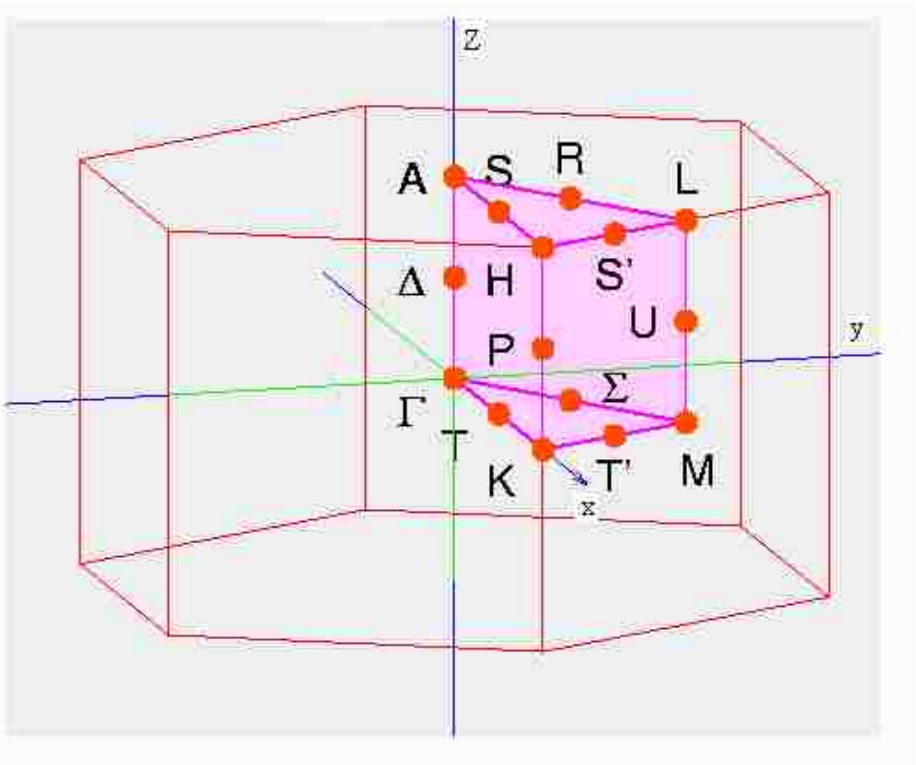

Figure 4-4 The first Brilluoin zone of graphite with high symmetry k-points marked. The irreducible part of the Brilluoin zone is highlighted [91].

Table 4-3 The standard notations for highest symmetry points in the hexagonal Brilluoin zone, and their corresponding coordinates

Notation	Coordinates (l_1, l_2, l_3)
Γ	(0, 0, 0)
M	(½, 0, 0), (0, ½, 0), (½, -½, 0)
K	(1/3, 1/3, 0), (2/3, -1/3, 0)
A	(0, 0, ½)
L	(½,0, ½), (0, ½, ½), (½, -½, ½)
H	(1/3, 1/3, ½), (2/3, -1/3, ½)

Monkhorst-Pack scheme [76], corresponding to k-spacing of $0.494 \times 0.494 \times 0.470$ Å^{-1}. A plane-wave basis set with default energy cutoff (400 eV) and medium precision were applied. Figure 4-5 shows the corresponding dispersion relations along the highest symmetry points compared to experimental data. The dark green circles represent neutron scattering data [39], the light green circles represent inelastic x-ray scattering data [49], the black, red and blue circles represent the HREELS data [47, 46, and 48], the yellow circles represent inelastic He-atom scattering [44], and the pink circles represent infrared and Raman data [43].

As seen, drastic dispersion relations were obtained, that is the phonon frequencies are wrong and do not match the experimental data. Also, negative (imaginary) frequencies are seen due to the very small size of the supercell. That is, due to the strong covalent bond in the graphitic planes and the too small size of the supercell, the Hellmann-Feynman forces from outside the supercell are neglected; as a consequence the missing force constants caused the imaginary frequencies.

The next step was increasing the supercell size to a $2 \times 2 \times 1$ supercell (16 atoms). The integration over the Brillouin zone was confined to a $4 \times 4 \times 3$ k-mesh (12 irreducible k-points) generated by the Monkhorst-Pack scheme, corresponding to a k-spacing of $0.371 \times 0.371 \times 0.371$ Å^{-1}. A plane-wave basis set with energy cutoff (400 eV) and medium precision were applied. Figure 4-6 shows the corresponding dispersion relations along the highest symmetry points compared to experimental data.

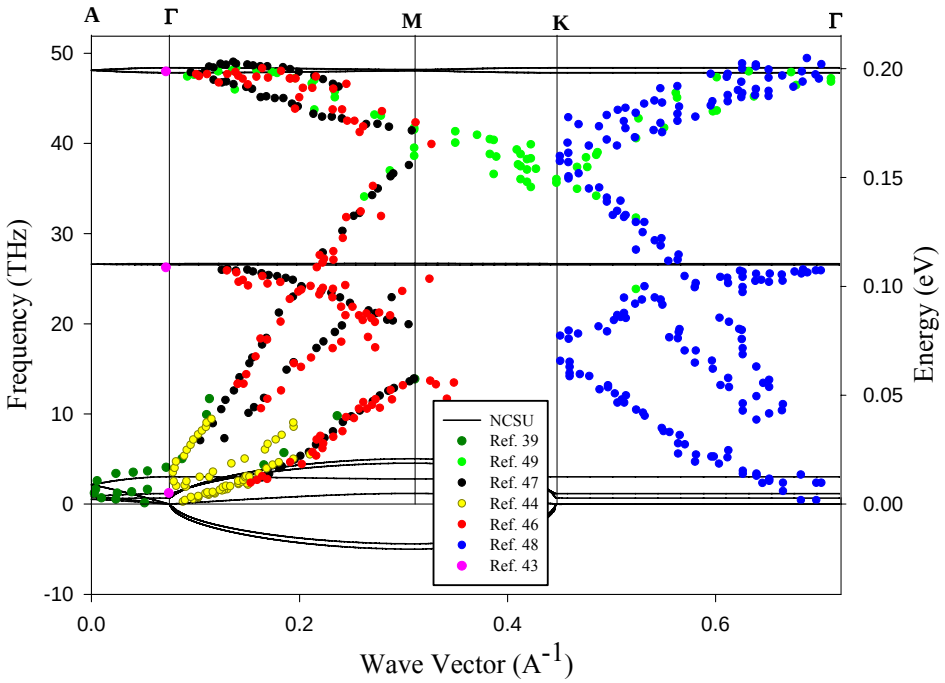

Figure 4-5 The calculated dispersion relations for graphite along the highest symmetry directions of the first Brilluoin zone compared to experimental data. Based on a $1\times1\times1$ supercell, a $6\times6\times2$ k-mesh and using a 400 eV energy cutoff with a medium precision.

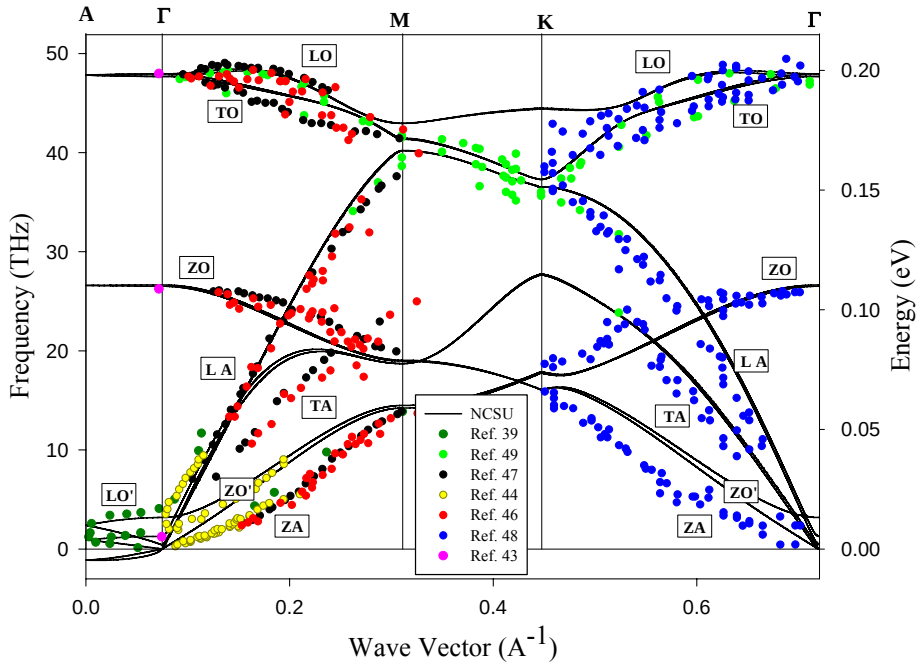

Figure 4-6 The calculated dispersion relations for graphite along the highest symmetry directions of the first Brilluoin zone compared to experimental data. Based on a $2\times2\times1$ supercell, a $4\times4\times3$ k-mesh and using a 400 eV energy cutoff with a medium precision.

As seen from figure 4-6, significant improvement was achieved by increasing the supercell size. This is an indication that interactions in graphite are long range and larger supercells should be investigated. Since the graphite layers are bonded together by weak Van der Waals forces, only one unit cell (two layers) was used in the z-directions. As a result of strong intraplanar bonding and the light carbon atomic weight, some vibrational energies reach (0.20 eV). While the weak interplanar bonding produces very low energy optical modes of order (0.01 eV). Since graphite unit cell has four atoms, it has twelve vibrational modes. The lowest three branches, starting from Γ are called the acoustical modes, while the highest branches are called the optical modes. The modes in the figure are labeled as: A stands for acoustic mode, and (O) for optical mode. The primed optical mode (O') indicates an optical mode where the two atoms in each layer of the unit cell oscillate together and in phase, but in opposition to the atoms of the other layer. Non primed optical mode is a mode where atoms inside the same layer are optical with respect to each other. (L) stands for longitudinal polarization, (T) stands for in-plane transversal polarization, and (Z) for out of plane transversal polarization. As it can be seen, unlike the $1\times1\times1$ dispersion relations, the branches of the $2\times2\times1$ are distinguishable, and cover the wide range of graphite vibrational energies. Good agreement with Raman and infrared data is observed at the zone center (Γ point). However, the agreement with the other experimental data is still poor especially for the modes (TO, ZO, TA, and ZA), in addition imaginary frequencies still exist.

The next step was increasing the supercell size to a $4\times4\times1$ (64 atoms). The integration

over the Brillouin zone was confined to a $2\times2\times3$ k-mesh (4 irreducible k-points) generated by the Monkhorst-Pack scheme, corresponding to k-spacing of $0.371\times0.371\times0.314$ $Å^{-1}$. A plane-wave basis set with energy cutoff (400 eV) and medium precision were applied. Figure 4-7 shows the corresponding dispersion relations along the highest symmetry points compared to experimental data. As seen from the figure, the agreement with experimental data is improved significantly, especially for the modes (TO, ZO, TA, and ZA). Also the imaginary frequencies were reduced even though they still appear.

Finally, a $6\times6\times1$ supercell (144 atoms) was used. The integration over the Brillouin zone was confined to a $4\times4\times3$ k-mesh (6 irreducible k-points) corresponding to a spacing

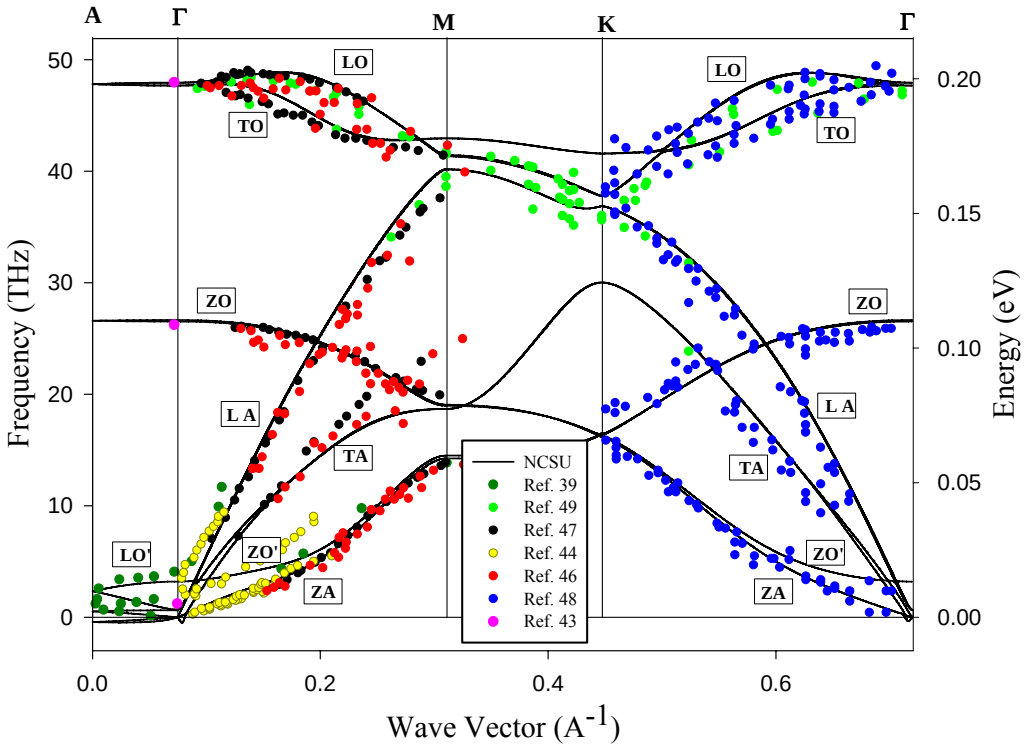

Figure 4-7 The calculated dispersion relations for graphite along the highest symmetry directions of the first Brilluoin zone compared to experimental data. Based on a 4x4x1 supercell, a 2x2x3 k-mesh, and using a 400 eV energy cutoff with a medium precision.

of $0.165 \times 0.165 \times 0.165$ Å^{-1}. Since high precision was applied, the default energy cutoff (400 eV) was raised to (500 eV). Figure 4-8 shows the corresponding dispersion relations along the highest symmetry points compared to experimental data. As seen from figure 4-8, the LO/TO modes are improved in matching the experimental data compared with the previous case. Also, the imaginary frequencies are removed.

This case will be used to generate the phonon frequency distribution and proceed in studying the thermal neutron scattering. Finally, the Niklow *et al*, [39] calculated dispersion relations were compared with experimental data, as shown in figure 4-9. As it can be seen, there is a nice agreement with the dark blue circles; this is not surprising, since

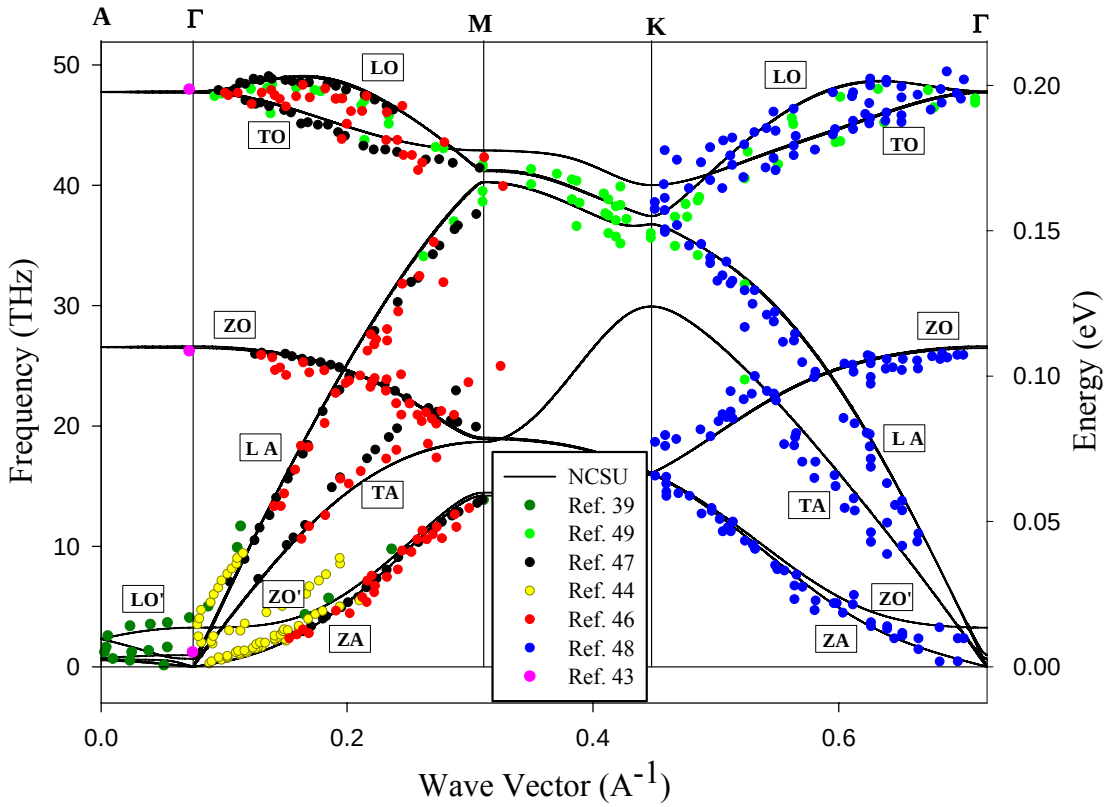

Figure 4-8 The calculated dispersion relations for graphite along the highest symmetry directions of the first Brilluoin zone compared to experimental data. Based on a $6 \times 6 \times 1$ supercell, a $3 \times 3 \times 4$ k-mesh and using high precision with a 500 eV energy cutoff.

they fitted there central force model to these data they had measured at Oak Ridge National Laboratory. Also, there is in general good agreement at low frequencies with experimental data. However, as the vibrational energies get higher the deviation from experimental data becomes larger at the ZO and LA modes.

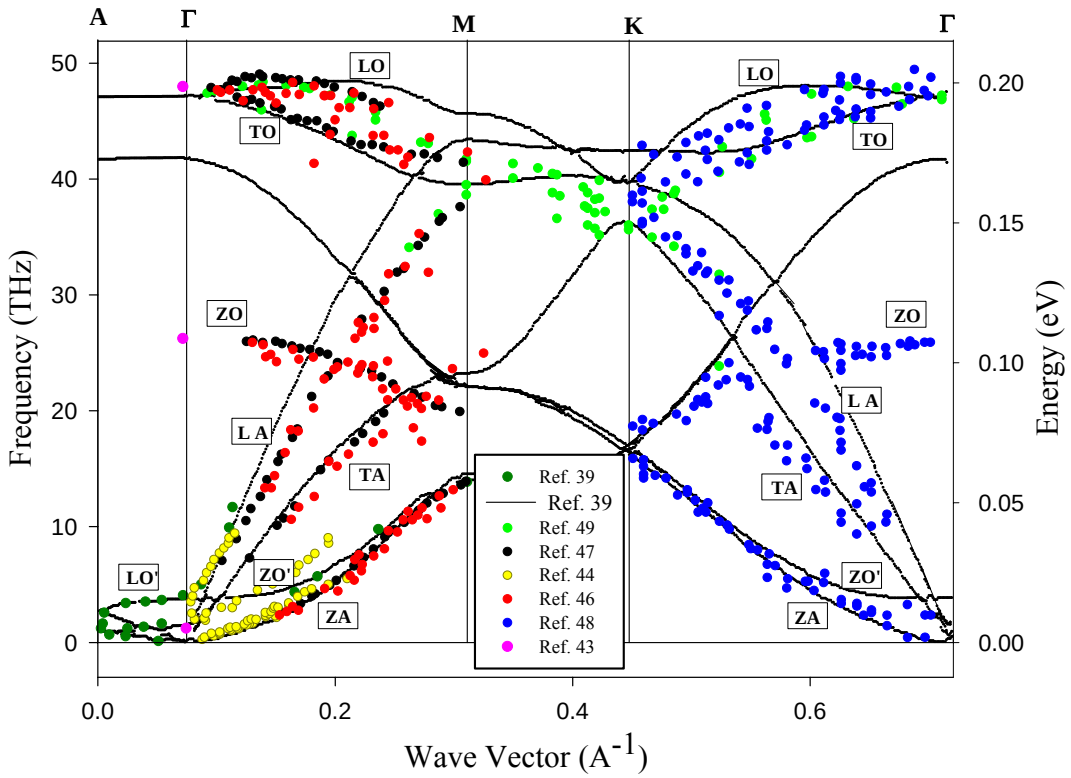

Figure 4-9 The calculated and measured dispersion relations by Nickow *et al* [39] using the central force model compared to experimental data.

4.1.3 Phonon Frequency Distribution

The phonon frequency distribution was constructed by using 200 bins according to equation (3.17), 50000 k wave vectors are randomly selected (by Monte-Carlo sampling) over the first Brilluoin zone. Figure 4-10 shows the (a) parallel, (b) perpendicular, and (c) total

phonon frequency distributions. The parallel partial phonon frequency distribution contributes 1/3 to the total distribution, while the perpendicular partial phonon frequency distribution contributes 2/3 to the total distribution. As it can be seen, the parallel phonon frequency distribution has shorter range (~0.112 eV) compared to the perpendicular distribution which has relatively high energy vibrational modes (~0.20 eV). As mentioned earlier this is due to weak interplanar bonding and strong intraplanar bonding. As seen from figure 4-10 (c), the phonon frequency distribution contains sharp peaks known as Van Hove singularities [92]. These singularities arise from points of zero slope in the dispersion relations $\frac{\partial\omega(\vec{q},j)}{\partial\vec{q}}=0$ and they yield discontinuities in the first derivative of the phonon frequency distribution with respect to the frequency; $\frac{\partial\rho(\omega)}{\partial\omega}$. The wave vectors at which Van Hove singularities occur are often referred to as critical points of the Brillouin zone. Neutron scattering from powdered graphite was used to obtain the phonon frequency distribution [66]. The inelastic neutron scattering spectrum has similar features to that of graphite as shown in figure 4-11. The calculated phonon frequency distribution was used to calculate the heat capacity of graphite between 0 K and 2000 K. The agreement with experimental data [36] is good, as shown in figure 4-12.

Figure 4-13 shows the Young-Koppel spectrum compared to the *ab initio* (NCSU) spectrum. Note that YK spectrum is normalized in units of (eV). As seen the Young-Koppel spectrum's Van Hove singularities (ZA, ZO+TA, ZO, and TO) have good agreement with the *ab initio* singularities but they are wider and less pronounced. However, the LO singularity is

completely missing, and there is an extra one at 0.137 eV. The behavior of YK spectrum up to the first singular point ZO' is parabolic and has lower phonon contribution than the NCSU spectrum. This will affect the cross section values as it will be discussed later.

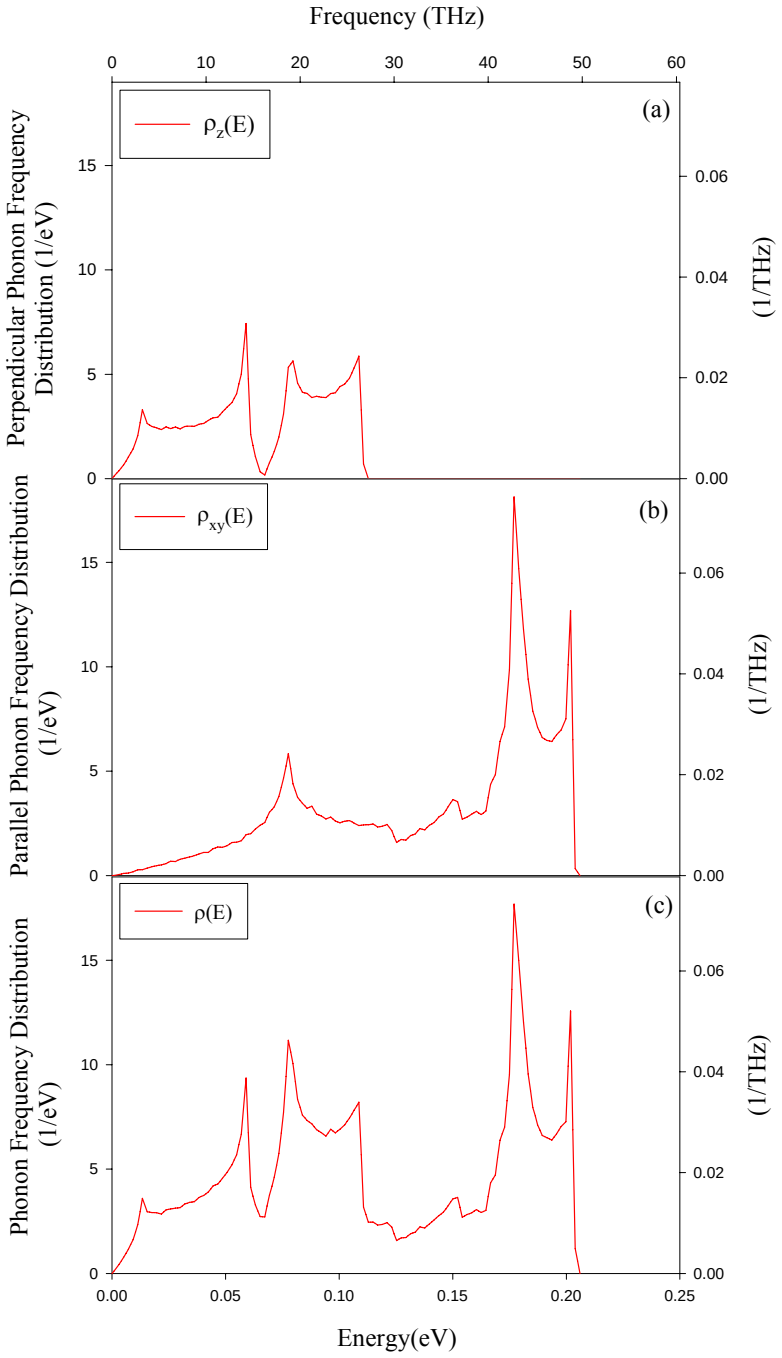

Figure 4-10 The calculated phonon frequency distributions of graphite (a) parallel, (b) perpendicular to the basal plane, and (c) total, based on a $6\times6\times1$ supercell, a $3\times3\times4$ k-mesh, and high precision with a 500 eV energy cutoff, and using 50000 q-wave vectors.

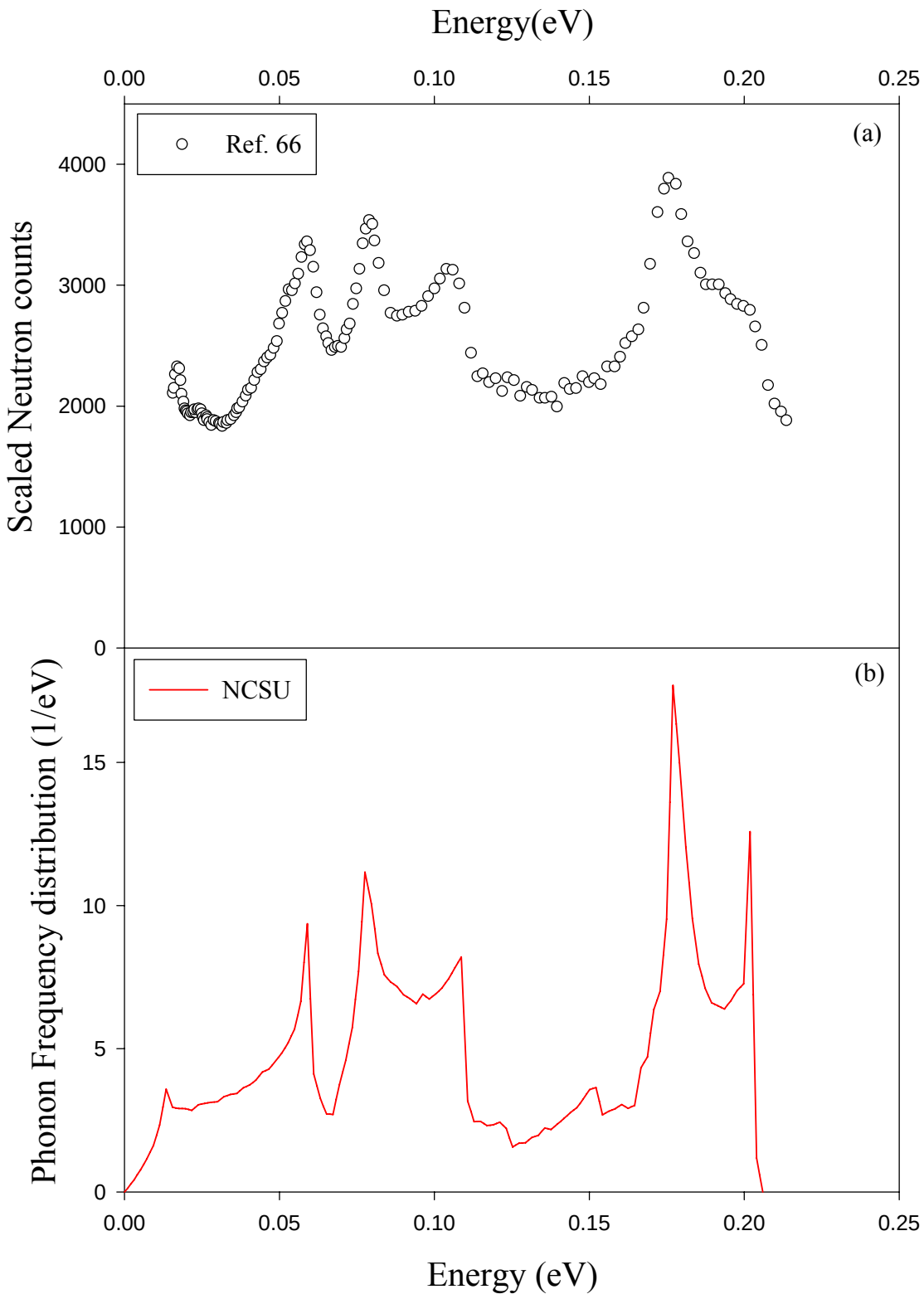

Figure 4-11 The graphite phonon frequency distribution (a) measured by inelastic neutron scattering [66]. (b) calculated based on the $6\times6\times1$ supercell with a $3\times3\times4$ k-mesh, and high precision with a 500 eV energy cutoff and using 50000 q-wave vectors.

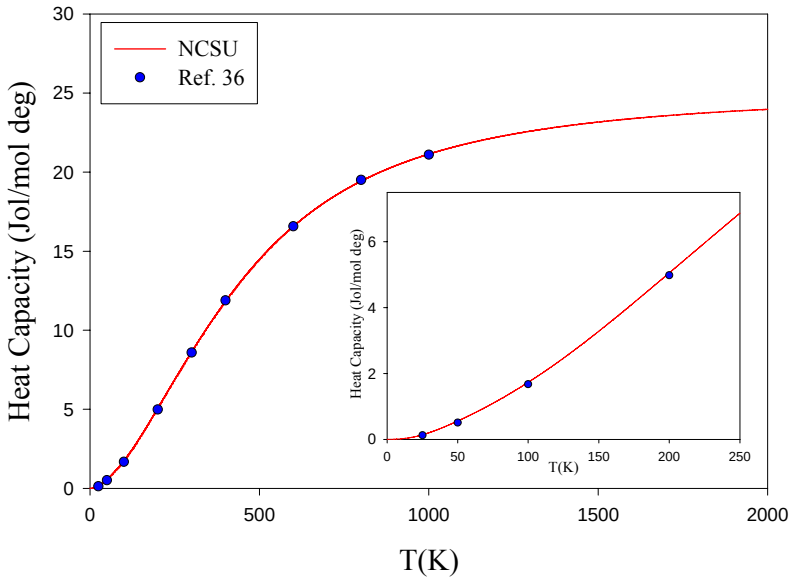

Figure 4-12 The calculated heat capacity using the NCSU phonon frequency distribution as compared to experimental data [36].

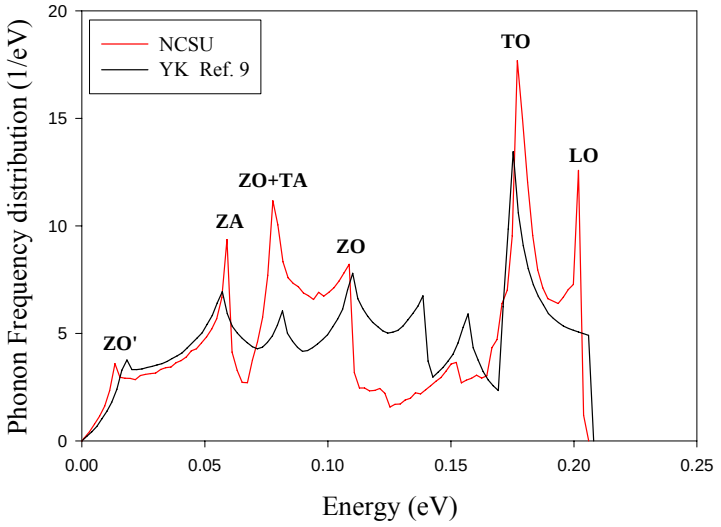

Figure 4-13 The Young-Koppel phonon frequency distribution [9] compared to the NCSU distribution.

The next figure 4-14 compares the NWS spectrum with the NCSU spectrum. Note that, the unnormalized NWS spectrum that appeared in figure 3-2 is renormalized and

represented in units of (eV) to be consistent with the NCSU spectrum. As seen the NWS spectrum Van Hove singularities (ZO', ZA, TO, and LO) have good agreement with the NCSU Van Hove singularities. However, the TO and LO singularities are much more pronounced. The ZO+TA and ZO singularity are completely missing, and other extra singularities appear at 0.09062, 0.09593, and 0.16602 eV. As mentioned, the force constants of this model were obtained by fitting to neutron scattering data. This data represents low phonon frequency values (< 0.06 eV). Therefore, there is a good match with the NCSU spectrum at low energy. However, the NCSU spectrum has higher phonons contribution compared to NWS spectrum up to the first singular point ZO'.

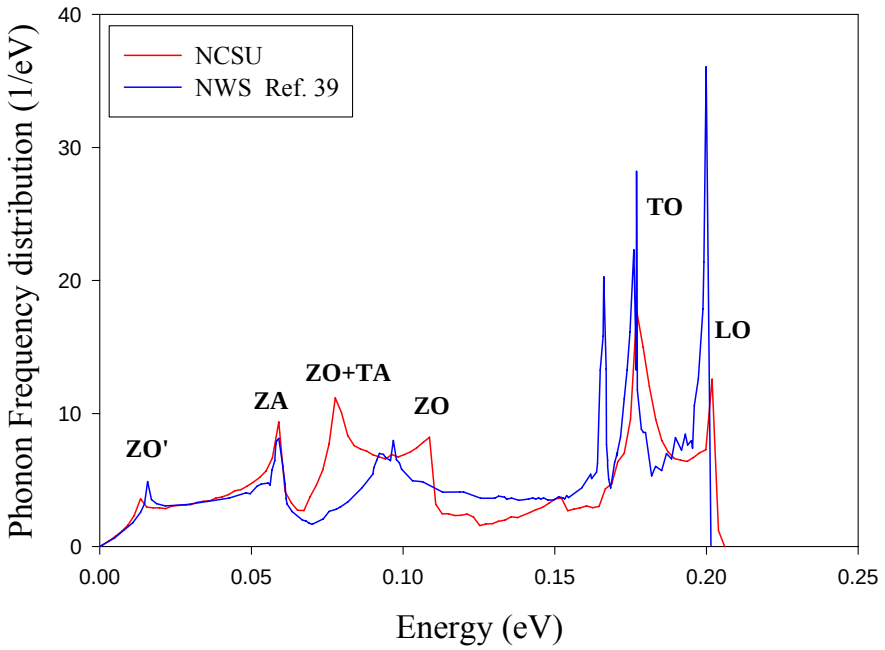

Figure 4-14 The NWS Phonon frequency distribution [39] compared to the NCSU distribution.

Figure 4-15 shows the dispersion relations of graphite combined with phonon frequency distribution, the singular points are labeled and related to the high symmetry points of the dispersion relations.

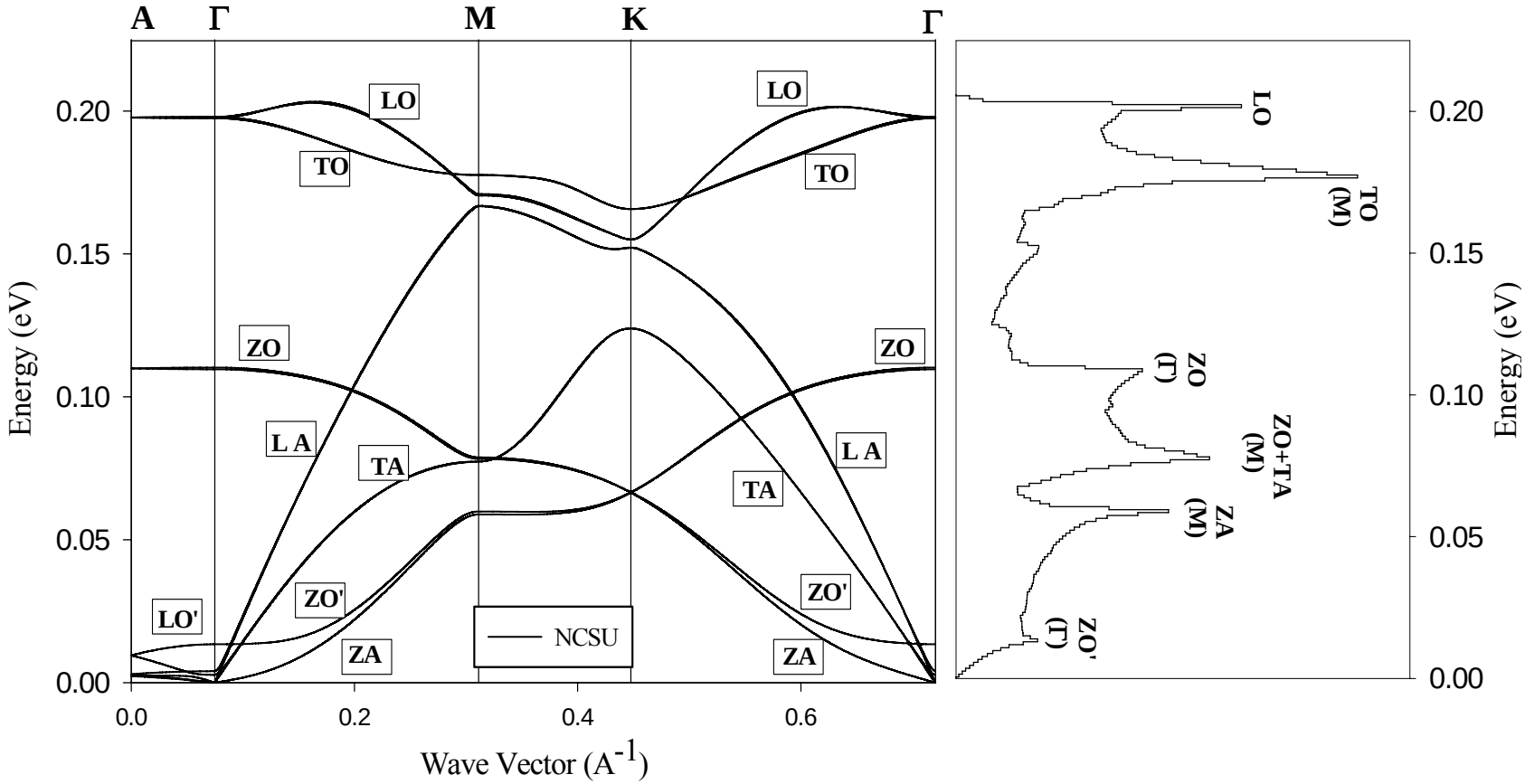

Figure 4-15 The NCSU graphite dispersion relations and phonon frequency distribution. The Van Hove singularities can be related to the flattened regions of the dispersion relations.

4.2 Thermal Neutron Scattering

4.1.1 Graphite Phonon Frequency Distribution Parabolic Behavior ω^2

As mentioned earlier (section 2.4), LEAPR calculates the double differential scattering cross section by using equations (2.61 and 2.62). For solid-type frequency spectra, LEAPR utilizes the phonon expansion shown in Appendix A (equation A.13), and writes the scattering law as

$$\mathsf{S}(\alpha,\beta) = e^{-\alpha\lambda}\sum_{n=0}\frac{\alpha^n}{n!}\frac{1}{2\pi}\int_{-\infty}^{\infty}e^{i\beta\hat{t}}\left[\int_{-\infty}^{\infty}\frac{\rho(\beta')}{2\beta'}\frac{e^{-\beta'/2}}{\sinh(\beta'/2)}e^{-i\beta\hat{t}}\,d\beta'\right]^n d\hat{t}\,. \tag{4.2}$$

For simplicity, the above equation can be written as

$$\mathsf{S}(\alpha,\beta) = e^{-\alpha\lambda}\sum_{n=0}\frac{1}{n!}[\alpha\lambda]^n\,\mathrm{T}_n(\beta), \tag{4.3}$$

Where

$$\lambda^n\mathrm{T}_n(\beta) = \frac{1}{2\pi}\int_{-\infty}^{\infty}e^{i\beta\hat{t}}\left[\int_{-\infty}^{\infty}\frac{\rho(\beta')}{2\beta'}\frac{e^{-\beta'/2}}{\sinh(\beta'/2)}e^{-i\beta\hat{t}}\,d\beta'\right]^n d\hat{t}\,, \tag{4.4}$$

where λ is the Debye-Waller coefficient defined by eq (A.11). The $\mathrm{T}_n(\beta)$ functions obey the recursion relation

$$\mathrm{T}_n(\beta) = \int_{-\infty}^{\infty}\mathrm{T}_1(\beta')\mathrm{T}_{n-1}(\beta-\beta')d\beta'\,, \tag{4.5}$$

where

$$\mathrm{T}_0(\beta) = \int_{-\infty}^{\infty}e^{i\beta\hat{t}}\,d\hat{t} = \delta(\beta), \tag{4.6}$$

$$\mathrm{T}_1(\beta) = \frac{e^{-\beta/2}}{\lambda} P(\beta), \tag{4.7}$$

where

$$P(\beta) = \frac{\rho(\beta)}{2\beta \sinh(\beta/2)}. \tag{4.8}$$

In order to utilize equation (4.5), $\mathrm{T}_1(\beta)$ must be a well behaved function. Note that as β goes to zero, $2\beta \sinh(\beta/2)$ goes to β^2, therefore $\rho(\beta)$ must vary as β^2 as β goes to zero. That is

$$\lim_{\beta \to 0} \rho(\beta)\beta^{-2} = c \tag{4.9}$$

where c is finite positive constant. The behavior of $\rho(\beta)$as β goes to zero describes the behavior of neutron scattering for small energy transfers. As mentioned earlier (section 3.1.1), graphite as a quasi-two-dimensional material obeys the Debye behavior for a small range of phonon frequency distributions, such that the phonon expansion does exist (harmonic lattice vibrations of crystal) but converges slowly, and is associated with the emission of many low-frequency phonons. This multiple phonon emission is manifested in the scattering as a large narrow peak of inelastically scattered neutron in the neighborhood of zero-energy transfer [93].

LEAPR requires a uniform mesh in frequency space of the phonon frequency distribution, and assumes that below the first point (the point after (0,0)) there is a parabolic behavior of the phonon frequency distribution. The phonon frequency distribution input to LEAPR for solid –type oscillators starts with the point $(\beta_1, \rho(\beta_1)) = (0,0)$. For this point

LEAPR assigns a value for $P(\beta)$ by scaling it to the next point $(\beta_2, \rho(\beta_2))$ using the relation $P(\beta_1) = \frac{\rho(\beta_2)}{\beta_2^2}$. In fact the parabolic range of the phonon frequency distribution affects the peak sharpness of the thermal neutron emission spectra as a function of the secondary energy, the behavior of the inelastic scattering cross section, and also the decay of the coherent elastic scattering cross section as will be shown later (Debye –Waller factor value). Therefore, it is critical to define precisely the energy limit up to which the phonon frequency distribution has parabolic behavior. Based on the physics of graphite three cases will be considered for treating the NCSU *ab initio* phonon frequency distribution.

Case 1: **Based on the graphite heat capacity**

This choice assumes that the real phonon spectrum and the Debye spectrum match each other up to a certain energy. The determination of the energy limit of matching is based on the Debye behavior of the heat capacity. Assuming that the true spectrum and the Debye spectrum coincide up to frequencies ω_P such that $\hbar\omega_P \sim \gamma k_B \Theta_D$, where ω_P is the frequency limit up to which the spectrum has parabolic behavior, and γ is a constant (<1). Note that the heat capacity at low temperatures is mainly a function of $\rho(\omega)$. In the limit of low temperatures the integrand of the heat capacity, equation (3.19), written as $\frac{x^4 e^x}{(e^x - 1)^2}$ increases as x^2 for small values of x, and has a maximum value at x=3.83 as shown in figure (4-16), where $x = \frac{\hbar\omega}{k_B T}$. Therefore, the departure of Debye spectrum from the true spectrum will be reflected in the temperature dependence of the heat capacity for

temperatures $k_B T > \hbar\omega_P / 3.83$. Thus, if the true spectrum coincides with the Debye spectrum up to $\hbar\omega_P \sim \gamma k_B \Theta_D$, then the Debye expression for the heat capacity will accurately describe the temperature dependence of the heat capacity in the temperature range $T < \gamma \Theta_D / 3.83$. As mentioned earlier the graphite heat capacity has a Debye behavior up to 2 K. As a result $\gamma \Theta_D \sim 2 * 3.83 \sim 7.66$ K ~ 8 K. That is based on heat capacity calculation; the graphite phonon frequency distribution has a parabolic behavior up to ($\hbar\omega = 8$ K = 0.69 meV). This value is in a good agreement with the value obtained by Egelstaff ($\hbar\omega = 9$ K = 0.776 meV) in constructing his simplified phonon frequency distribution [Appendix of Ref. 94]. The corresponding phonon frequency distribution is represented by 300 points and no parabolic fitting is included. In this case, LEAPR will treat this spectrum as it has parabolic behavior up to the second point.

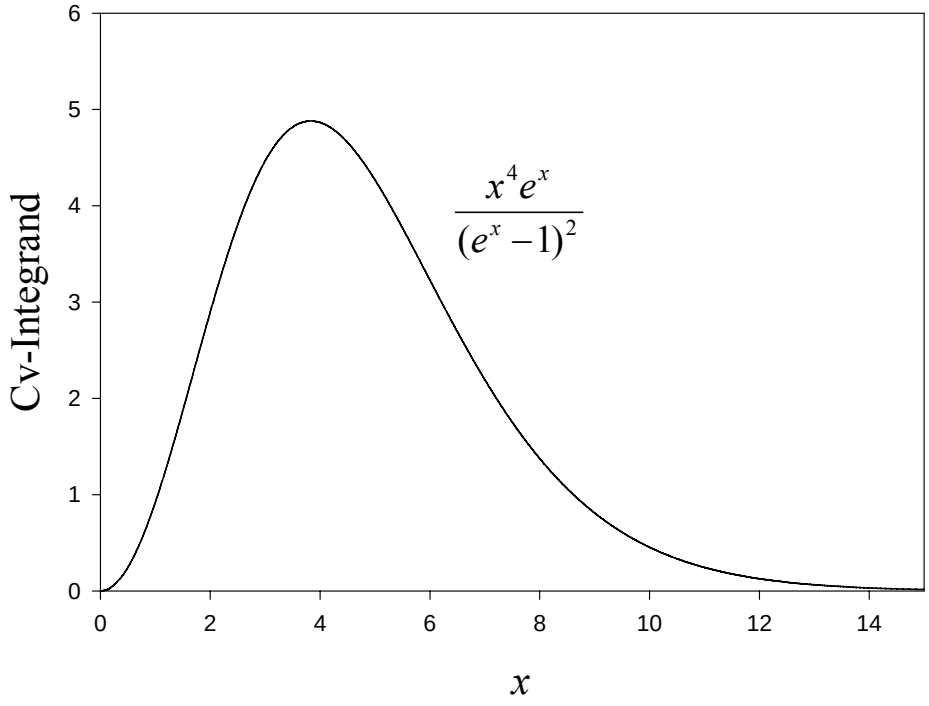

Figure 4-16 The heat capacity integrand in the limit of low temperature.

Case 2: **Based on the graphite mean square displacement**

Case 1 mentioned above determines a very small parabolic energy range. That is, it is considering graphite as a two dimensional material rather than quasi two dimensional material. In fact, the dynamics of a carbon layer is dependent upon where the layer under consideration is located with respect to other layers. That is, there is a cross over from two dimensional dynamics to quasi two-dimensional dynamics by moving from a surface layer to a bulk layer. Recently, the cross-over of the dynamics from nearly two-dimensional to quasi two-dimensional is studied by utilizing the temperature dependent mean square displacement of carbon atoms in graphite perpendicular to the plane [95]. The mean square displacement $\left\langle u_i^2 \right\rangle$ is a function of the partial phonon frequency distribution $\rho_i(\omega)$

$$\left\langle u_i^2 \right\rangle = \frac{\hbar r}{2M_\mu} \int_0^\infty \frac{1}{\omega} \rho_i(\omega) \coth\left(\frac{\hbar\omega}{2k_B T} \right) d\omega , \tag{4.10}$$

where i corresponds to x, y , or z direction, r is the number of degrees of freedom in the unit cell. As seen from equation (4.10) for small ω the phonon frequency distribution should behave parabolically, since

$$\lim_{\omega \to 0} \frac{1}{\omega} \coth(\omega) \to \omega^{-2} . \tag{4.11}$$

This represents a similar situation to the behavior of $P(\beta)$ at low β as represented in equation (4.8). So, utilizing the mean square displacement in determining the parabolic energy range is useful in constructing the true $P(\beta)$ and as a consequence in calculations of thermal neutron cross section. Tewari *et al*., [95] calculated the variation of the phonon frequency distribution as the number of layers is changed, using the unfolding technique for different numbers of graphite layers ranging from 3 to 13 and then to a very large number.

In their study, it was found that for an infinite number of layers, the partial phonon frequency distribution $\rho_z(\omega)$ has a parabolic energy range corresponds to 60 K (5.175 meV). As a consequence, a phonon frequency distribution was constructed by using 160 points (159 bins) with energy interval (15 K). That is, the fifth point (4th point after (0,0)) corresponds to energy equal to 5.175 meV (60 K). Since the value of this point is critical, 5×105 q-points were used in sampling the first Brillouin zone giving an uncertainty in $\rho(E = 5.175\, meV)$ about ~1.3%. The resulting total phonon frequency distribution $\rho(\omega)$ was fitted parabolically up to this point (5th point), in order to be used in LEAPR.

The parabolic energy cutoff limit could be further tuned such that better matching is produced between the one-phonon thermal neutron scattering cross section calculated in the incoherent approximation and the self part of the exact coherent one-phonon thermal neutron scattering cross section using isotropic Debye-Waller factor, as shown in figures 4-17 and 4-18. This can be achieved by increasing the parabolic energy limit of the phonon spectrum up to 5.606 meV (65 K). Also 5×10^5 q-points were used in sampling the first Brillouin zone to construct $\rho(\omega)$ giving uncertainty in $\rho(E = 5.606\, meV)$ about ~1.2%. 148 points (147 bins) were used in constructing this distribution. Figure 4-18, shows better agreement between the two cross section curves compared to figure 4-17, especially at high energies, where it is expected that the incoherent approximation and the exact calculation are matching each other.

Figure 4-19 shows $P(\beta)$ given by eq (4.8) at 300 K, to illustrate the effect of the parabolic range in the phonon frequency distribution for the three cases mentioned above.

As mentioned earlier LEAPR assumes parabolic fitting up to the 2nd point, where $P(\beta_1)$ was calculated based on the relation $P(\beta_1) = \frac{\rho(\beta_2)}{\beta_2^2}$, this explains why in case1 the first two

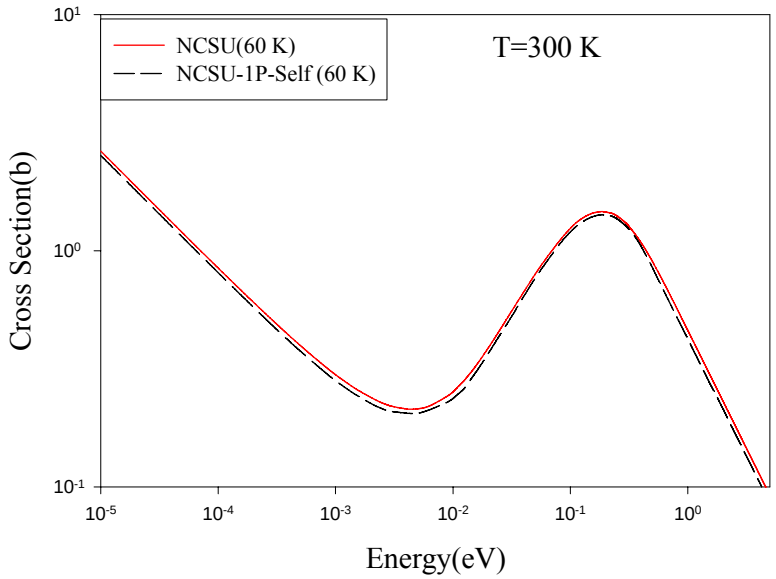

Figure 4-17 The one phonon scattering cross section in the incoherent approximation (red solid line) and the self coherent one-phonon scattering cross section (black dashed line) at 300 K. The calculations are based on the NCSU phonon spectrum with parabolic range equivalent to 60 K.

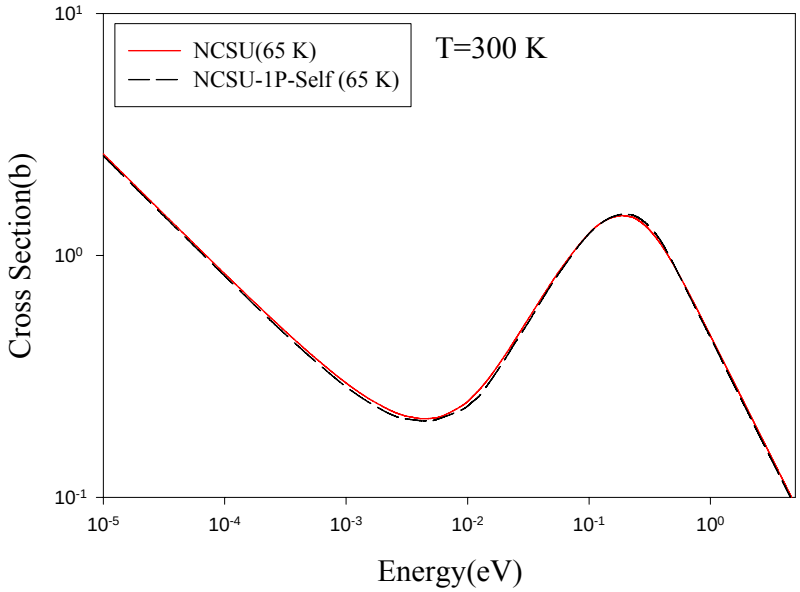

Figure 4-18 The one phonon scattering cross section in the incoherent approximation (red solid line) and the self coherent one-phonon scattering cross section (black dashed line) at 300 K. The calculations are based on the NCSU phonon spectrum with parabolic range equivalent to 65 K.

$P(\beta)$ points are almost equal[3]. While for case 2 the first 5 points do so, since the phonon spectrum was fitted parabolically up to the 5th point. As seen, case1 has the highest $P(\beta)$ at low betas; this is due to the short parabolic range of the Phonon frequency distribution, and the use of fine phonon spectrum intervals (0.69 meV). However, Case 2 has lower $P(\beta)$ compared to case1, this is due to the longer parabolic range, and the use of wider phonon spectrum bins (1.4015 meV). Moreover, forcing the phonon frequency distribution to have parabolic behavior for more than 2 points makes $P(\beta)$ values to be aligned straightly up to that point.

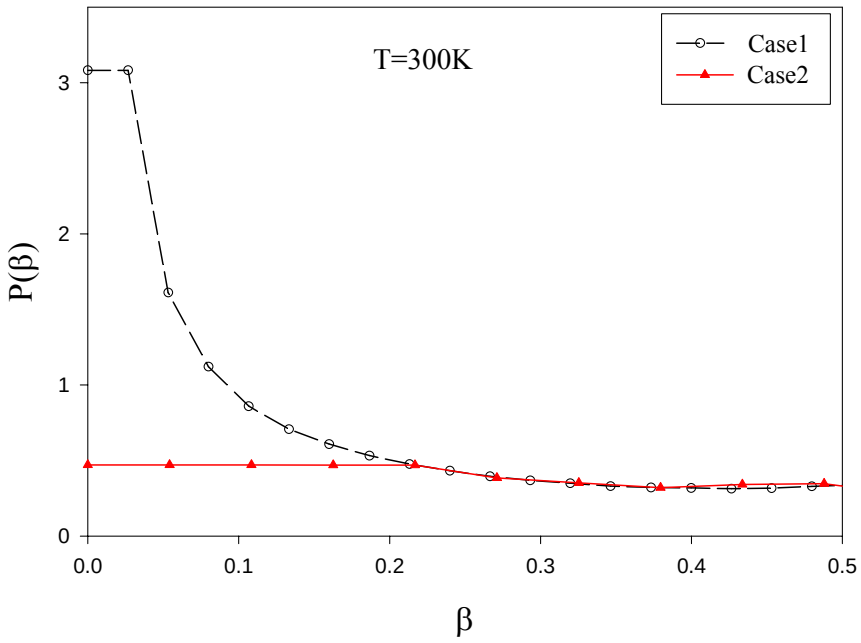

Figure 4-19 $P(\beta)$ at *T*=300 K for the two cases mentioned above.

From figure 4-19 one can read the following information, for case 1 the phonon frequency distribution has parabolic behavior up to the second point, while case 2 has parabolic behavior up to the 5th point. Also, case1 will have the sharpest peaks of thermal

[3] The difference between Sinhβ and β as β tends toward zero is small.

neutron emission spectra, while case 2 will have the widest. Moreover, the inelastic scattering cross section will be higher in case1 compared to case 2, as shown in figure 4-20. The physical behavior of thermal neutron scattering cross section shown in the figure below will be discussed later. However, the behavior of the two cases is consistent with figure 4-19.

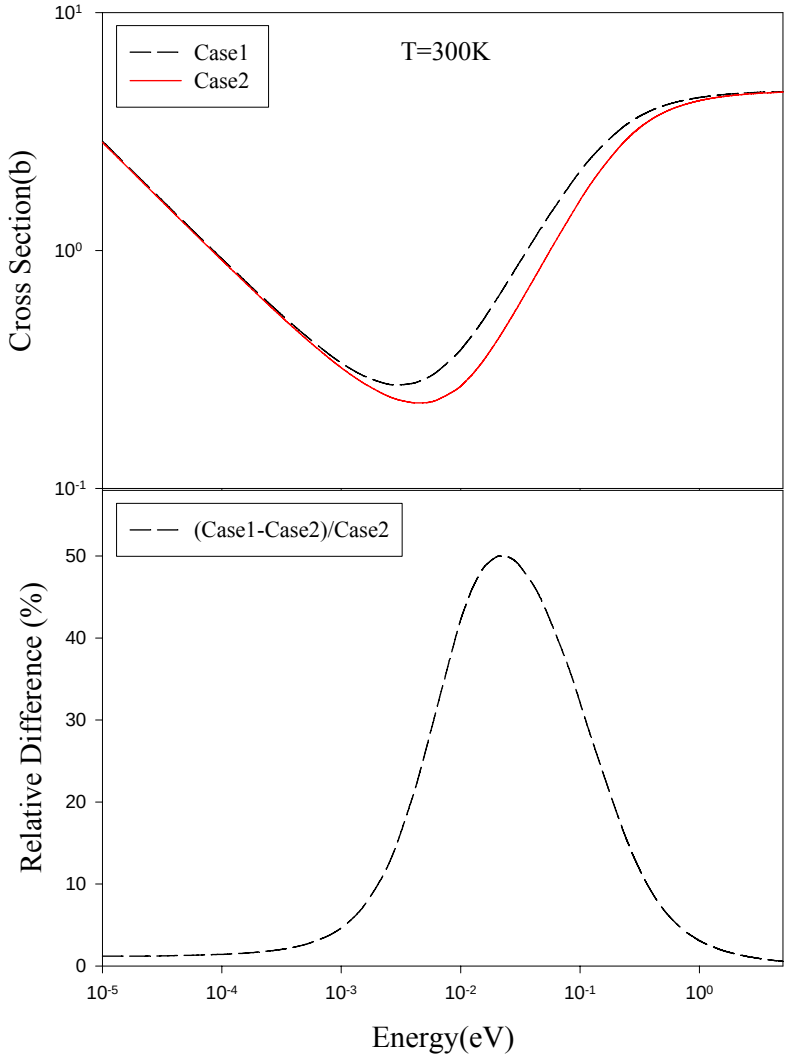

Figure 4-20 The inelastic scattering cross section in the incoherent approximation and the corresponding relative difference at T=300 K for the two cases discussed above.

Figure 4-21 show the secondary neutron spectrum at 300 K for the neutron incident energy 0.0106 eV for the tow cases discussed above. The area under each curve represents

the total inelastic scattering cross section for this particular energy. As seen from the figure, case 1 has a sharper peak of inelastically scattered neutron in the neighborhood of zero-energy transfer compared to case 2, this is due to the fact that, case 1 has a shorter parabolic range compared to case 2. That is, the shorter the parabolic range of the phonon spectrum will cause sharper and narrower peak of the inelastically scattered neutron in the neighborhood of zero-energy transfer.

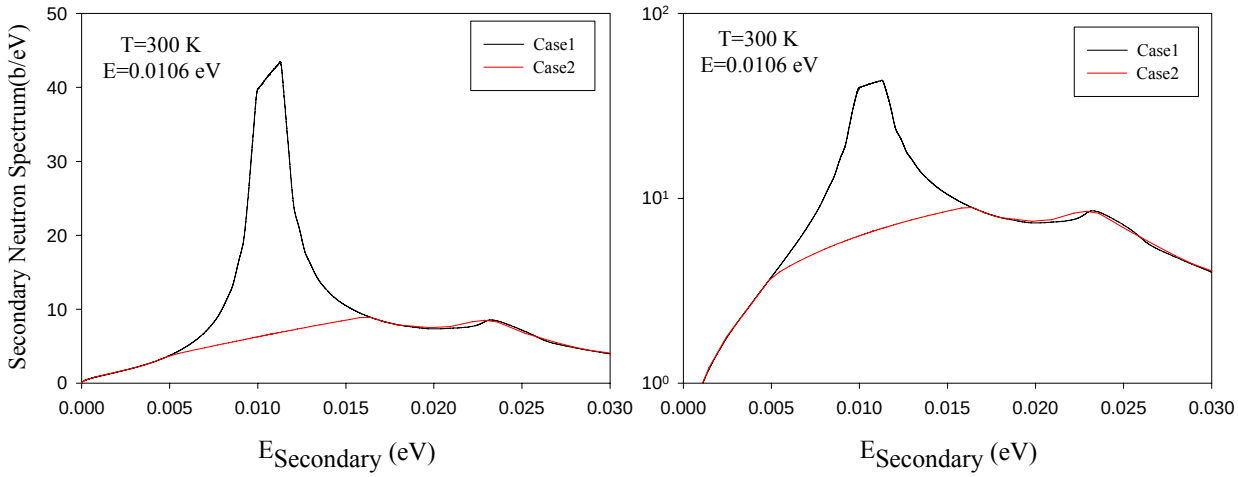

Figure 4- 21 The secondary neutron spectrum at 300 K for neutron incident energy 0.0106 eV, in linear-linear scale (left), and semi-log scale (right).

4.1.2 Cross Section Calculations and Comparison to Experimental Data

From now on, case 2 will be considered only for the rest of calculations, it will labeled by NCSU. The results based on case 2 (NCSU) will be compared to the corresponding results based on using the Young-Koppel (YK) [9] and NWS spectrums [39]. The Young-Koppel (YK) spectrum shown in figure 2-1 was processed in 1960s for generating the scattering cross section libraries by using GASKET. Later on, the same processed spectrum was used in LEAPR. The spectrum has a bin width of 5.485 meV (~64 K) and represented by 40 points,

as shown in figure 4-22. As seen it smoothes out the original one, and has a parabolic behavior up to 16.455 meV (up to the 4th point) and obeys a Deby temperature of 743.4 K. However, two things to be mentioned regarding the YK spectra, first, its bin width (64 K) is almost equal to the parabolic range of the NCSU spectrum (65 K), second, it has a large parabolic behavior which is not true for a quasi-two dimensional material like graphite. In this work, the NWS spectrum shown in figure 3-2 is processed by having a parabolic range up to 65 K, and represented by 145 points (parabolic up to the 5th point). Figure 4-23 shows a comparison of the three spectra that will be used in LEAPR.

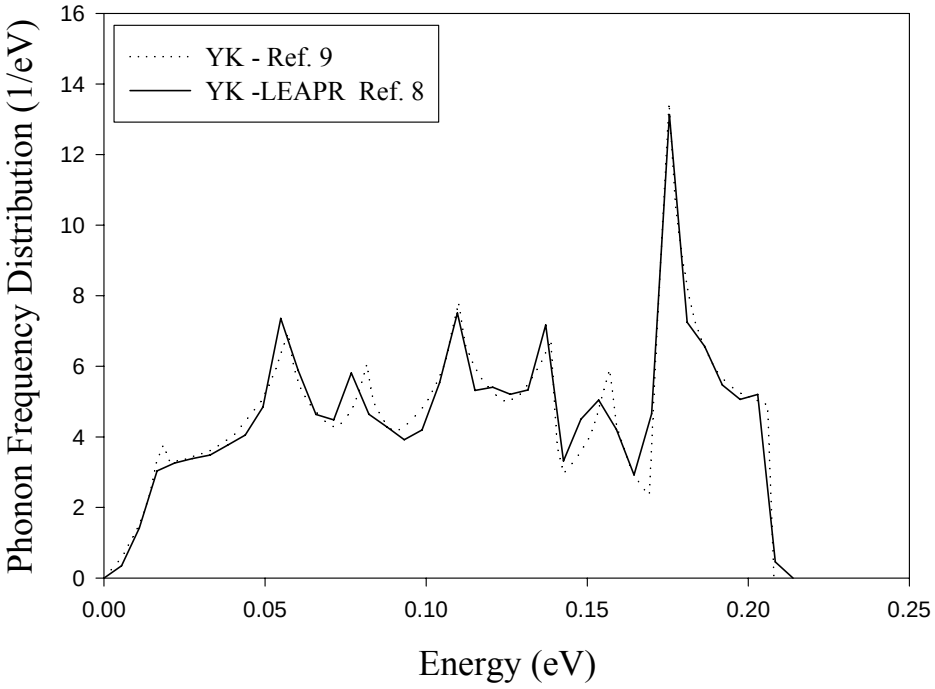

Figure 4-22 The YK phonon frequency distribution appeared in the Ref. [9] (dotted line), and the one used in LEAPR [8] (solid line).

Figure 4-24 shows $P(\beta)$ as given by equation (4.8) based on the NCSU, YK, and NWS spectra. The NCSU and NWS spectra have higher phonon density of states at low energies than the YK spectrum. Therefore, their corresponding $P(\beta)$ are higher at low β values.

As a consequence, it is expected that the cross section generated by using the NCSU and NWS spectra to be close to each other while that generated by using the YK spectrum is the lowest.

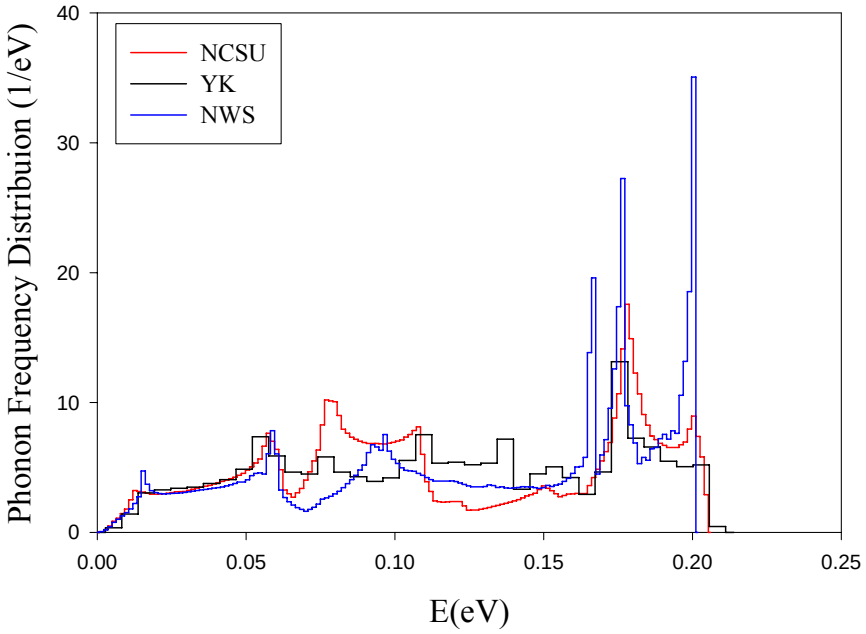

Figure 4-23 The phonon frequency distributions used in LEAPR: (*ab initio*) NCSU (red), YK (black), and NWS (blue).

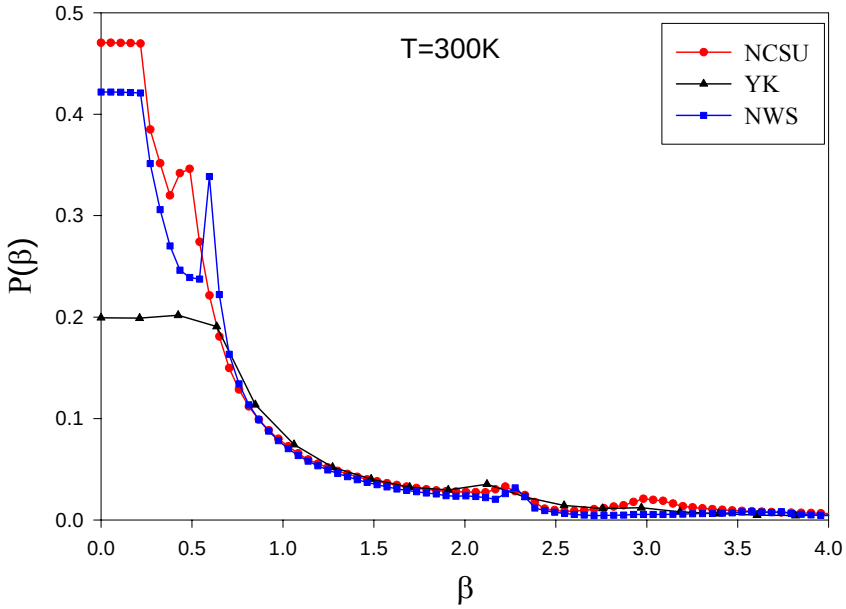

Figure 4-24 $P(\beta)$ at *T*=300 K for *Ab initio* (NCSU), Young-Koppel, and NWS spectra.

Furthermore, as seen from the figure, the flat region shows that the NCSU spectrum has a parabolic behavior up to the 5th point, and so does the NWS spectrum, while YK spectrum is parabolic up to the 4th point with a larger bin width. Figure 4-25 shows the inelastic scattering cross section at 300 K generated in the incoherent approximation using equations (2.61 and 2.62) using the NCSU, YK, and NWS spectra.

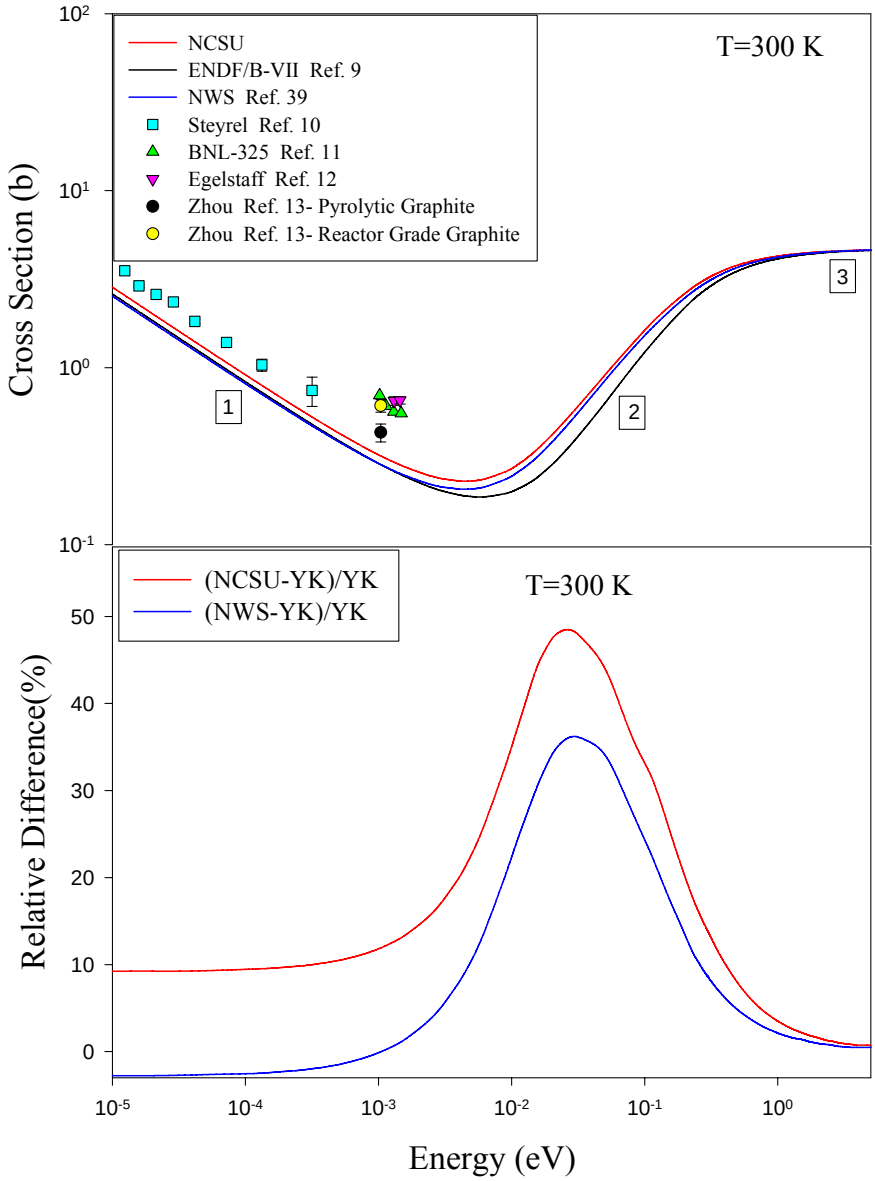

Figure 4-25 The inelastic scattering cross section in the incoherent approximation equations (2.61 and 2.62) at T=300 K based on the NCSU, YK (ENDF/B-VII), and NWS spectra, compared to experimental data (above), the relative difference with respect to YK is shown (below).

The curves show a typical behavior for crystalline materials. At neutron energies above~1eV (region 3), the atom acts as if it is free. That is, the neutron wavelength in this region is small compared to the atomic spacing, so it interacts with individual atoms. At lower energies (region 2) neutrons have sufficient incident energy to create phonons (phonon emission) via its scattering, so the lattice gains energy from the neutron. At very low energies, of order 1 meV and lower (region 1), the scattered neutron is more energetic than the incident neutron. That is, the neutron will gain energy from the lattice via phonon absorption. The cross section in this region has 1/v behavior (or ~λ). As it can be seen, the cross section behavior is consistent with figure 4-8. The NCSU spectrum made some improvements on the cross section compared to the Young-Koppel and NWS phonon spectra. However, the deviation from experimental data remains. Two sets of experimental data for pyrolytic graphite measured by Steyrel [10] and Zhou [13] are shown in the figure and for reactor grade graphite measured by Egelstaff [12] and Zhou [13]. It is not clear what kind of graphite the BNL-325 [11] represents. Unfortunately, details regarding this data are not published, and a little is known about it. However, this data is consistent with Egelstaff [12] and Zhou [13] data for reactor –grade graphite. As it can be seen, improving the phonon frequency distribution of graphite by utilizing the *ab initio* approach was not sufficient to match the experimental data of Steyrel [10] and Zhou [13]. The relative differences of the cross section curves with respect to young-Koppel cross section reach ~ 48% (at E = 0.0253 eV) and ~36% (at E = 0.0306eV) for the NCSU and NWS cases, respectively.

The secondary neutron emission spectra for the incident neutron energy E = 0.3011 eV at T=300 K, is shown in figure 4-26. The emission spectra based on the NCSU and NWS

phonon frequency distributions have sharper peaks of inelastically scattered neutrons in the neighborhood of zero energy transfer than in the case of YK, whereas, the emission spectra based on YK spectrum is smoothed out due to the longer rage parabolic behavior. The area under each curve represents the cross section corresponding to the incident neutron energy.

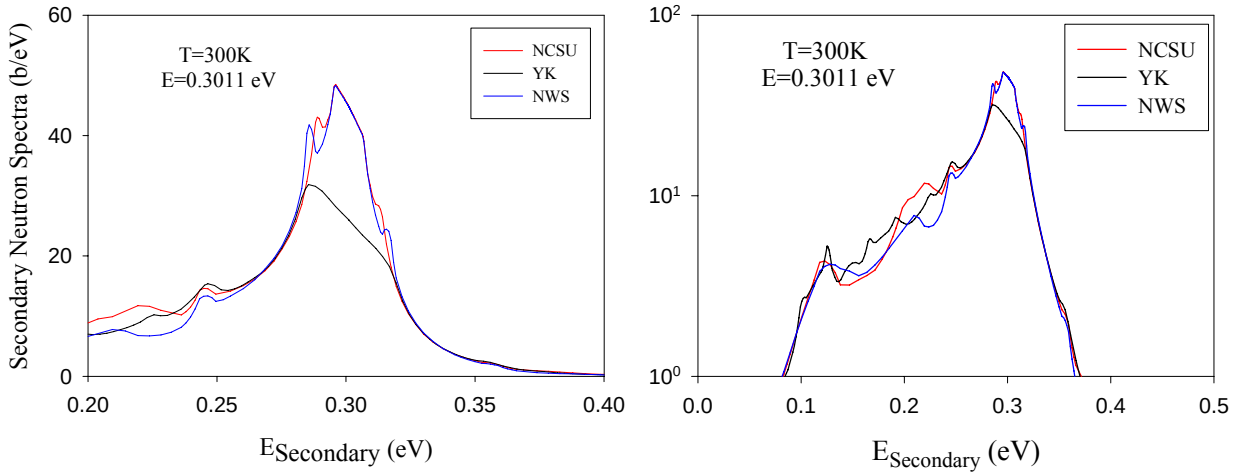

Figure 4-26 The secondary neutron spectrum at 300 K for neutron incident energy 0.3011 eV, in linear-linear scale (left), and semi-log scale (right) based on the NCSU (red), YK (black), and NWS (blue) phonon frequency distributions.

As the temperature of the scattering medium increases, the cross section increases because there are more phonons in the crystal. That is, as the temperature increases, the average number of phonons $\langle n_{\bar{q}j} \rangle$ excited at temperature T becomes directly proportional to the temperature T, $\langle n_{\bar{q}j} \rangle \cong \frac{k_B T}{\hbar \omega_{\bar{q}j}}$. That is, the higher the temperature the more excited phonons. Figure 4-27 shows the NCSU phonon frequency distribution in dimensionless units at different temperatures. These distributions renormalized as a function of beta. That is, the horizontal axis which represents the energy transfer is divided by $k_B T$ for the temperature of interest, and the vertical axis which represents the phonons population is multiplied by $k_B T$. Note that, both axes become dimensionless, and the area under each

curve is unity. As seen, as the temperature increases there are higher phonons, and as a consequence, $P(\beta)$ will be higher as shown in figure 4-28.

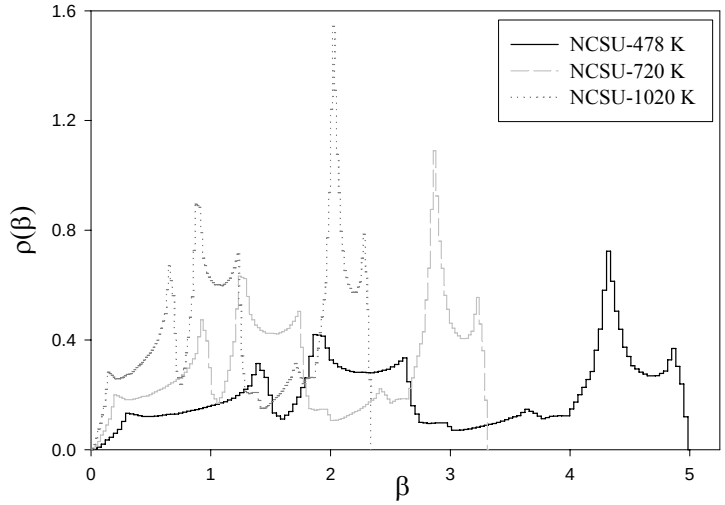

Figure 4-27 The NCSU phonon frequency distributions as a function of beta, corresponding to different temperatures *T*= 478 K (solid), 720 K (dashed), and 1020 K (dotted).

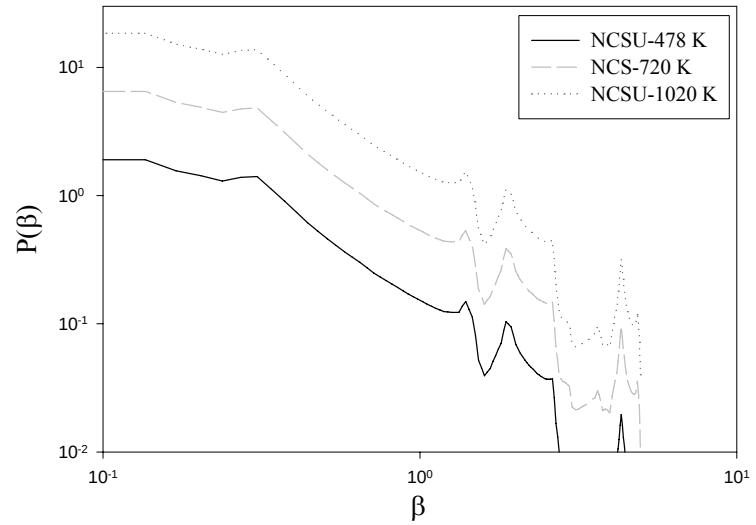

Figure 4-28 P(β) for NCSU spectrum at 478 K, 720 K, and 1020 K.

The inelastic scattering cross section in the incoherent approximation for T = 478 K, 720 K, and 1020 K, using NCSU, YK, and NWS spectrums are shown in figures 4-29, 4-30, and 4-31, respectively. The cross section increases as the temperature increased. The

relative differences decreases with temperature. The low energy neutrons (cold neutrons) have cross sections higher than the free cross section, and it changes by an order of magnitude by raising the temperature from room temperature to about 1000 K.

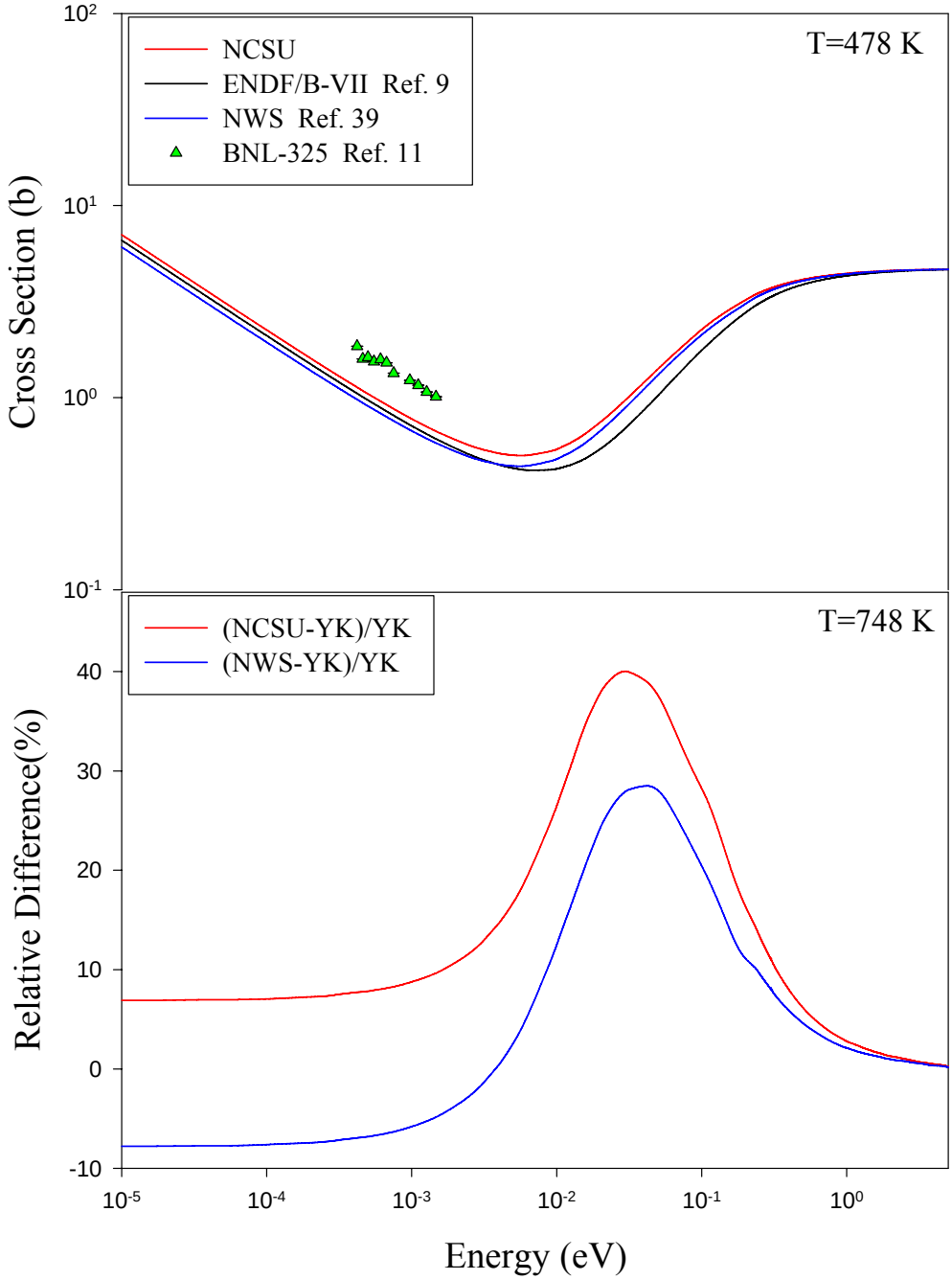

Figure 4-29 The inelastic scattering cross section in the incoherent approximation equations (2.61 and 2.62) at T=478 K based on the NCSU, YK (ENDF/B-VII), and NWS spectra, compared to experimental data (above), the relative difference with respect to YK is shown (below).

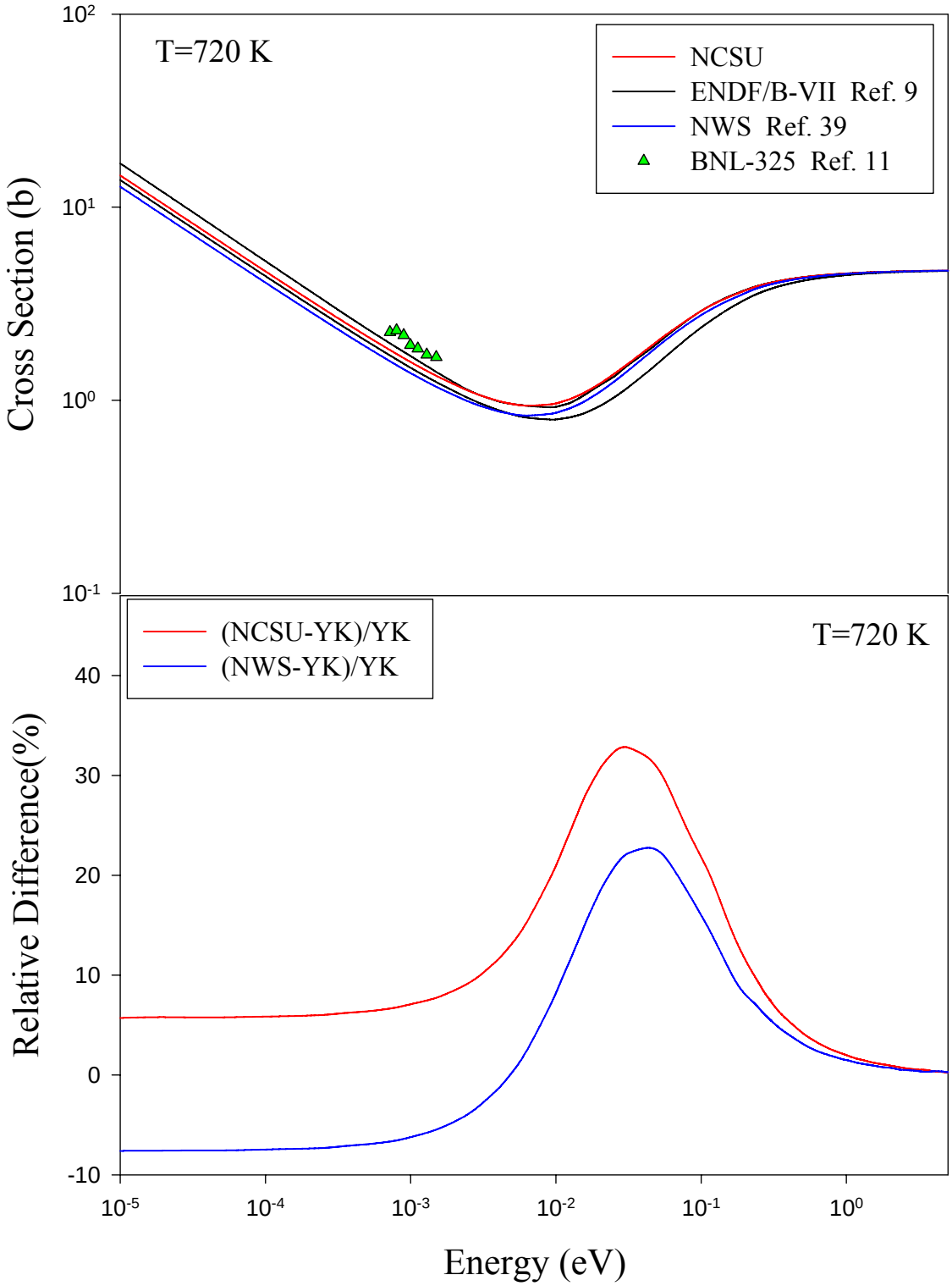

Figure 4-30 The inelastic scattering cross section in the incoherent approximation equations (2.61 and 2.62) at T= 720 K based on the NCSU, YK (ENDF/B-VII), and NWS spectra, compared to experimental data (above), the relative difference with respect to YK is shown (below).

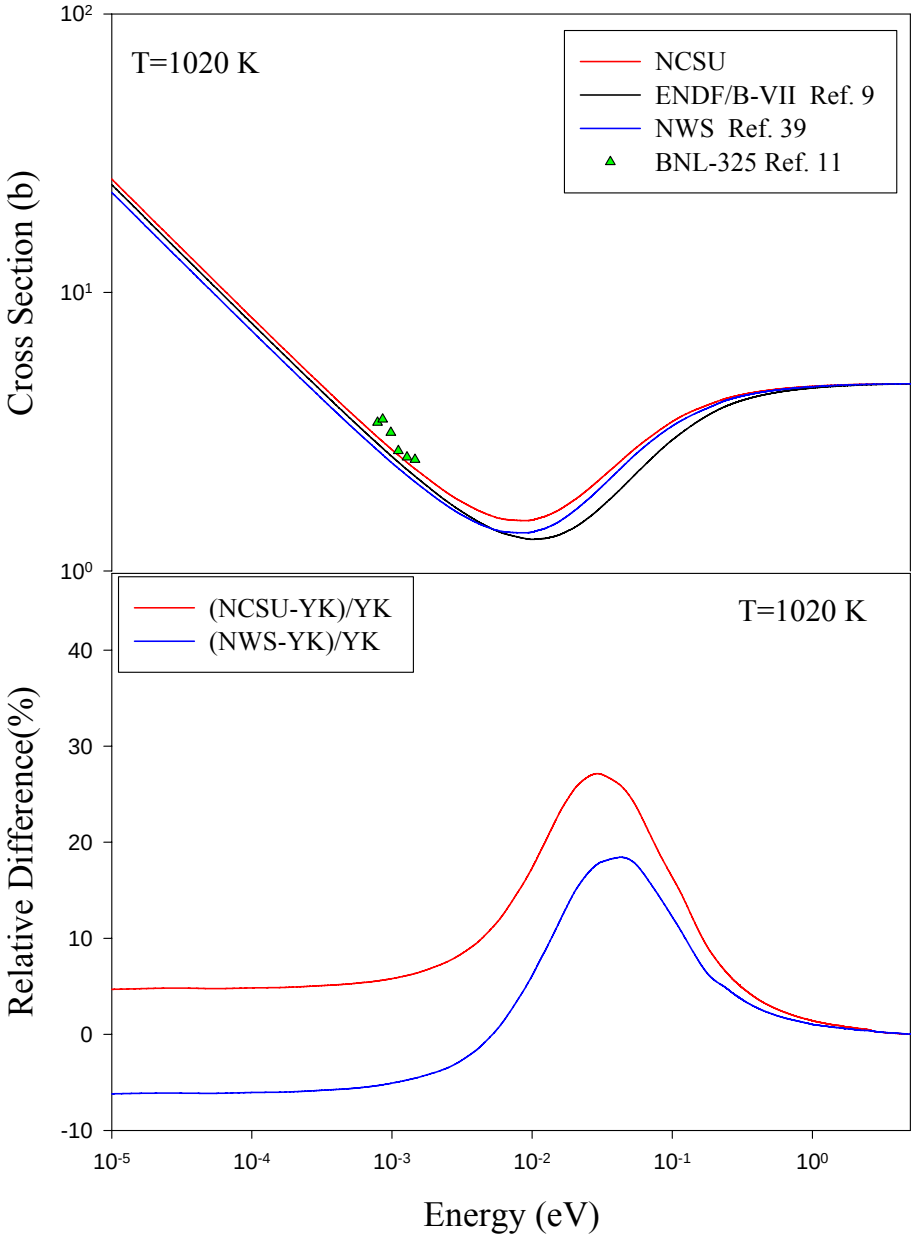

Figure 4-31 The inelastic scattering cross section in the incoherent approximation equations (2.61 and 2.62) at T=1020 K based on the NCSU, YK (ENDF/B-VII), and NWS spectra, compared to experimental data (above), the relative difference with respect to YK is shown (below).

4.1.3 Scattering Law Development and Comparison to Experimental Data

To facilitate comparison to experimental data, a direct relation between the phonon frequency distribution and the scattering law is constructed for small momentum transfer in

the coherent approximation [96]. That is,

$$\lim_{\alpha\to 0}\frac{S_s(\alpha,\beta)}{\alpha}=\frac{\rho(\beta)}{2\beta\sinh(\beta/2)}=P(\beta). \tag{4.12}$$

Based on the above relation, figure 4-24 can be utilized to compare the scattering law $S_s(\alpha,\beta)$ calculated based on the NCSU, YK, and NWS spectra. Figure 4-17 shows $\frac{S_s(\alpha,\beta)}{\alpha}$, calculated by LEAPR and using the NCSU, YK, and NWS spectra for β =0.2, 0.3, 0.4, and 0.5, at T=300 K, compared to the data from Wikner [94]. As it can be seen, in the incoherent approximation, the scattering law has a smooth behavior. The scattering law curves are consistent with figure 4-24. That is, at β= 0.2, 0.3, 0.4, and 0.5 the NCSU phonon spectrum is higher than the NWS phonon spectrum, which in turn is higher than the YK phonon spectrum. The overall picture, the incoherent approximation could predict on average the scattering law shape, but clearly it is not enough to describe precisely the scattering law. Another set of experimental data was performed by Carvalho [57] at T=533 K, such data shows more detailed structure and more points than previous one [94]. In his work, Carvalho determined the scattering law experimentally by utilizing equation (2.51). In addition, he removed the back ground contribution, separated the elastic peak from the inelastic scattering, and corrected for the multiple scattering contribution. Figure 4-33 compares the scattering law for β = 0.15, 0.2, 0.25, and 0.3 in the incoherent approximation using the NCSU, YK, and NWS spectra with Carvalho data. By examining figures 4-32 and 4-33, it can be seen that the calculation of the scattering law using the incoherent approximation fails to reproduce the structure observed experimentally especially at low α and β values. Most of the time and depending on the value of b the NCSU spectrum seems to be closest to the experimental values.

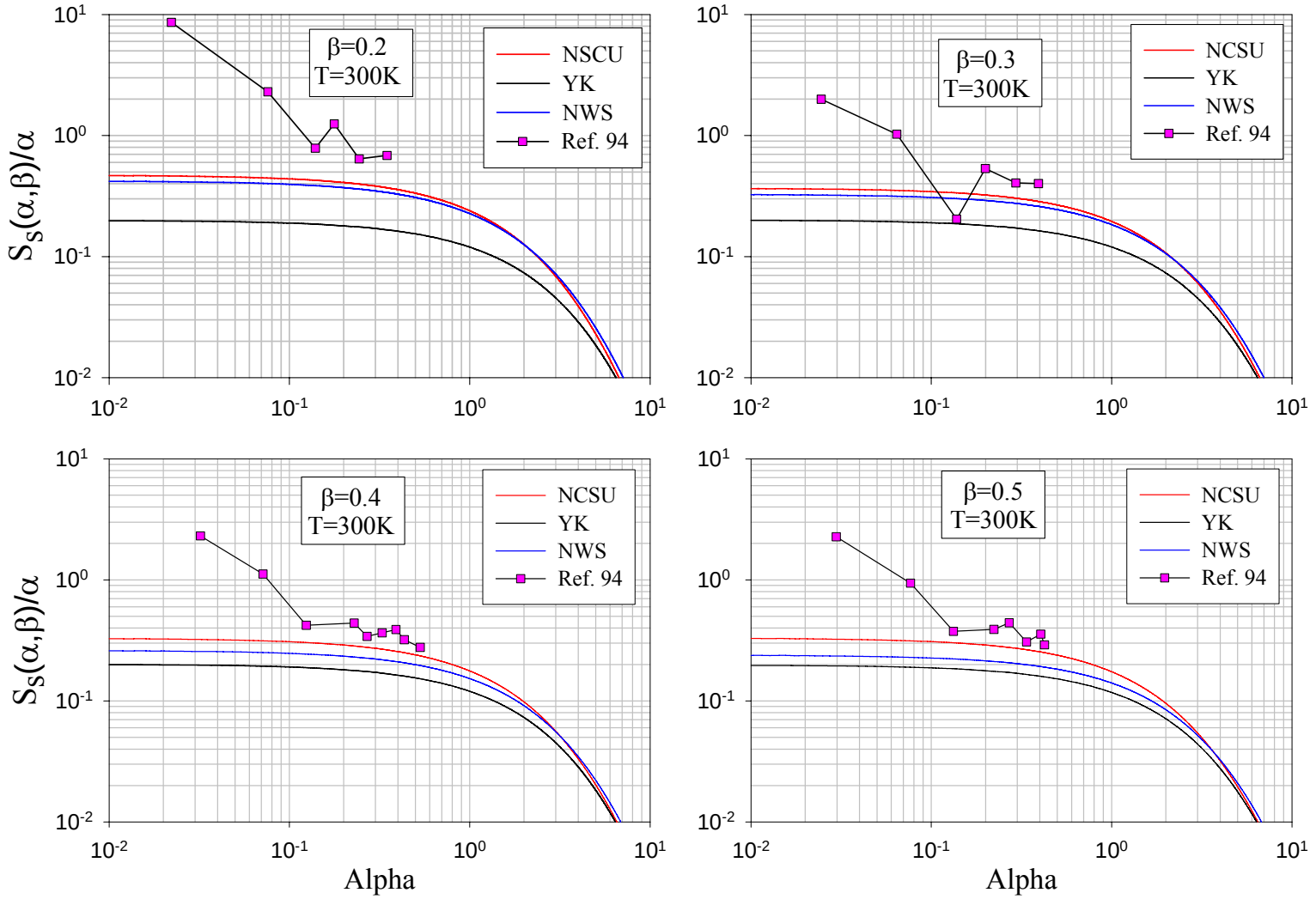

Figure 4-32 $\frac{S_s(\alpha,\beta)}{\alpha}$ **corresponding to the NCSU, YK, and NWS libraries, compared to Wikner *et al* data,[94], at T=300 K.**

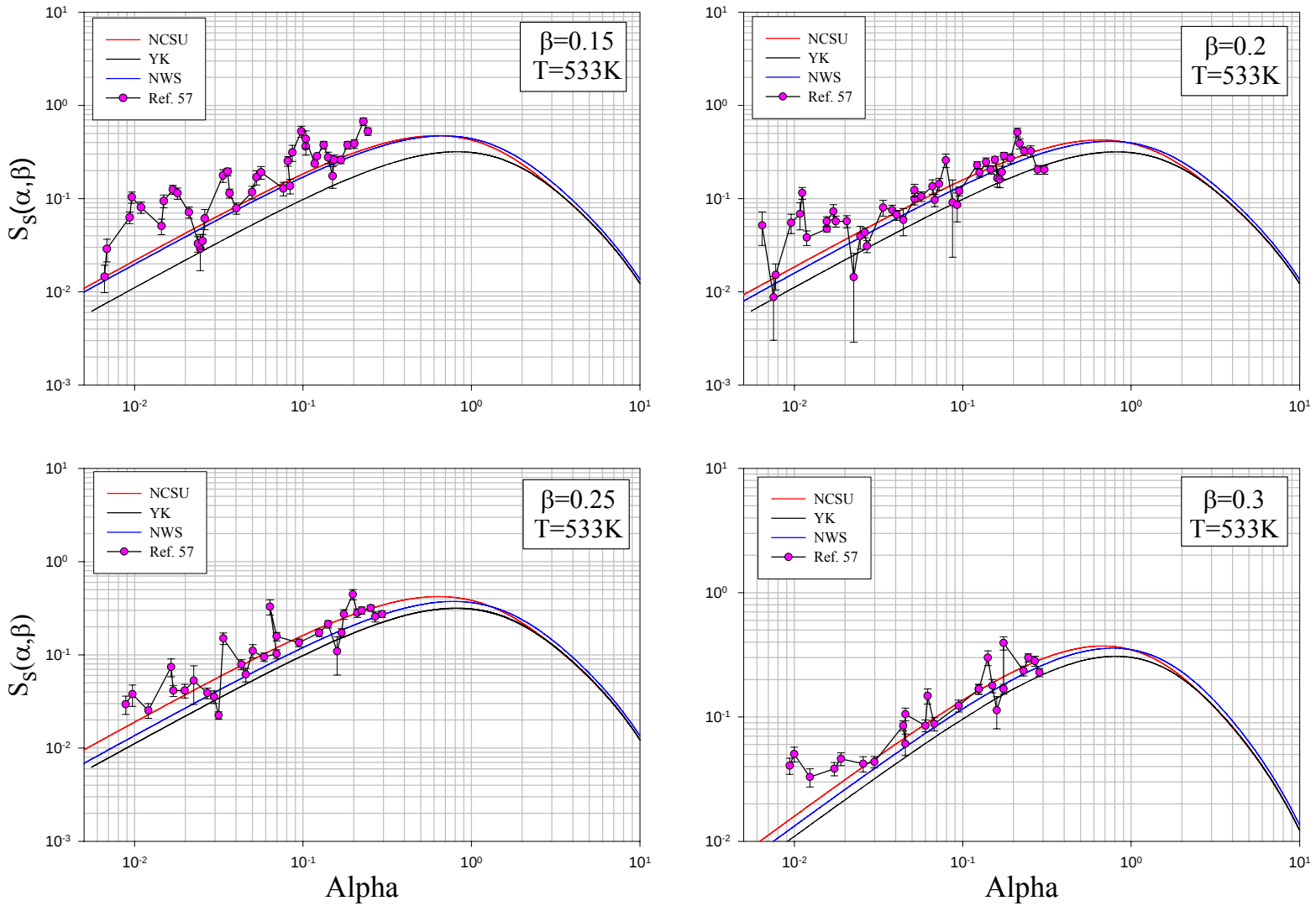

Figure 4-33 $S_s(\alpha,\beta)$ **corresponding to the NCSU, YK, and NWS libraries, compared to Carvalho data [57] at T=533 K.**

4.3 The Coherent One Phonon Contribution

Since graphite is a strong coherent scatterer, the structure appears in the experimental results for the scattering law shown in the previous figures can not be explained by the incoherent approximation. Consequently, examination was performed of restoring the coherent inelastic component. Earlier work exists in the literature on analyzing coherent inelastic scattering in Be and graphite [97, 98, and 99]. However, the current work is a more complete approach that aimed at producing the thermal neutron scattering cross sections of graphite.

Recall that the inclusion of the one-phonon component in the total double differential scattering cross section was given by equation (2.87), where the coherent one-phonon scattering law was given by equation by (2.85). Note that *s* represents sum over $\vec{q}$ and *j*. and the first part of equation (2.85) corresponds to $\langle n_{\vec{q}j} \rangle$ and describes an energy gain process, that is $\beta > 0$, considering this term, the sum over $\vec{q}$ and $\vec{\tau}$ can be replaced by an integral over $\vec{\kappa}$, by utilizing the relation

$$\sum_{\vec{q},\vec{\tau}} (\cdots) = \frac{N v}{(2\pi)^3} \int (\cdots) d\vec{\kappa}. \tag{4.13}$$

Performing this integral will lead to

$$^{1}S_{-}(\vec{\kappa},\omega) = \frac{1}{2Mn} \sum_{j\vec{\kappa}_{-}} \frac{F_{\vec{q}j}^{2}(\vec{\kappa})}{\omega_{\vec{q}j}} \langle n_{\vec{q}j} \rangle \delta(\omega + \omega_{\vec{q}j}), \tag{4.14}$$

where $\vec{\kappa} = \vec{\tau} - \vec{q}$, and $^{1}S_{-}(\vec{\kappa},\omega)$ corresponds to $\langle n_{\vec{q}j} \rangle$ while $^{1}S_{+}(\vec{\kappa},\omega)$ corresponds to $\langle n_{\vec{q}j} + 1 \rangle$ term. Where $S_{-}(\alpha,\beta) = \mathrm{e}^{-\beta} S_{+}(\alpha,-\beta)$, and defining the structure factor

$F_{\vec{q}j}(\vec{\kappa})$ as

$$F_{\vec{q}j}(\vec{\kappa}) = \sum_{d} e^{i\vec{\kappa}\cdot(\vec{d})} e^{-W_d}(\vec{\kappa}\cdot\vec{e}_{ds}), \tag{4.15}$$

and noting that

$$\langle n_{\vec{q}j} \rangle = \frac{1}{\exp(\hbar\omega_{\vec{q}j}/k_B T)-1}, \tag{4.16}$$

equation (4.14) can be written in terms of α and β, as

$${}^{1}S_{-}(\alpha,\beta) = \frac{\hbar^2}{2Mnk_B T}\frac{1}{\beta(e^{\beta}-1)}\frac{e^{\beta/2}}{\Delta\beta}\sum_{j\vec{\kappa}_{-}}\frac{F^2_{\vec{q}j}(\vec{\kappa})}{l(\alpha,\Delta\alpha)}. \tag{4.17}$$

Notice that this replaces ω by β, and assumes that for a small interval $\Delta\beta$, the delta function can be replaced by $1/\Delta\beta$, and $l(\alpha,\Delta\alpha)$ is the number of the mesh points inside the interval $\Delta\alpha$. Evaluating the scattering law, starts by evaluating the sum in equation (4.17), where the polarization vectors and dispersion relations are required as input to the structure factor. After performing the sum, the contribution of each $\vec{\kappa}$ to the scattering law is added and stored in an interval $\Delta\alpha$, $\Delta\beta$, around α and β, that is, the scattering law is an average over a space $\Delta\alpha$, $\Delta\beta$. The sum over $\vec{\kappa}$ is made over a mesh of points in the reciprocal space. Due to the crystal symmetry, the number of $\vec{\kappa}$ vectors can be reduced by using the reduced first Brillouin zone. That is, to generate the $\vec{\kappa}$ mesh, reduced first Brillouin zone is used to generate $\vec{q}$ mesh. Then by using the translational constraints $\vec{\kappa} = \vec{\tau} - \vec{q}$, the $\vec{\kappa}$ mesh can be generated. For each reciprocal lattice vetor $\vec{\tau}$ the structure factor is calculated for all $\vec{q}$ vectors and is added to the sum. The effect of the coherent one phonon cross section contribution appears clearly when compared with the experimental data [10].

Figures (4-34 - 4-37) compare the scattering cross section at 300 K, 478 K, 720 K, and 1020 K after adding the coherent one phonon cross section using non-isotropic Debye Waller factor with cross section in the incoherent approximation. As seen, excellent agreement is achieved in comparison with experimental data of pyrolytic graphite (ρ = 2.24 g/cm^3) at 300 K [10, and 13]. Since its density is very close to the theoretical density (2.26 g/cm^3), it indicates that pyrolytic graphite can be treated as perfect graphite. However, the BNL-325 [11], Egelstaff [12], and Zhou [13] data represent reactor grade graphite cross section, and it is not appropriate to be treated in this work, since reactor grade graphite is a porous material (~30% porosity), and has two phases, graphite crystal (pyrolytic graphite) and binder carbons which can be treated as amorphous -like carbon. The binder carbons have different lattice dynamics properties than that of crystalline graphite. As a consequence, the inelastic scattering crosses section of reactor grade graphite is different than that of pyrolytic graphite.

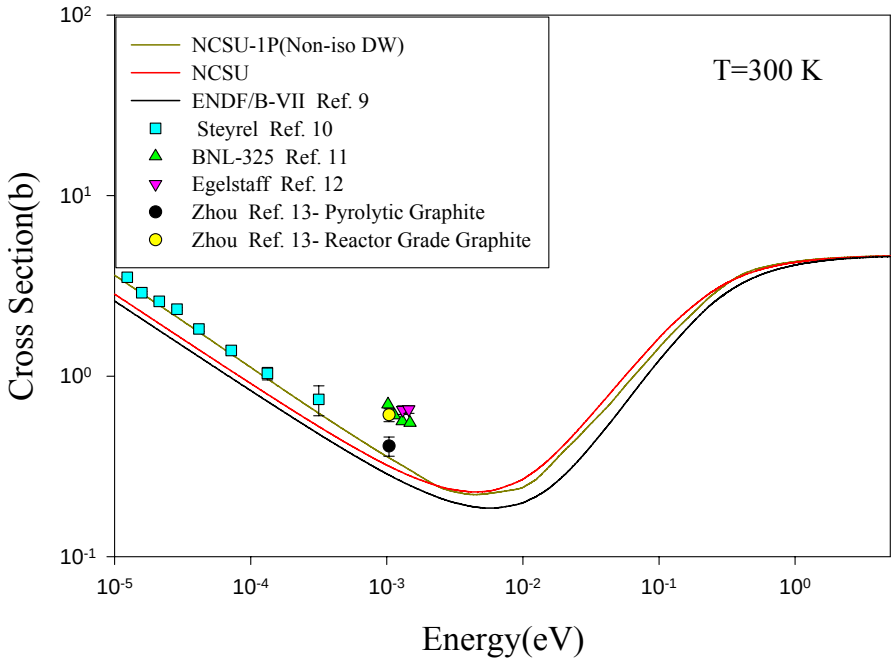

Figure 4-34 The inelastic scattering cross section including the coherent one-phonon (NCSU-1P), using a non-isotropic Debye-Waller factor at 300 K compared to the cross section in the incoherent approximation using the NCSU and YK spectra, and experimental data.

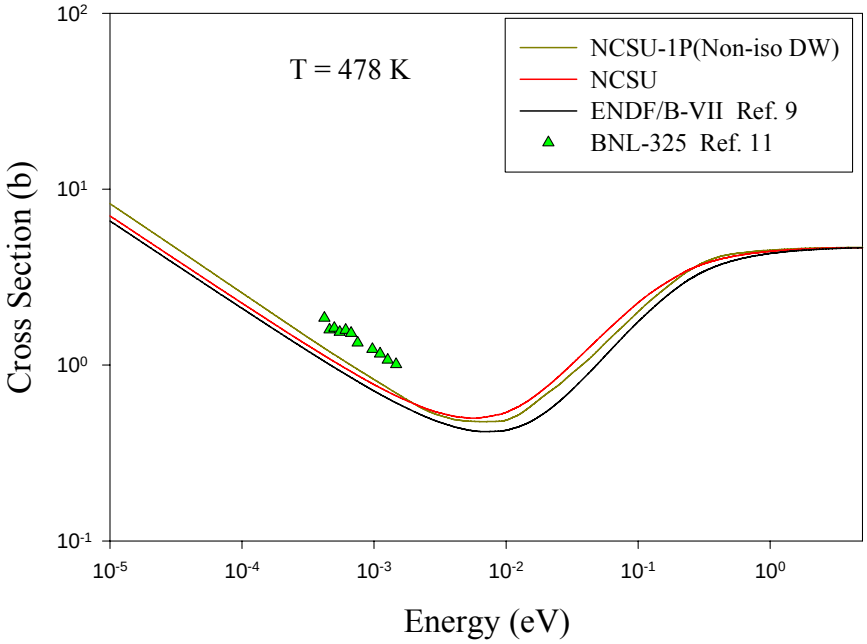

Figure 4-35 The inelastic scattering cross section including the coherent one-phonon (NCSU-1P), using a non-isotropic Debye-Waller factor at 478 K compared to the cross section in the incoherent approximation using the NCSU and YK spectra, and experimental data.

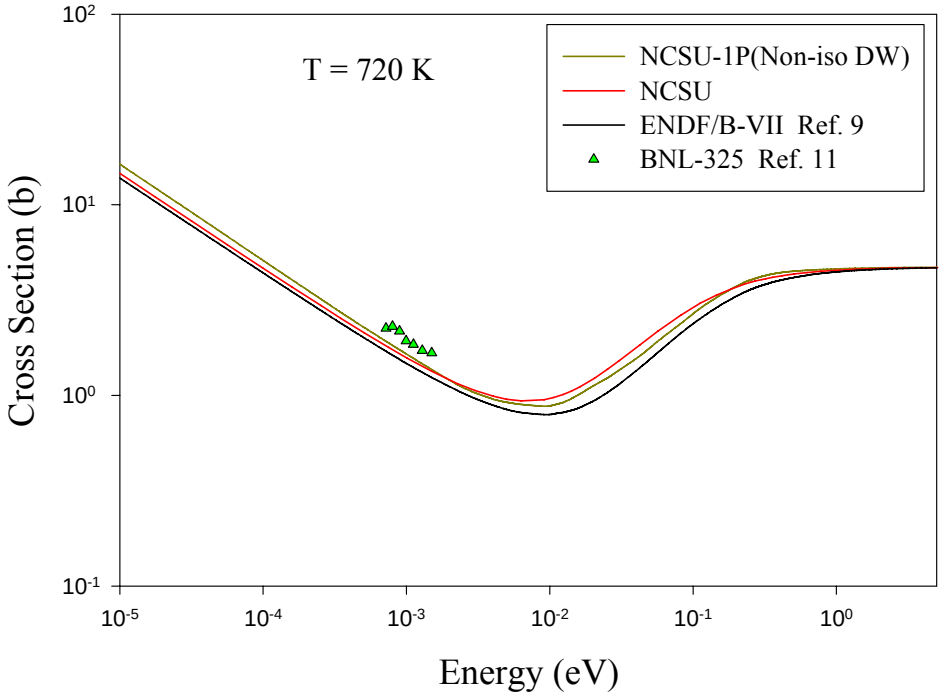

Figure 4-36 The inelastic scattering cross section including the coherent one-phonon (NCSU-1P), using a non-isotropic Debye-Waller factor at 720 K compared to the cross section in the incoherent approximation using the NCSU and YK spectra, and experimental data.

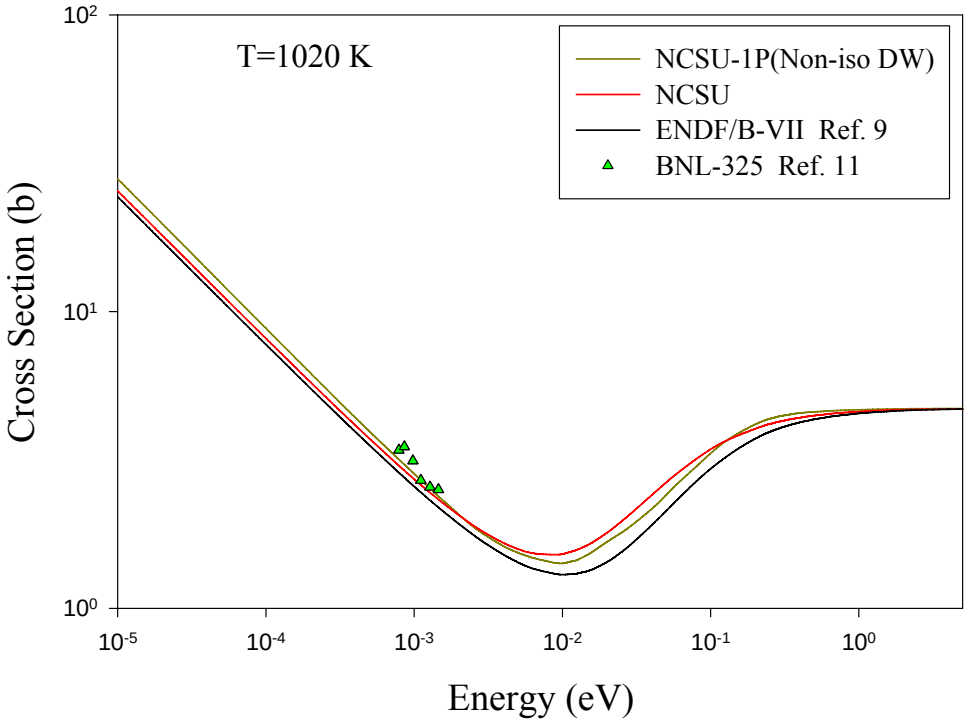

Figure 4-37 The inelastic scattering cross section including the coherent one-phonon (NCSU-1P), using a non-isotropic Debye-Waller factor at 1020 K compared to the cross section in the incoherent approximation using NCSU and YK spectra, and experimental data.

The coherent one-phonon scattering cross section contribution was calculated using a non-isotropic Debye Waller factor e^{-2W}. Where $2W = \left\langle (\kappa \cdot u)^2 \right\rangle$. In the incoherent approximation $2W$ is considered isotropic. In this work, $2W$ is treated isotropically and non-isotrpically. The Isotropic case assumes $2W$ is equal in all directions, that is

$$\left\langle u_x^2 \right\rangle = \left\langle u_y^2 \right\rangle = \left\langle u_z^2 \right\rangle \quad , \tag{4.18}$$

where the mean square displacement (MSD) is given by equation (4.10). The NCSU phonon frequency distribution that has a parabolic range up to 65 K was used to calculate the isotropic displacement for graphite atom. While in the non-isotropic case, the phonon frequency distribution is separated into three parts representing the partial phonon frequency distributions $\rho_x(\omega), \rho_y(\omega)$, and $\rho_z(\omega)$. The partial phonon frequency distributions were

fitted parabolically up to 65 K. The MSD at 300 K, 478 K, 720 K, and 1020 K for isotropic and non-isotropic cases are listed in table 4-4.

Table 4-4 Isotropic and non-isotropic MSD for graphite as a function of temperature

T (K)	$\langle u^2 \rangle_{isotropic}$ (Å^2)	$\langle u_x^2 \rangle = \langle u_y^2 \rangle$ (Å^2)	$\langle u_z^2 \rangle$ (Å^2)
300	0.005892	0.002352	0.012994
478	0.008627	0.003070	0.019775
720	0.012503	0.004163	0.029234
1020	0.017413	0.005607	0.041096

As seen from the above table, the MSDs in the *x* and *y* directions are equal, due to the symmetry in the graphite *xy*-plane. The non-isotropic case has MSD in the z-direction that is one order of magnitude larger the displacement in *xy*-plane. However, the isotropic case greatly underestimates the z-component of MSD. Due to the graphite structure, which is highly anisotropic (see section 1.6), $2W$ should be treated non-isotropically. The effect of Debye-Waller factor isotropy at 300 K is shown in figure 4-38.

The coherent one phonon scattering cross sections using isotropic and non-isotropic Debye Waller factor are compared to the one-phonon cross section in the incoherent approximation, as shown in figure 4-39. Also the figure compares the self part of the coherent one-phonon scattering cross section with the one-phonon cross section in the

incoherent approximation, and shows the distinct part of the coherent one-phonon cross section. As seen at low energies the distinct term has a significant contribution. Figure 4-40, also compares the self part of the coherent one phonon cross section with one phonon cross section in incoherent approximation.

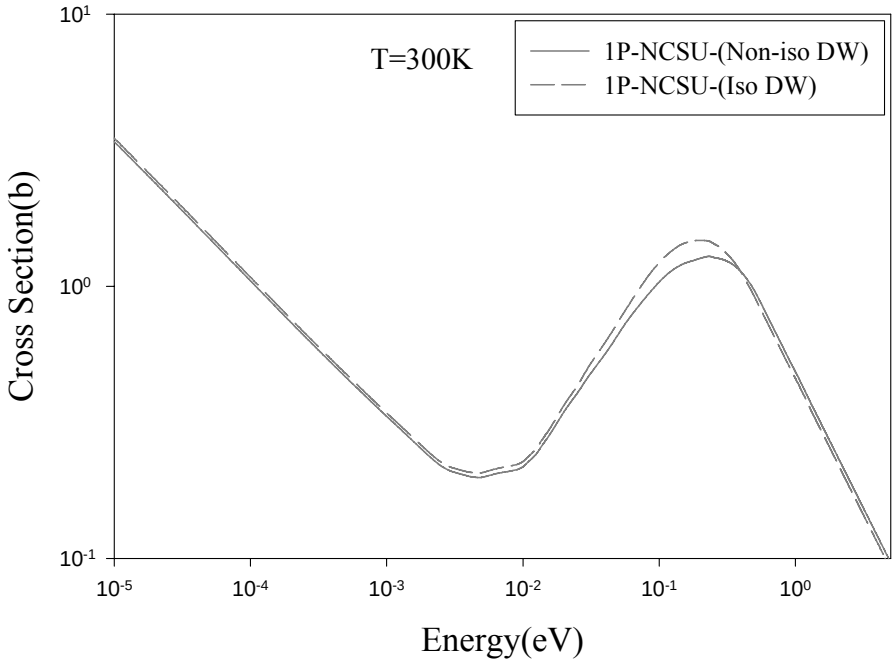

Figure 4-38 The coherent one-phonon (1P) cross section using a non-isotropic (solid) and isotropic (dashed) Debye-Waller factor at 300 K.

Figures 4-40 and 4-41 compare the scattering law produced by including the coherent one-phonon contribution based on equation (2.87), and those produced in the incoherent approximation using the NCSU, YK, and NWS spectra. As seen the coherent contribution effect is clear as wiggles in the scattering law. An excellent agreement was obtained in comparison with the experimental data [94, and 57], indicating the importance of adding the coherent contribution to the scattering law, and removing the incoherent approximation as much as possible.

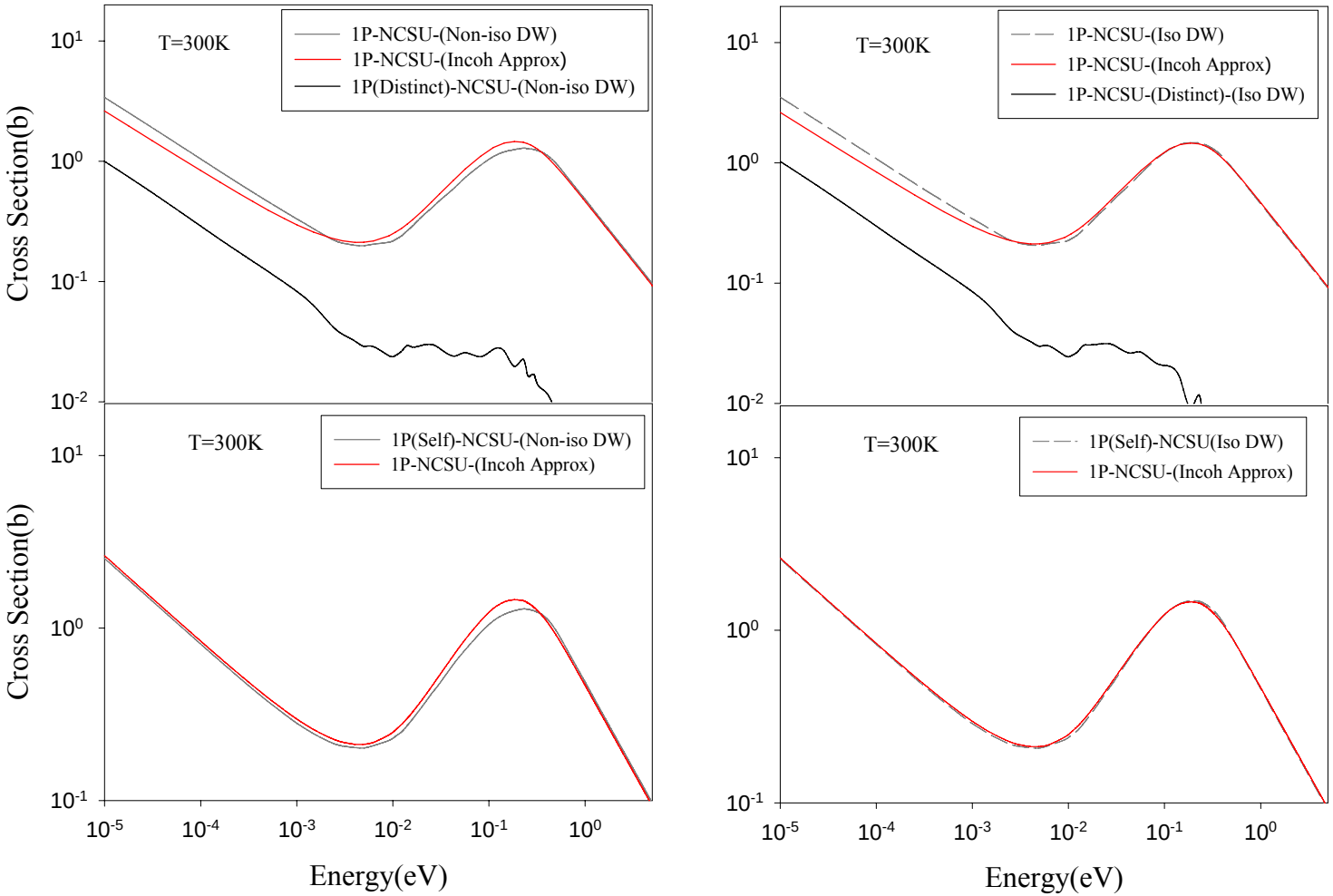

Figure 4-39 The coherent one-phonon (1P) scattering cross section using non-isotropic (solid) and isotropic (dashed) Debye-Waller factor at 300 K compared to the one-phonon scattering cross section in the incoherent approximation, similar comparison is shown between the self coherent one-phonon scattering cross section and the one-phonon scattering cross section in the incoherent approximation.

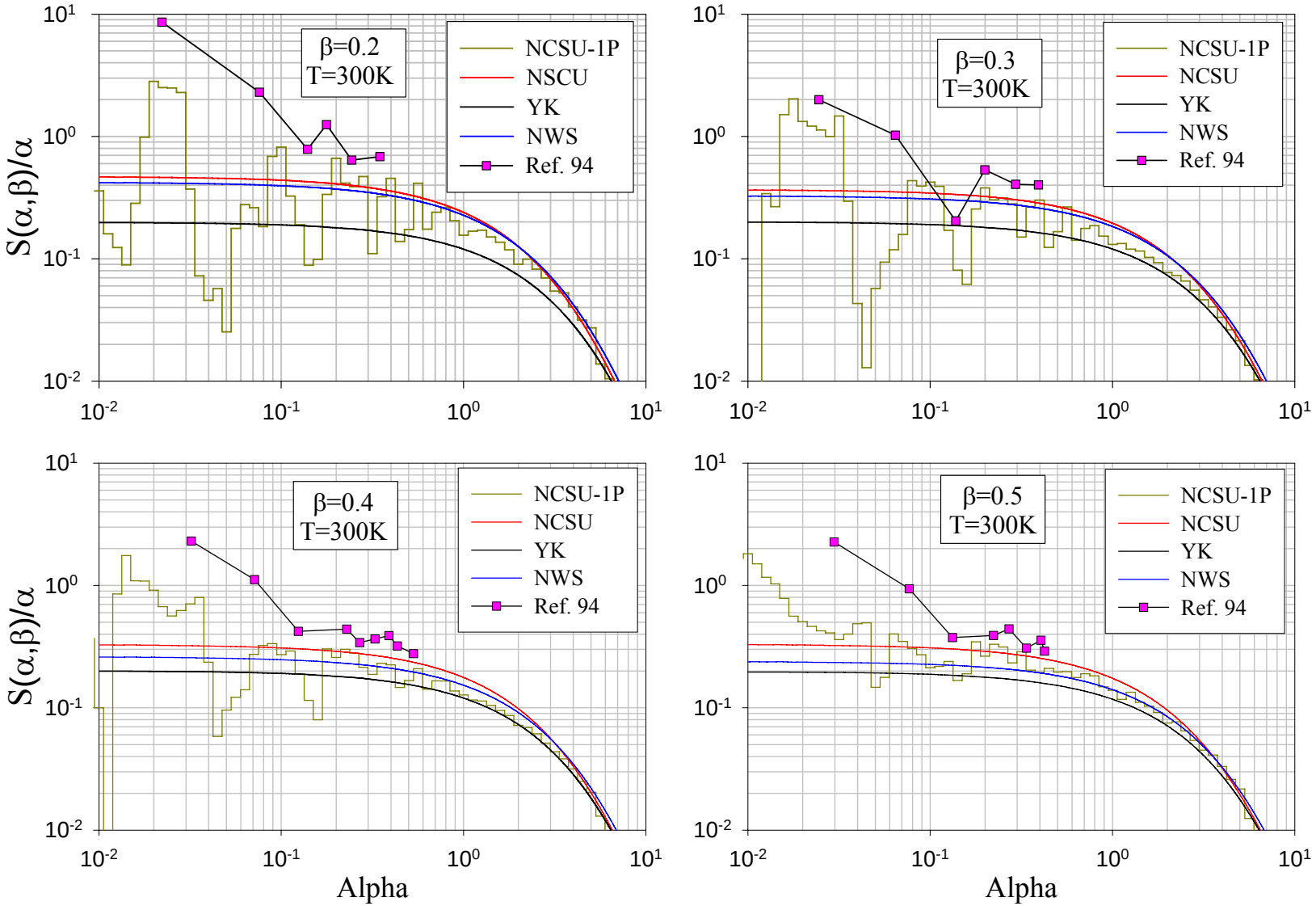

Figure 4-40 $S(\alpha,\beta)/\alpha$ **corresponding to the NCSU, YK, and NWS libraries, compared to Wikner *et al* data,[94], at T=300 K.**

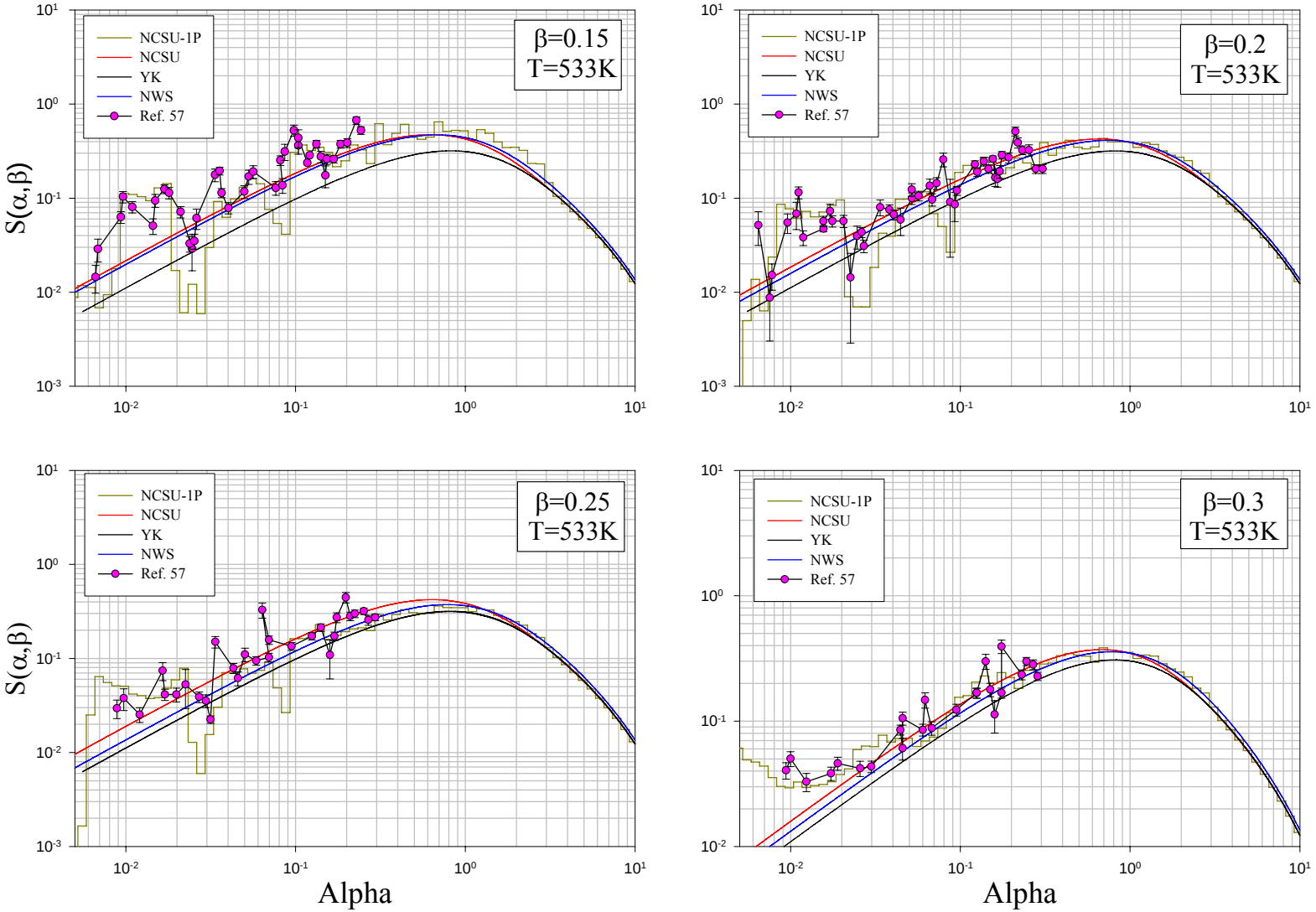

Figure 4-41 $S(\alpha,\beta)$ **corresponding to the NCSU, YK, and NWS libraries, compared to Carvalho [57], at T=533 K.**

4.4 Anharmonicity

In deriving the equation of motion (chapter three), it is assumed that the crystal is harmonic and the higher orders (third interactions and higher) of the potential are neglected. As the temperature of the crystal is raised up, these higher orders become more important. These higher orders terms represent phonon-phonon interactions; these interactions are responsible for the thermal expansion and finite thermal conductivity of the crystal. The presence of these terms prevents the diagonalization of the Hamiltonian, and since these terms are smaller than the harmonic term (second term), the harmonic frequency $\omega(\vec{q}, j)$ of the mode $(\vec{q}, j)$ is given by [100]

$$\omega(\vec{q}, j) + \Delta(\vec{q}, j) + i\Gamma(\vec{q}, j), \tag{4.19}$$

where $\Delta(\vec{q}, j)$ represents the shift from the harmonic frequency, and $\Gamma(\vec{q}, j)$ is a decay constant (half-width at half maximum). Both are temperature dependent. The real part shows up as a shift in the center of the peak in the energy distribution of the scattered neutrons. The main contribution to $\Delta(\vec{q}, j)$ is due to the thermal expansion contribution, while for $\Gamma(\vec{q}, j)$ is due to the thermal conductivity. The imaginary part shows up experimentally in the broadening of the peak. At temperatures $T << \hbar\omega_m / k$, the thermal displacements of the atoms in the crystal are small, so the dominant term is the quadratic term in the Hamiltonian, and it is expected that $\Delta(\vec{q}, j)$ and $\Gamma(\vec{q}, j)$ to be small. For small $\omega(\vec{q}, j)$ the probability of two phonons scattering is small, therefore, it is expected that $\Delta(\vec{q}, j)$ and $\Gamma(\vec{q}, j)$ to be small.

In this section the effect of anharmonicity on the phonon frequency distribution as shift

and broadening will be discussed. The shift and broadening effects are represented by a Lorentzian shape function.

4.4.1 Calculations

4.4.1.1 Energy Shift $\Delta(\vec{q}, j, T)$

Expansivity $\varepsilon(T)$

Due to the thermal expansion contribution, the shift from the harmonic frequency is written as [101]:

$$\Delta(\vec{q}, j, T) = -3\,\varepsilon(T)\,\gamma(\vec{q}, j)\,\omega(\vec{q}, j)\,, \tag{4.20}$$

where $\varepsilon(T)$ is called the thermal expansivity given by

$$\varepsilon = \overline{\beta} T\,, \tag{4.21}$$

where $\overline{\beta}$ is the *average* thermal expansion coefficient

$$\overline{\beta} = \frac{2}{3}\beta_{\parallel} + \frac{1}{3}\beta_{\perp}\,, \tag{4.22}$$

$\beta_{\parallel}$, and $\beta_{\perp}$ are the linear thermal expansion coefficient parallel and perpendicular to the basal plane, respectively.

$\gamma(\vec{q}, j)$ is called Gruniesen parameter [38], given by

$$\gamma(\vec{q}, j) = -\frac{V}{\omega(\vec{q}, j)}\frac{\partial\omega(\vec{q}, j)}{\partial V}\,, \tag{4.23}$$

where V is the volume of the crystal. As it can be seen, the starting point to calculate $\Delta(\vec{q}, j)$ is to know the average thermal expansion coefficients $\overline{\beta}$ as a function of temperature. The experimental data of Bailey and Yates [102] and Morgan [103] is

interpolated to obtain $\beta_{\|}$ for the temperature of interest [104]. While for $\beta_{\perp}$ the formulae produced by Nihira and Iwata [105] for modeling the experimental data of Bailey and Yates [102] were used. Table 4-5 shows the thermal expansion coefficients and linear expansivity as a function of temperature.

Table 4-5 Thermal expansion coefficient and thermal expansivity

T(K)	$\beta_{\|}$ (1/ K)	$\beta_{\perp}$ (1/ K)	$\overline{\beta}$ (1/ K)	ε
600	-2.4010 x10^{-7}	2.81927 x10^{-5}	9.2375 x10^{-6}	0.00554
900	3.9122 x10^{-7}	2.88595 x10^{-5}	9.88065 x10^{-6}	0.00889
1200	8.1140 x10^{-7}	2.93194 x10^{-5}	1.03677 x10^{-5}	0.01244
1500	1.0633 x10^{-6}	3.01330 x10^{-5}	1.07532 x10^{-5}	0.01613
1800	1.1790 x10^{-6}	3.07659 x10^{-5}	1.10413 x10^{-5}	0.01987

Gruniesen Consatant $\gamma(\vec{q}, j)$

So far, the thermal expansivity as a function of temperature is known. To apply equation 4.20, for each frequency $\omega(\vec{q}, j)$, its corresponding Gruniesen constant $\gamma(\vec{q}, j)$ for the same modes $(\vec{q}, j)$ need to be calculated. The volume of the unit cell varied by changing the lattice parameter *a* uniformly, in steps of 0.01 Å, and changing the lattice parameter *c* according to the *c/a*= 2.793 (corresponds to T=1200 K). As a consequence the dispersion relations are calculated for each volume using a 6x6x1 supercell and 50000 wave vectors sampled randomly over the full Brillioun zone. The derivative of the dispersion relations with respect to the volume $\frac{\partial \omega(\vec{q}, j)}{\partial V}$ was rewritten in the difference form as:

$$\frac{\partial \omega}{\partial V} = \frac{1}{2}\left[\frac{\omega_{i+1} - \omega_i}{V_{i+1} - V_i} + \frac{\omega_i - \omega_{i-1}}{V_i - V_{i-1}}\right]. \tag{4.24}$$

Gruneisen constants are usually positive, since phonon frequencies decrease with unit cell expansion. However, negative Gruneisen constants exist for the low-acoustic modes. This effect is well-known in layered materials and known as the membrane effect [106, and 107]. As a consequence, the negativity of the Gruneisen constants for wave vectors correspond to low frequency values will cause an opposite shift in the phonon frequency. That is, instead of shifting the frequencies to the left these low frequencies will be shifted to the right. So far, for each mode $(\vec{q}, j)$ the frequency $\omega(\vec{q}, j)$ and the Gruniesen constant $\gamma(\vec{q}, j)$ are known. Therefore, equation (4.20) can be applied exactly.

4.4.1.2 Broadening Γ

The effect of temperature is to decrease graphite thermal conductivity K (increase its thermal resistance). In graphite, heat is transferred by lattice vibrations (phonons) rather than by electrons or defects. Approximately, the thermal conductivity of graphite can be expressed as [108]

$$K = \frac{1}{3} C v \lambda \quad , \tag{4.25}$$

where C is the heat capacity per unit volume, v is the phonon speed (speed of sound), and λ is the phonon mean free path that depends on three contributions;

$$\frac{1}{\lambda} = \frac{1}{\lambda_B} + \frac{1}{\lambda_{PH}} + \frac{1}{\lambda_D}, \tag{4.26}$$

where λ_B is the mean free path due to scattering of phonons from boundaries (geometrical

scattering). It is dominant at low temperatures, λ_D is the mean free path due to lattice defects, (becomes significant in the case of irradiating graphite), and λ_{PH} is the mean free path due to the phonon-phonon scattering, if the forces between atoms were purely harmonic, there would be no mechanism for collisions between different phonons (temperature dependent) [108]. The speed of sound v can be written as

$$v = \lambda / \tau \ , \tag{4.27}$$

τ is the mean time between collisions. So by combining equation (4.25) and (4.27), it is given by

$$\tau = \frac{3K}{C v^2} \ . \tag{4.28}$$

Using

$$\Gamma = \frac{1}{\tau} . \tag{4.29}$$

Equation (4.29) can now be rewritten as temperature dependent

$$\Gamma(T) = \frac{C(T)\, v^2(T)}{3K(T)} . \tag{4.30}$$

For $kT << \hbar\omega_m$, $C(T)$ is proportional to T^n where n is equal 3 for three dimensional solids, and for the case of graphite, 2< n <3. Also K (T) is proportional to 1/T. The speed of sound is assumed to be a weak function of temperature, then

$$\Gamma \sim T^{n+1} . \tag{4.31}$$

For $kT >> \hbar\omega_m$, $C_p(T)$ is constant, so

$$\Gamma \sim T . \tag{4.32}$$

The asymptotic equations (4.31 and 4.32) agree with [109], and the numerical values of the physical quantities of equation (4.30) are obtainable.

Speed of Sound v

The mean sound velocity v_m is given by

$$v_m = \left(\frac{1}{3} \left(\frac{2}{v_t^3} + \frac{1}{v_l^3} \right) \right)^{-1/3} \tag{4.33}$$

where v_t and v_l are the transverse and longitudinal sound velocities respectively given by

$$v_l = \left(\frac{1}{\rho} \left(C_{11} - \frac{C_{13}^2}{C_{33}} \right) \right)^{1/2} \tag{4.34}$$

$$v_t = \left(\frac{1}{2\rho} \left(C_{11} - C_{12} \right) \right)^{1/2} \tag{4.35}$$

where ρ and C_{ij} are the density and the elastic constants, respectively [105]. So to have the sound velocity as a function of temperature, ρ and C_{ij} should be provided as a function of temperature. The models of Nihira and Iwata [105] are used to obtain the elastic constants,

$$C_{ij}(T) = \begin{cases} C_{ij}(293) \left(\dfrac{f(T)}{0.959} \right) & for \quad C_{33} \; and \; C_{44} \\ C_{ij}(293) \left(\dfrac{1 + f(T)}{0.959} \right) & for \; C_{11}, C_{12}, \; and \; C_{13} \end{cases} \tag{4.36}$$

where

$$f(T) = 1.0145 - 1.990 \times 10^{-4} T + 3.20 \times 10^{-8} T^2 \tag{4.37}$$

At T=293K; $C_{11} = 106 \times 10^{11}$, $C_{12} = 18 \times 10^{11}$, $C_{13} = 1.5 \times 10^{11}$, $C_{33} = 3.65 \times 10^{11}$, and $C_{44} = 0.425 \times 10^{11}$ dyn/cm^2.

Table 4-6 shows the numerical values for the elastic constants at the temperatures of interest.

Table 4-6 Elastic constants of graphite as a function of temperature

T (K)	$C_{11} \times 10^{13}$ (dyn/cm^2)	$C_{12} \times 10^{12}$ (dyn/cm^2)	$C_{13} \times 10^{11}$ (dyn/cm^2)	$C_{33} \times 10^{11}$ (dyn/cm^2)	$C_{44} \times 10^{10}$ (dyn/cm^2)
600	1.032	1.752	1.460	3.451	4.018
900	1.007	1.710	1.425	3.279	3.817
1200	0.986	1.674	1.395	3.128	3.642
1500	0.968	1.643	1.369	2.999	3.492
1800	0.952	1.617	1.347	2.893	3.368

Table 4-7 shows the calculated density, and speed of sound for the temperatures of interest. As seen, the sound velocity is a weak function of temperature. In order to calculate Γ, the heat capacity per unit volume, and the thermal conductivity are still needed. For the heat capacity, the values calculated based on the *ab initio* phonon frequency distribution were, figure 4-12. Experimental values of the thermal conductivity for pyrolytic graphite were used [110].

Table 4-7 Volume, density and sound velocity for the temperatures of interest

T (K)	ρ (gm/cm^3)	v_t x 10^6 (cm/s)	v_l x 10^6 (cm/s)	v_m x 10^6 (cm/s)
600	2.2455	1.38097	2.13701	1.51551
900	2.22621	1.37037	2.12043	1.50386
1200	2.20604	1.36192	2.10718	1.49457
1500	2.18514	1.35567	2.09736	1.48770
1800	2.16381	1.35162	2.09095	1.48324

Table 4-8 shows heat capacity, and thermal conductivity for the temperatures of interest. Thermal conductivity has two components one parallel ($K_{\|}$) and the other is perpendicular ($K_{\perp}$) to the layer planes. The $K_{\|}$ values are two orders (~300 times) of magnitudes higher than $K_{\perp}$ values. That is, $K_{\perp}$ are negligible, therefore they are not included in the calculations. Table 4-9 shows Γ values for temperatures of interest, in terms of (THz) and (eV).

Table 4-8 Graphite heat capacity and thermal conductivity for temperatures of interest

T (K)	Heat capacity (Jol/mol. K)	$C \times 10^6$ (Jol/m^3. K)	Thermal conductivity (W/m. K)
600	16.441	3.07652	892
900	20.245	3.75579	600.50
1200	22.056	4.05469	448
1500	23.011	4.19017	358.50
1800	23.565	4.24916	293

Table 4-9 The FWHM for temperatures of interest in terms of THz and eV

T(K)	Γ (THz)	Γ (eV)
600	0.26405	0.00109
900	0.47150	0.00195
1200	0.67389	0.00279
1500	0.86229	0.00357
1800	1.06350	0.00440

4.4.2 Results

In order to broaden the i^{th} bin of the phonon frequency distribution, a Lorentzian shape function is used; the area of each bin is conserved, after broadening. Let the i^{th} bin has height $\rho_i(E_i)$ and width ΔE, such that its area is $\rho_i(E_i)\Delta E$. The Lorentzian function has the form

$$L_i(E) = \frac{A_i}{\pi} \frac{\Gamma}{(E - E_i)^2 + \Gamma^2}, \tag{4.38}$$

where A_i is normalization constant. The area under the Lorentzian function in the interval [a, b] is

$$\int_a^b L_i(E) dE = \frac{A_i}{\pi} \left\{ \tan^{-1}\left(\frac{b - E_i}{\Gamma} \right) - \tan^{-1}\left(\frac{a - E_i}{\Gamma} \right) \right\}. \tag{4.39}$$

By setting the right hand side of equation (4.39) equal to the area of the i^{th} bin, A_i can be determined

$$A_i = \frac{\pi \Delta E \, \rho_i(E_i)}{\tan^{-1}\left(\frac{b - E_i}{\Gamma} \right) - \tan^{-1}\left(\frac{a - E_i}{\Gamma} \right)}. \tag{4.40}$$

To broaden the density of states, a bin width for constructing density of states equal $\Gamma/2$ was used, so each two bins have Γ width. The effect of the broadening is assumed to be one Γ to the right of the bin of interest and one Γ to the left of the bin of interest. The figures below show the shifted and shifted plus broadened phonon spectra compared to the original spectrum that neither shifted nor broadened.

4.4.2.1 Phonon Frequency Distribution

T=600 K

At T=600 K, $\varepsilon = 0.00554$, and $\Gamma = 0.00109$ eV. The bin width was set equal to 0.000545 eV, so 381 bins are used to represent the DOS at T=600 K to show the shift and broadening. In order to generate the cross section at 600 K, the shifted and broadened phonon distributions were reconstructed using 149 bins, and fitted parabolically up to the 5th point corresponding to 65 K. Figure 4-42 compares the shifted spectrum with the original spectrum. While figure 4-43 compares the shifted and broadened spectrum with the original one.

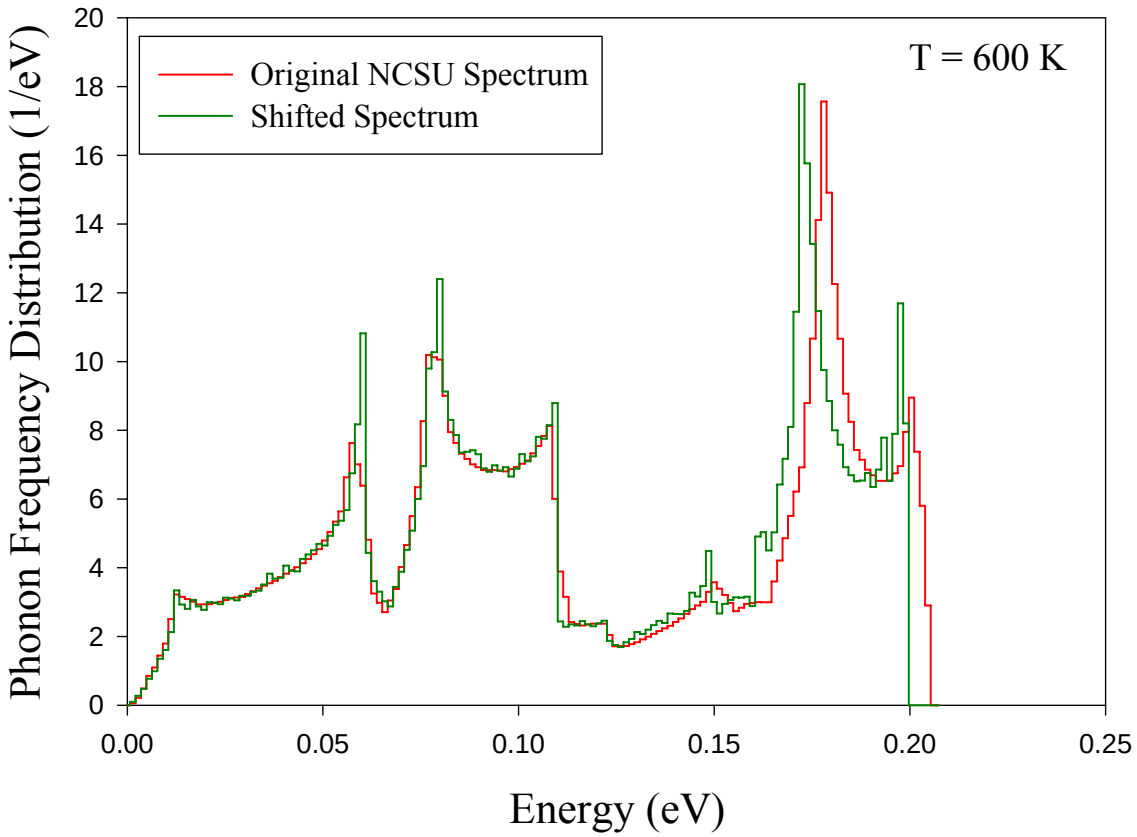

Figure 4-42 The shifted spectrum and the corresponding original NSCU spectrum at T = 600 K . Both spectra are calculated using the *ab initio* NCSU models.

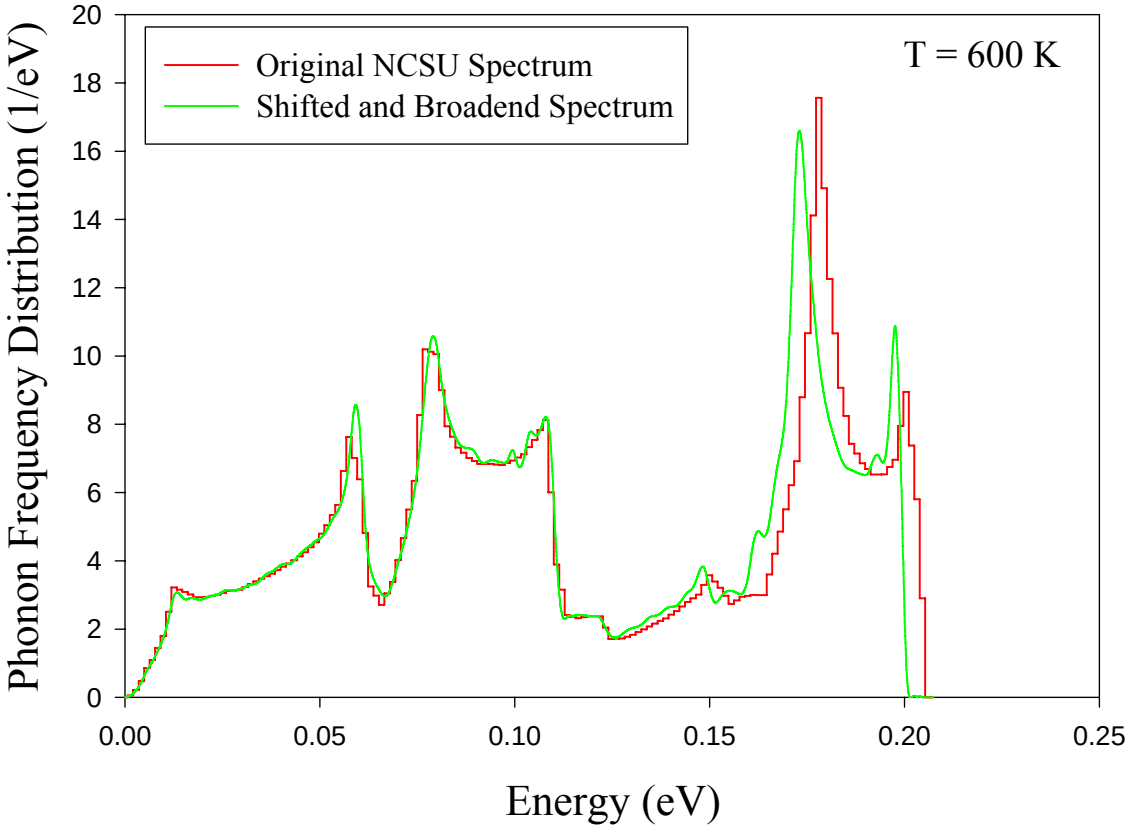

Figure 4- 43 The shifted and broadened spectra compared to the original NCSU spectrum at T=600 K. Both spectra are calculated using the *ab initio* NCSU models.

T=900 K

At T=900 K, $\varepsilon = 0.00889$, and $\Gamma = 0.00195$ eV. The bin width was set equal to 0.000975 eV, so 213 bins are used to represent the DOS at T=900 K to show the shift and broadening. In order to generate the cross section at 900 °K, the shifted and broadened phonon distribution was reconstructed using 149 bins, and fitted parabolically up to the 5th point corresponding to 65 K. Figure 4-44 compares the shifted spectrum with the original spectrum. While figure 4-45 compares the shifted and broadened spectrum with the original NCSU spectrum.

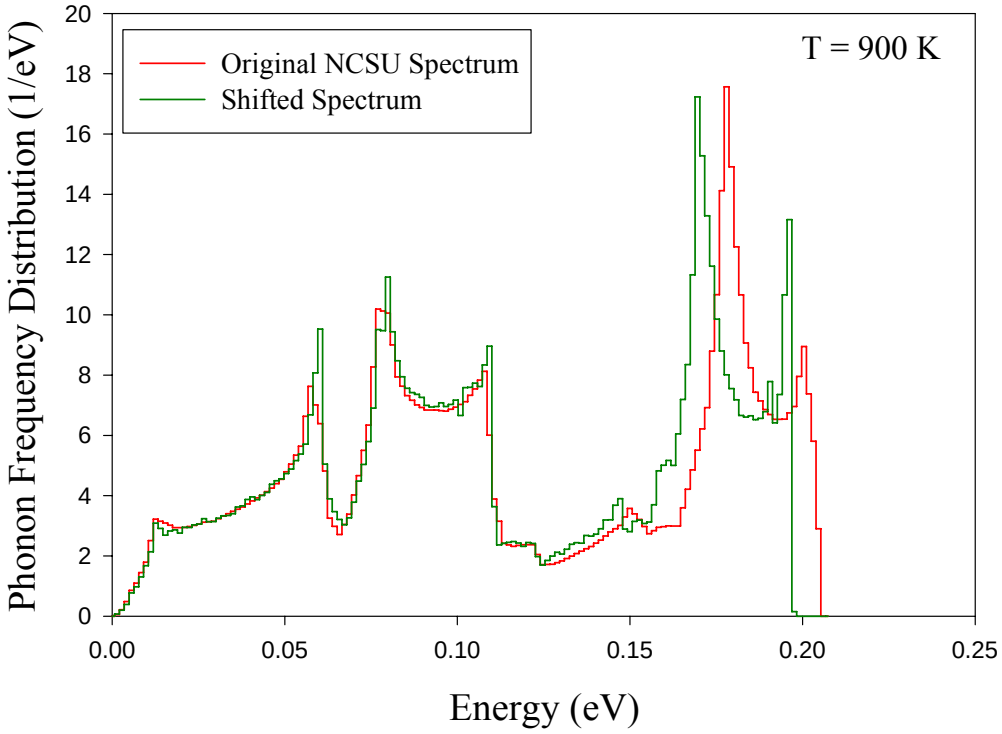

Figure 4-44 The shifted spectrum compared to the original NCSU spectrum at T=900 K. Both spectra are calculated using the *ab initio* NCSU models.

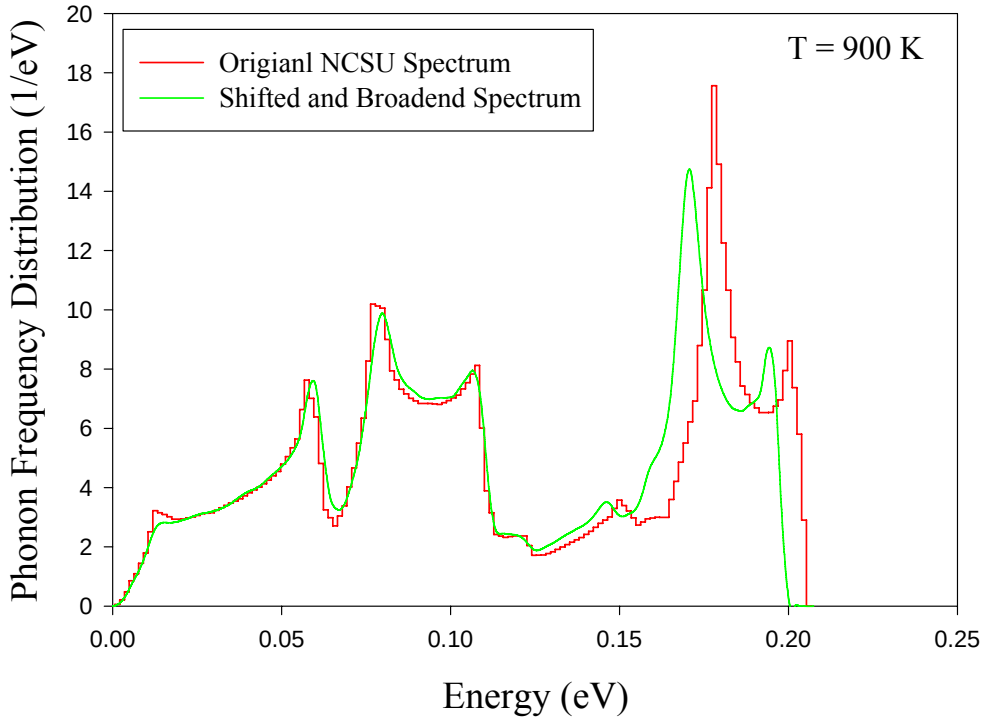

Figure 4-45 The shifted and broadened spectra compared to the original NCSU spectrum at T=900 K. Both spectra are calculated using the *ab initio* NCSU models.

T=1200 K

At T=1200 K, $\varepsilon = 0.01244$, and $\Gamma = 0.00279$ eV. The bin width was set equal to 0.001395 eV, so 149 bins are used to represents the DOS at T=1200 K to show the shift and broadening. In order to generate the cross section at 1200 K, the shifted and broadened phonon distributions was fitted parabolically up to the 5th point corresponding to 65 K. Figure 4-46 compares the shifted spectrum with the original spectrum. While figure 4-47 compares the shifted and broadened spectrum with the original NCSU spectrum.

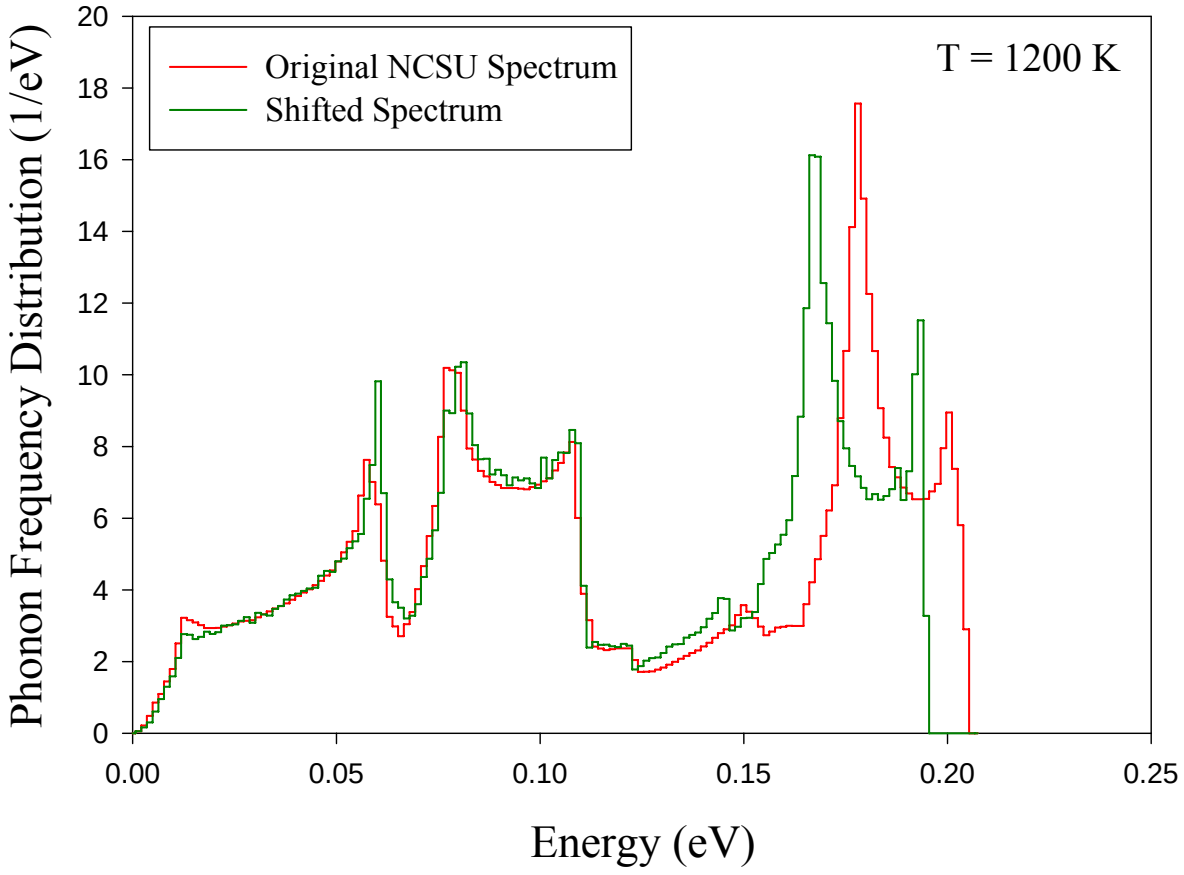

Figure 4-46 The shifted spectrum compared to the original NCSU spectrum at T=1200 K. Both spectra are calculated using the *ab initio* NCSU models.

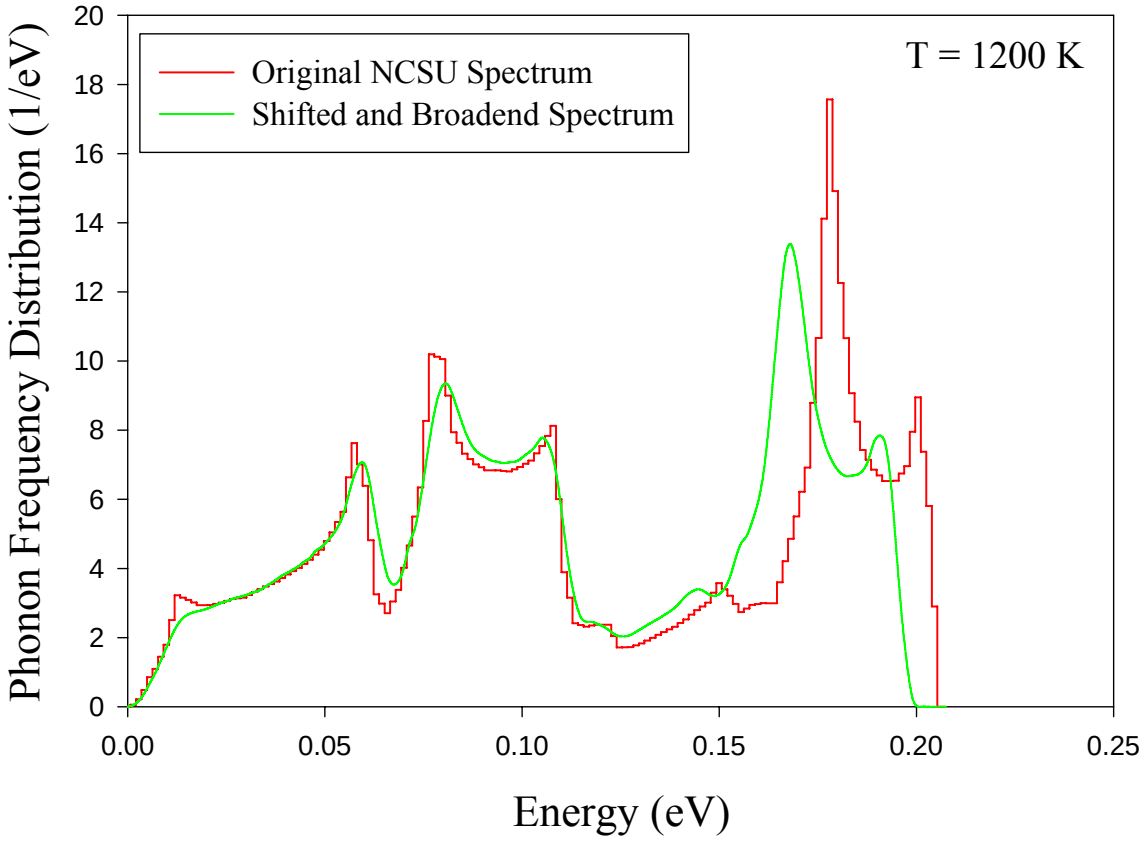

Figure 4-47 The shifted and broadened spectra compared to the original NCSU spectrum at T= 1200 K. Both spectra are calculated using the *ab initio* NCSU models.

T=1500 K

At T=1500 K, $\varepsilon = 0.01613$, and $\Gamma = 0.00357$ eV. The bin width was set equal to 0.001785 eV, so 117 bins are used to represents the DOS at T=1500 K to show the shift and broadening. In order to generate the cross section at 1500 K, the shifted and broadened phonon distributions was reconstructed using 149 bins, and fitted parabolically up to the 5th point corresponding to 65 K. Figure 4-48 compares the shifted spectrum with the original spectrum. While figure 4-49 compares the shifted and broadened spectrum with the original NCSU spectrum.

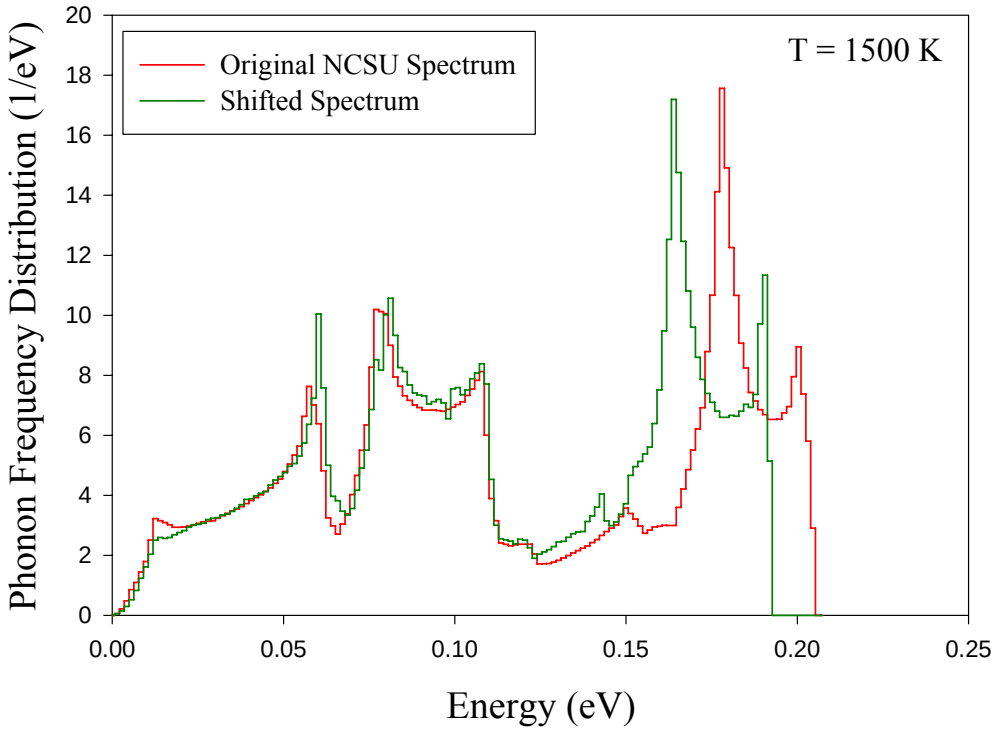

Figure 4-48 The shifted spectrum compared to the original NCSU spectrum at T=1500 K. Both spectra are calculated using the *ab initio* NCSU models.

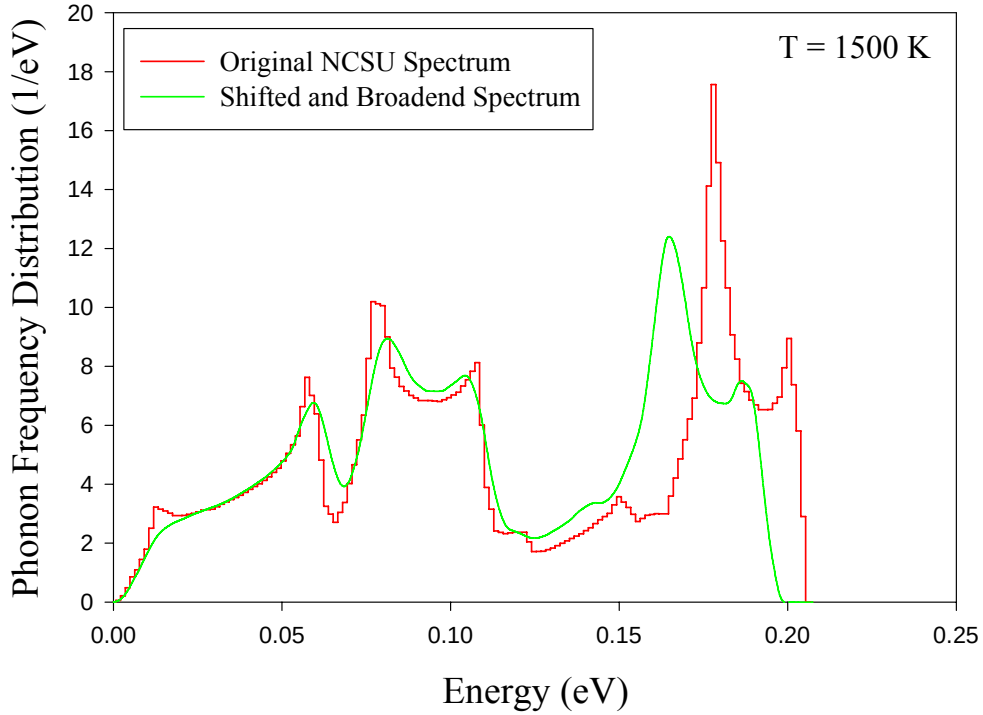

Figure 4-49 The shifted and broadened spectra compared to the original NCSU spectrum at T= 1500 K. Both spectra are calculated using the *ab initio* NCSU models.

T=1800 K

At T=1800 K, $\varepsilon = 0.01987$, and $\Gamma = 0.0044$ eV. The bin width was set equal to 0.0022 eV, so 95 bins are used to represents the DOS at T=1800 K to show the shift and broadening. In order to generate the cross section at 1800 K, the shifted and broadened phonon distribution was reconstructed using 149 bins, and fitted parabolically up to the 5th point corresponding to 65 K. Figure 4-50 compares the shifted spectrum with the original spectrum. While figure 4-51 compares the shifted and broadened spectrum with the original NCSU spectrum.

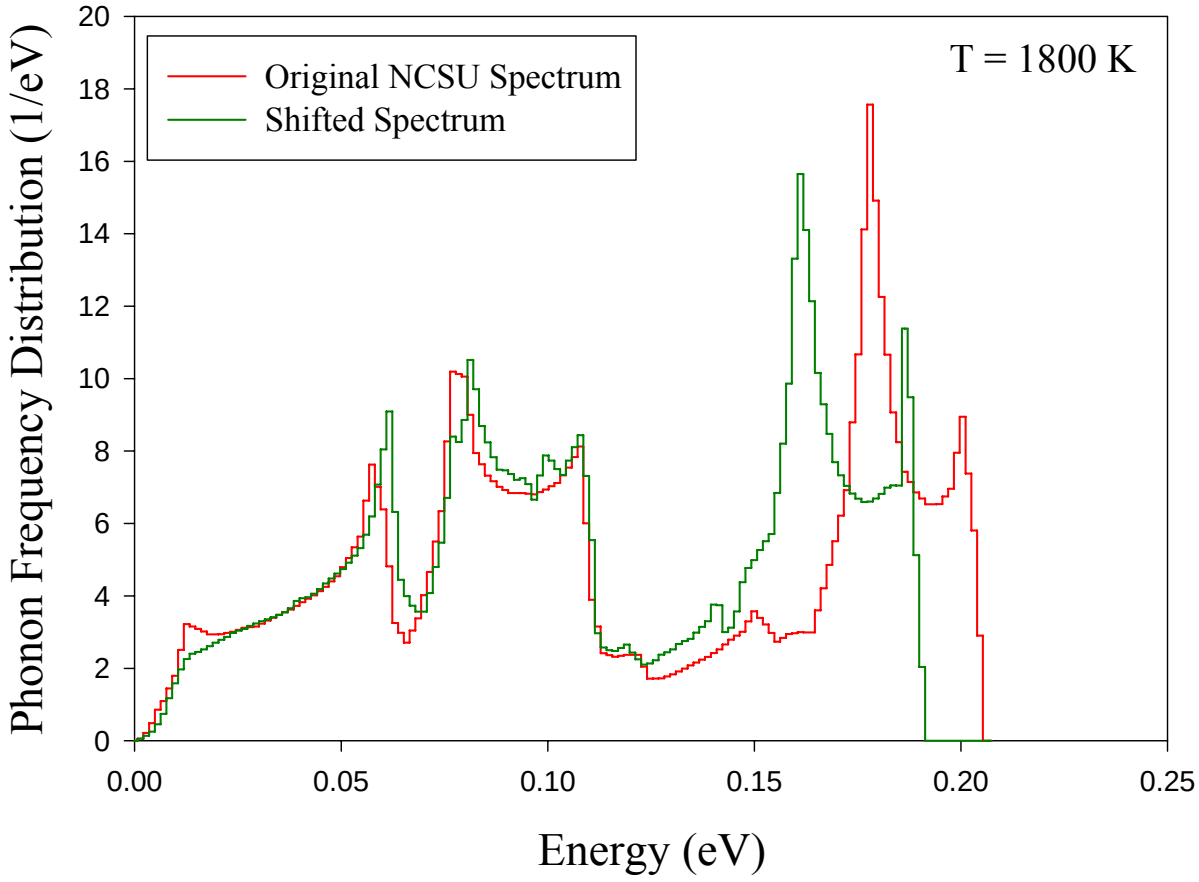

Figure 4-50 The shifted spectrum compared to the original NCSU spectrum at T= 1800 K. Both spectra are calculated using the *ab initio* NCSU models.

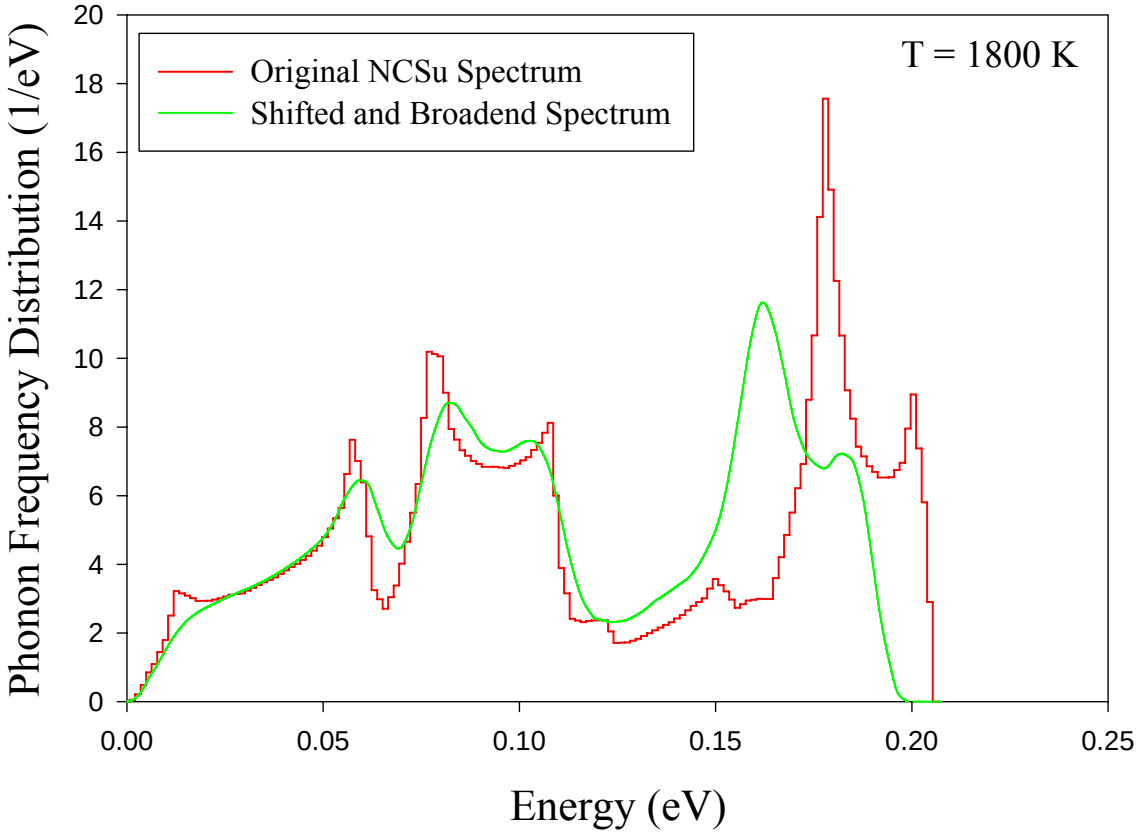

Figure 4-51 The shifted and broadened spectra compared to the original NCSU spectrum at T= 1800 K. Both spectra are calculated using the *ab initio* NCSU models.

As seen from the above figures, the shift of the frequency $\omega(\vec{q}, j)$ is proportional to $(1 - 3\varepsilon(T)\gamma(\vec{q}, j))$. Therefore, the shift is the highest at higher frequencies. To summaries, the previous figures are compared to each other, to show the progress of shift and broadening as a function of temperature. Figure 4-52 shows the results of the shifted spectra for different temperatures, while figure 4-53 shows the shifted and broadened spectra.

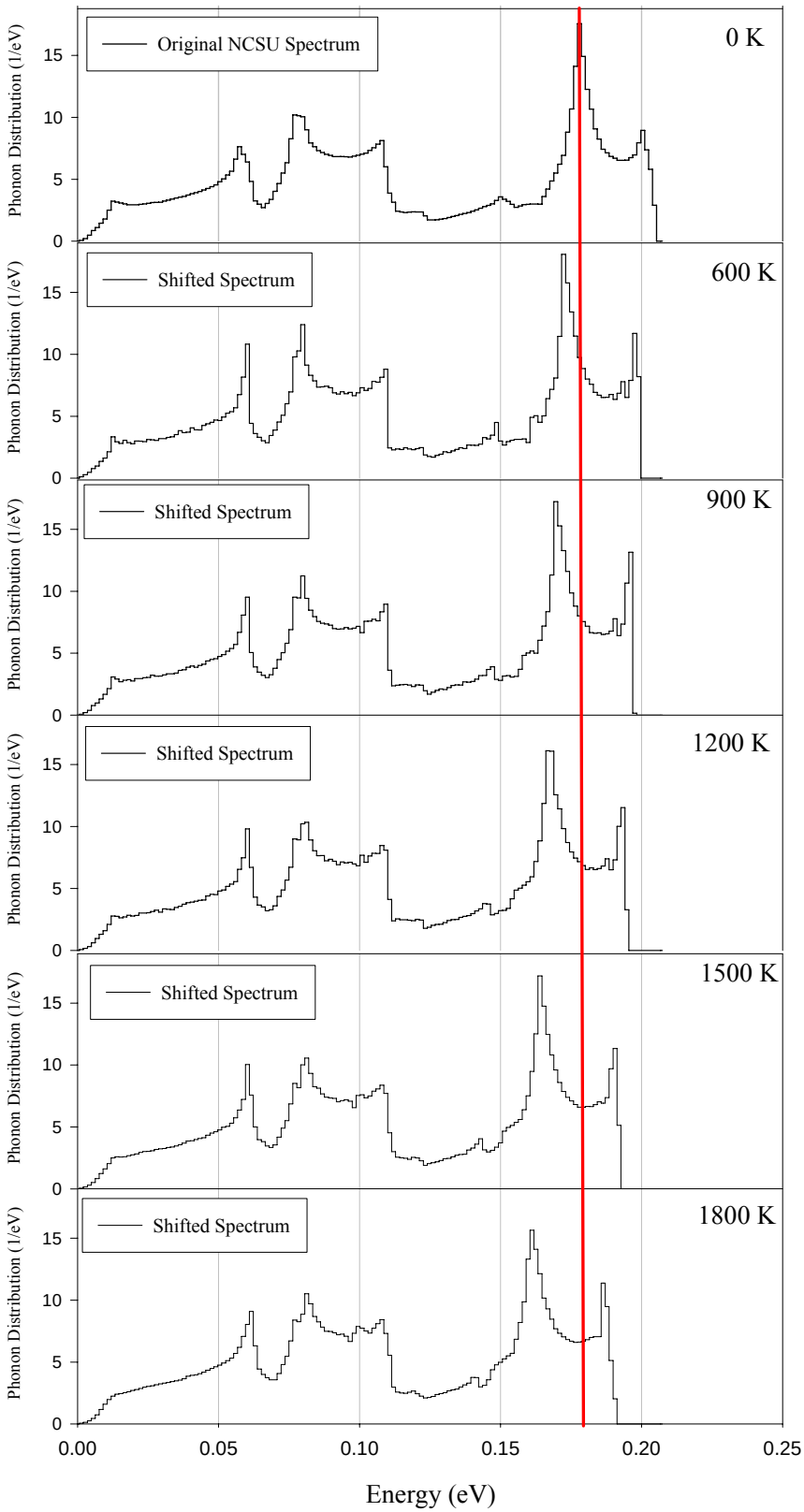

Figure 4-52 The shifted spectra at different temperatures compared to the original spectrum calculated at 0 K.

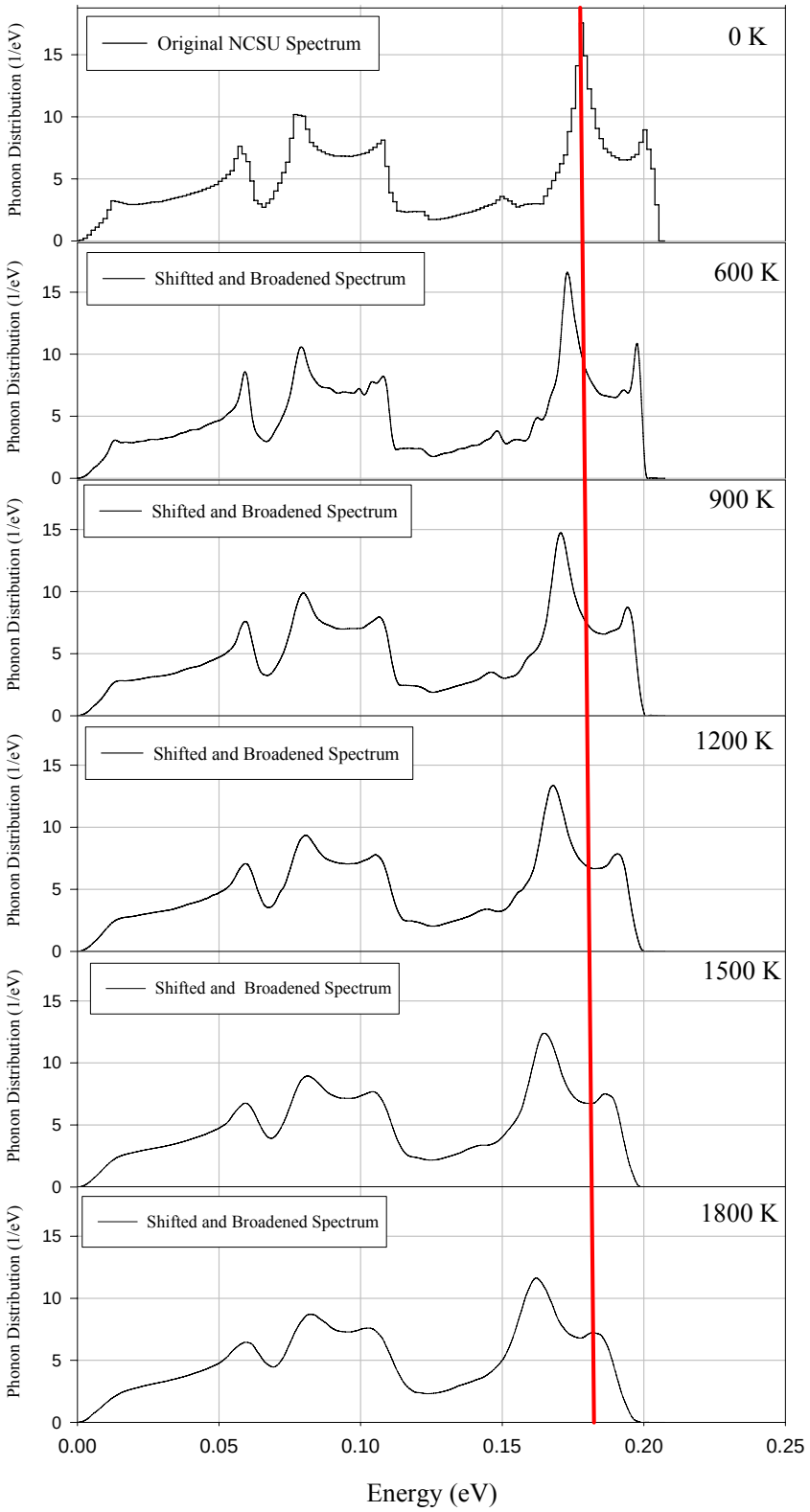

Figure 4-53 The shifted and broadened spectra at different temperatures compared to the original spectrum calculated at 0 K.

4.4.2.2 Cross Section

T=600 K

Figure 4.54 shows the cross section at T=600 K, using the shifted and broadened spectrum. The cross section is compared to the one generated by using the original spectrum. The cross section due to the original spectrum shows higher cross section that reaches a maximum difference of ~ 4% between 0.01 and 0.1 eV.

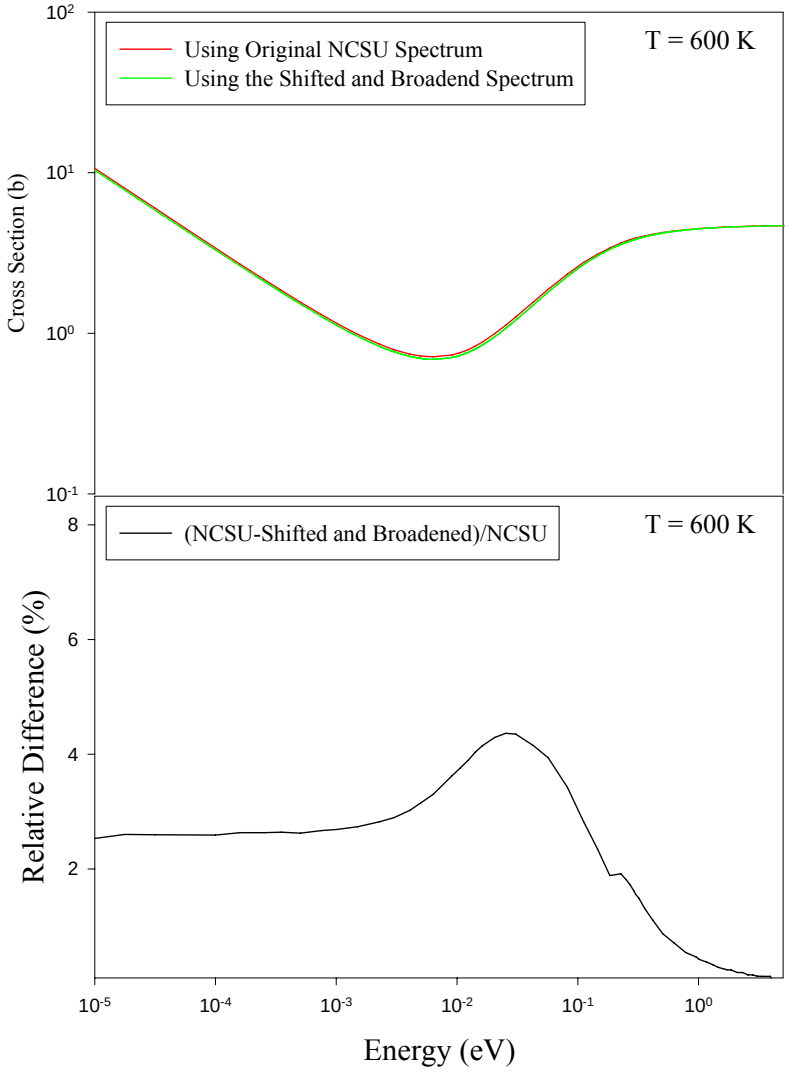

Figure 4-54 The scattering cross sections at 600 K generated by using the original NCSU, and shifted and broadened spectra (above) and the corresponding cross sections relative difference (below).

T=900 K

Figure 4-55 shows the cross section at T=900 K, using the shifted and broadened spectrum. The cross section is compared to the one generated by using the original spectrum. The cross section due to the original spectrum shows higher cross section that reaches a maximum difference of ~ 6% between 0.01 and 0.1 eV.

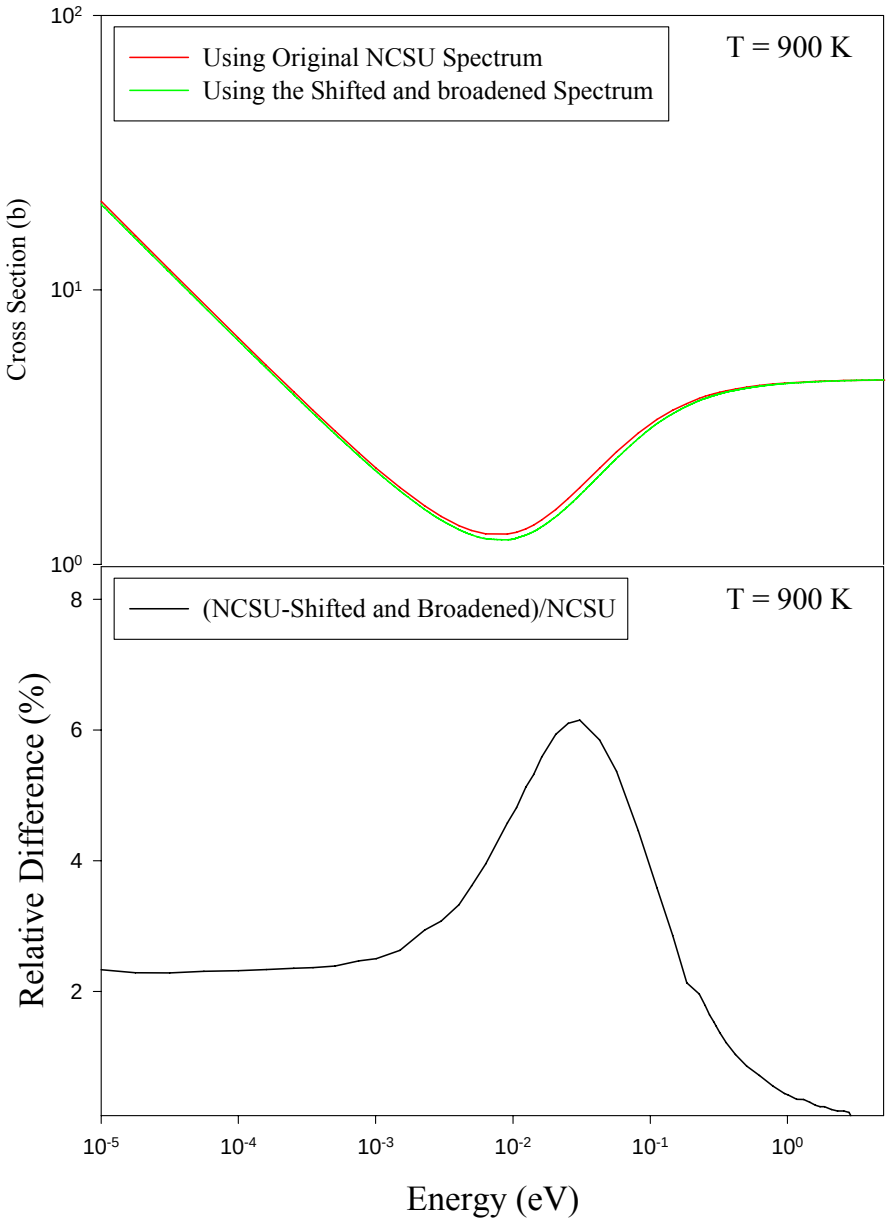

Figure 4-55 The scattering cross sections at 900 K generated by using the original NCSU, and shifted and broadened spectra (above) and the corresponding cross sections relative difference (below).

T=1200 K

Figure 4-56 shows the cross section at T=1200 K, using the shifted and broadened spectrum. The cross section is compared to the one generated by using the original spectrum. The cross section due to the original spectrum shows higher cross section that reaches a maximum difference of ~ 7% between 0.01 and 0.1 eV.

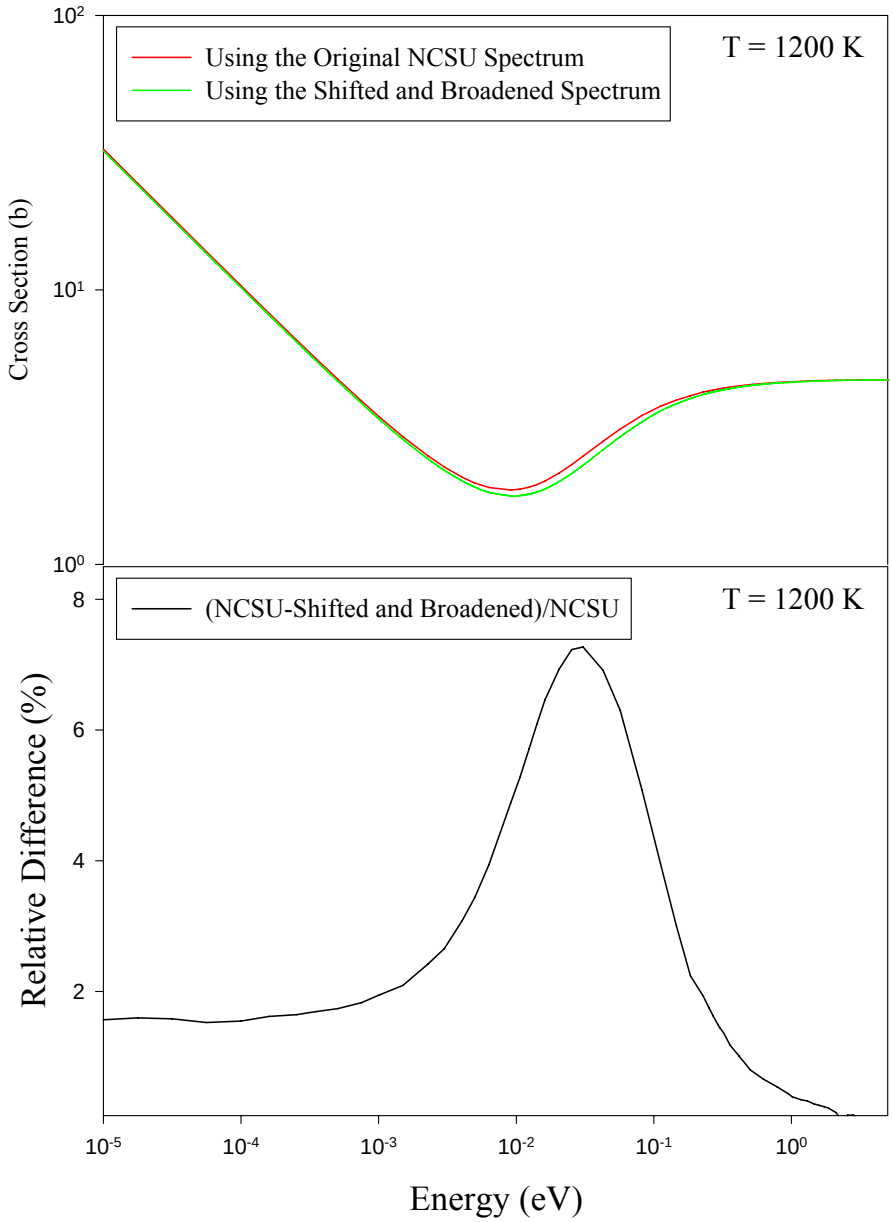

Figure 4-56 The scattering cross sections at 1200 K generated by using the original NCSU, and shifted and broadened spectra (above) and the corresponding cross sections relative difference (below).

T=1500 K

Figure 4-57 shows the cross section at T=1500 K, using the shifted and broadened spectrum. The cross section is compared to the one generated by using the original spectrum. The cross section due to the original spectrum shows higher cross section that reaches a maximum difference of ~ 7% between 0.01 and 0.1 eV.

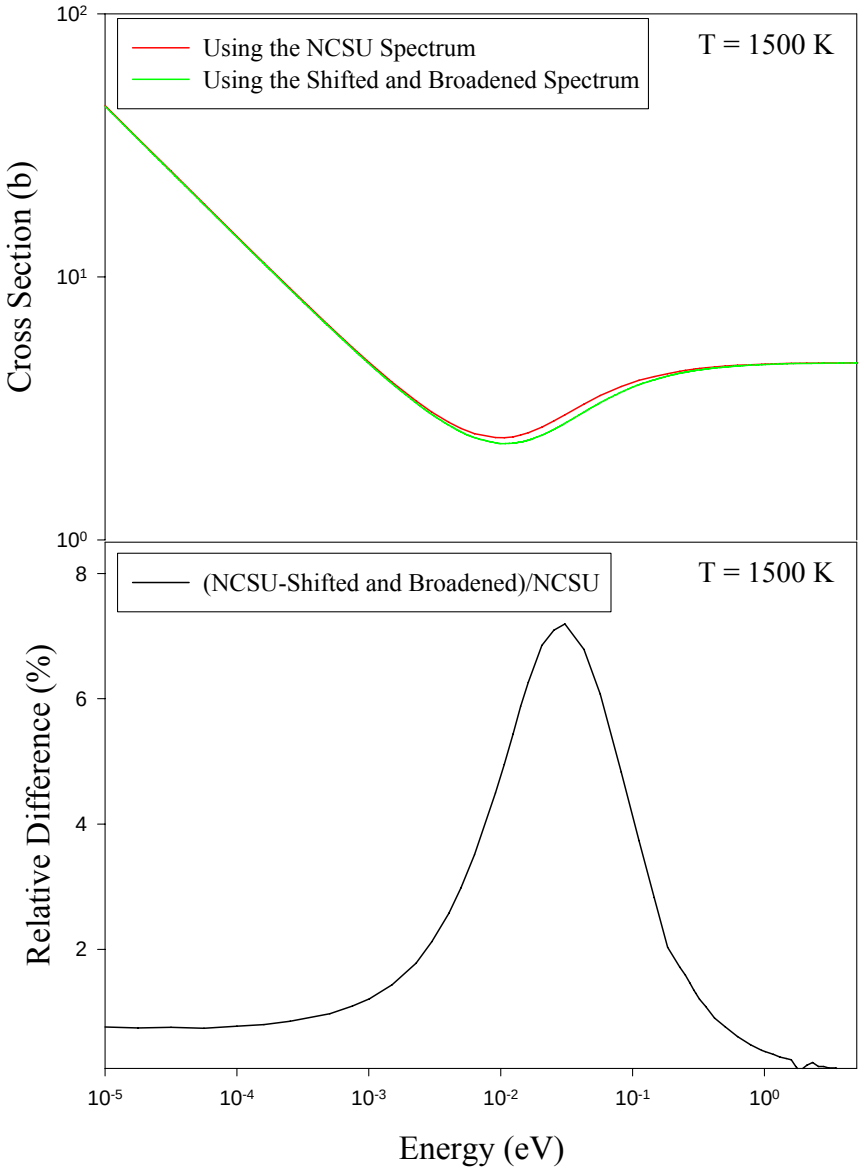

Figure 4-57 The scattering cross sections at 1500 K generated by using the original NCSU, and shifted and broadened spectra (above) and the corresponding cross sections relative difference (below).

T=1800 K

Figure 4-58 shows the cross section at T=1800 K, using the shifted and broadened spectrum. The cross section is compared to the one generated by using the original spectrum. The cross section due to the original spectrum shows higher cross section that reaches a maximum difference of ~ 7% between 0.01 and 0.1 eV.

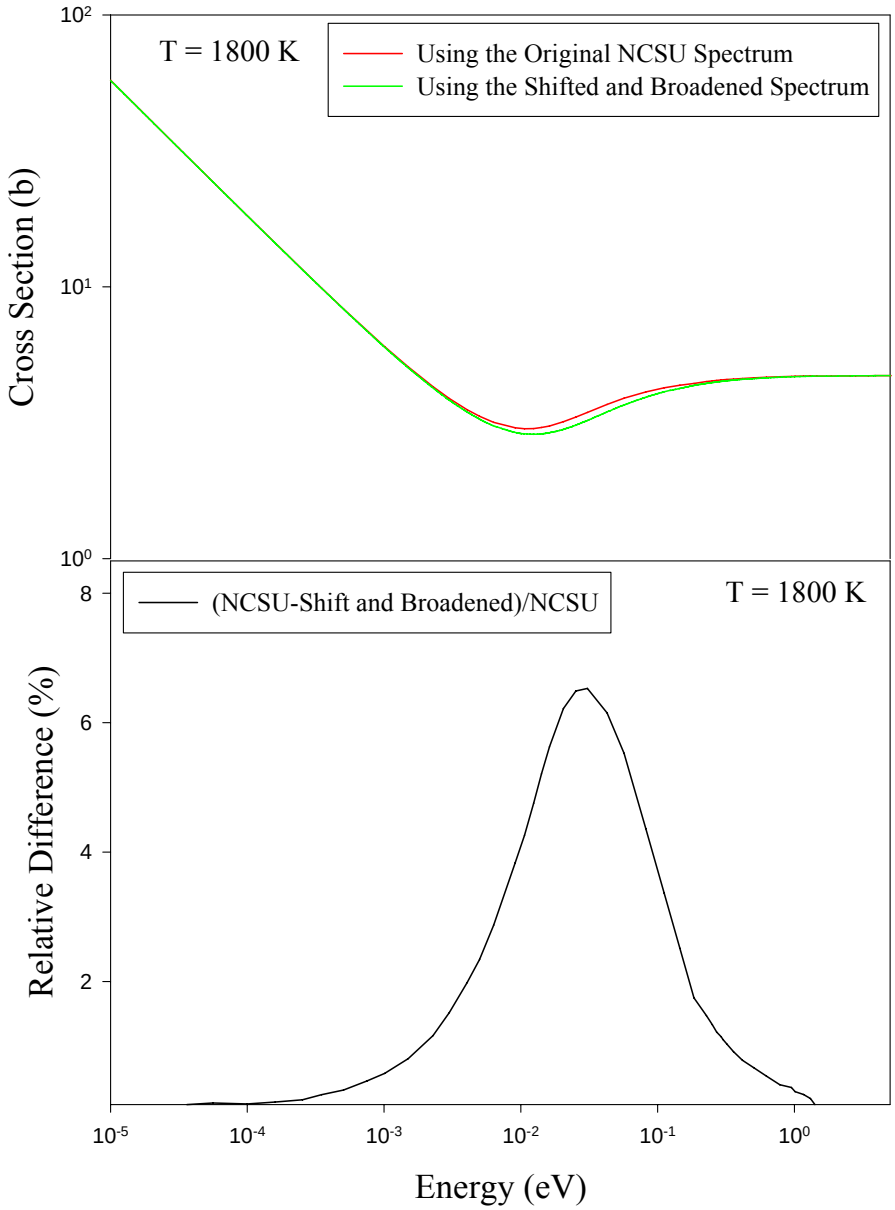

Figure 4-58 The scattering cross sections at 1800 K generated by using the original NCSU, and shifted and broadened spectra (above) and the corresponding cross section relative difference (below).

Chapter 5 Conclusions and Future Work

In this work, graphite thermal neutron scattering cross sections and complete libraries were generated as a function of temperature, and using different approaches. The first step was generating the phonon frequency distribution using the lattice dynamics direct method supercell approach and utilizing quantum mechanical electronic structure (*ab initio*) simulations. Due to the strong intraplaner covalent interactions and the weak interplaner Van der Waal interaction, a 6×6×1 supercell with 144 atoms was used to generate the phonon frequency distribution. The VASP code was used to calculate the Hellmann- Feynman forces by using the local density approximation (LDA), with the projected augmented wave (PAW) pseudopotential. The integration over the Brillouin zone was confined to a 3×3×4 k-mesh generated by the Monkhorst –Pack scheme, and a plane-wave basis set with 500 eV energy cutoff was applied. The corresponding dispersion relations and phonon frequency distribution shown in figure 5-1 exhibit excellent agreement with the experimental data, illustrating the power and utility of the *ab initio* approach.

The resulting phonon spectrum was used in the LEAPR module of the NJOY code to calculate the scattering law, whereas the module THERMR was used to generate the inelastic scattering cross section, respectively, at different temperatures. However, the examination of the results indicated persistence of the inconsistencies between calculations and measurements at neutron energies below the Bragg energy cutoff. Since the phonon frequency distribution- the only input to the formula of the scattering law built in LEAPR- was calculated accurately, this led the investigation more deeply into the scattering theory of

graphite. Therefore, the coherent one-phonon scattering law and cross section were calculated exactly. The input data required to perform such calculations was taken from *ab initio* lattice dynamics results such as the dispersion relations, polarization vectors, and mean square displacement. As a result, excellent agreement was achieved between calculated and measured scattering law, and also between the calculated inelastic scattering cross section and the measured data of pyrolytic graphite, as shown in figure 5-2.

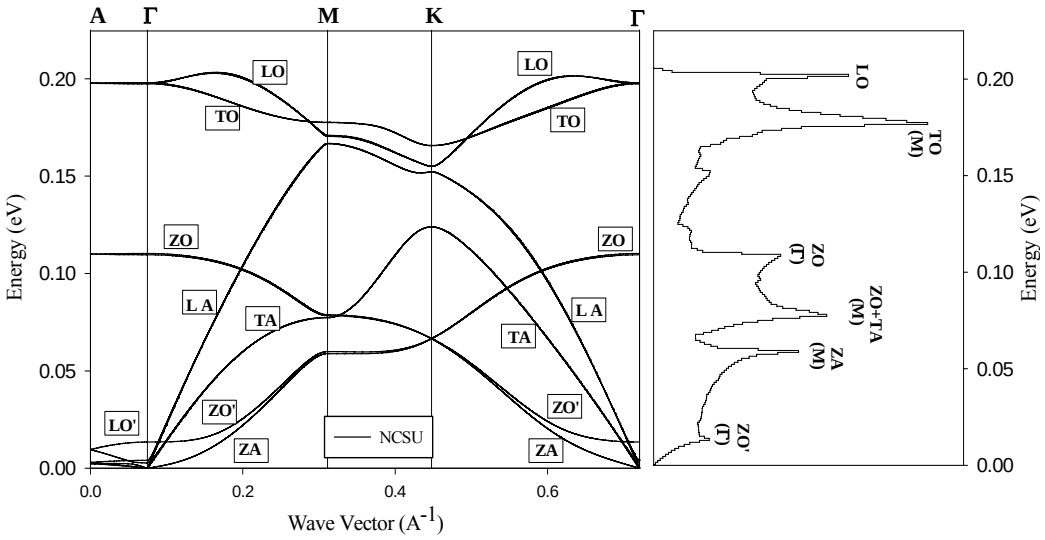

Figure 5-1The graphite dispersion relations and phonon frequency distribution.

Due to the graphite structure, a non-isotropic Debye-Waller factor was used in producing the one-phonon results, where the perpendicular mean square displacements is one order of magnitude higher than the parallel on. Furthermore, based on the mean square displacements as a function of temperature and the agreement of the one-phonon cross sections as generated using both the incoherent approximation and the self part of the coherent one-phonon cross section , the parabolic energy range for the graphite phonon frequency distribution was taken to extend to 5.60 meV (equivalent to 65 K). Such

parabolic range minimizes the pseudo-inelastic sharp peak around the zero energy transfer.

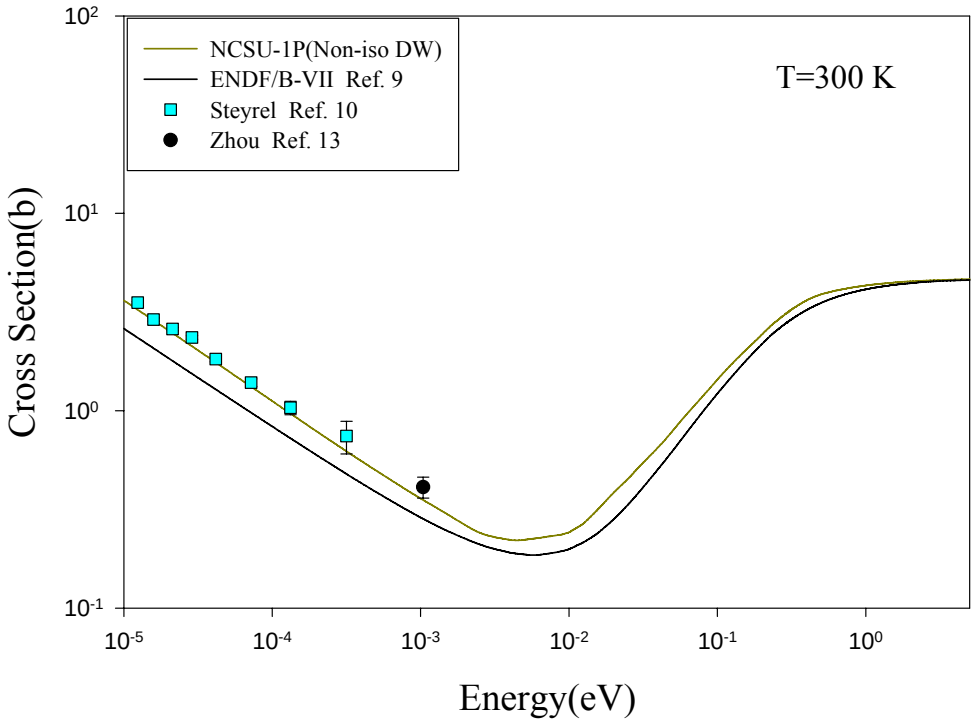

Figure 5-2 The graphite thermal neutron scattering cross section including the coherent one-phonon contribution (NCSU-1p) and the cross section in the incoherent approximation (NCSU) compared to experimental data of pyrolytic graphite at 300 K.

Finally, the effect of temperature (anharmonicity) on the phonon frequency distribution in the form of shift and broadening was studied and discussed. The shift and broadening effects were related to other physical values as a function of temperature. The energy shift was calculated as mode dependent (by calculating the Gruniesen parameter form the *ab initio* dispersion relations) and temperature dependent (by relating the thermal expansivity to the thermal expansion coefficient). A simple formula was developed for the decay constant Γ as a function of temperature such that its asymptotic behavior agrees with the asymptotic behavior of more complicated formulae. This formula is responsible for broadening effects and it relates the graphite thermal conductivity, speed of sound, and heat capacity, as a

function of temperature. The broadening effect is represented by a Lorentzian shape function. It was found that in graphite at low energies, the shift was toward the right, unlike at high energies. This is due to the negative Gruniesen parameters. The shifting and broadening were found to be two competing processes at low energies, resulting in relative differences in the calculated cross sections of less than 10% at all temperatures.

Future Work

The methodology used in this study produced accurate thermal neutron scattering cross section libraries for pyrolytic graphite, and pointed to the need for further investigation of the structure and dynamics of reactor grade graphite. Unlike pyrolytic graphite, which is a single phase material (crystalline graphite) and displays the features of perfect graphite, reactor grade graphite is a two phase material (crystalline graphite and binder carbon) (see section 4.3), therefore it is expected to have different thermal neutron scattering properties from pyrolytic graphite.

An accurate thermal neutron scattering cross section library for reactor grade graphite needs to be developed. This requires the investigation of the dynamics and volume fraction of the binder phase. However, for the crystalline phase the results of this study should be applicable.

The graphite moderator of Very High Temperature Reactors (VHTR) is expected to reach exposure levels of 10^{21} to 10^{22} n/cm^2 over the lifetime of the reactor. This exposure results in damage to the graphite structure. Therefore, it is expected that alterations in the

dynamics of the graphite lattice would have an impact on the thermal neutron scattering properties. In fact, a significant amount of literature over the past fifty years is related to the effect of neutron radiation on the mechanical, thermal, and electrical properties of graphite [108, and 111]. However, the potential effect of radiation on the neutronic behavior (i.e., thermal neutron scattering properties) of this material was rarely investigated. Recently, an investigation was initiated in this area [112]. The initial results show a potential noticeable impact on the graphite thermal neutron scattering cross sections. However, further work is needed to verify these results and accurately assess the magnitude of the expected impact.

References

1. U.S. DOE Nuclear Energy Research Advisory Committee and Generation IV International Forum, "A Technology Roadmap for Generation IV Nuclear Energy Systems: Executive Summary" March (2003).
2. DOE's Generation IV web site, http://nuclear.energy.gov/genIV/neGenIV1.html
3. INL's Generation IV web site, http://nuclear.inl.gov/gen4/
4. A. V. Nero, "A Guidbook to Nuclear Reactors," University of California Press, Berkeley, USA (1979).
5. C. L. Mantell, " Carbon and Graphite Handbook," John Wiley and Sons, Inc. USA (1968).
6. J. J. Duderstadt, and L. J. Hamilton, "Nuclear Reactor Analysis,"John Wiley and Sons, USA (1976).
7. M. B. Chadiwick, et al., Nuclear Data Sheets, **107**, 2931 (2006).
8. R. E. MacFarlane, "New Thermal Neutron Scattering Files for ENDF/B-VI, Release 2," LA-12639-MS, Los Alamos National Laboratory (1994).
9. J. A. Young and J. U. Koppel, J. Chem. Phys. **42**, 357(1965).
10. A. Steyrel, W. D. Trustedt, Z. Phyik. **267**, 379 (1974).
11. D. J. Hughes, and R. B. Schwartz, "Neutron Cross Sections-BNL325," second edition, 95 (1958).
12. P. A. Egelstaff, J. Nuclear Energy **5**, 203 (1957).
13. T. Zhou, "Benchmarking thermal neutron scattering in graphite," Ph.D. dissertation, North Carolina State University, (2006).
14. T. D. Burchell, "Carbon Materials for Advanced Technologies," Pergamon (1999).
15. R. J. Nemanich, and S. A. Solin, Phys. Rev. **20**, 392(1972).
16. H. O. Pierson, " Handbook of Carbon, Graphite, Diamond and Fullerences; Properties, Processing and Applications," Noyes Publications, New Jersey, USA(1993).
17. A. R. Ubbelohde, and F. A. Lewis, " Graphite and its Crystal Compounds," Oxford University Press, UK (1960).
18. G. I. Bell, S. Glasstone, "Nuclear Reactor Theory," Van Nostrand, New York (1970).

19. G. L. Squires, "Introduction to the theory of Thermal Neutron Scattering," Cambridge University Press, Cambridge, UK (1977).
20. W. Marshall, and S. W. Lovesy, "Theory of thermal neutron Scattering," Oxford University Press, UK (1970).
21. L. Van Hove, Phys. Rev. **95**, 249 (1954).
22. U. Koppel, J. R. Triplett, and Y. D. Naliboff, "GASKET: A Unified Code for Thermal Neutron Scattering," General atomic report GA-7417(Rev.) (1967).
23. R. E. MacFarlane, and D. W. Muir, "The NJOY Nuclear Data Processing System, Version 91," LA-12740-MS, Los Alamos National Laboratory (1994).
24. A. A. Maradudin, *et al*, "Theory of Lattice Dynamics in the Harmonic Approximation," Academic Press, New York (1971).
25. H. Bottger, "Principles of the Theory of Lattice Dynamics," Weinheim-Physik-Verlag, Germany (1983).
26. Wikipedia, The free Encyclopedia, http://en.wikipedia.org/wiki/Main_Page
27. T. Paszkiewics, "Physics of Phonons," Springer-Verlag, Heidelberg, Germany (1987).
28. K. Ohno, K. Esfarjani, and Y. Kawazoe, "Computational Materials Science, From *Ab Iinito* to Monte Carlo Methods," Springer-Verlag, Berlin, Heidelberg, Germany (1999).
29. K. Parlinski, Z. Q. Li. And Y. Kawazoe, Phys. Rev. Lett.**78**, 4063 (1997).
30. S. Wei, and M. Y. Chou, Phys. Rev. Lett. **19**, 2799 (1992).
31. K. Parlinski, "PHONON manual, version 3.11," Krakow (2002).
32. R. P. Feynman, Phys. Rev. **56**, 340 (1939).
33. W. DeSorbo, and W. W. Tayler, J. Chem. Phys. **21**, 1660 (1953).
34. J. A. Krumahansal, and K. Brooks, J. Chem. Phys. **21**, 1663 (1953).
35. K. Komatsu, J. Phys. Chem. Solids **6**, 380 (1958).
36. W. DeSorbo, and G. E. Nichols, J. Phys. Chem. Solids **6**, 352 (1958).
37. B. Dey, and S. Singh, Phys. Rev. Lett. **81A**,147 (1981).
38. C. Kittel, "Introduction to Solid State Physics," Wiley, New York, USA(1972).
39. R. Niklow, N. Wakabayashi, and H. G. Smith, Phys. Rev. B **5**, 4951 (1972).
40. R. J. Nemanich, G. Lucovky, and S. A. Splin, Solid State. Commun. **23**, 117 (1977).
41. Y. Sato, J. Phys. Soc. Japan **24**, 489 (1968).
42. F. Tuinstra, and J. L. Keoing, J. Chem. Phys. **53**, 1126 (1970).

43. G. Benedek, F. Hofmann, P. Ruggerone, G. Onida, and L. Miglio, Surf. Sci. Rep. **20**, 1(1994).
44. G. Benedek, G. Brusdeylins, C. Heimlich, J. P. Toennis, and U. Valbusa, Surf. Sci. **178**, 545 (1986).
45. D. P. Smith, G. Binning, and C. F. Quate, Appl. Phys. Lett. **49**, 1641 (1986).
46. J. L. Wilkes, R. E. Palmer, and R. F., J. Electron Spectrosc. Relat. Phenom. **44**, 355 (1987).
47. C. Oshima, T. Aizawa, R. Souda, Y. Ishizawa, and Y. Sumiyoshi, Solid State Commun. **65**, 1601 (1988).
48. S. Siebentritt, R. Pues. And K. Rieder, Phys. Rev. B **55**, 7927 (1997).
49. J. Maultzsch, S. Reich C. Thomsen, H. Requardt, and P. Ordjon,Phys. Rev. Lett. **92**, 075501-1 (2004).
50. K. Komatsu, I. Nagamiya, J. Phys. Soc. Japan **6**, 438 (1951).
51. K. Komatsu, I. Nagamiya, J. Chem. Phys. **22**, 1457 (1954).
52. A. Yoshimori, and Y. Kitano, J. Phys. Soc. Japan **2**, 325 (1956).
53. A. A. Ahmadieh, and H. A. Rafizadeh, Phys. Rev. B **7**, 4527 (1973).
54. R. Al-Jishi, and G. Dresselhaus, Phys. Rev. B **15**, 4514 (1982).
55. M. Maeda, Y. Kuramoto, and C. Horie, J. Phys. Soc. Japan **47**, 337 (1979).
56. P. A. Egelstaff, and S. J. Cocking, "Proc. Symp. Inelastic Scattering of Neutrons in Solids and liquids," International Atomic Energy Agency, Vienna (1961).
57. F .Carvalho, Nucl. Sci. Eng. **34**, 224 (1968).
58. D. I. Page, " Proc. Symp. Inelastic Scattering of Neutrons in Solids and liquids," International Atomic Energy Agency, Vienna (1968).
59. Y. Miyamoto, M. L. Cohen, and S. G. Louie, Phys. Rev. B **52**, 14971 (1995).
60. G. Kresse, J. Furthmuller, and J. Hafner, Europhys. Lett. **32**, 729 (1996).
61. P. Pavone, R. Bauer, K. Karch. O. Schutt, S. Vent, W. Windl, D. Strauch, S. Baroni, and S. de Gironcoli, Physica B **219& 220**, 439 (1996).
62. O. Dubay, and G. Kresse, Phys. Rev. B **67**, 035401-1 (2003).
63. L. Wirtz, and A. Rubio, Solid State Commun. **131**, 141(2004).
64. L. Vitali, M. A. Schneider, and K. Kern, Phys. Rev. B **69**, 121414-1 (2004).
65. A. I. Hawari, I. I. Al-Qasir, V. H. Gillette, B. W. Wehring, and T. Zhou, "*Ab initio*

generation of thermal neutron scattering cross sections," Proceedings of the PHYSOR 2004: The Physics of Fuel Cycles and Advanced Nuclear Systems - Global Developments, p 551-560 (2004).

66. S. Rols, Z. Benes, E. Anglaret, J. L. Sauvajol, P. Papanek, J. E. Fischer, G. Coddens, H. Schober, and A. J. Dianoux, Phys. Rev. Lett. 85, 5222 (2000).
67. I. I. Al-Qasir, A. I. Hawari, V. H. Gillette, B.W. Wehring, and T. Zhou, "Thermal neutron scattering cross sections of thorium hydride," Proceedings of the PHYSOR 2004: The Physics of Fuel Cycles and Advanced Nuclear Systems - Global Developments, p 527-533 (2004).
68. P. Hohenberg, W. Kohn, Phys. Rev. **136**, B864 (1964).
69. W. Kohn and L. J. Sham, Phys. Rev. **140**, A1133 (1965).
70. I. N. Levine, "Quantum Chemistry," Allyn and Bacon, Inc. Boston, USA (1974).
71. C. Payne, et al., Rev. Mod. Phys. **64**, 1045 (1992).
72. J. P. Perdew, and A. Zunger, Phys. Rev. B **23**, 5048 (1981).
73. W. Koch, and M. C. Holthausen, "A Chemists'Guide to Density Functional Theory," Wiley-VCH, Weinheim (2001).
74. J. Perdew, and K. Burke, Int. J. Quant. Chem. **57,** 309(1996).
75. D. J. Chadi, and M. L. Cohen, Phys. Rev. B **8**, 5747 (1973).
76. H. J. Monkhorst, and J. D. Pack, Phys. Rev. B **13**, 5188 (1976).
77. W. Pickett, Comput. Phys. Rep. **9**, 115 (1989).
78. D. R. Hamann, M. Schluter, and C. Chiang, Phys. Rev. Lett. **48**, 1425 (1979).
79. D. Vanderbilt, Phys. Rev. B **41**, 7892 (1990).
80. P. E. Blochl, Phys. Rev. B **50**, 17953 (1994).
81. G. Kresse, and J. Furthmuller, "Vienna *Ab-Initio* Simulation Package, VASP the Guide," Vienna (2002).
82. M. T. Yin, and M. L. Cohen, Phys. Rev. B **29**, 6996 (1984),
83. D. S. Portal, E. Artacho, and J. M. Soler, Phys. Rev. B **95**, 12678 (1999).
84. H. Girifalco, Phys. Rev. B **55**, 11202 (1997).
85. Y. Baskin, and L. Mayer, Phys. Rev. **100**, 544 (1955).
86. M. Hasegawa, and K. Nishidate, Phys. Rev. B **70**, 205431 (2004).
87. H. F. Jansen, and A. J. Freeman, Phys. Rev. B **35**, 8207 (1987).

88. Y. Wang, K. Scheerschmidt, and U. Gosele, Phys. Rev. B **61**, 12864 (2000).
89. Von A. Ludsteck, Acta Cryst. A **28**, 59 (1972).
90. W. Lynch, and H. Drickamer, J. Chem. Phys. **44**, 181(1966).
91. http://cst-www.nrl.navy.mil/~mehl/phonons/hcp/
92. L. Van Hove, Phys. Rev. **89**, 1189 (1953).
93. D. E. Parks et al., " Slow Neutron Scatering and Thermailzation," W. A. Benjamin, New York, USA (1970).
94. N. F. Wikner, G. D. Joanou, and D. E. Parks, Nucl. Sci. Eng. **19**, 108 (1964).
95. S. P. Tewari, P. Siloitia, and A. Sxena, Ind. J. Pure Appl. Phys. **41**, 707 (2003).
96. P. A. Egelstaff, and P. Schofield, Nucl. Sci. Eng. **12**, 260 (1962).
97. G. M. Borgonovi, "Coherent Scattering Law for Polycrystalline Beryllium," GA-9364 (1969).
98. H. Takahshi, Nucl. Sci. Eng. **37**, 198 (1969).
99. I. I. Al-Qasir, and A. I. Hawari, **"**Graphite Thermal Neutron Scattering Calculations Including Coherent 1-Phonon Effects," Transactions of American Nuclear Society, v **96**, (2007).
100. A. A. Maradudin, and A. E. Fein, Phys. Rev. **128**, 2589 (1962).
101. S. W. Lovesey, "Theory of Neutron Scattering From Condensed Matter," Vol. 1, Clarendon Press, Oxford, UK (1984).
102. A. Baily, and B. Yates, J. Appl. Phys. **41**, 5088 (1970).
103. W. Morgan, BNWL-SA-3838.
104. B. T. Kelly, Carbon **10**, 429 (1972).
105. T. Nihira, and T. Iwata, Phys. Rev. B **68**, 134305 (2003).
106. N. A. Abdullaev, Phys. Solid State **43**, 727 (2001).
107. N. A. Abdullaev, R. A. Suleimanov, M. A. Aldzhanov, and L. N. Alieva, Phys. Solid State **44**, 1859 (2002).
108. R. E. Nightingale, " Nuclear Graphite," Academic Press, New York, USA (1962).
109. H. Yoshizawa, K. Hirakawa, J. Phys. Soc. Jap. **43**, 793 (1997).
110. D. L. Lide, " CRC Handbook of Chemistry and Physics," 85th ed, CRC Press. FL. USA (2004-2005).
111. B. T. Kelley, "Physics of Graphite," Applied Science Publishers LTD, UK (1981).

112. A. I. Hawari, I. I. Al-Qasir, and A. M. Ougouag, Nucl. Sci. Eng.**155**, 449 (2007).

113. http://www.materialsdesign.com/

Appendix

Appendix A

A.1- Solid-Type Scatterers Scattering Law in the Incoherent Approximation

Starting from equation (2.55), setting $S_d(\vec{\kappa},\omega)=0$, replacing $\sigma_{coh}+\sigma_{incoh}$ by σ_b and $\frac{k'}{k}$ by $\sqrt{\frac{E'}{E}}$ we get

$$\frac{d\sigma}{d\Omega\, dE'}=\frac{\sigma_b}{4\pi}\sqrt{\frac{E'}{E}}S_s(\vec{\kappa},\omega) \tag{A.1}$$

where

$$S_s(\vec{\kappa},\omega)=\frac{1}{2\pi\hbar}\int_{-\infty}^{\infty}I_{incoh}(\vec{\kappa},t)e^{-i\omega t}dt \tag{A.2}$$

where under the assumptions mentioned in section 2.5 the incoherent intermediate function $I_{incoh}(\vec{\kappa},t)$ is given by

$$I_{incoh}(\vec{\kappa},t)=\exp\left[\frac{\hbar\kappa^2}{2A}\{\gamma(t)-\gamma(0)\}\right] \tag{A.3}$$

where

$$\gamma(t)=\int_0^{\infty}\left\{\coth\frac{\hbar\omega}{2k_BT}\cos\omega t+i\sin\omega t\right\}\frac{\rho(\omega)}{\omega}d\omega \tag{A.4}$$

and

$$\gamma(t)-\gamma(0)=\int_0^{\infty}\left\{\coth\frac{\hbar\omega}{2k_BT}(\cos\omega t-1)+i\sin\omega t\right\}\frac{\rho(\omega)}{\omega}d\omega \tag{A.5}$$

The phonon frequency distribution is an even function of ω, therefore, the integral on equation (A.5) can be extended from $-\infty$ to ∞

$$\gamma(t)-\gamma(0)=\int_{-\infty}^{\infty}\frac{\rho(\omega)}{2\omega}\frac{e^{\frac{-\hbar\omega}{2k_BT}}}{\sinh(\hbar\omega/2k_BT)}\left(e^{-i\omega t}-1\right)d\omega \tag{A.6}$$

So by combining equations (A.6), (A.3), (A.2) and (A.1) we get

$$\frac{d^2\sigma}{d\Omega dE'}=\frac{\sigma_b}{4\pi}\sqrt{\frac{E'}{E}}\frac{1}{2\pi\hbar}\int_{-\infty}^{\infty}e^{-i\omega t}\exp\left[\frac{\hbar\kappa^2}{2A}\int_{-\infty}^{\infty}\frac{\rho(\omega)}{2\omega}\frac{e^{\frac{-\hbar\omega}{2k_BT}}}{\sinh(\hbar\omega/2k_BT)}(e^{-i\omega t}-1)\,d\omega\right]dt \tag{A.7}$$

Utilizing equations (2.57 and 2.58) and defining the dimensionless parameter $\hat{t}=\frac{k_BT}{\hbar}t$, the following form is obtained

$$\frac{d^2\sigma}{d\Omega dE'}=\frac{\sigma_b}{4\pi}\sqrt{\frac{E'}{E}}\frac{1}{KT}\frac{1}{2\pi}\int_{-\infty}^{\infty}e^{i\beta\hat{t}}\exp\left[\alpha\int_{-\infty}^{\infty}\frac{\rho(\beta)}{2\beta}\frac{e^{-\beta/2}}{\sinh(\beta/2)}(e^{-i\beta\hat{t}}-1)\,d\beta\right]d\hat{t} \tag{A.8}$$

The above equation is the LEAPR fundamental equation to calculate the double differential scattering cross section for solid-type oscillators. The asymmetric scattering law $\mathsf{S}(\alpha,\beta)$ is given by

$$\mathsf{S}(\alpha,\beta)=\frac{1}{2\pi}\int_{-\infty}^{\infty}e^{i\beta\hat{t}}\exp\left[\alpha\int_{-\infty}^{\infty}\frac{\rho(\beta)}{2\beta}\frac{e^{-\beta/2}}{\sinh(\beta/2)}(e^{-i\beta\hat{t}}-1)\,d\beta\right]d\hat{t} \tag{A.9}$$

Where the relation between the scattering law and the asymmetric scattering law is given by

$$S(\alpha,\beta)=e^{\beta/2}\ \ \mathsf{S}(\alpha,\beta) \tag{A.10}$$

The Debye-Waller coefficient λ for a Bravais cubic unit cell is is defined as

$$\lambda=\int_{-\infty}^{\infty}\frac{\rho(\beta)\,e^{-\beta/2}}{2\beta\sinh(\beta/2)}d\beta \tag{A.11}$$

$\mathsf{S}(\alpha,\beta)$ can be rewritten as

$$S(\alpha,\beta)=\frac{1}{2\pi}e^{-\alpha\lambda}\int_{-\infty}^{\infty}e^{i\beta\hat{t}}\exp\left[\alpha\int_{-\infty}^{\infty}\frac{\rho(\beta')}{2\beta'}\frac{e^{-\beta'/2}}{\sinh(\beta'/2)}e^{-i\beta\hat{t}}\,d\beta'\right]d\hat{t} \tag{A.12}$$

$e^{-\alpha\lambda}$ is called the Debye-Waller factor, as we see later it is equivalent to e^{-2W}

A.2- One Phonon Cross Section in the Incoherent Approximation

Let us expand the exponential integrand in equation (A.12) as power series, then

$$S(\alpha,\beta)=\frac{1}{2\pi}e^{-\alpha\lambda}\sum_{n=0}\frac{1}{n!}\int_{-\infty}^{\infty}e^{i\beta\hat{t}}\left[\alpha\int_{-\infty}^{\infty}\frac{\rho(\beta')}{2\beta'}\frac{e^{-\beta'/2}}{\sinh(\beta'/2)}e^{-i\beta\hat{t}}\,d\beta'\right]^{n}d\hat{t} \tag{A.13}$$

Consider the term corresponds to n=1

$$S^{1}(\alpha,\beta)=\alpha\,e^{-\alpha\lambda}\,\frac{1}{2\pi}\int_{-\infty}^{\infty}e^{i(\beta-\beta')\hat{t}}\left[\int_{-\infty}^{\infty}\frac{\rho(\beta')}{2\beta'}\frac{e^{-\beta'/2}}{\sinh(\beta'/2)}d\beta'\right]d\hat{t} \tag{A.14}$$

But

$$\frac{1}{2\pi}\int_{-\infty}^{\infty}e^{i(\beta-\beta')\hat{t}}\,d\hat{t}=\delta(\beta-\beta') \tag{A.15}$$

so

$$S^{1}(\alpha,\beta)=\alpha\,e^{-\alpha\lambda}\,\frac{\rho(\beta)}{2\beta}\frac{e^{-\beta/2}}{\sinh(\beta/2)} \tag{A.16}$$

And the one phonon double differential scattering cross section in the incoherent approximation is

$$\left.\frac{d^{2}\sigma}{d\Omega dE'}\right|_{1}=\frac{\sigma_{b}}{4\pi}\sqrt{\frac{E'}{E}}\,\frac{1}{KT}\,\alpha\,e^{-\alpha\lambda}\,\frac{\rho(\beta)}{2\beta}\frac{e^{-\beta/2}}{\sinh(\beta/2)} \tag{A.17}$$

A.3- A Step by Step Derivation of the One Phonon Scattering Cross Section in the Incoherent Approximation Starting From the Coherent One Phonon Equation

Let us start from equation (2.83)-the exact coherent one-phonon double differential scattering cross section equation- where the subscript is replaced by $\vec{q}j$

$$\left.\frac{d^2\sigma}{d\Omega dE'}\right|_{coh(1ph)} = \frac{\sigma_{coh}}{4\pi}\sqrt{\frac{E'}{E}}\frac{1}{4\pi M}\frac{1}{N}\sum_{\vec{q}\,j}\frac{1}{\omega_{\vec{q}j}}\left|\sum_d e^{-W_d}\left(\vec{\kappa}\cdot\vec{e}_{d\vec{q}j}\right)e^{i\vec{\kappa}\cdot\vec{d}}\right|^2 \times \sum_l e^{i\vec{\kappa}\cdot\vec{l}}\int_{-\infty}^{\infty}e^{-i\omega t}\left\{e^{-i(\vec{q}\cdot\vec{l}-\omega_{qj}t)}\left\langle n_{\vec{q}j}+1\right\rangle + e^{i(\vec{q}\cdot\vec{l}-\omega_{qj}t)}\left\langle n_{\vec{q}j}\right\rangle\right\}dt \tag{A.18}$$

The difference between the coherent and incoherent scattering cross section is the momentum conservation, so let us first relax the momentum constraint. That is

$$\sum_l e^{i(\vec{\kappa}\pm\vec{q})\cdot\vec{l}} = \frac{(2\pi)^3}{V}\sum_{\vec{\tau}}\delta\left(\vec{\kappa}\pm\vec{q}-\vec{\tau}\right) \tag{A.19}$$

and

$$\sum_{\vec{q}\,\vec{\tau}}(...) = \frac{NV}{(2\pi)^3}\int(...)d\vec{\kappa}$$

set $\vec{\kappa}_+ = \vec{\kappa}_- = \vec{\kappa}$, where $\kappa_+ = \vec{q}+\vec{\tau}$ and $\kappa_- = \vec{q}-\vec{\tau}$, we get

$$\left.\frac{d^2\sigma}{d\Omega dE'}\right|_{(1ph)} = \frac{\sigma_{coh}}{4\pi}\sqrt{\frac{E'}{E}}\frac{1}{4\pi M}\sum_{j\vec{\kappa}}\frac{1}{\omega_{\vec{q}j}}\left\{\left|\sum_d e^{-W_d}\left(\vec{\kappa}\cdot\vec{e}_{d\vec{q}j}\right)e^{i\vec{\kappa}\cdot\vec{d}}\right|^2\int_{-\infty}^{\infty}e^{i\omega_{qj}t}\left\langle n_{\vec{q}j}+1\right\rangle + \left|\sum_d e^{-W_d}\left(\vec{\kappa}\cdot\vec{e}_{d\vec{q}j}\right)e^{i\vec{\kappa}\cdot\vec{d}}\right|^2\int_{-\infty}^{\infty}e^{-i\omega_{qj}t}\left\langle n_{\vec{q}j}\right\rangle\right\}e^{-i\omega t}dt \tag{A.20}$$

this equation is equivalent to the one phonon incoherent double differential scattering cross section, therefore, the subscript $coh(1ph)$ was replaced by $(1ph)$ for clarity. Next, to assume we have one atom per unit cell, in this case $e^{-W_d}\to e^{-W}$, $e^{i\vec{\kappa}\cdot\vec{d}}=1$, and $\vec{e}_{dqj}\to\vec{e}_{qj}$, thus,

$$\left.\frac{d^2\sigma}{d\Omega dE'}\right|_{(1ph)} = \frac{\sigma_{coh}}{4\pi}\sqrt{\frac{E'}{E}}\frac{1}{4\pi M}e^{-2W}\sum_{j\vec{\kappa}}\frac{1}{\omega_{\vec{q}j}}\left\{\left|\left(\vec{\kappa}\cdot\vec{e}_{\vec{q}j}\right)\right|^2\int_{-\infty}^{\infty}e^{i\omega_{qj}t}\left\langle n_{\vec{q}j}+1\right\rangle + \left|\left(\vec{\kappa}\cdot\vec{e}_{\vec{q}j}\right)\right|^2\int_{-\infty}^{\infty}e^{-i\omega_{qj}t}\left\langle n_{\vec{q}j}\right\rangle\right\}e^{-i\omega t}dt \tag{A.21}$$

For cubic crystal, the mean value of $\left(\vec{\kappa}\cdot\vec{e}_{qj}\right)^2$ is $\kappa^2/3$,

$$\left.\frac{d^2\sigma}{d\Omega dE'}\right|_{(1ph)} = \frac{\sigma_{coh}}{4\pi}\sqrt{\frac{E'}{E}}\frac{1}{4\pi M}\frac{\kappa^2}{3}e^{-2W}\sum_{j}\frac{1}{\omega_{\vec{q}j}}\int_{-\infty}^{\infty}\left\{e^{i\omega_{\vec{q}j}t}\left\langle n_{\vec{q}j}+1\right\rangle + e^{-i\omega_{\vec{q}j}t}\left\langle n_{\vec{q}j}\right\rangle\right\}e^{-i\omega t}dt \tag{A.22}$$

Next, to replace the sum by an integral over ω, since

$$\sum_{\vec{q}j}\frac{f(\omega_{qj})}{\omega_{qj}} = 3\int_0^{\infty}\frac{f(\omega')\rho(\omega')}{\omega'}d\omega' \tag{A.23}$$

So equation (A.22) becomes

$$\left.\frac{d^2\sigma}{d\Omega dE'}\right|_{(1ph)} = \frac{\sigma_{coh}}{4\pi}\sqrt{\frac{E'}{E}}\frac{1}{4\pi M}\kappa^2e^{-2W}\int_0^{\infty}\frac{\rho(\omega')}{\omega'}\int_{-\infty}^{\infty}\left\{e^{i\omega' t}\left\langle n'+1\right\rangle + e^{-i\omega' t}\left\langle n'\right\rangle\right\}e^{-i\omega t}dtd\omega' \tag{A.24}$$

but

$$e^{i\omega' t}\left\langle n'+1\right\rangle + e^{-i\omega' t}\left\langle n'\right\rangle = \coth\frac{\hbar\omega'}{2KT}\cos\omega' t + i\sin\omega' t \tag{A.25}$$

So equation (A.24) becomes

$$\left.\frac{d^2\sigma}{d\Omega dE'}\right|_{(1ph)} = \frac{\sigma_{coh}}{4\pi}\sqrt{\frac{E'}{E}}\frac{\kappa^2}{4\pi M}e^{-2W}\int_{-\infty}^{\infty}dt\int_0^{\infty}\left(\frac{\rho(\omega')}{\omega'}\coth\frac{\hbar\omega'}{2KT}\cos\omega' t + i\sin\omega' t\right)e^{-i\omega t}d\omega' \tag{A.26}$$

but

$$\int_0^{\infty}\left(\frac{\rho(\omega')}{\omega'}\coth\frac{\hbar\omega'}{2KT}\cos\omega' t + i\sin\omega' t\right)d\omega' = \int_{-\infty}^{\infty}\frac{\rho(\omega')}{2\omega'}\frac{e^{-\hbar\omega'/2KT}}{\sinh(\hbar\omega'/2KT)}e^{-i\omega' t}d\omega' \tag{A.27}$$

so equation (A.26) becomes

$$\left.\frac{d^2\sigma}{d\Omega dE'}\right|_{(1ph)} = \frac{\sigma_{coh}}{4\pi}\sqrt{\frac{E'}{E}}\frac{1}{4\pi M}\kappa^2e^{-2W}\int_{-\infty}^{\infty}dt\int_{-\infty}^{\infty}\frac{\rho(\omega')}{2\omega'}\frac{e^{-\hbar\omega'/2KT}}{\sinh(\hbar\omega'/2KT)}e^{-i\omega' t}e^{-i\omega t}d\omega' \tag{A.28}$$

but

$$\frac{1}{2\pi}\int_{-\infty}^{\infty} e^{-i(\omega+\omega')\hat{t}}\, d\hat{t} = \delta(\omega+\omega') \tag{A.29}$$

so

$$\left.\frac{d^2\sigma}{d\Omega dE'}\right|_{(1ph)} = \frac{\sigma_{coh}}{4\pi}\sqrt{\frac{E'}{E}}\frac{1}{2M}\kappa^2 e^{-2W}\frac{\rho(\omega)}{2\omega}\frac{e^{\hbar\omega/2KT}}{\sinh(\hbar\omega/2KT)} \tag{A.30}$$

Rewrite the above equation in terms of β rather than ω, we get

$$\left.\frac{d^2\sigma}{d\Omega dE'}\right|_{(1ph)} = \frac{\sigma_{coh}}{4\pi}\sqrt{\frac{E'}{E}}\frac{1}{KT}\frac{\hbar^2\kappa^2}{2MKT}e^{-2W}\frac{\rho(\beta)}{2\beta}\frac{e^{-\beta/2}}{\sinh(\beta/2)} \tag{A.31}$$

but $\frac{\hbar^2\kappa^2}{2MKT} = \alpha$, so equation (A.31) is similar to equation (A.17), where 2W = $\alpha\lambda$

Appendix B

B.1- VASP Input

As mentioned in section 3.2.10, VASP (Vienna *Ab initio* Simulation Package) is used to optimize the lattice parameters of the graphite unit cell, and to calculate Hellmann-Feynman forces. The following discussion pertains to the graphical interface of VASP supported by MedeA software [113]. Figure B1-1 shows the VASP graphical interface. As seen from the figure below, it consists of panels; the panels that are relevant to this work (Calculation, Potentials, SCF, advanced/Restart, and Preview input) will be discussed.

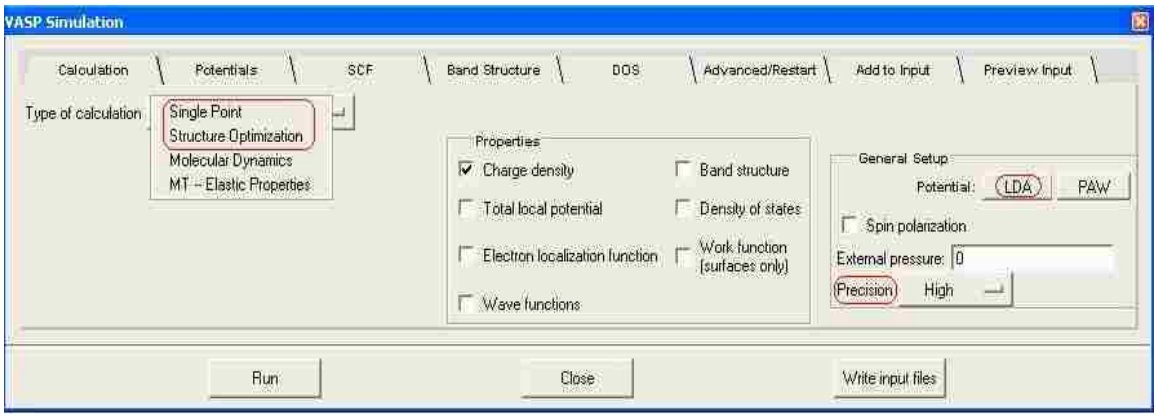

Figure B1- 1 The VASP interface supported by MedeA software.

a) Calculation

VASP offers four types of calculations, as shown in the figure above. The Single Point option is used to perform an electronic structure calculation on the geometry of interest. So for Hellmann-Feynman forces calculation, this option should be used. The other important option is structure optimization, for relaxing the atomic positions and optimizing the lattice parameters of the structure of interest at 0 K. Also shown on the right side of the panel is the type of the Density Functional Theory (DFT) to be chosen, namely the Local Density

Approximation (LDA) or the Generalized Gradient Approximation (GGA). The Precision option has three choices that influence the accuracy of calculations- High, Medium, and Low.

b) Potentials

This panel allows the user to choose the pseudopotential for the individual atoms used in the model. The potential panel, as shown in figureB1-2, allows the use of either the Projected Augmented Wave (PAW) or the Ultra Soft (US) pseudopotential.

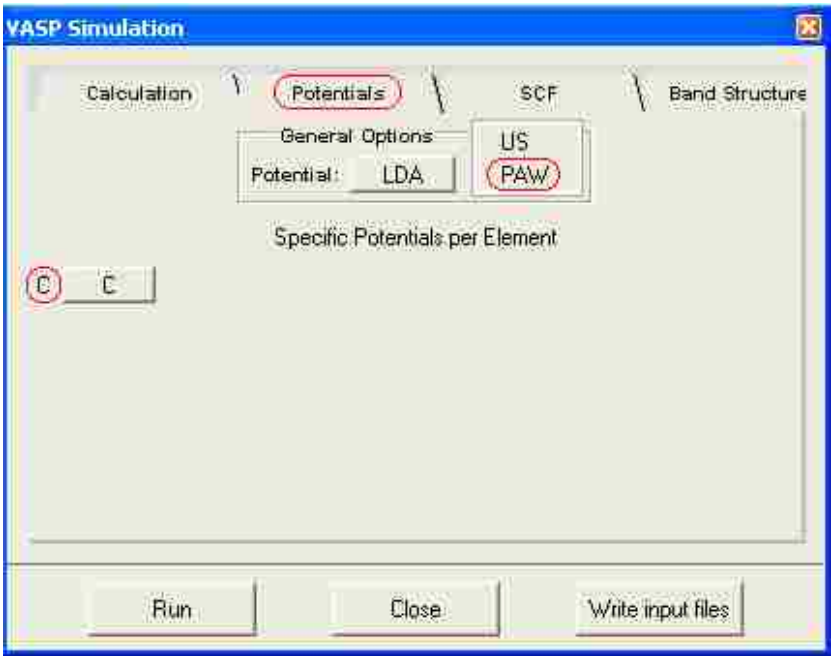

Figure B1- 2 The potential panel in VASP interface.

c) SCF

The choice of the k-mesh is an essential factor in the accuracy of the Self Consistent Field (SCF) calculation used in solving the Kohn-Sham equations. As shown in figure1B-3, one can set the k-points in the irreducible part of the Brillouin zone. In addition the panel shows the spacing of the k-points in (1/Å).

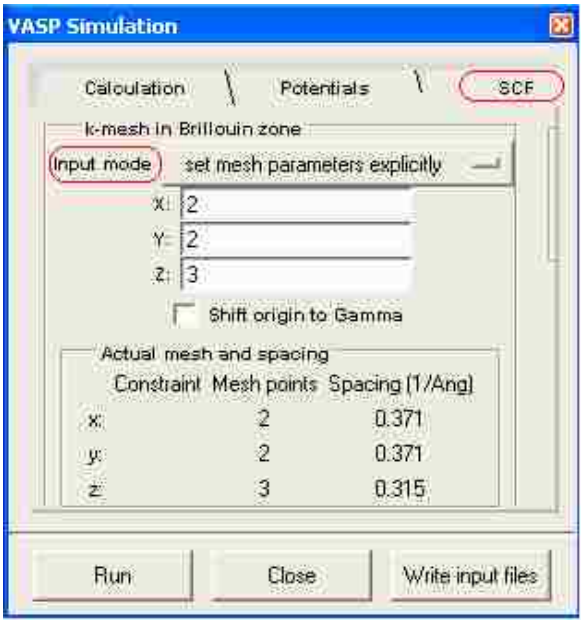

Figure B1- 3 The SCF panel in VASP interface.

d) Advanced/Restart

The advanced settings, shown in figure B1-4, govern the iterative scheme for determining the wave functions, the real or reciprocal space projection, number of bands, energy cutoff, and energy cutoff for augmentation charge.

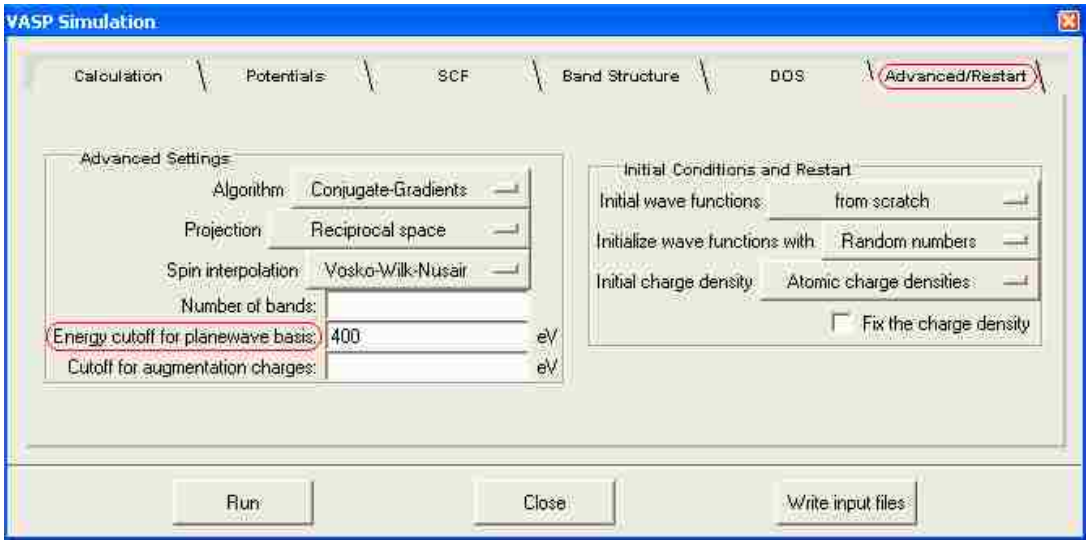

Figure B1- 4 The Advanced/Restart panel in VASP interface.

It is unlikely that the initial conditions need to be changed from their default values.

d) Preview Input

This panel, as shown in figure B1-5, allow the user to see the necessary input files for running VASP. These files are the POTCAR file which contains the pseudopotential for each atomic species used in the calculation., the INCAR file which is the main input file for VASP. It contains a large number of parameter. Most of these parameters are set as default, the KPOINTS file which contains the k-point mesh coordinates generated by Monkhorst-Pack scheme, and the POSCAR file which contains the supercell geometry matrix, and the fractional ionic positions.

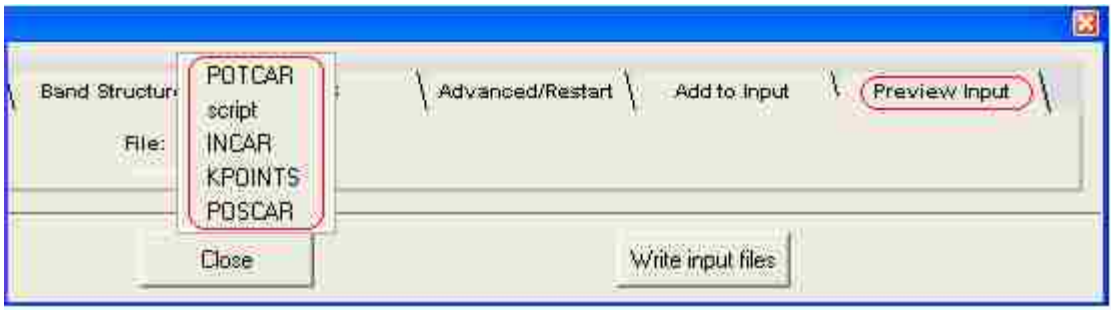

Figure B1- 5 The preview Input panel in VASP interface.

B.2- PHONON Input

The PHONON software is used to calculate the dispersion relations, phonon frequency distribution, and corresponding thermodynamical quantities. The necessary input data for PHONON are discussed below.

a) Symmetry and Unit Cell

Figure B2-1 shows the space group, the lattice parameters (in angstroms) and angles (in degrees), and the number of non-equivalent particles in the unit cell for the structure of interest (graphite in this case).

Figure B2- 1 The symmetry and unit cell inputs panel.

b) Particles Positions

The position of non-equivalent particles is given in fractional coordinates of the unit cell

basic vectors, as shown in figure B2-2. Utilizing the symmetry of the structure of interest specified by the given space group, PHONON generates the remaining. For graphite the displacive coordinates were activated by setting (x, y, z) = (1, 1, 1), and the rotational coordinates were deactivated by setting (Rx, Ry, Rz) = (0, 0, 0) .

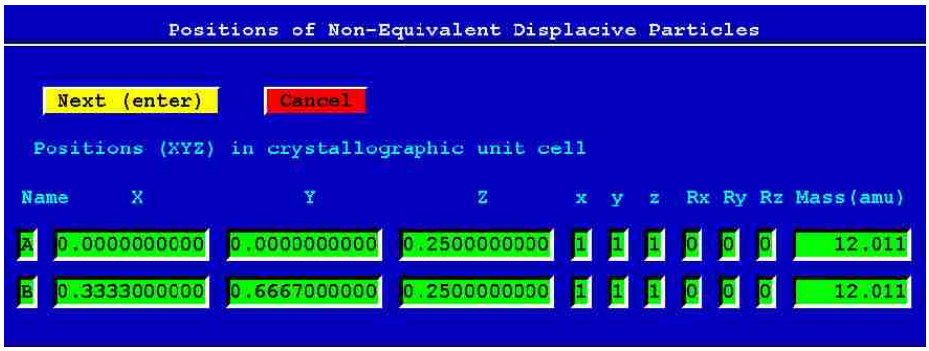

Figure B2- 2 The atomic positions and masses panel.

c) Supercell

The volume of the supercell is a multiple of the volume of the primitive unit cell. Figure B2-3 shows the transformation matrix L that is used to build the supercell S from the unit cell C. Also, the displacement in angstrom should be specified to calculate Hellmann-Feynman forces.

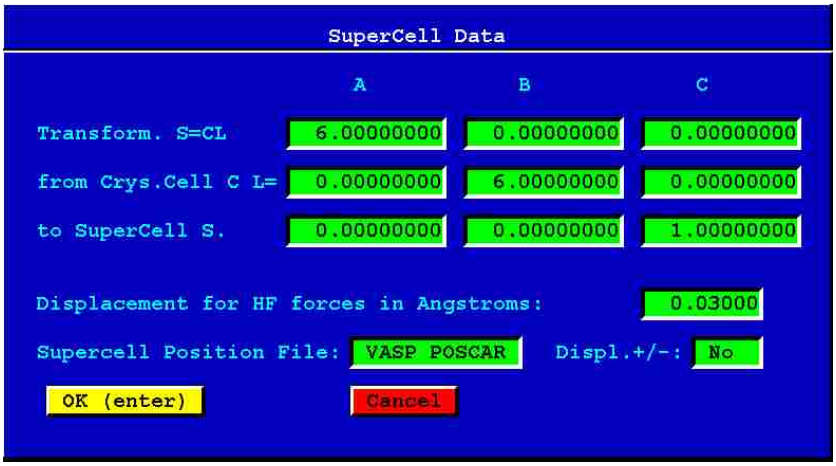

Figure B2- 3 The supercell transformation matrix panel.

Figure B2-4 shows the total number of atoms in the supercell used in the calculations. Also shown in Cartesian coordinates are the supercell lattice constants.

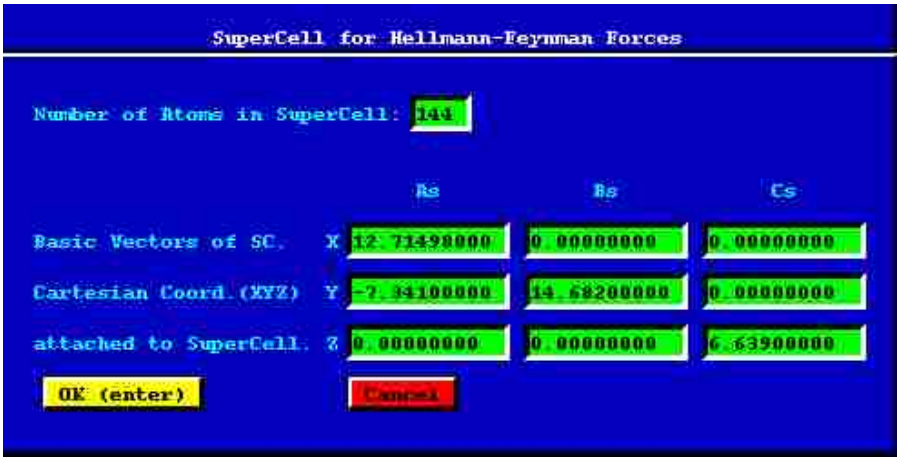

Figure B2- 4 The cartesian supercell lattice basis vectors.

d) Dispersion Relations

After importing the Hellmann-Feynman files produced by VASP, PHONON calculates the force constants, and solves the dynamical matrix along the desired direction in the Brillouin zone. Therefore, one must specify the fractional coordinates of the wave vectors, and the number of points between these vectors. In addition, PHONON is capable of providing the polarization vectors, as shown in figure B2-5.

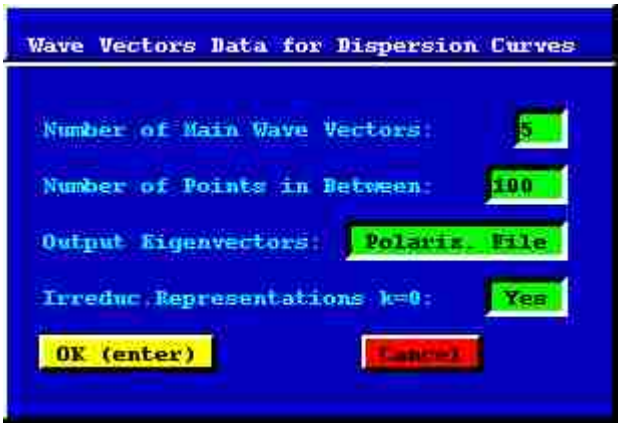

Figure B2- 5 The wave vectors, and eigenvectors panel.

Figure B2-6 shows the coordinates of the 5 wave vectors along which the dispersion relations

are calculated. Note that the symbol C# stands for Γ .

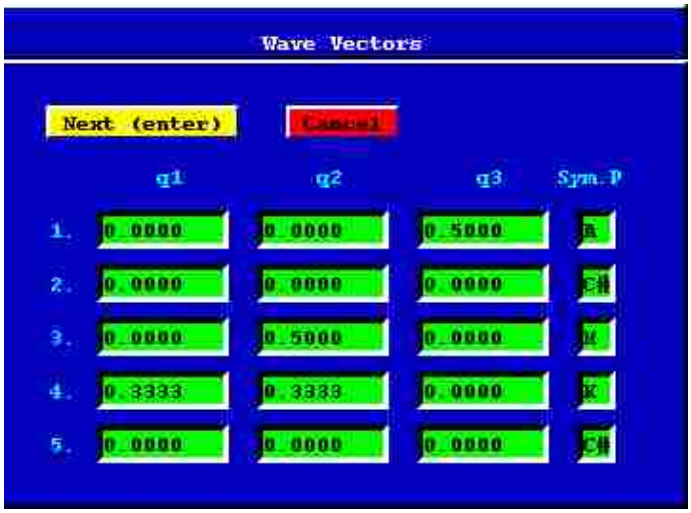

Figure B2- 6 The wave vectors coordinates panel.

e) Phonon Frequency Distribution

To generate the total and partial phonon frequency distribution, PHONON carries out Monte Carlo sampling of the k-points. One can choose small, middle, large, fine, or can specify the number of k-points explicitly (e.g., 50000 in figure B2-7). Similarly, one can choose auto frequency bin width for the phonon frequency distribution, or can specify its bin width manually.

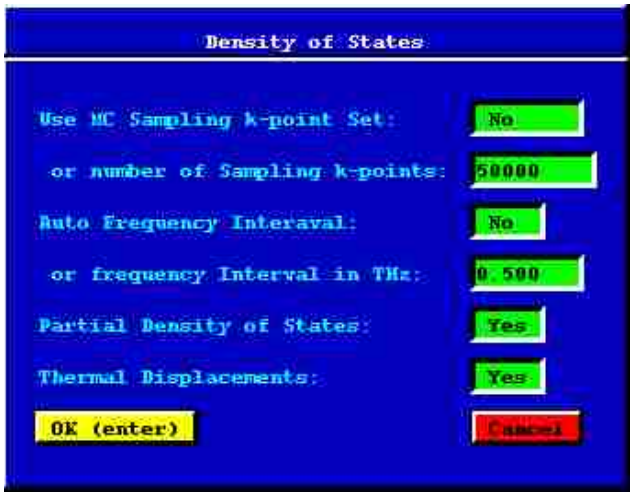

Figure B2- 7 The density of states panel.